

Department of Chemistry

Sensitisation of Lanthanide Luminescence by Rhenium  
Tetrazolato Complexes

Phillip James Wright

This thesis is presented for the degree of  
Doctor of Philosophy  
of  
Curtin University

January 2016



## **Declaration**

To the best of my knowledge and belief this thesis contains no material previously published by any other person except where due acknowledgment has been made.

This thesis contains no material which has been accepted for the award of any other degree or diploma in any university.

Signature:

Date:



# Abstract

In this investigation, mononuclear and polynuclear complexes of Re(I) combined with aryl tetrazole ligands, such as 2-(1H-tetrazol-5-yl)pyridine, were synthesised and their photophysical and electrochemical properties were investigated. The new structural motifs were reformed utilising larger ligands, such as 4'-[6-(1H-tetrazol-5-yl)pyridin-3-yl]-2,2':6',2''-terpyridine, and their properties were studied along with the ability to sensitise Ln<sup>3+</sup> emission.

Two simple aryl tetrazoles, 5-phenyl-1H-tetrazole and 2-(1H-tetrazol-5-yl)-pyridine, and their alkylated derivatives were found to form five interesting complexes when combined with [Re(CO)<sub>5</sub>X] (X = Cl, Br). Two complexes were structurally analogous to literature Re(I) diimine complexes of the type *fac*-[Re(CO)<sub>3</sub>(N<sup>^</sup>N)X] (N<sup>^</sup>N = 1,10-phenanthroline), however, the pyridyl-tetrazole chelated the metal centre in place of the diimine ligand. A "propeller" type dinuclear complex was synthesised, in which two Re(I) centres were bridged by three tetrazolato ligands, and a labile dinuclear complex was also formed, in which two Re(I) centres were bridged by a tetrazolato ligand and two Br<sup>-</sup> ligands. A unique triangular metallacalix[3]arene was synthesised, in which three Re(I) centres behaved as corners of a triangle and three pyridyl-tetrazolato ligand behaved as the edges. The complexes which were structurally similar to Re(I) diimine complexes, of the type [Re(CO)<sub>3</sub>(N<sup>^</sup>N)X], have similar photophysical and electrochemical properties ( $\lambda_{max} = 570$  nm). The triangular metallacalix[3]arene displays particularly interesting photophysical and electrochemical behaviour, where the emission band ( $\lambda_{max} = 490$  nm) is significantly blue-shifted in comparison to most reported neutral Re(I) complexes, and three reversible oxidation peaks appear in the cyclic voltammogram.

The extension of the aryl tetrazole ligands to include terpyridine moieties was successful in forming 4'-[4-(1H-tetrazol-5-yl)phenyl]-2,2':6',2''-terpyridine, 4'-[6-(1H-tetrazol-5-yl)pyridin-3-yl]-2,2':6',2''-terpyridine, and their alkylated derivatives. These ligands displayed photophysical absorption and emission properties in solution that change with the degree of acidity, which appears to be related to protonation of the tetrazolate and terpyridine moieties.

The synthesis of Re(I) complexes with tetrazole functionalised terpyridines suc-

cessfully formed three target complexes. Two mononuclear complexes were synthesised in which the tetrazole functionalised terpyridine was utilised as the ancillary ligand, these structures were similar to previously reported Re(I) tetrazolato complexes of the form  $[\text{Re}(\text{CO})_3(\text{N}^{\wedge}\text{N})\text{L}]$  (L = tetrazolate).<sup>1</sup> A triangular metallacalix[3]arene of Re(I) was also formed which was structurally similar to the aforementioned triangular assembly. The mononuclear complexes displayed photophysical and electrochemical properties similar to previously reported Re(I) tetrazolato complexes, with emission from the triplet charge transfer excited state centred at ca. 580 nm.<sup>2</sup> The triangular Re(I) complex, synthesised with a tetrazole functionalised terpyridine, displayed a red-shifted emission ( $\lambda_{em} = 510$  nm) in comparison to the previously mentioned metallacalix[3]arene, however, the quantum yield and lifetime had improved significantly which was attributed to a reduction of the non-radiative decay rate.

The Re(I) complexes of tetrazole functionalised terpyridines successfully sensitised  $\text{Eu}^{3+}$  and  $\text{Yb}^{3+}$  via energy transfer from the triplet excited state, except in one case of sensitisation of  $\text{Yb}^{3+}$  by the mononuclear Re(I) complex containing a 2-(5-tetrazolato)pyridine moiety. The sensitisation rate and efficiency were obtained by comparison of the lifetime decay of the complex in the presence of  $\text{Gd}^{3+}$  to  $\text{Eu}^{3+}$  or  $\text{Yb}^{3+}$ . Interestingly, the mononuclear complexes displayed more efficient sensitisation of  $\text{Eu}^{3+}$  ( $\phi_{EnT} = 0.26$  to  $0.38$ ), than  $\text{Yb}^{3+}$  ( $\phi_{EnT} = 0$  to  $0.30$ ). It was noted that the triangular Re(I) complex was the most efficient sensitiser of both lanthanides with a quantum efficiency greater than 0.90 in both cases.

This investigation documents novel structural motifs, including a peculiar metallacalix[3]arene, formed with a tetrazolate ligand which displays intense, near-blue, luminescence. This novel complex, when combined with  $\text{Ln}^{3+}$  cations, also gives the most efficient sensitisation of  $\text{Yb}^{3+}$  reported by a Re(I) complex and the first report of efficient sensitisation of  $\text{Eu}^{3+}$  by a Re(I) complex.

Supporting publications include:

Wright, P. J.; Muzzioli, S.; Werrett, M. V.; Raiteri, P.; Skelton, B. W.; Silvester, D. S.; Stagni, S.; Massi, M. *Organometallics* **2012**, *31*, 7566–7578

Wright, P. J.; Affleck, M. G.; Muzzioli, S.; Skelton, B. W.; Raiteri, P.; Silvester, D. S.; Stagni, S.; Massi, M. *Organometallics* **2013**, *32*, 3728–3737

Wright, P. J.; Muzzioli, S.; Skelton, B. W.; Raiteri, P.; Lee, J.; Koutsantonis, G.; Silvester, D. S.; Stagni, S.; Massi, M. *Dalton Transactions* **2013**, *42*, 8188–8191

# Acknowledgements

Firstly to Dr Max Massi, I owe a great deal of gratitude for your exquisite supervision since my first research project. Your enthusiasm for this research has been so encouraging and has helped me to think of new ways to explore this field. I have learnt so much from you, and the opportunity of living and working in Italy was an amazing experience that I am so grateful for.

To Assoc Prof. Stefano Stagni and Dr Sara Muzzioli, thank you for all the advice and help during my research stay in Italy. It was great to be with such knowledgeable and positive people. Further, my biggest thank you to all the friendly Italians, you guys aren't as bad as you look. You made my stay in Italy one of the most enjoyable experiences i've had in my life.

Thank you also to Dr Paolo Raiteri, you have helped to explain the unexplainable, thank you for helping me with the computational chemistry. Without having your programs, advice, and help with the scripts this part of the research would have been an impossible task.

Thank you also to every one else at Curtin, UWA, and Bologna for help with other areas of the research. To the electrochemistry group, thank you for letting me use your instruments and time to analyse my samples. Thank you to Ching, Chappy, Rob, and Grant for making sure that Curtin chem is functioning. Thanks also to Brian and Alexandre at UWA for all of the crystal structure analysis.

Also thanks to the research group here at Curtin, particularly Brodie, this has been such an entertaining experience, and I have all you guys to thank for it.

I also want to thank my friends and family for their encouragement, support, and time to enjoy during the times away from research.

Most of all I want to thank Lauren Brand, meeting you was the greatest thing that could have happened to me. You have been the greatest support and source of encouragement. Thank you for sticking by me and also for the infinite supply of chocolatey things.



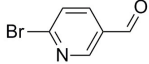
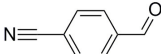
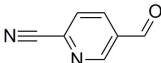
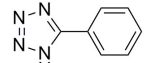
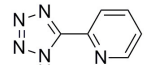
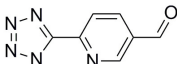
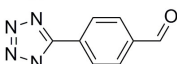
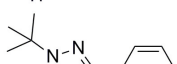
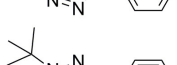
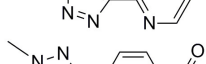
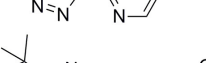

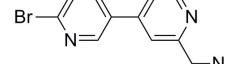


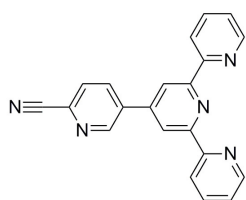
# Commonly used Abbreviations and Symbols

$\tau$	Emission lifetime
$\phi$	Quantum yield
$\lambda$	Peak wavelength
$\varepsilon$	Molar absorptivity
B3LYP	Becke 3 exchange with Lee, Yang, Parr correlation functional
ca.	circa/approximately
CAM-B3LYP	Coulomb attenuated method B3LYP
C6mim[FAP]	1-hexyl-3-methylimidazolium tris(pentafluoroethyl)trifluorophosphate
<b>bipy</b>	2,2-bipyridine
CDCl <sub>3</sub>	Deuterated chloroform
DCM	Dichloromethane
dec.	Decomposition
DFT	Density functional theory
DMSO	Dimethylsulphoxide
eV	Electron volt
$E_{pf}$	Potential of peak in forward scan
$E_p$	Half wave potential
$E_{pr}$	Potential of peak in return scan
EnT	Energy transfer
ES	Excited state
Fc	Ferrocene
Fc/Fc <sup>+</sup>	Ferrocene/Ferrocenium <sup>+</sup> couple
FRET	Förster resonance energy transfer
GS	Ground state

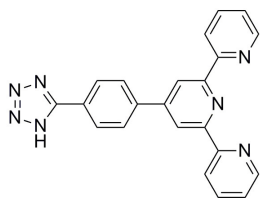
HF	Hartree Fock
HOMO	Highest occupied molecular orbital
$i_{pf}$	Peak current of forward scan
$i_{pr}$	Peak current of return scan
IC	Internal Conversion
IL	Intra-ligand
IR	Infra-red
ISC	Inter-system crossing
J	Coupling constant (NMR)
$k_{EnT}$	Energy transfer rate
$k_{nr}$	Non-radiative decay rate constant
$k_r$	Radiative decay rate constant
LED	Light emitting device
LLCT	Ligand to ligand charge transfer
LMCT	Ligand to metal charge transfer
LUMO	Lowest unoccupied molecular orbital
MC	Metal centred
MLCT	Metal to Ligand Charge Transfer
MLLCT	Metal-ligand to ligand charge transfer
NIR	Near infra-red
NMR	Nuclear magnetic resonance
<b>phen</b>	1,10-phenanthroline
r.t.	Room temperature
RTIL	Room temperature ionic liquid
SALC	Symmetry adapted linear combination
TBAPF <sub>6</sub>	Tetrabutylammonium hexafluorophosphate
TCSPC	Time correlated single photon counting
TDDFT	Time dependent density functional theory
VR	Vibrational relaxation

# Commonly used abbreviations of compounds

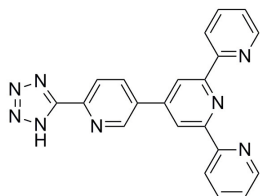
	BrPyCHO
	NCP <sub>h</sub> CHO
	NCPyCHO
	HTzPh
	HTzPy
	HTzPyCHO
	HTzPhCHO
	<i>t</i> BuTzPh
	<i>t</i> BuTzPy
	MeTzPyCHO
	<i>t</i> BuTzPhCHO
	BrPyTpy
	NCTzPhTpy



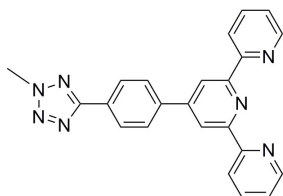
NCPyTpy



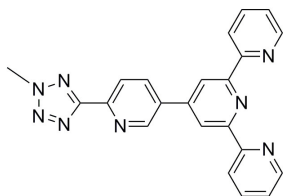
HTzPhTpy



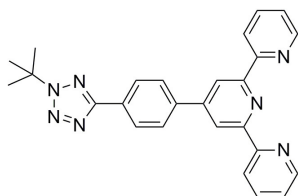
HTzPyTpy



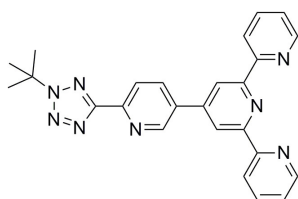
MeTzPhTpy



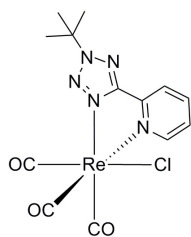
MeTzPyTpy



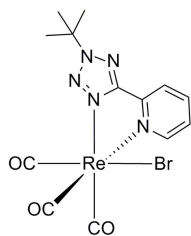
*t*BuTzPhTpy



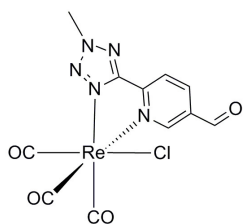
*t*BuTzPyTpy



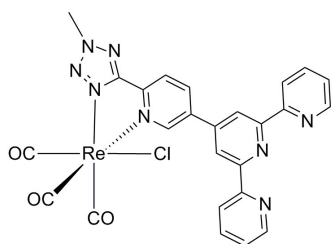
[Re(<sup>t</sup>BuTzPy)Cl]



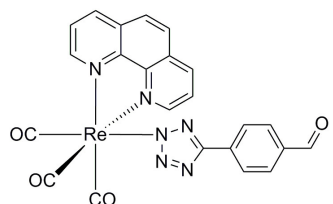
[Re(<sup>t</sup>BuTzPy)Br]



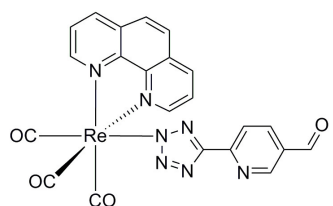
[Re(MeTzPyCHO)Cl]



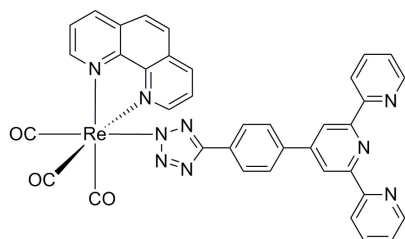
[Re(MeTzPyTpy)Cl]



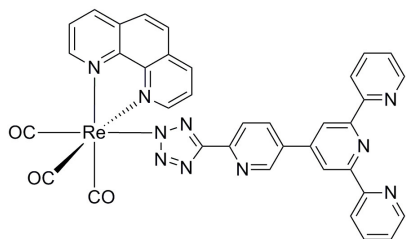
[Re-TzPhCHO]



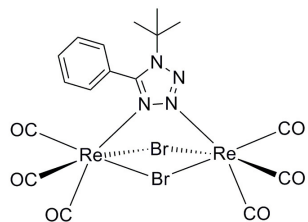
[Re-TzPyCHO]



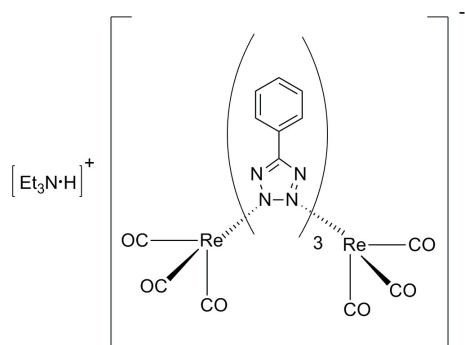
[Re-TzPhTpy]



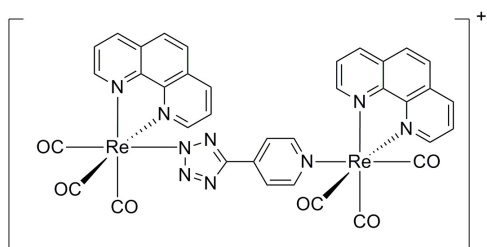
$[\text{Re-TzPyTpy}]$



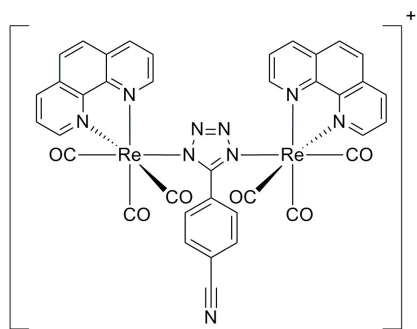
$[\text{Re}_2(\text{}^t\text{BuTzPh})\text{Br}_2]$



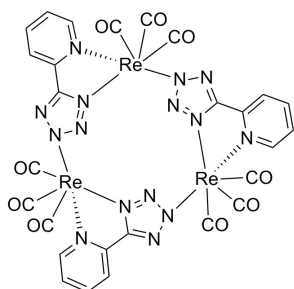
$[\text{HNEt}_3][\text{Re}_2(\text{TzPh})_3]$   
 $[\text{Re}_2(\text{TzPh})_3]^-$



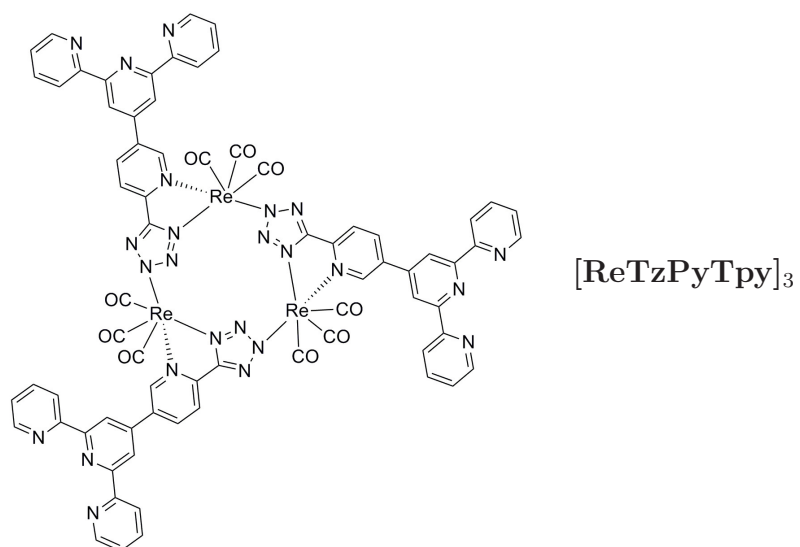
$[\text{Re-TzpPy-Re}]^+$



$[\text{Re}_2\text{TzPhCN}]^+$



$[\text{ReTzPy}]_3$







# Contents

<b>Abstract</b>	<b>i</b>
<b>Acknowledgements</b>	<b>iii</b>
<b>Commonly used Abbreviations and Symbols</b>	<b>v</b>
<b>Commonly used abbreviations of compounds</b>	<b>vii</b>
<b>1 Introduction</b>	<b>1</b>
1.1 Luminescent metal complexes . . . . .	1
1.2 Luminescent Re(I) complexes . . . . .	2
1.3 Photophysical properties of d-metal complexes . . . . .	5
1.3.1 Fundamental concepts of electronic transitions . . . . .	5
1.3.2 Selection rules for electronic transitions . . . . .	6
1.3.3 The fate of the excited state . . . . .	6
1.3.4 Energy transfer . . . . .	8
1.3.5 Electronic structure of Re(I) complexes and related transi- tions . . . . .	9
1.3.6 Modulation of photophysical properties of Re(I) complexes	12
1.4 Multinuclear metal complexes . . . . .	14
1.4.1 Multinuclear d-d complexes . . . . .	14
1.4.2 Multinuclear Re(I) complexes . . . . .	15
1.4.3 Multinuclear d-f complexes . . . . .	17
1.5 Tetrazolato complexes . . . . .	21
1.6 Computational Quantum Mechanics . . . . .	23
1.6.1 Theoretical Background . . . . .	23
1.6.2 Molecular Orbitals and the Hartree-Fock Approximation .	25
1.6.3 Density Functional Theory and Kohn-Sham equations . . .	26
1.6.4 Functionals and Level-of-Theory . . . . .	28
1.6.5 Basis Sets . . . . .	28
1.6.6 Time-Dependent Density Functional Theory . . . . .	29
1.7 This investigation and scope . . . . .	30

<b>2</b>	<b>Ligand modulated structural diversity</b>	<b>33</b>
2.1	Introduction . . . . .	33
2.2	Chapter goal . . . . .	34
2.3	Synthesis of aryl-tetrazole ligands . . . . .	35
2.3.1	Aryl-tetrazole synthesis . . . . .	35
2.3.2	Alkylated tetrazole synthesis . . . . .	35
2.4	Synthesis of Re(I) complexes . . . . .	36
2.4.1	Synthesis of Re(I) complex with <b><i>t</i>BuTzPy</b> . . . . .	36
2.4.2	Synthesis of Re(I) complex using <b><i>t</i>BuTzPh</b> . . . . .	37
2.4.3	Synthesis of Re(I) complex with <b>HTzPh</b> . . . . .	38
2.4.4	Synthesis of Re(I) complex with <b>HTzPy</b> . . . . .	40
2.5	Photophysical and computational investigation . . . . .	42
2.5.1	Absorption and computational results . . . . .	42
2.5.2	Emission properties of the complexes . . . . .	52
2.6	Electrochemical investigation . . . . .	55
2.7	Conclusion . . . . .	58
<b>3</b>	<b>Functionalisation of tetrazole ligands with terpyridine</b>	<b>61</b>
3.1	Introduction . . . . .	61
3.2	Synthesis of aryl-tetrazole functionalised terpyridines . . . . .	63
3.2.1	Phenyl-tetrazole functionalised terpyridine . . . . .	63
3.2.2	Alkylation of <b>HTzPhTpy</b> . . . . .	65
3.2.3	Pyridyl-tetrazole functionalised terpyridine . . . . .	67
3.2.4	Alkylation of <b>HTzPyTpy</b> . . . . .	71
3.3	Photophysical properties . . . . .	73
3.4	Modulation of the photophysical properties in acidic or alkali conditions . . . . .	75
3.5	Conclusion . . . . .	91
<b>4</b>	<b>Terpyridine-functionalised Re(I) tricarbonyl tetrazolato complexes</b>	<b>93</b>
4.1	Introduction . . . . .	93
4.2	Synthesis of the target complexes . . . . .	95
4.2.1	Synthesis of [ <b>Re-TzPhTpy</b> ] and [ <b>Re-TzPyTpy</b> ] . . . . .	95
4.2.2	Synthesis of [ <b>ReTzPyTpy</b> ] <sub>3</sub> . . . . .	99
4.2.3	Synthesis of [ <b>Re(MeTzPyTpy)Cl</b> ] . . . . .	101
4.3	Photophysical and computational investigation . . . . .	103
4.4	Electrochemical properties of the synthesised complexes . . . . .	113
4.5	Conclusion . . . . .	115

<b>5</b>	<b>Sensitisation of red-emitting <math>\text{Eu}^{3+}</math> and NIR-emitting <math>\text{Yb}^{3+}</math></b>	<b>117</b>
5.1	Introduction . . . . .	117
5.1.1	f-block metals . . . . .	117
5.1.2	Photophysical properties and spectra of trivalent lanthanide ions . . . . .	117
5.1.3	Sensitisation of lanthanides . . . . .	119
5.1.4	Methodology for the assessment of $\text{Eu}^{3+}$ and $\text{Yb}^{3+}$ sensitisation. . . . .	121
5.2	Photophysical properties of ligands in the presence of $\text{Ln}^{3+}$ . . . . .	122
5.2.1	Emission from ligands in the presence of $\text{Gd}^{3+}$ . . . . .	122
5.2.2	Sensitisation of $\text{Eu}^{3+}$ emission by the ligands. . . . .	123
5.2.3	Sensitisation of $\text{Yb}^{3+}$ by the synthesised ligands. . . . .	126
5.3	Photophysical properties of the Re(I) complexes in the presence of $\text{Ln}^{3+}$ . . . . .	128
5.3.1	Absorption and emission properties of the synthesised complexes in the presence of $\text{Gd}^{3+}$ . . . . .	128
5.3.2	Computational Investigation . . . . .	136
5.3.3	Determination of triplet state energy of the complexes in the presence of $\text{Gd}^{3+}$ . . . . .	143
5.3.4	Sensitisation of $\text{Eu}^{3+}$ by the Re(I) complexes. . . . .	145
5.3.5	Sensitisation of $\text{Yb}^{3+}$ by the synthesised complexes. . . . .	153
5.4	Conclusion . . . . .	160
<b>6</b>	<b>Conclusions and future work</b>	<b>161</b>
<b>7</b>	<b>Experimental</b>	<b>165</b>
	<b>References</b>	<b>179</b>
	<b>Appendix A</b>	<b>201</b>

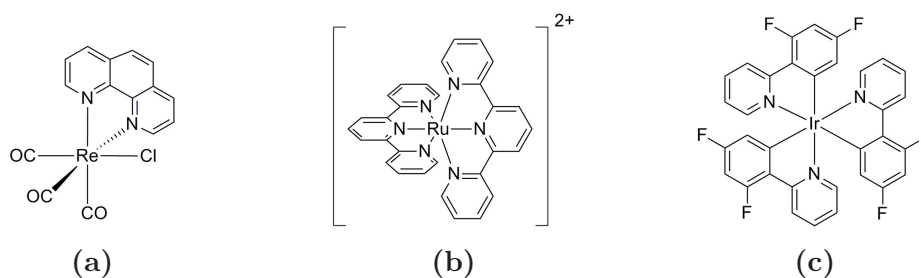


# Chapter 1

## Introduction

### 1.1 Luminescent metal complexes

Photophysical studies of metal complexes, such as those of Re(I), Ir(III), Ru(II), Au(I), Pt(II), and Ln<sup>3+</sup> cations, have garnered a great deal of attention in scientific literature. The research focus into such complexes is due to their potential applications in light emitting devices,<sup>3-5</sup> cellular labelling,<sup>6-14</sup> sensors,<sup>15-18</sup> photovoltaics,<sup>19</sup> photocatalysts,<sup>20-24</sup> and energy transfer applications.<sup>25-35</sup>

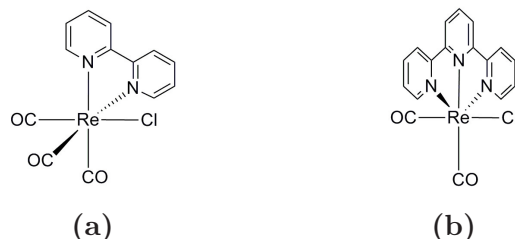


**Figure 1.1:** Example of luminescent complexes: a) Re(I). b) Ru(II). c) Ir(III).

In the case of d-metal complexes, such as those shown in Figure 1.1, the photophysical properties ( $\epsilon$ ,  $\lambda_{abs}$ ,  $\lambda_{em}$ ,  $\phi$ , and  $\tau$ ) are tunable by chemical modification of the coordinated ligands.<sup>36</sup> The modifications of the ligands also leads to physical and chemical property changes.<sup>37,38</sup> Complexes which contain Ln<sup>3+</sup> cations, however, have emission spectra largely independent of the chemical environment due to the "inner core" nature of the 4f electrons. Research into transition metal and lanthanide complexes therefore attempt to optimise their properties for specific applications.<sup>39</sup>

## 1.2 Luminescent Re(I) complexes

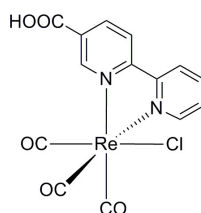
Among the d-metals utilised in luminescent studies, Re(I) diimine type complexes have received a great deal of attention since their photophysical properties were explicated in 1974.<sup>40–43</sup> Of the photophysically active Re(I) complexes, many are of the form *fac*-[Re(CO)<sub>3</sub>(N<sup>^</sup>N)L]<sup>0/+</sup> (Figure 1.2a) with some exceptions forming other coordination modes (Figure 1.2b).<sup>44,45</sup>



**Figure 1.2:** Example of different coordination modes of Re(I) complexes. a) *facial* coordination of CO ligands. b) *meridional* coordination of a terpyridine ligand.<sup>44</sup>

In a photophysical study of the coordination modes illustrated in Figure 1.2, it was found that the complex in Figure 1.2a displayed luminescence in solution. However, the complex shown in Figure 1.2b did not. The change in the photophysical properties was found to be dependent on the structure of the complex,<sup>44</sup> and due to the luminescence properties of Re(I) complexes with *facially* coordinated CO ligands, such as the complex shown in Figure 1.2a, many photophysical investigations of Re(I) utilise this structural motif.

The relationship between structural and photophysical properties has resulted in studies of Re(I) complexes that may be used as sensors to external stimuli.<sup>46–48</sup>

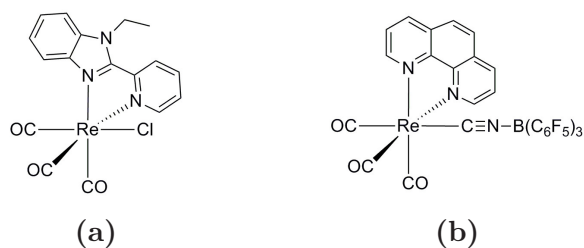


**Figure 1.3:** Example Re(I) diimine complex utilised for as a pH dependent probe.<sup>49</sup>

Zaccheroni *et al.* synthesised a complex sensitive to pH changes in solution (Figure 1.3), and it was found that at low pH (2.5) the complex displayed an emission at 648 nm with low quantum yield ( $\phi = 0.0002$ ) and very short lifetime ( $\tau = 0.5$  ns). As the pH was increased (up to 8) the emission blue-shifted ( $\lambda_{em} = 625$  nm) and the quantum yield and lifetime increased ( $\phi = 0.002$ ,  $\tau = 7$  ns). It was

concluded that at low pH the carboxylic acid was protonated, and at higher pH the carboxylic acid would be deprotonated and a negative charge would be placed on the bipyridine ligand. This negative charge increased the energy necessary to transfer an electron from the Re(I) centre to the bipyridine ligand resulting in the blue-shift of emission wavelength and increase in quantum yield and lifetime. This was confirmed when an analogous complex, where an ester moiety was used in place of the carboxylic acid, did not show any variation in luminescence under the same conditions.<sup>49</sup>

The relationship between structural and photophysical properties of Re(I) complexes has also been studied in light emitting device (LED) applications.<sup>10,50–53</sup> In studies of vacuum sublimable Re(I) complexes in LEDs, the target complex must be stable to thermal deposition and display targeted photophysical characteristics. Several investigations have obtained complexes of Re(I) with high electroluminescence performance.<sup>54,55</sup>

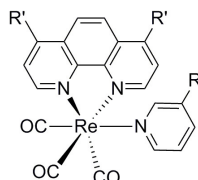


**Figure 1.4:** Example Re(I) complexes utilised for vacuum sublimation into luminescent devices. a) Orange red LED.<sup>56</sup> b) Sky-blue LED.<sup>57</sup>

Figure 1.4a illustrates one of the first complexes investigated in this area.<sup>56</sup> This complex has an emission maximum at 606 nm in DCM solution and 573 nm in the constructed LED. It was concluded this blue-shift in emission wavelength was a result of the rigidochromic effect. The device formed with this complex exhibited a low turn on voltage of 3 V, maximum efficiency of 0.09 % photons/electrons, and power efficiency of 0.2 lm/W.<sup>56</sup> The blue-shift caused by the rigidochromic effect assists in the formation of blue coloured devices, and a recent investigation obtained blue emitting vacuum sublimable Re(I) complexes.<sup>57</sup> The synthesised isocyanoborate complex shown in Figure 1.4b displayed emission wavelengths of 538 nm in solution and 515 nm in the constructed device. The emission of this complex in solution is blue-shifted in comparison to typical Re(I) diimine complex, which was attributed to the  $\pi$  accepting strength of the isocyanoborate ligand. This complex exhibited high electroluminescence performance with a turn on voltage of 5.5 V, maximum quantum efficiency of 3.7 %, and power efficiency of 5.3 lm/W.

The ability to modify physical properties of Re(I) complexes while maintaining

luminescence has been exploited in biological imaging applications.<sup>58-61</sup> The application of Re(I) complexes in biological imaging is promoted by a few important photophysical properties. These complexes typically have large Stokes shift, long emission lifetime, and are considered photostable in comparison to organic labels, which are often prone to photobleaching during analysis. Large Stokes shifts and long emission lifetime allows better contrast of the label with scattered light and autofluorescence of endogenous species.<sup>62-69</sup>



**Figure 1.5:** Example Re(I) complex utilised in cellular imaging studies, where  $R = \text{H}, \text{CH}_2\text{OH}$  and  $R' = \text{H}, \text{PhSO}_3^-$ .<sup>4</sup>

Coogan *et al.* synthesised a library of Re(I) complexes, with an example shown in Figure 1.5 for studying cellular uptake, toxicity and luminescence in *Spironucleus vortens*, a parasitic flagellate. It was found that the complexes retained their photophysical properties when incubated in cells, however the different structures varied in their photostability and toxicity in cells. Thus it was concluded that the toxicity of Re(I) complexes, and their emission properties in cells, would vary with the coordinated ligands.

The research into luminescent Re(I) complexes suggests that they may have the potential for application, and further investigations attempt to manipulate the relevant properties of the complexes. Literature reports of multinuclear complexes of Re(I) are quite scarce in comparison to investigations involving mononuclear complexes. Hence, the work in this thesis will attempt to broaden the research into the synthesis and properties of multinuclear Re(I) complexes.



## 1.3 Photophysical properties of d-metal complexes

### 1.3.1 Fundamental concepts of electronic transitions

The absorption of light by a molecule dissolved in solution is described by the Beer-Lambert law, Equation 1.1,

$$I = I_0 \times 10^{\epsilon bc} \quad (1.1)$$

where  $I$  is the intensity of the transmitted radiation (at a given wavelength),  $I_0$  is the intensity of the incoming radiation (at the given wavelength),  $\epsilon$  is the molar absorptivity coefficient,  $b$  is the optical path, and  $c$  is the concentration. The molar absorptivity coefficient ( $\epsilon$ ) describes the propensity for a compound to absorb a specific wavelength of light.

The absorption of light of appropriate energy excites a molecule to an electronically excited state. From this excited state, the molecule can undergo a chemical reaction or a photophysical process such as emission or non-radiative decay. In this study, only radiative and non-radiative decay processes are considered. The decay constants are given as  $k_r$  and  $k_{nr}$ , respectively. The overall decay rate of the species from the excited state will therefore be a sum of the decay rates, and the lifetime of the excited state ( $\tau$ ) will be the inverse of the sum of these rates, as shown in Equation 1.2.

$$\tau = \frac{1}{k_r + k_{nr}} \quad (1.2)$$

The quantum yield of emission ( $\phi$ ) is described in Equation 1.3.

$$\phi = \frac{\text{number of emitted photons}}{\text{number of absorbed photons}} \quad (1.3)$$

The quantum yield is therefore a proportion of the rate of radiative decay to the overall decay from the excited state as shown in Equation 1.4 and 1.5, and the rate of non-radiative decay can be described similarly in Equation 1.6

$$\phi = \frac{k_r}{k_r + k_{nr}} \quad (1.4)$$

$$\phi = k_r \tau \quad (1.5)$$

$$(1 - \phi) = k_{nr} \tau \quad (1.6)$$

### 1.3.2 Selection rules for electronic transitions

The probability of an electronic transition occurring is governed by selection rules, which are based on electronic wavefunction symmetry, overlap, and multiplicity of states. Based on these selection rules, a transition is considered to be forbidden or allowed. These selection rules apply for excitation and emission transitions.

The LaPorte selection rule applies to centrosymmetric molecules and states that transitions between states of the same parity are forbidden. This selection rule can be relaxed by asymmetric vibrations of the molecule, which remove the centre of inversion. This process is termed "vibronic coupling". As a consequence, forbidden transitions may be observed, such as d-d transitions in octahedral metal complexes.

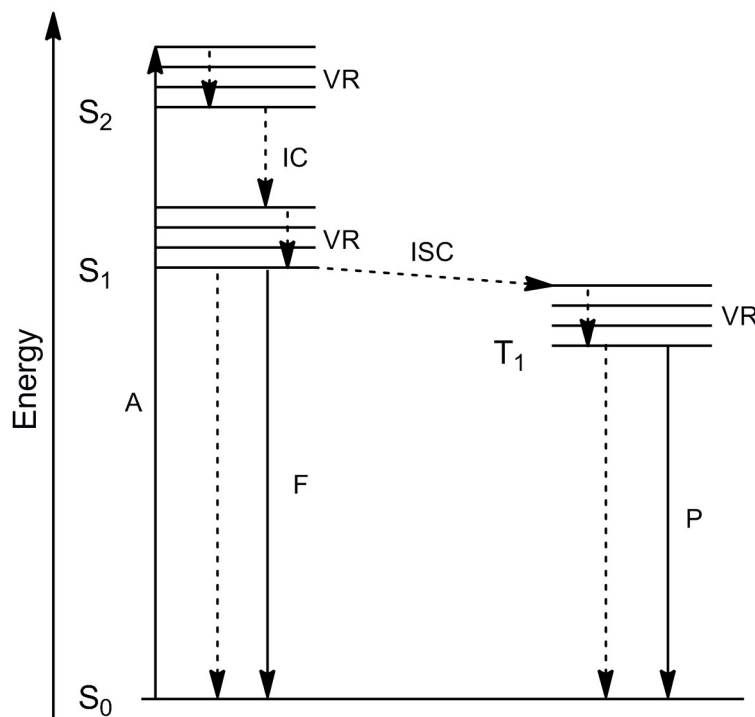
The spin selection rule states that transitions that include a change in spin multiplicity are forbidden. However, in the case of complexes with heavy atoms, the spin selection rule can be relaxed. In the presence of heavy atoms the magnetic moment vector produced from the orbit and the spin of the electron are no longer isolated, resulting in what is known as spin-orbit coupling (SOC). Strong SOC favours the mixing of states with different multiplicity, and transitions between these two states becomes more probable.

### 1.3.3 The fate of the excited state

Upon absorption of a photon, a molecule will typically be in an upper vibrational level of an electronically excited state, in accordance with the Franck-Condon principle. The most rapid occurring event is vibrational relaxation, where vibrational energy gained in the electronic transition is redistributed and the molecule moves to the lowest vibrational level of the electronic excited state. This is illustrated in Figure 1.6 as a dashed arrow labelled VR.<sup>70</sup>

Non-radiative decay between electronically excited states is separated into two types. A transition between states of the same spin multiplicity is known as internal conversion, this is shown in Figure 1.6 as a dashed line between the  $S_2$  and  $S_1$  states labelled IC. A non-radiative transition between states of different spin multiplicities is known as inter-system crossing, this is illustrated in Figure 1.6 as a transition from  $S_1$  to  $T_1$  labelled ISC. ISC is considered a forbidden transition as it violates the spin selection rule.<sup>70,71</sup>

Non-radiative decay is governed by the overlap of the lowest vibrational level of the electronically excited state with the vibrational levels of the ground state. The overlap of these levels is related to the energy gap between the excited state and the ground state. This relationship of energy and non-radiative decay is



**Figure 1.6:** Jablonski diagram illustrating the processes of absorption (A), vibrational relaxation (VR), internal conversion (IC), inter-system crossing (ISC), fluorescence (F), and phosphorescence (P). F and P are shown with radiative and non-radiative processes as solid and dashed arrows, respectively.

commonly known as the energy gap law, and it is shown in Equation 1.7

$$k_{nr} = Ae^{-\alpha\Delta E} \quad (1.7)$$

where  $k_{nr}$  is the rate of non-radiative decay, A is the pre-exponent coefficient,  $\alpha$  is a proportionality constant, and  $\Delta E$  is the energy gap between the two states. Equation 1.7 basically states that the greater the energy gap between the two states, the slower the non-radiative decay rate.<sup>36</sup>

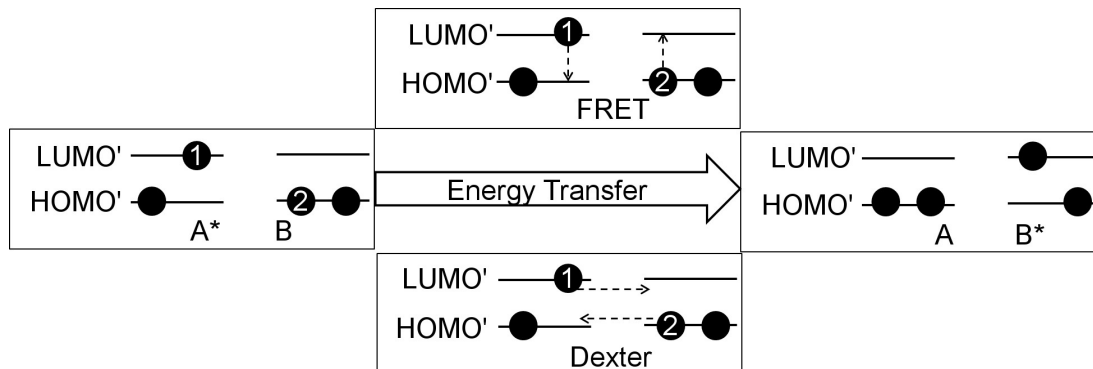
Along with non-radiative decay pathways, such as those described above, an excited state can also transition to the ground state by the spontaneous emission of a photon. This process is termed radiative decay, and radiative transitions can be separated into two types. Transitions involving no change in spin are described as *fluorescence* and are shown as F in Figure 1.6. A radiative transition involving a change in spin is described as *phosphorescence*, shown as P in Figure 1.6. In heavy metal complexes such as Re(I) the presence of the heavy metal induces spin-orbit coupling, relaxing the spin selection rule.<sup>70,71</sup>

Due to the relaxation processes of the excited species after absorption of a photon, the emitted photon is typically of longer wavelength, or lower energy, than that of

the absorbed photon. This difference between measured absorption wavelength and emission wavelength is known as the Stokes shift.

### 1.3.4 Energy transfer

To add further to the fate of the excited state of a molecule, it is possible that the excited state will relax to the ground state by transfer of energy to another species.



**Figure 1.7:** Representation of energy transfer mechanisms adapted from Balzani *et al.*<sup>70</sup> Where two species "A" and "B", are undergoing energy transfer through Förster resonance energy transfer (FRET) or Dexter energy transfer.

Energy transfer can be classified as coulombic (Förster) energy transfer and exchange (Dexter) energy transfer, which are illustrated in Figure 1.7. The overall rate of energy transfer between two excited states is potentially a combination of both contributions.

Förster resonance energy transfer is considered a long range mechanism and does not require the entities to be in physical contact, i.e bound together.<sup>70</sup>

$$k_{en}^F = 8.8 \times 10^{-25} \frac{K^2 \phi}{n^4 r_{AB}^6 \tau} J_F \quad (1.8)$$

$$J_F = \frac{\int F(\bar{\nu}) \varepsilon(\bar{\nu}) / \bar{\nu}^4 d\bar{\nu}}{\int F(\bar{\nu}) d\bar{\nu}} \quad (1.9)$$

The above equations describe the rate of FRET to be inversely dependent to the separation between the species to the sixth power  $r_{AB}^6$  and the Förster overlap ( $J_F$ ). The Förster overlap is considered to be the term of major significance, and is primarily a function of the overlap of the emission spectrum of the donor and the absorption spectrum of the acceptor. Other terms  $K^2$ ,  $\phi$ ,  $n$ , and  $\tau$  relate to the dipole dipole interaction ( $\frac{2}{3}$  for random orientation), quantum yield of the donor, refractive index, distance between donor-acceptor, and lifetime of the donor, respectively.

The exchange mechanism (Dexter) can be considered as a two-electron transfer process between the donor and the acceptor. In this process one electron is transferred from the LUMO of the donor to the LUMO of the acceptor, and one electron is transferred from the HOMO of the acceptor to the HOMO of the donor.<sup>70</sup>

$$k_{en}^D = \frac{4\pi^2}{h} (H^{en})^2 J_D \quad (1.10)$$

$$J_D = \frac{\int F(\bar{\nu})\varepsilon(\bar{\nu})d\bar{\nu}}{\int F(\bar{\nu})d\bar{\nu} \int \varepsilon(\bar{\nu})d\bar{\nu}} \quad (1.11)$$

In the Dexter energy transfer mechanism, the rate of energy transfer ( $k_{en}^D$ ) relates to the overlap of the electronic wavefunctions of the donor and acceptor ( $H^{en}$ ) and the Dexter overlap integral ( $J_D$ ). The Dexter overlap integral relates to the overlap of the normalised emission spectra of the donor, and the normalised absorption spectra of the acceptor.<sup>70</sup> The wavefunction overlap generally requires an overlap of orbitals for electron transfer to occur, and this term is dependent on properties of the system such as two species separated by space or a bridging ligand.

This mechanism of energy transfer is particularly important in regards to quenching processes. In the case of species where the lowest excited state is a triplet, collisions with ground state triplet oxygen can quench the excited state via Dexter energy transfer. A comparison of the lifetime and quantum yield in air-equilibrated/deoxygenated solutions will generally indicate if the complex undergoes quenching by triplet oxygen. Also detection of emission from  $^1\text{O}_2$  at 1275 nm is suggestive of this process.<sup>72</sup>

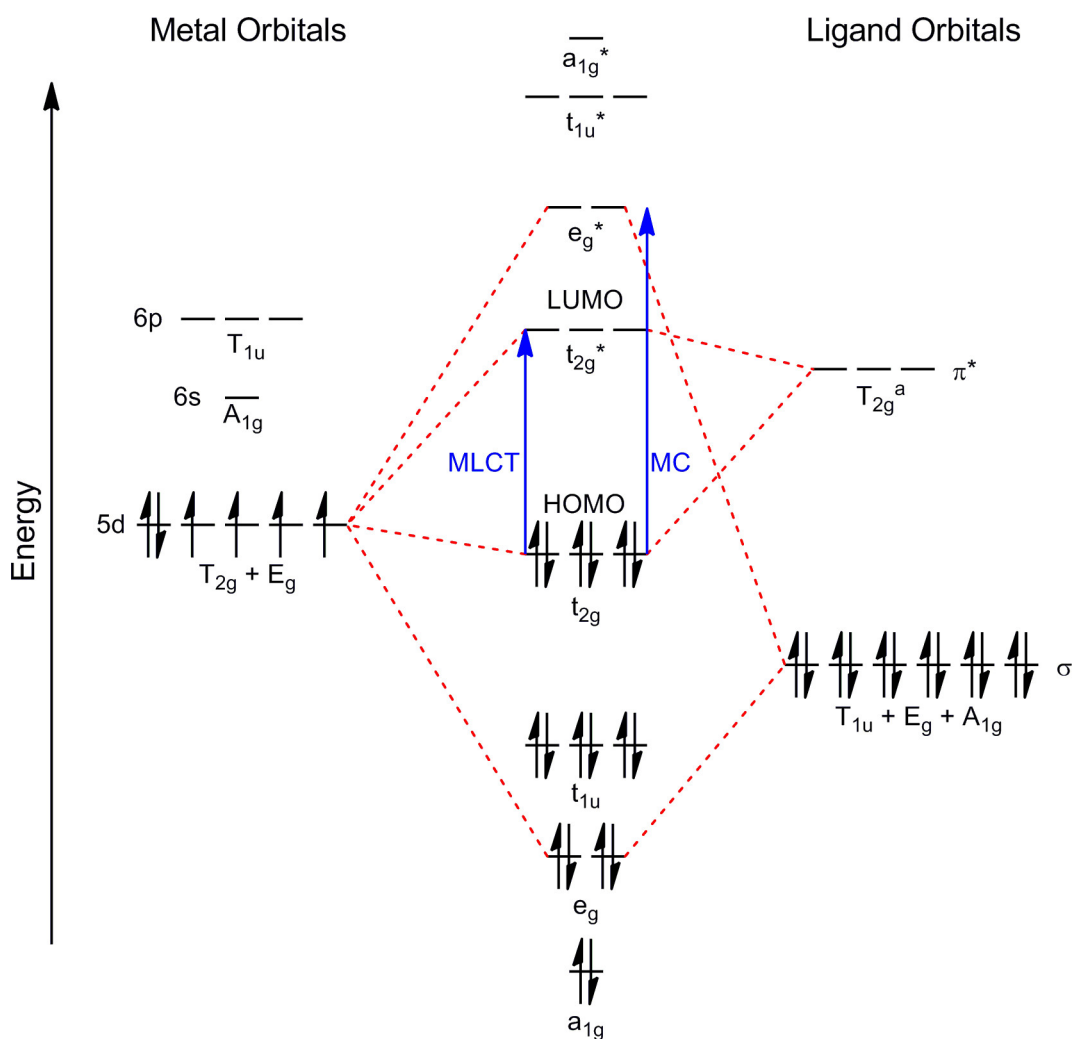
### 1.3.5 Electronic structure of Re(I) complexes and related transitions

The electronic states, such as the excited states and ground state, correspond to different electronic structures of a particular complex. In the case of a low spin  $d^6$  "octahedral" complex, such as those of Re(I), a simplified molecular orbital diagram can be constructed as shown in Figure 1.8.<sup>60</sup>

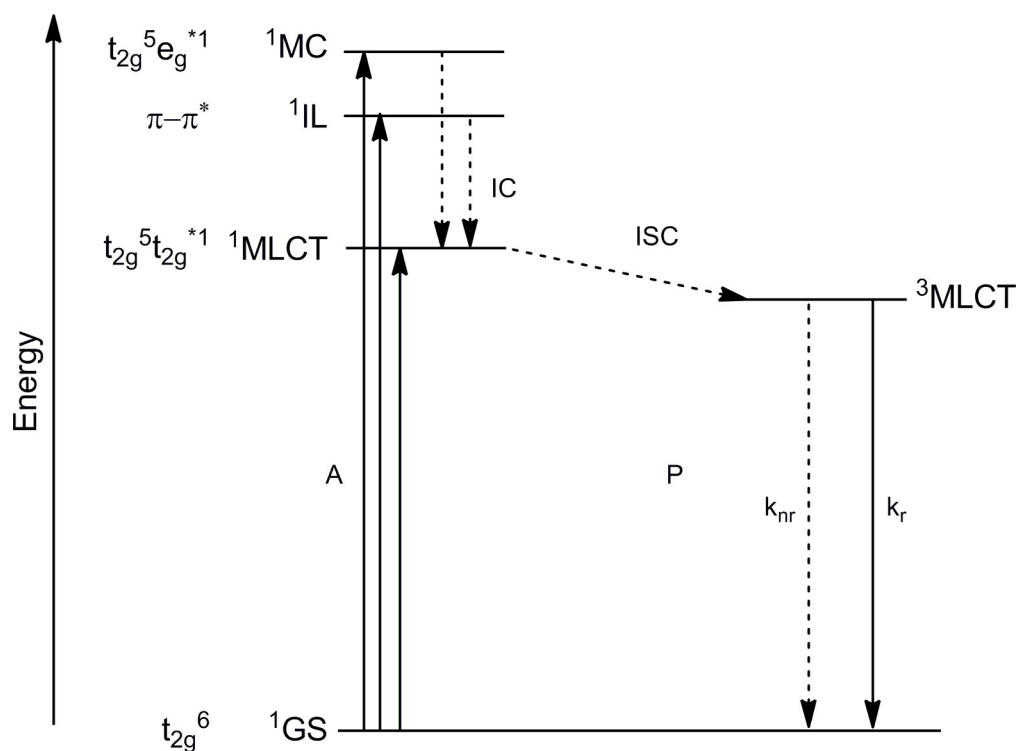
If the complex is approximated under octahedral symmetry, the metal centre can be considered to contribute the 5d, 6s, and 6p orbitals for bonding. These orbitals are classified according to their symmetry in the octahedral point group as shown in Figure 1.8. The 5d orbitals are represented by symmetry labels  $T_{2g}$  and  $E_g$ , the 6s orbital is represented as  $A_{1g}$ , and the 6p orbitals are represented as  $T_{1u}$ . The ligand orbitals considered to have  $\sigma$  symmetry, in relation to the metal-ligand axis, can be represented by the symmetry adapted linear combinations (SALCs)  $A_{1g}$ ,  $E_g$ , and  $T_{1u}$ . The  $A_{1g}$ ,  $E_g$ , and  $T_{1u}$  metal orbitals combine with the relevant

ligand SALCs to form the molecular orbitals with  $a_{1g}$ ,  $e_g$ , and  $t_{1u}$  symmetry as shown in Figure 1.8. In the case of complexes where the ligands have orbitals of  $\pi$  symmetry, in relation to the metal-ligand axis, these orbitals can be represented with the SALCs  $T_{2g}$ ,  $T_{2u}$ ,  $T_{1g}$ , and  $T_{1u}$ . Of these SALCs, the  $T_{2g}$  can combine with the  $T_{2g}$  metal orbitals to form the molecular orbitals  $t_{2g}$  and  $t_{2g}^*$ . This is shown in Figure 1.8 for the case of a  $\pi^*$  accepting ligand.

Figure 1.8 demonstrates a general case of second and third row transition metals, with  $\pi^*$  accepting ligands, which experience a strong crystal field. The  $e_g^*$  orbitals are therefore considered higher in energy than the  $t_{2g}^*$  orbitals, and the  $t_{2g}$  and  $t_{2g}^*$  are the HOMO and LUMO, respectively.



**Figure 1.8:** Simplified molecular orbital diagram for a Re(I) metal complex coordinated to 6 equivalent  $\pi$  accepting ligands. In this case, formation of important molecular orbitals ( $e_g$ ,  $e_g^*$ ,  $t_{2g}$ ,  $t_{2g}^*$ ) are illustrated with dashed lines. <sup>a</sup>Non-bonding  $\pi^*$  orbitals ( $T_{2u}$ ,  $T_{1g}$ ,  $T_{1u}$ ) are excluded for simplicity. MLCT and MC transitions are noted in blue.



**Figure 1.9:** Simplified Jablonski diagram for a Re(I) complex with lowest MLCT excited state. Adapted from Balzani *et al.*<sup>70</sup> Showing electron configuration from Figure 1.8 associated with each energy level. The process of phosphorescence (P) is shown with the rate of non-radiative decay ( $k_{nr}$ ) and radiative decay ( $k_r$ ). VR and the LLCT excited state are omitted for simplicity.

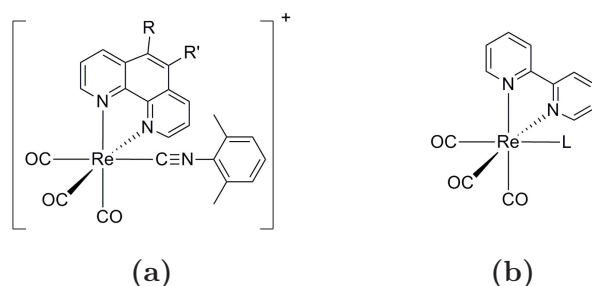
The absorption of a photon can induce different types of transitions within a Re(I) complex, these transitions are related to the arrangement of electrons in the molecular orbital diagram shown in Figure 1.8. The transition of an electron from the  $t_{2g}$  (HOMO), which are predominantly metal in character, to the  $t_{2g}^*$  (LUMO), which are antibonding orbitals that are predominantly ligand in character, is shown in Figure 1.8 by the arrow labelled MLCT. This transition is known as a metal to ligand charge transfer (MLCT). The excitation of an electron from the  $t_{2g}$  orbitals to the  $e_g^*$  orbitals, which are antibonding orbitals of the metal-ligand  $\sigma$  bond, is shown in Figure 1.8 as an arrow labelled MC. This transition is known as a metal centred (MC) transition. A further possible transition occurs primarily on the ligands themselves, and is known as an intra-ligand (IL) transition, these are analogous to  $\pi - \pi^*$  transitions.

If the surrounding ligands are not all equivalent, it is also possible that ligand-to-ligand charge transfer (LLCT) transitions can also occur. The LLCT, not illustrated in Figure 1.8 or Figure 1.9, is considered to be a transition of an electron from the occupied  $\pi$  orbitals of a ligand to the  $\pi^*$  orbitals of a different ligand. This type of transition has been studied rigorously in Re(I) complexes,<sup>73–78</sup> and

it is possible that the LLCT can mix with the MLCT to form a metal-ligand-to-ligand (MLLCT) excited state. Different diimine and ancillary ligands can change the energy of the LLCT such that it can be the lowest excited state.<sup>79</sup> In a simplified representation, shown in the Jablonski diagram in Figure 1.9, the absorption of a photon can excite a Re(I) complex to the  $^1\text{MLCT}$ ,  $^1\text{IL}$ , or  $^1\text{MC}$  state, depending on its energy.<sup>60,70,75</sup> The complex then relaxes to the lowest excited state ( $^1\text{MLCT}$ ) via vibrational relaxation and internal conversion in accordance with Kasha's rule. Due to the presence of the heavy atom (Re(I)) the character of the  $^1\text{MLCT}$  and  $^3\text{MLCT}$  states mix and the complex transitions to the  $^3\text{MLCT}$  excited state via inter-system crossing. The complex then decays to the ground state ( $^1\text{GS}$ ) radiatively and non-radiatively, with rates  $k_r$  and  $k_{nr}$  respectively.<sup>37,70,71,80</sup>

### 1.3.6 Modulation of photophysical properties of Re(I) complexes

To obtain specific photophysical characteristics, the energy of the transitions must be altered. In complexes of Re(I), the MLCT transition is usually modified because it is typically the lowest excited state. This transition can simplistically be described as simultaneous reduction of the diimine ligand and oxidation of the Re(I) centre, as these are the localisations of the LUMO and HOMO, respectively. Thus modifications to the complex which alter the energy of these processes will change the character of the MLCT transition.



**Figure 1.10:** a)  $\text{fac-}[\text{Re}(\text{phenRR}')(\text{CO})_3\text{R}'']$  where R and R' represent substituted organic group shown in Table 1.1.<sup>81</sup> b)  $\text{fac-}[\text{Re}(\text{bpy})(\text{CO})_3\text{L}]$  where L represents an ancillary ligand shown in Table 1.2.<sup>36</sup>

The complexes displayed in Figure 1.10 are representative examples of structural modifications where changes to the groups labelled R and L alter the energy of the reduction (Figure 1.10a) and oxidation (Figure 1.10b) processes. As seen in Figure 1.10a, the diimine ligand can be altered by changing the substituents R and R'. Alterations of the electron donating strength of these substituents changes



the required energy for reduction of the diimine ligand. Table 1.1 demonstrates that, as the electron donating strength of the ligand substituents increases, in the order  $\text{Cl} < \text{H} < \text{CH}_3$ , the emission wavelength decreases. This illustrates that the increase of the electron density of the diimine ligand destabilises the  $\pi^*$  orbitals, and increases the energy of the MLCT transition.

**Table 1.1:** Photophysical properties of Re(I) complexes  $fac\text{-}[\text{Re}(\text{phenRR}')(\text{CO})_3\text{R}'']^a$  (Figure 1.10a).<sup>81</sup>

R	R'	$\lambda_{em}$ (nm)	$\phi$	$\tau$ ( $\mu\text{s}$ )	$k_r$ ( $\text{s}^{-1}$ )	$k_{nr}$ ( $\text{s}^{-1}$ )
H	Cl	524	0.78	1.5	$5.2 \times 10^5$	$1.5 \times 10^5$
H	H	508	0.77	8.6	$9.0 \times 10^4$	$2.7 \times 10^4$
H	$\text{CH}_3$	510	0.83	20.2	$4.1 \times 10^4$	$8.4 \times 10^3$
$\text{CH}_3$	$\text{CH}_3$	493	0.56	30.9	$1.81 \times 10^4$	$1.4 \times 10^4$

The energy requirement of the Re(I)/Re(II) oxidation can be altered by changes to the ancillary ligand (Figure 1.10b), and will be influenced by the presence of electron donating groups on the ancillary ligand. Table 1.2 demonstrates that as the electron donating strength of the ancillary ligand decreases, in the order  $\text{Cl}^- > 4\text{-NH}_2\text{Py} > \text{Py} > \text{CH}_3\text{CN}$ , the emission wavelength decreases.

**Table 1.2:** Photophysical properties of Re(I) complexes  $fac\text{-}[\text{Re}(\text{bpy})(\text{CO})_3\text{L}]$  (Figure 1.10b).<sup>36</sup>

L	$\lambda_{em}$ (nm)	$\phi$	$\tau$ (ns)	$k_r$ ( $\text{s}^{-1}$ )	$k_{nr}$ ( $\text{s}^{-1}$ )
$\text{Cl}^-$	622	0.005	51	$9.79 \times 10^4$	$1.95 \times 10^7$
4-NH <sub>2</sub> Py	597	0.052	129	$4.06 \times 10^5$	$7.34 \times 10^6$
Py	558	0.16	669	$2.36 \times 10^5$	$1.26 \times 10^6$
$\text{CH}_3\text{CN}$	536	0.41	1201	$3.43 \times 10^5$	$4.90 \times 10^5$

This illustrates that reducing the electron donation strength of the ligand stabilises the HOMO, and increases the energy of the MLCT transition. In this case, when decreasing the electron donating strength of the ancillary ligand, the quantum yield and lifetime increase. The calculated non-radiative decay rates (Table 1.2) decrease linearly with the increase of the transition energy. This relationship of  $k_{nr}$  and energy is in accordance with the energy gap law.

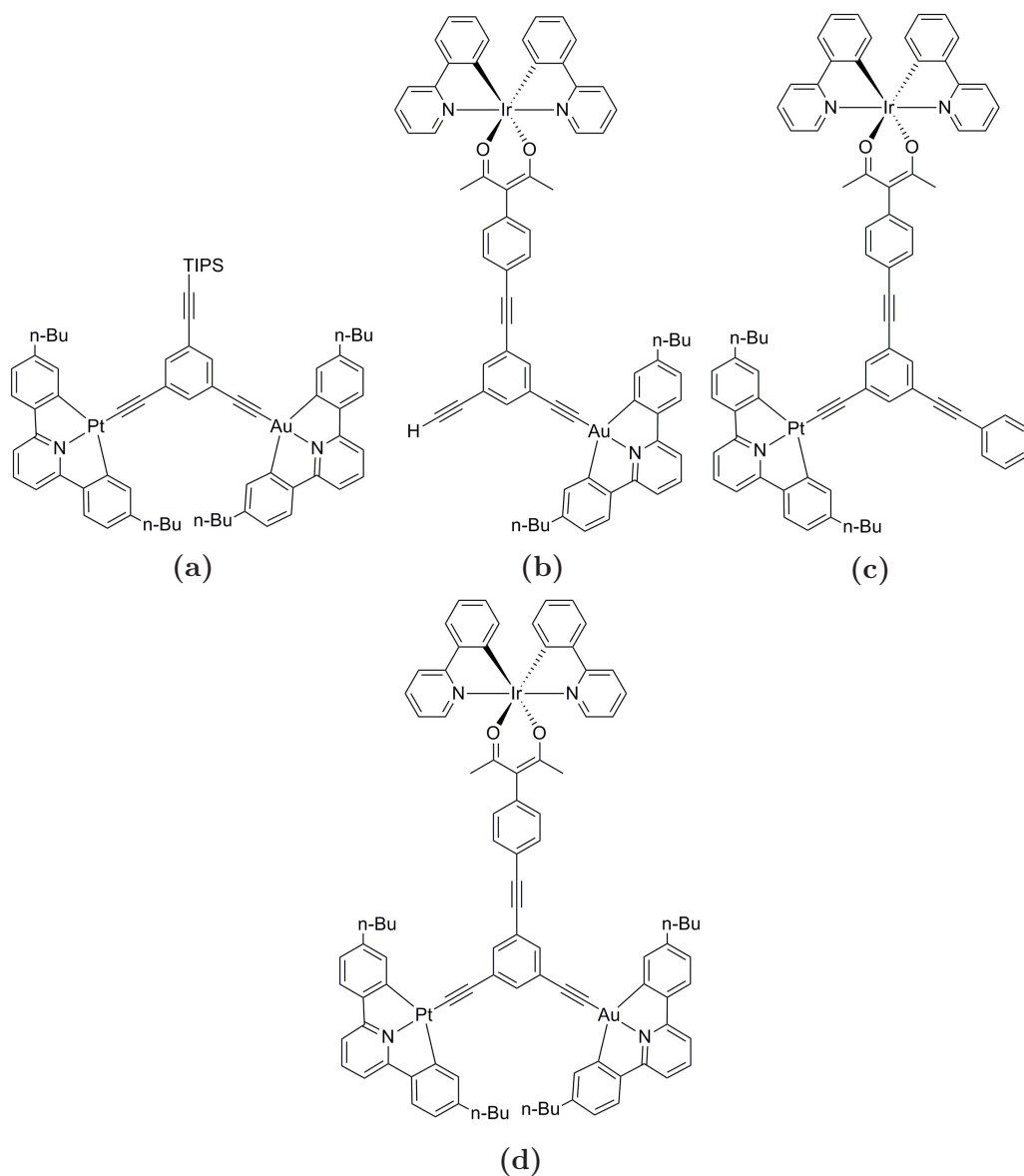
## 1.4 Multinuclear metal complexes

### 1.4.1 Multinuclear d-d complexes

Research into multinuclear transition metal complexes have demonstrated that the photophysical, chemical, electrochemical, and magnetic properties can be much different than the mononuclear analogues or subunits.<sup>82-103</sup> The photophysical properties of such complexes are of particular interest, as differences in excited state energies can lead to partial or complete energy transfer to a preferred emissive species. This has been reported in a variety of heterometallic complexes where different rates of energy transfer lead to various emission wavelengths and efficiencies.<sup>104-108</sup>

An example of one such heterometallic multinuclear complex is shown in Figure 1.11d. This species was formed from luminescent subunits of Pt(II), Ir(III), and Au(III). Modification of the structure, by different combinations of the metal centres, leads to a change in the rate of energy transfer via Förster and Dexter mechanisms. The mononuclear complexes displayed emission properties typical for the respective metal centres; the Au(III) complex displayed an emission at  $\lambda_{em} = 484 - 591$  nm with a lifetime of  $\tau = 120$  ns, the Pt(II) complex displayed an emission at  $\lambda_{em} = 586$  nm a lifetime of  $\tau = 570$  ns, and the Ir(III) complex displayed an emission at  $\lambda_{em} = 523$  nm a lifetime of  $\tau = 880$  ns. In the dinuclear complexes of Au(III), with Pt(II) (Figure 1.11a) or Ir(III) (Figure 1.11b), emission from Au(III) is not detectable, and these complexes displayed photophysical properties similar to the mononuclear complex of the paired metal centre. This indicated that energy transfer to the paired metal centre occurs rapidly. The dinuclear complex of Pt(II) and Ir(III), Figure 1.11c, gave an emission profile with contributions of both metal centres, having an emission band at 577 nm with a shoulder at 520 nm. Comparison of the lifetime of this profile gave a biexponential decay at 520 nm of 560 and 25 ns. The contribution with a lifetime of 25 ns, corresponding to emission from Ir(III), was dramatically lower than that of the mononuclear Ir(III) complex. This suggested energy transfer was occurring from Ir(III) to Pt(II). A similar observation was also made with the trinuclear species, which displayed a broad emission band centred at 520 nm. This emission exhibited a biexponential lifetime with components of 670 and 42 ns. It was rationalised that the excited state of Au(III) was rapidly transferring energy to Pt(II) and Ir(III), and the excited state of Ir(III) was also undergoing energy transfer to Pt(II). Calculations of the rate of energy transfer using the Ir(III) emission lifetime resulted in an approximate rate of  $k_{EnT} = 4 \times 10^7$  s<sup>-1</sup>. Estimations of energy transfer rates indicated that the Ir(III)  $\rightarrow$  Pt(II) energy transfer

was occurring primarily through an exchange (Dexter) mechanism.<sup>109,110</sup>

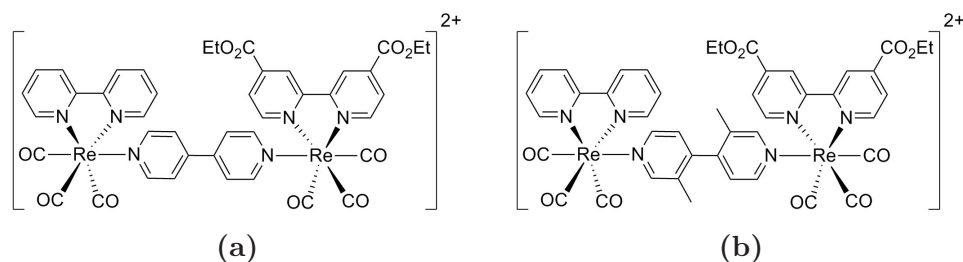


**Figure 1.11:** Heterotrimetallic complexes of Ir(III), Au(III), and Pt(II) studied for energy transfer mechanisms.<sup>109</sup> a) Dinuclear complex of Pt(II) and Au(III). b) Dinuclear complex of Ir(III) and Au(III). c) Dinuclear complex of Ir(III) and Pt(II). d) Trinuclear complex of Ir(III), Au(III), and Pt(II).

### 1.4.2 Multinuclear Re(I) complexes

Investigations into energy transfer mechanisms are not limited to polymetallic complexes. Homometallic complexes where the metal centres are considered non-equivalent have also been studied.<sup>2,111</sup>

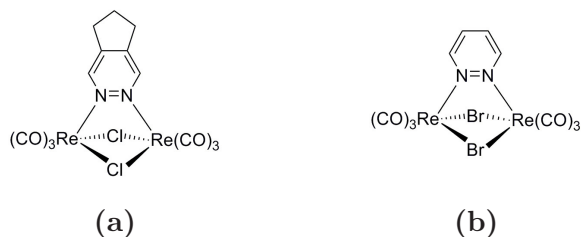
In an example of such research performed by Tapolsky, Duesing, and Meyer, intramolecular energy transfer in dinuclear Re(I) complexes was studied. In this



**Figure 1.12:** Dinuclear Re(I) complexes containing Re(bpy) and Re((CO<sub>2</sub>Et)<sub>2</sub>·bpy) moieties utilised for bridge mediated energy transfer studies.<sup>111</sup> a) Bridged by 4,4'-bipyridine. b) Bridged by 3,3'-dimethyl-4,4'-bipyridine.

research, two Re(I) moieties, Re(bpy) and Re((CO<sub>2</sub>Et)<sub>2</sub>·bpy), were bridged by bipyridine ligands with different substituents. The formation of non-symmetrical molecules, such as those seen in Figure 1.12, leads to a difference in energy of the two localised excited states. It was observed that bridging the two metal centres with a 4,4'-bipyridine ligand (Figure 1.12a) would facilitate rapid and efficient energy transfer to the lowest localised MLCT excited state. This was determined by emission resembling that from the Re((CO<sub>2</sub>Et)<sub>2</sub>·bpy) excited state, along with a transient absorption feature characteristic of such a state. This was further confirmed by the absence of a transient absorption feature characteristic of an excited state localised on Re(bpy). When 3,3'-dimethyl-4,4'-bipyridine was used as a bridging ligand, the rate of energy transfer was reduced. This was determined by analysis of the transient absorption spectrum where features corresponding to excited states localised on both Re(bpy) and Re((CO<sub>2</sub>Et)<sub>2</sub>·bpy) are present. This was further suggested by the transient absorption spectrum where the feature corresponding to the Re(bpy) excited state persists after 315 ns, when the Re((CO<sub>2</sub>Et)<sub>2</sub>·bpy) excited state has decayed. The emission spectrum also appeared superimposable with that of a solution containing both mononuclear derivatives, and biexponential decay rates could be fit with characteristic lifetimes of the mononuclear derivatives. The reduction of energy transfer, which results in these photophysical properties, was concluded to be a result of a reduction in conjugation across the bridging ligand. This was suggested to be a result of methyl substituents making a coplanar arrangement less energetically favourable, which would decrease the exchange interactions that facilitate energy transfer.<sup>106,111,112</sup>

Although energy transfer mechanisms are an interesting area of research, the photophysical properties of multinuclear Re(I) complexes have also been studied in regards to potential applications. Dinuclear Re(I) complexes, such as those shown in Figure 1.13, have indicated possible applications in light emitting devices due to high luminescence performance.<sup>55</sup>



**Figure 1.13:** Dinuclear Re(I) complexes utilised as dopants in phosphorescent OLEDs. a) 547 nm emission with quantum efficiency of 5.9 %. b) 620 nm emission with quantum efficiency of 9.8 %.<sup>55</sup>

The complex in Figure 1.13a displayed emission at 547 nm with quantum yield and lifetime of 0.53 and 5.3  $\mu\text{s}$ , respectively in degassed toluene. The complex in Figure 1.13b displayed emission at 620 nm with quantum yield and lifetime of 0.002 and 20 ns, respectively under the same conditions. The photophysical properties of these complexes were also measured in the solid state, finding that the complex shown in Figure 1.13a displayed an increase of non-radiative decay rate when moving from in solution to the solid state. However, the complex shown in Figure 1.13b displayed the opposite trend, where the non-radiative decay rate reduced significantly from  $4.99 \times 10^7$  to  $2.4 \times 10^5$ . This suggested that the relatively bulky  $\text{Br}^-$  ligands distorted the coordination sphere and caused the complex (1.13b) to be labile in solution, which quenched the photophysical performance. The complex displayed in Figure 1.13b displayed a substantial increase in luminescence in the solid state, attributed to aggregation induced emission, which is a unique property that does not appear in general to be displayed by mononuclear Re(I) complexes.<sup>113,114</sup> When measuring these complexes in devices, it was found that Figure 1.13b displayed a high efficiency of 9.8 % even though the photophysical properties in solution were poor. This increased performance was attributed to the large polarisability of the  $\text{Br}^-$  groups, and its good charge transport properties.<sup>55</sup>

### 1.4.3 Multinuclear d-f complexes

Research into energy transfer mechanisms of luminescent complexes is not restricted to d-d complexes. Obtaining  $\text{Ln}^{3+}$  emission from multinuclear d-f complexes is an interesting area of investigation, as the ability to excite the transition metal MLCT at wavelengths in the visible region implies there are potential biological applications.<sup>115-117</sup>

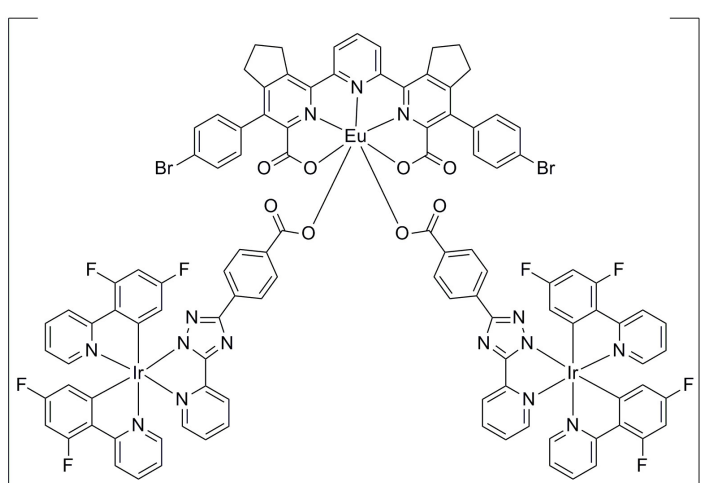
In the investigation of energy transfer in d-f metal complexes, the efficiency and rate of energy transfer from the d-metal to a lanthanide can be approximated by measurements of the residual emission of the d-metal complex, as illustrated

by Van Veggel and Faulkner.<sup>118,119</sup> The rate of energy transfer ( $k_{EnT}$ ) and the quantum efficiency of energy transfer ( $\phi_{EnT}$ ) can be calculated according to Equation 5.5 and Equation 5.6, respectively:

$$k_{EnT} = 1/\tau_q - 1/\tau_u \quad (1.12)$$

$$\phi_{EnT} = 1 - \tau_q/\tau_u \quad (1.13)$$

where  $\tau_q$  is the decay lifetime in the presence of a quenching  $\text{Ln}^{3+}$  cation, and  $\tau_u$  is the decay lifetime in the absence of a quencher, which is assumed to be very similar to that of the analogous  $\text{Gd}^{3+}$  or  $\text{Lu}^{3+}$  complex under the same conditions.



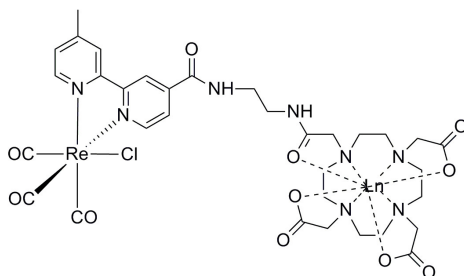
**Figure 1.14:** Structural representation of white-light emitting assembly. The emission of white light comes from a combination of a blue-emitting Ir(III) complex and a red-emitting  $\text{Eu}^{3+}$  complex.<sup>120</sup>

Investigations into sensitisation of NIR  $\text{Ln}^{3+}$  species ( $\text{Ln} = \text{Nd}, \text{Yb}, \text{Er}, \text{Pr}$ ) have involved complexes of Ru(II), Re(I), Os(II), Pt(II), Cr(III), Co(III), Zn(II), and Ir(III).<sup>115,117,120–132</sup>

$^3\text{MLCT} \rightarrow \text{Ln}^{3+}$  energy transfer to visible emitting  $\text{Ln}^{3+}$  cations ( $\text{Ln} = \text{Tb}, \text{Eu}$ ) is more difficult to achieve because the lowest excited states of  $\text{Eu}^{3+}$  and  $\text{Tb}^{3+}$  are relatively higher in energy ( $17,500 \text{ cm}^{-1}$  and  $20,500 \text{ cm}^{-1}$ ).  $\text{Tb}^{3+}$  sensitisation has not been reported in a d-f metal complex, however complexes of Pt(II) and Ir(III) are typically used to sensitise  $\text{Eu}^{3+}$  because they can readily be formed with excited states of energy  $> 20,000 \text{ cm}^{-1}$  for sensitising  $\text{Eu}^{3+}$ .<sup>115,120,123,133–139</sup> In an investigation of  $\text{Eu}^{3+}$  sensitisation by an Ir(III) complex, De Cola *et al.* synthesised the compound represented in Figure 1.14. The comparison of the emission lifetime of Ir(III) in the multinuclear complex ( $\tau = 480 \text{ ns}$ ) to the analogous mononuclear subunits ( $\tau = 1400 \text{ ns}$ ), demonstrated that the emission

from Ir(III) was quenched in the presence of  $\text{Eu}^{3+}$ . Excitation of the assembly at 400 nm, where only excitation to the MLCT occurs, yielded emission from  $\text{Eu}^{3+}$  illustrating further that  ${}^3\text{MLCT} \rightarrow \text{Eu}^{3+}$  energy transfer was sensitising emission from  $\text{Eu}^{3+}$ . The presence of residual blue emission from the Ir(III) moiety along with red emission from  $\text{Eu}^{3+}$  resulted in white light emitted from a single complex.<sup>120</sup>

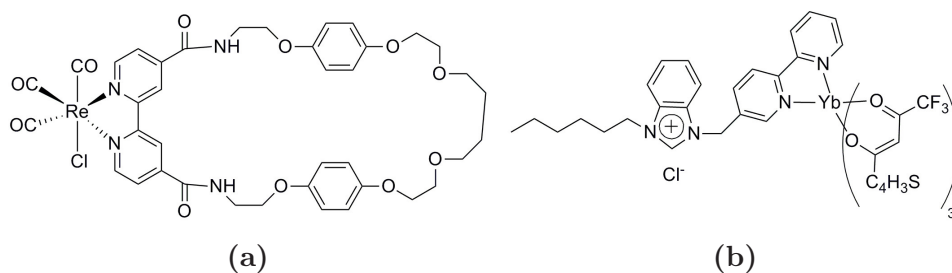
Although investigations into d-f complexes can be performed with the entire range of emissive  $\text{Ln}^{3+}$  cations, studies which involve Re(I) complexes primarily focus on the sensitisation of NIR emitting lanthanides. This is because most Re(I) complexes have excited states much lower in energy than that required for optimal sensitisation of  $\text{Eu}^{3+}$  ( $20,000 \text{ cm}^{-1}$ ) and  $\text{Tb}^{3+}$  ( $22,900 \text{ cm}^{-1}$ ).<sup>133,140</sup> In addition, the investigations of  $\text{Ln}^{3+}$  sensitisation by Re(I) complexes are relatively sparse in comparison to cases utilising Ir(III) or Pt(II).<sup>128,129,141–145</sup>



**Figure 1.15:** Example Re(I) complex for sensitisation of  $\text{Yb}^{3+}$  and  $\text{Nd}^{3+}$ .<sup>124</sup>

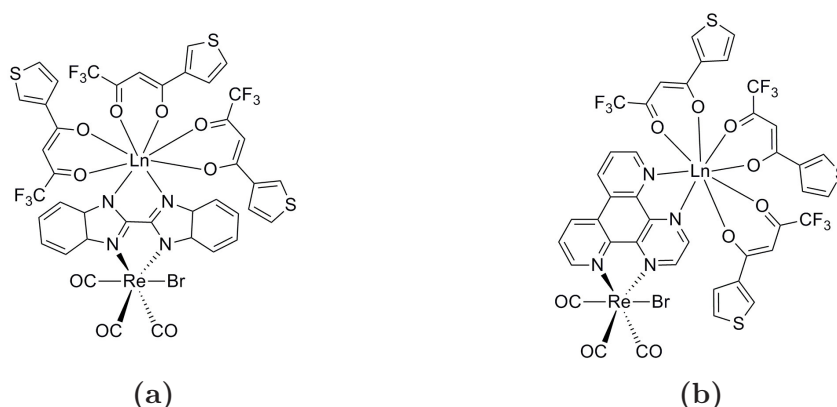
In the research of Re(I) sensitised  $\text{Ln}^{3+}$  luminescence, the largest contributions are made by Faulkner, Pope, and Ward. In one such investigation, a bimetallic complex which covalently links a Re(I) centre and a  $\text{Ln}^{3+}$  cation ( $\text{Ln} = \text{Nd}, \text{Yb}$ ) such as that shown in Figure 1.15 was formed. The investigation of this complex demonstrated that in the case of  $\text{Yb}^{3+}$  the sensitisation process can be difficult to elucidate, as the lifetime of the  ${}^3\text{MLCT}$  lifetime reduced from 11.4 ns to 8.1 ns in the presence of  $\text{Yb}^{3+}$ . Conversely the reduction of the  ${}^3\text{MLCT}$  lifetime from 11.4 ns to 5.2 ns in the presence of  $\text{Nd}^{3+}$  demonstrated direct involvement of the  ${}^3\text{MLCT}$  in the sensitisation process of  $\text{Nd}^{3+}$ , and the energy transfer rate and efficiency could be quantified as  $3.32 \times 10^7 \text{ s}^{-1}$  and 0.32, respectively.<sup>124</sup>

This investigation was pursued further, where a similar set of complexes to that shown in Figure 1.15 were formed, where two lanthanides were present with one Re(I) centre along with a shorter spacer between the  $\text{Ln}^{3+}$  and the Re(I) centre.<sup>141</sup> In this study the  ${}^3\text{MLCT}$  was implicated in the sensitisation process of  $\text{Yb}^{3+}$ , giving a rate and efficiency of energy transfer of  $\tau_{EnT} = 1.13 \times 10^8 \text{ s}^{-1}$  and  $\phi_{EnT} = 0.62$  which was surprising in light of the previous result. The conclusion of this research was that the structure as a whole is as important a factor in sensitisation as the relative energies of the excited states.



**Figure 1.16:** Structure of pseudorotaxane utilised for anion templated assembly for  $\text{Yb}^{3+}$  sensitisation.<sup>146</sup> a)  $\text{Re(I)}$  macrocycle. b)  $\text{Yb}^{3+}$  containing template.

The most efficient report of the sensitisation of  $\text{Yb}^{3+}$  by a  $\text{Re(I)}$  complex utilised an anion-templated assembly of a  $\text{Yb}^{3+}$ - $\text{Re(I)}$  [2]pseudorotaxane (Figure 1.16).<sup>146</sup> In this report the energy transfer rate constant and quantum efficiency of  $1.35 \times 10^7 \text{ s}^{-1}$  and 0.74, respectively, were obtained. These results demonstrated that close proximity of the donor and acceptor contributed to the rapid rate constant.



**Figure 1.17:**  $\text{Re(I)}$  complexes utilised for sensitisation of  $\text{Yb}^{3+}$  and  $\text{Nd}^{3+}$ .<sup>147</sup> a) Complex with close proximity of energy donor and acceptor. b) Complex with greater separation of energy donor and acceptor.

The relationship of structure to sensitisation efficiency has also been explored by other groups. In such an example, shown in Figure 1.17a, it was found that the lifetime of the  $^3\text{MLCT}$  emission decreased from 120 ns in solution without any  $\text{Ln}^{3+}$  cation present, and 40 ns in solution in the presence of  $\text{Yb}^{3+}$ . Although it may have been optimal to compare to the complex formed in the presence of  $\text{Gd}^{3+}$  or  $\text{Lu}^{3+}$ , a rate and efficiency of energy transfer of  $k_{EnT} = 1.6 \times 10^7 \text{ s}^{-1}$  and  $\phi_{EnT} = 0.67$  were obtained.<sup>147</sup> The complex in Figure 1.17a was compared to an analogous complex, Figure 1.17b, which places the  $\text{Ln}^{3+}$  cation more distant from the MLCT excited state. It was found that the complex shown in Figure 1.17b had an energy transfer rate and efficiency of  $k_{EnT} = 9.8 \times 10^6 \text{ s}^{-1}$  and  $\phi_{EnT} = 0.25$ . This demonstrates that increasing the spacing between the donor and acceptor



in d-f complexes also affects the rate and efficiency of energy transfer.

Although there is precedence in literature for the sensitisation of  $\text{Eu}^{3+}$  by other transition metals,<sup>115</sup> no literature reports of sensitisation of  $\text{Eu}^{3+}$  via the  $^3\text{MLCT}$  of a Re(I) complex were found. In this investigation, obtaining a sufficiently blue-shifted emission of a Re(I) complex may facilitate energy transfer to  $\text{Eu}^{3+}$ . Further, investigations of the sensitisation of  $\text{Ln}^{3+}$  cations by Re(I) complexes has very few examples of multinuclear complexes, or those with extended ligand conjugation between the donor and acceptor, this area requires further investigation to include such multinuclear sensitisers and those with highly conjugated ligands.

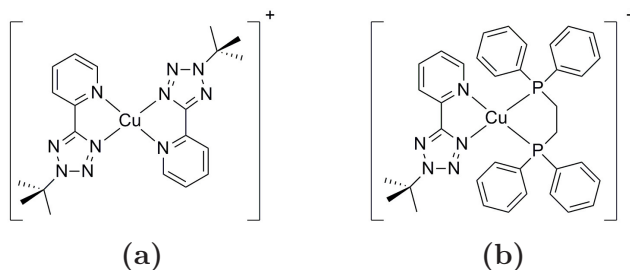
## 1.5 Tetrazolato complexes



**Figure 1.18:** Structural example of a tetrazole type molecule. Where R can be substituted for various functional groups.

Tetrazoles contain an aromatic ring comprised of four nitrogen atoms and one carbon atom in a structure similar to that shown in Figure 1.18. This type of ligand can potentially bind to a metal centre in various ways and be functionalised quite readily. Tetrazoles can also be synthesised quite expediently for a variety of applications including biological research.<sup>148–164</sup>

The coordination chemistry of tetrazoles has been researched in conjugation with Ir(III), Ru(II), Cu(I), Pt(II), and  $\text{Ln}^{3+}$  complexes, where it can be utilised as an ancillary ligand, chelating ligand, or bridging ligand between multiple metal centres.<sup>12,165–201</sup>

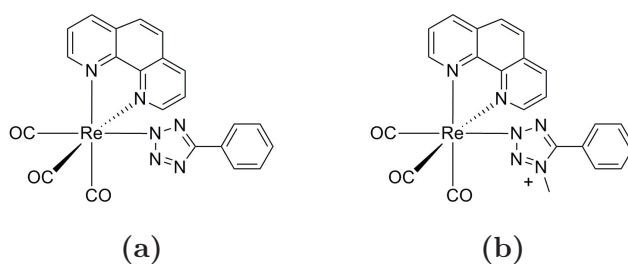


**Figure 1.19:** Example Cu(I) tetrazolato complexes investigated for photophysical applications.<sup>192</sup>

An example of such an investigation utilised 2-(2-*tert*-butyl-2*H*-tetrazol-5-yl)pyridine as a chelating ligand for copper. This

led to the formation of complexes such as those shown in Figure 1.19. The photophysical properties of these complexes were poor in solution. However, at 77 K, in KBr pellets, and in PMMA films the heteroleptic complexes containing the tetrazole ligand (Figure 1.19b) displayed intense emission ( $\phi$  up to 45 %) with long lived luminescence ( $\tau \approx 20\mu\text{s}$ ). It was concluded that, although poorly emissive in solution, such complexes could be utilised in light emitting devices due to their high photophysical performance in the solid state.

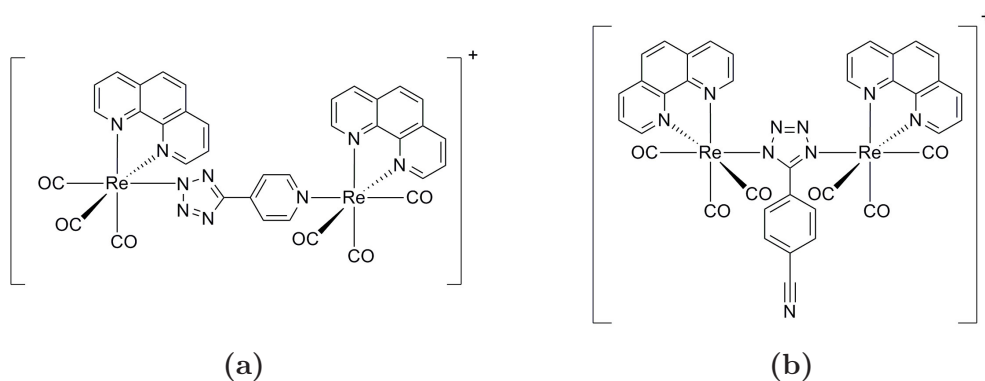
Recently, our research group has expanded the investigations of tetrazolato complexes to include Re(I). In these investigations the tetrazolato ligand is shown to enable the modulation of luminescence properties.<sup>1</sup> The optical imaging applications of Re(I) tetrazolato complexes have demonstrated the first case of phosphorescent labelling of lipid droplets.<sup>202</sup> Further, *in situ* changes to the chemical environment can lead to significant changes to the photophysical properties of the complexes.<sup>196</sup>



**Figure 1.20:** Representation of alteration to ancillary ligand to change emission properties of Re(I) complexes.<sup>1,196</sup> a) Emission at 571 nm. b) Emission at 536 nm.

In the study of complexes such as those shown in Figure 1.20, the addition of a methyl group would place a positive charge on the tetrazolate ligand. The presence of this positive charge increased the energy of the MLCT transition by stabilising the HOMO of the complexes. It was also shown that this change in photophysical properties could also be achieved by the reversible addition of a proton.<sup>196</sup>

Our research into the use of tetrazoles as bridging ligands between Re(I) diimine complexes has also indicated that the conjugation across an aryl tetrazole will facilitate energy transfer.<sup>2</sup> In the research of the dinuclear Re(I) tetrazolato complexes shown in Figure 1.21, the photophysical properties of cationic and neutral mononuclear analogues were investigated. It was shown that the dinuclear complexes displayed superimposable emission profiles where the emission wavelength was in between the blue-shifted cationic and red-shifted neutral analogues. This was suggestive that the tetrazole ligand was facilitating energy transfer to the lowest excited state.



**Figure 1.21:** Dinuclear Re(I) tetrazolato complexes which displayed superimposable emission profiles  $\lambda_{em} = 558 \text{ nm}$ .<sup>2</sup>

As the research into Re(I) tetrazolato complexes still appears to be in its infancy, this area can be extended to investigate the role of the tetrazole ligand as a chelating ligand, and as a conjugated spacer between Re(I) complexes and lanthanides, to determine how well such a ligand facilitates energy transfer to a  $\text{Ln}^{3+}$  cation.

## 1.6 Computational Quantum Mechanics

Computational chemistry can assist in understanding the photophysical properties of metal complexes. The ability to relate theoretic transitions between electronic states to experimental absorption spectra enables the ability to describe electronic properties of these complexes rigorously.

As part of this investigation into the photophysical properties of these compounds, Density Functional Theory (DFT) and Time-Dependant Density Functional Theory (TD-DFT), will be utilized to understand the electronic properties and energy levels of the discussed molecules.

### 1.6.1 Theoretical Background

Computational chemistry is centred around solving the Schroedinger equation (Equation 1.14) for a molecule in space and time experiencing some external influence.

$$\hat{H}\Psi = E\Psi \quad (1.14)$$

The wavefunction  $\Psi$  describes the particle's properties, the Hamiltonian operator  $\hat{H}$  holds terms related to kinetic and potential energy of a particle, and  $E$  describes the energy of the system as a scalar quantity.

Exact solutions to the Schroedinger equation can only be obtained for relatively simple systems such as a particle in a box or on a string, or the hydrogen atom. It is not yet possible to solve the Schroedinger equation exactly for many electron

systems, as a result considerable efforts have been made to find approximate solutions to it.

The Hamiltonian operator  $\hat{H}$ , can be separated into the following set, where for brevity each term is reported in atomic units<sup>203,204</sup>

$$\hat{H} = \hat{T}_e + \hat{T}_N + \hat{V}_{ee} + \hat{V}_{NN} + \hat{V}_{eN}. \quad (1.15)$$

For a system with N electrons and M nuclei, the terms in Equation 1.15 are: the electron kinetic energy term ( $\hat{T}_e$ ), the nuclei kinetic energy term ( $\hat{T}_N$ ), the potential energy term or electron-electron interaction ( $\hat{V}_{ee}$ ), the potential energy term for nuclei nuclei interaction ( $\hat{V}_{NN}$ ), and the potential energy term for electron-nuclei interaction ( $\hat{V}_{eN}$ ).

The first approximation that is normally made to solve (Equation 1.14) was proposed by Born and Oppenheimer, and it assumes that the time scale of electronic relaxation is much faster than the motion of the nuclei. Hence the electrons are assumed to be always in their ground state and the nuclei are treated as classical particles. The kinetic energy of the nuclei term  $\hat{T}_N$  can therefore be neglected, and the potential energy term for the nuclei-nuclei interaction  $\hat{V}_{NN}$  can be considered a constant value, and the Hamiltonian simplifies to Equation 1.16.

$$\hat{H}_{elec} = \hat{T}_e + \hat{V}_{ee} + \hat{V}_{eN} \quad (1.16)$$

Where the terms are described as follows.

$$\hat{T}_e = -\frac{1}{2} \sum_{i=1}^N \nabla_i^2 \quad (1.17)$$

$$\hat{V}_{ee} = -\sum_{i=1}^N \sum_{j \neq i}^N \frac{1}{r_{ij}} \quad (1.18)$$

$$\hat{V}_{eN} = -\sum_{i=1}^N \sum_{A=1}^M \frac{Z_A}{r_{iA}} \quad (1.19)$$

$\nabla_i^2$  is the laplace operator for the kinetic energy of electron  $i$ ,  $r_{ij}$ ,  $r_{iA}$ , and  $r_{AB}$  are the distances between electrons  $i$  and  $j$ , electron  $i$  and nucleus  $A$ , and nuclei  $A$  and  $B$ , respectively.  $Z_A$  is the charge of nucleus  $A$ , and  $m_A$  is the mass of nucleus  $A$ , all given in atomic units.

Now that the electronic Hamiltonian is described an approximate solution to the Schroedinger equation for the electronic wavefunction, Equation 1.14, can be obtained.

$$\hat{H}_{elec} \Psi_{elec} = E \Psi_{elec} \quad (1.20)$$

For a many-electron system it is not yet possible to solve Equation 1.16 exactly because the mathematical form of the wavefunction is unknown and many theories have been developed to find approximate solutions. One of such methods is the Hartree-Fock theory.

### 1.6.2 Molecular Orbitals and the Hartree-Fock Approximation

Due to the inability to exactly solve the Schroedinger equation, the Hartree-Fock (HF) method allows the approximate solution of the wavefunction and energy of a many body problem at a stationary point. It employs the variational principal to be able to progressively iterate to a minimal energy point.

In the variational principal, it is stated that the energy expectation value of any wavefunction will always be greater than or equal to that of the true ground state wavefunction. Thus an initial guess is made for the wavefunction, and then an iterative approach is used to obtain a better solutions to Equation 1.16 by minimising the energy of the system as a function of  $\Psi$ . This iterative process continues until the differences in the calculated energies differs by an amount less than the threshold for such a computation, and then a stationary point has been found.

The electron-electron interaction that makes exact solutions to the wavefunction difficult to obtain becomes simplified in the case of the HF approximation, and the N-electron wavefunction is approximated by a Slater Determinant of N one-electron spin-orbit wavefunctions. These spin-orbit wavefunctions comprise of a spatial orbital and one of two spins.

$$\chi(r) = \phi(r)\sigma(s), \sigma = \alpha, \beta \quad (1.21)$$

The variational method is utilised to determine the optimal Slater determinant of the set of spin-orbitals. The Hartree-Fock equations are quite complicated to solve, however they result in a *Fock* operator which is analogous to the Hamiltonian operator but for one electron, and takes into account the different effects on the electrons in the system. It is shown in Equation 1.22

$$\hat{f}\chi_i = \varepsilon_i\chi_i \quad (1.22)$$

Where  $\varepsilon_i$  is the energy of the orbital and  $\hat{f}$  is the *Fock* operator. The *Fock* operator takes into account the effects on the electron and can be separated as

follows in Equation 1.23

$$\hat{f}_i = H^{core} + \sum_{j=1}^N \{J_j - K_j\} \quad (1.23)$$

in this case the core Hamiltonian operator  $H^{core}$  corresponds to the motion of a single electron moving in the presence of a single nuclei shown in Equation 1.24

$$H^{core}(i) = -\frac{1}{2} \nabla_i^2 - \sum_{A=1}^M \frac{Z_A}{r_{iA}} \quad (1.24)$$

Of the two remaining operators in Equation 1.23,  $J_j$  corresponds to the coulomb operator and corresponds to an electron  $i$  in a average potential of another electron  $j$ . The term  $K_j$  corresponds to the exchange term, which arises due to the interaction of spins of the two electrons and has a non-zero value when considering two electrons of the same spin, and is zero when two electrons have opposite spin.

In this way, each electron is considered to move in a *static* field comprising of all the nuclei and all other electrons. Thus a solution for this electron will then affect the solutions obtained for the other electrons as they are solved in turn. Hence this becomes an iterative approach to the solution of the electronic wavefunctions.

### 1.6.3 Density Functional Theory and Kohn-Sham equations

Density Functional Theory (DFT) is an approach to computational chemistry that has been of great interest since the 1980s and 90s.<sup>205,206</sup> This approach to obtain the properties of a system assumes that these properties can be calculated based on the electronic density because of the relationship between the overall electronic density and the total electronic energy. Where the Hartree-Fock theory calculates the full N-electron wavefunction, DFT only attempts to calculate the overall electronic density distribution. A major breakthrough in DFT came from Hohenberg and Kohn<sup>207</sup> where it was shown that the ground-state energy and other system properties were defined by the electron density. In this case it is expressed as the energy  $E$ , is a unique *functional* of the electron density  $\rho(r)$ .<sup>208</sup> The energy functional is written as a sum of two terms.

$$E[\rho(r)] = \int V_{ext}(r)\rho(r)dr + F[\rho(r)] \quad (1.25)$$

Where the first term is due to the interaction of the electrons with an external potential  $V_{ext}(r)$  such as the nuclei, and  $F[\rho(r)]$  is the sum of the kinetic energy

of the electrons and their inter-electronic interactions.

In DFT the number of electrons in the system is constrained as in Equation 1.26

$$N = \int \rho(r) dr \quad (1.26)$$

The total electron density is then obtained as the sum of the square moduli of a set of one-electron orbitals.

$$\rho(r) = \sum_{i=1}^N |\psi_i(r)|^2 \quad (1.27)$$

The difficulty with solving Equation 1.25 is that the function  $F[\rho(r)]$  is unknown. Kohn and Sham<sup>209</sup> suggested that it should be written as the sum of three terms, Equation 1.28.

$$F[\rho(r)] = E_{KE}[\rho(r)] + E_H[\rho(r)] + E_{XC}[\rho(r)] \quad (1.28)$$

where  $E_{KE}[\rho(r)]$  is the kinetic energy,  $E_H[\rho(r)]$  is the electron-electron Coulombic energy, and  $E_{XC}[\rho(r)]$  contains terms for exchange and correlation, which is unknown.

$E_{KE}[\rho(r)]$  is the kinetic energy of a system of electrons neglecting their interaction.

$$E_{KE}[\rho(r)] = \sum_{i=1}^N \int \psi_i(r) \left( -\frac{\nabla^2}{2} \right) \psi_i(r) dr \quad (1.29)$$

$E_H[\rho(r)]$  is known as the Hartree electrostatic energy. It arises from the interaction of two electron charge densities which are summed over all possible two-density interactions.

$$E_H[\rho(r)] = \frac{1}{2} \int \int \frac{\rho(r_1)\rho(r_2)}{|r_1 - r_2|} dr_1 dr_2 \quad (1.30)$$

combining these terms for the energy of the system along with the electron density the Kohn-Sham Equations result:

$$\left\{ -\frac{\nabla^2}{2} - \left( \sum_{A=1}^M \frac{Z_A}{r_{1A}} \right) + \int \frac{\rho(r_2)}{r_{12}} dr_2 + V_{XC}[r_1] \right\} \psi_i(r_1) = \varepsilon_i \psi_i(r_1) \quad (1.31)$$

In Equation 1.31 the external potential shows an interaction with  $M$  nuclei, where  $\varepsilon_i$  are the orbital energies and  $V_{XC}$  is the exchange-correlation functional. There are many types of DFT methods in literature, which mostly differ in the way the exchange and correlation terms are approximated.

The Kohn-Sham equations can be solved via a self-consistent approach, where an initial guess of the electron density is the input, then a set of orbitals can be

derived, then the electron density is improved and the iterations are continued until the results converge, or the difference between initial and calculated terms varies within a threshold value.

### 1.6.4 Functionals and Level-of-Theory

When applying DFT, it is necessary to choose a level of theory under which the calculations are performed, which determines the method of the computations. Hartree-Fock theory provides an almost exact means of dealing with the exchange contribution, and hence adding the correlation energy from DFT to that of HF results in another method for such calculation. Becke<sup>210</sup> took this approach and modified it to form a hybrid functional that incorporates approximations of the exchange-correlation energies from Hartree-Fock theory and DFT.

The B3LYP functional is often employed in DFT calculations due to the success it has in predicting the properties of a wide range of chemical systems.<sup>211</sup> However, in some cases such as for extended  $\pi$  systems, and for charge transfer transitions in TDDFT it is sub-optimal.<sup>212,213</sup> To address such discrepancies, the coulomb attenuated method CAM-B3LYP attempts to differ the way the exchange energy is approximated for these cases.<sup>214</sup> For this reason, CAM-B3LYP is the chosen level of theory for computational evaluation in this thesis unless otherwise stated.

### 1.6.5 Basis Sets

A basis set is a collection of functions that are used to describe the electronic density. Although it would be optimal to use Slater-type functions, these functions are difficult to implement and for systems larger than a few atoms sometimes impossible to integrate. Plane wave (PW) basis sets can also be utilised to describe electronic density.

Commonly, the substitution of Gaussian functions is often implemented to describe atomic orbitals. Generally these functions are of the form shown in Equation 1.6.5

$$x^a y^b z^c \exp(-\alpha r^2) \tag{1.32}$$

where  $\alpha$  describes the radial extent of the function, and the *order* of these functions is described by  $order = a + b + c$ . and functions can be zeroth-order, first order, etc.

An advantage of using Gaussian type functions is that they are mathematically more convenient. However, there are also some problems with employing Gaussian functions. The major disadvantage is that a single Gaussian function cannot



approximate the electron density of isolated atoms as well as a Slater function can. However, it has been shown that an atomic orbital can be represented by a linear combination of Gaussian functions. Thus an atomic orbital has the form shown in Equation 1.33

$$\phi_{\mu} = \sum_{i=1}^L d_{i\mu} \phi_i(\alpha_{i\mu}) \quad (1.33)$$

where  $d_{i\mu}$  is the coefficient of the single Gaussian function  $\phi_i$  with exponent  $\alpha_{i\mu}$ .  $L$  is the number of Gaussian functions to make up the orbital. It is accepted that at least three Gaussian type functions are sufficient to properly represent a Slater type orbital<sup>215</sup>

Due to these limitations the accuracy of the calculations depends on the number of Gaussian functions used in the calculation. A minimal basis set has the smallest number of functions to describe the filled orbitals of an atom. The double zeta basis set doubles the number of functions of that in the minimal basis set. In the use of PW basis sets the more functions used gives more accurate results, which is not necessarily true for basis sets comprised of Gaussian type orbitals.

The inclusion of additional functions to the basis set such as polarisation functions and diffuse functions enable deflection of the electron cloud and proper description on electron density that may be far from the nucleus.

Thus the selection of basis sets is important for computational chemistry, in this investigation, due to the consistency needed with previously published results,<sup>1,2,189,196,216</sup> and consistency across the calculations, the basis sets used will be the 6-311G\*\*, which includes polarisation functions for light atoms, and the SDDAll pseudo-potential will be used for the metal centre.

### 1.6.6 Time-Dependent Density Functional Theory

As for the case of the time dependent Schroedinger equation 1.34, a time dependent perturbation must be included in the calculation. In the application of TD-DFT the time dependent perturbation is applied to the Kohn-Sham treatment.

$$\hat{H}\Psi(\mathbf{r}, t) = i\hbar \frac{\partial}{\partial t} \Psi(\mathbf{r}, t) \quad (1.34)$$

The foundations of TD-DFT were made by Runge and Gross in 1984.<sup>217</sup> Where the calculation of differences in the ground-state and excited-state energies were possible without evaluation of the excited state itself. The properties of the excited state can be obtained from the derivatives of the energy of the ground state under such a perturbation.

In this thesis TD-DFT will be utilised to obtain the absorption spectra of molecules, and identify the orbitals involved in the transition, and compare this to the ex-

perimental data to understand the transitions within the compounds.

## 1.7 This investigation and scope

In the review of literature relating to Re(I) complexes, tetrazole containing complexes, multinuclear complexes, and lanthanide complexes, an area of interest has been identified. The research into mononuclear and multinuclear Re(I) tetrazolato complexes have not utilised a tetrazole as a chelating ligand. Thus, attempting to form such structures and investigating their properties may suggest areas of potential applications. There are also no reports of Re(I) tetrazolato complexes sensitising  $\text{Ln}^{3+}$  luminescence, thus comparison of the performance of Re(I) tetrazolato complexes to previously investigated complexes is important to grow this area of research. There have also been no reports of Re(I) sensitised emission from  $\text{Eu}^{3+}$ , and probing this area may lead to interesting results.

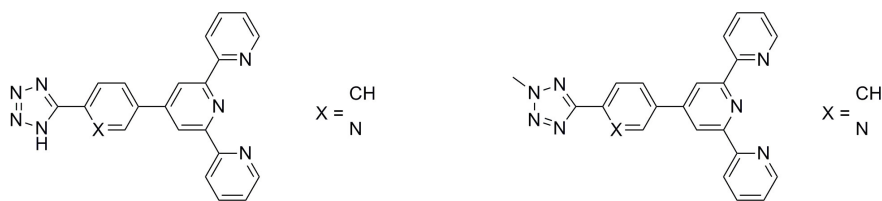
This investigation will expand on previous photophysical, electrochemical, computational, and structural research into Re(I) tetrazolato complexes. The primary goals are to obtain multinuclear Re(I) complexes where a tetrazole ligand is chelating the metal centre, and to attempt to sensitise  $\text{Ln}^{3+}$  luminescence by forming multinuclear Re(I)- $\text{Ln}^{3+}$  complexes.

Chapter 2 investigates the combination of Re(I) with the tetrazole containing compounds shown in Figure 1.22, with the intention of forming mononuclear and multinuclear complexes of Re(I) with such ligands, and to probe their photophysical properties.



**Figure 1.22:** Structures of target ligands in Chapter 2.

The complexes obtained utilising these ligands display diverse structural motifs and electronic properties. An interesting result of this initial investigation is that one such combination of gives a neutral, trinuclear, triangular type structure. This complex displays the shortest wavelength emission from a neutral Re(I) complex known ( $\lambda_{max} = 490 \text{ nm}$ ). This complex also displays interesting electrochemical properties with a progression of three reversible oxidation peaks. The results of Chapter 2 showed that the tetrazole ligand could be utilised as a chelating ligand for Re(I) complexes in a variety of modes. Chapter 3 attempts to form tetrazole functionalised 4'-ary-2,2':6',2''-terpyridines as shown in Figure 1.23.



**Figure 1.23:** Structures of target ligands in Chapter 3.

The synthesised ligands were photophysically characterised and their sensitivity to the addition of acid and base are investigated.

After successful synthesis of aryl-tetrazole functionalised terpyridines in Chapter 3. These ligands were utilised to form complexes of Re(I) similar to those reported in Chapter 2. Three of the intended complexes were successfully synthesised, including an analogous complex of the triangular structure obtained in Chapter 2. The photophysical and electrochemical properties of the complexes are reported in Chapter 4.

The final chapter investigates the ability of the synthesised ligands in Chapter 3 and complexes from Chapter 4 to sensitize lanthanide luminescence. It is found that all of the aforementioned compounds sensitise the lanthanides  $\text{Eu}^{3+}$  and  $\text{Yb}^{3+}$ . Each of the target complexes successfully sensitise the lanthanides, it is particularly interesting that the complexes are able to sensitise  $\text{Eu}^{3+}$  from the  $^3\text{MLLCT}$  excited state, which has not been reported in literature before. Also the triangular complex appears to efficiently sensitise both  $\text{Yb}^{3+}$  and  $\text{Eu}^{3+}$  with quantum efficiency above 0.90.

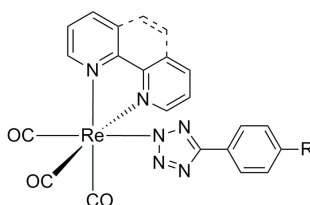


# Chapter 2

## Ligand modulated structural diversity

### 2.1 Introduction

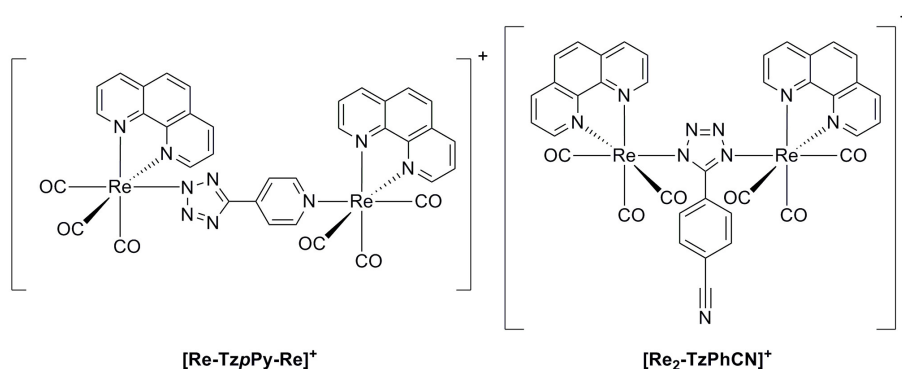
In previous research efforts, the photophysical properties of mononuclear Re(I) tetrazolato complexes were investigated. In these complexes, the Re(I) centres were chelated by bidentate 1,10-phenanthroline (**phen**) or 2,2'-bipyridine (**bipy**) ligands, and the tetrazolato anion was utilised as the ancillary ligand.<sup>1</sup> The library of investigated Re(I) tetrazolato complexes are represented in Figure 2.1.



**Figure 2.1:** Mononuclear Re(I) tetrazolato complexes utilising aryl tetrazolato anions as the ancillary ligand.<sup>1</sup>

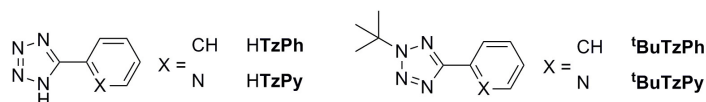
The investigation into these Re(I) complexes illustrated that their photophysical properties were tunable via chemical modification of the tetrazole containing ligand. This property promoted a subsequent investigation into the inclusion of a second Re(I) centre to determine what effect this would have on the photophysical and electrochemical behaviour.<sup>2</sup> The two dinuclear species in this investigation are shown in Figure 2.2.

The investigation into  $[\text{Re-Tz}p\text{Py-Re}]^+$  and  $[\text{Re}_2\text{-TzPhCN}]^+$  demonstrated that the tetrazolato bridging ligands could facilitate coupling between the two attached metal centres. The tetrazole moiety could offer unique binding modes such as that shown for  $[\text{Re}_2\text{-TzPhCN}]^+$ , where two Re(I) centres are directly attached to the tetrazole ring.

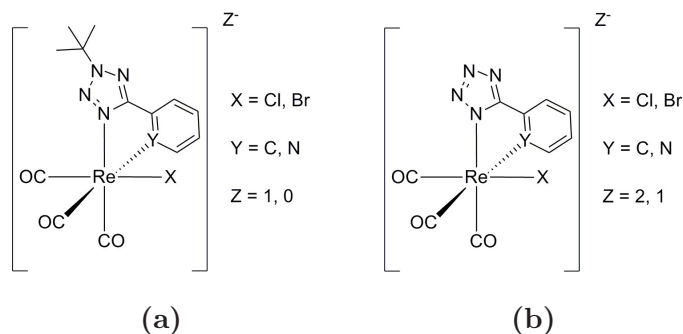


**Figure 2.2:** Structures of previously investigated dinuclear Re(I) complexes bridged by tetrazolato ligands.<sup>2</sup>

## 2.2 Chapter goal



**Figure 2.3:** Structures of target ligands in this investigation.



**Figure 2.4:** Structures of target complexes in this investigation, illustrating differences in charge, ancillary ligand, and ligated atom. a) Complexes with alkylated aryl-tetrazoles as chelating ligands. b) Complexes with aryl-tetrazolates as chelating ligands.

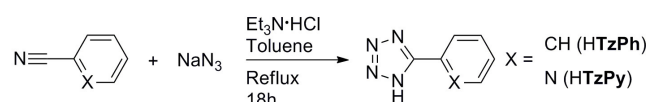
Photophysical studies of transition metal complexes utilising aryl-tetrazoles as chelating ligands are relatively scarce, and such investigations are restricted to complexes of Cu(I), Ir(III), Pt(II), and Ru(II).<sup>180,181,189,190,192–194,198,218–223</sup> The exclusion of Re(I) complexes in these studies has prompted this investigation, which will utilise aryl-tetrazoles as chelating ligands in mono and multi-nuclear Re(I) complexes. The two aryl tetrazoles and their alkylated derivatives that will be used are represented in Figure 2.3. These tetrazoles will be combined with  $[Re(CO)_5X]$  ( $X = Cl, Br$ ) in order to synthesise the proposed Re(I) complexes

shown in Figure 2.4. This investigation will also attempt to form a cyclometalated complex of Re(I) by utilising  ${}^t\text{BuTzPh}$  as a bidentate chelating ligand.

## 2.3 Synthesis of aryl-tetrazole ligands

### 2.3.1 Aryl-tetrazole synthesis

$\text{HTzPh}$  and  $\text{HTzPy}$  were synthesised following a literature procedure, shown in Figure 2.5, where an aryl nitrile was combined with sodium azide to yield the desired products.<sup>148</sup>



**Figure 2.5:** Reaction scheme for the synthesis of  $\text{HTzPh}$  and  $\text{HTzPy}$ .

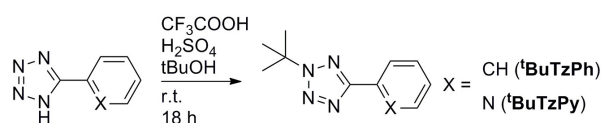
The synthesised species,  $\text{HTzPh}$  and  $\text{HTzPy}$ , were characterised by IR,  ${}^1\text{H}$ -NMR, and  ${}^{13}\text{C}$ -NMR spectroscopy. The presence of IR bands at  $1602\text{ cm}^{-1}$  and  $3420\text{ cm}^{-1}$  corresponding to tetrazole  $\text{C}=\text{N}$  and  $\text{NH}$  bonds, respectively, suggests formation of the tetrazole. The lack of a nitrile band at  $2230\text{ cm}^{-1}$  is indicative of the absence of starting material.

The  ${}^1\text{H}$ -NMR spectra of  $\text{HTzPh}$  and  $\text{HTzPy}$  in  $\text{DMSO-}d_6$  are consistent with previous reports of these compounds,<sup>152,224–226</sup> and both display a characteristic resonance in the  ${}^{13}\text{C}$ -NMR spectrum at ca. 155 ppm for the  $\text{C}5$  atom. Studies of aryl-tetrazoles and substituted aryl-tetrazoles by Butler suggest that this value signifies protonation at the N1 position.<sup>224,227</sup>

### 2.3.2 Alkylated tetrazole synthesis

The synthesised aryl tetrazoles were subsequently alkylated with a *tert*-butyl group. This group was selected to ensure that the tetrazole ring would be sterically hindered from binding to the Re(I) centre as an ancillary ligand. Alkylation at the N1 position was not expected due to being less favored by the presence of the aromatic ring and bulkiness of the *tert*-butyl group.

The synthesis scheme for alkylating  $\text{HTzPh}$  and  $\text{HTzPy}$  is shown in Figure 2.6.



**Figure 2.6:** Reaction scheme for the synthesis of  ${}^t\text{BuTzPh}$  and  ${}^t\text{BuTzPy}$ .

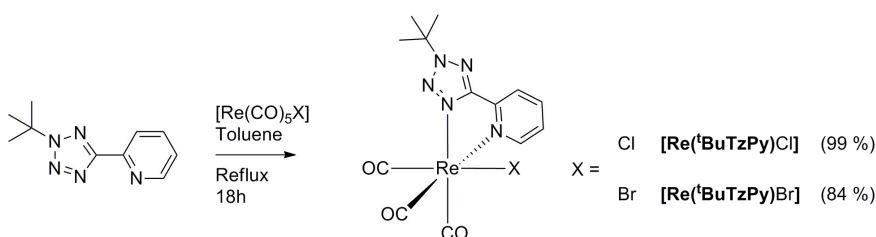
The alkylation of **HTzPh** and **HTzPy** was performed by the addition of the starting materials to a solution of *tert*-butanol in the presence of trifluoroacetic acid and sulfuric acid. This procedure has been reported in literature for the high selectivity of substitution of a tetrazole at the N2 position.<sup>190,228</sup>

IR spectroscopy of the alkylated tetrazoles ***t*BuTzPh** and ***t*BuTzPy** displayed a characteristic tetrazole C=N stretch at 1603 cm<sup>-1</sup> and lack of tetrazole NH stretch. The <sup>1</sup>H-NMR spectra for ***t*BuTzPh** and ***t*BuTzPy** in CDCl<sub>3</sub> are consistent with the proposed structures and display characteristic CH<sub>3</sub> singlet peaks appearing at 1.80 ppm, integrating to 9 protons. Three characteristic peaks are identified in the <sup>13</sup>C-NMR spectra of ***t*BuTzPh** and ***t*BuTzPy**. Signals at 30 ppm and 64 ppm are indicative of the presence of the *tert*-butyl group, and a signal at 165 ppm is indicative that the *tert*-butyl group is attached at the N2 position of the tetrazole moiety.<sup>224,227</sup> These spectra are consistent with literature reports of these compounds.<sup>190,225,229,230</sup>

## 2.4 Synthesis of Re(I) complexes

### 2.4.1 Synthesis of Re(I) complex with ***t*BuTzPy**

The first synthesised complexes [**Re(*t*BuTzPy)Cl**] and [**Re(*t*BuTzPy)Br**] were formed from the addition of ***t*BuTzPy** with [Re(CO)<sub>5</sub>X] (X= Cl, Br) in toluene, and stirred at reflux (Figure 2.7).



**Figure 2.7:** Reaction scheme for the synthesis of [**Re(*t*BuTzPy)X**].

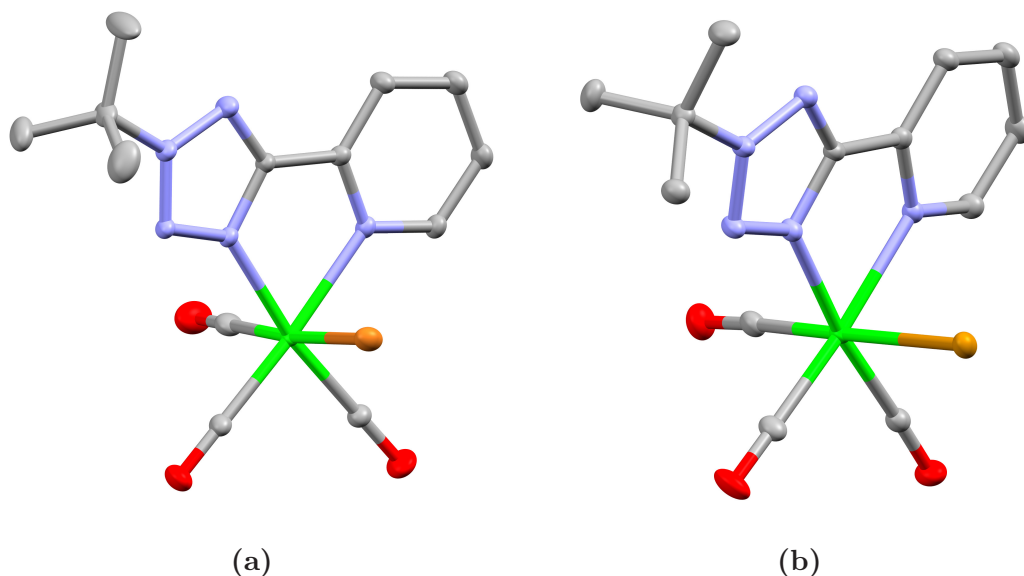
In the case of [**Re(*t*BuTzPy)Cl**], the product was readily obtained pure in high yield (99 %) after filtration and washing. However, [**Re(*t*BuTzPy)Br**] was impure after filtration, and required chromatographic separation for a final yield of 84 %.

The IR spectra for both complexes display characteristic carbonyl stretching peaks at ca. 2013 (A'(1)), 1923 (A'(2)), and 1875 (A'') cm<sup>-1</sup>, similar to those of reported Re(I) diimine complexes.<sup>1,2,43</sup>

The <sup>1</sup>H-NMR spectra for these complexes are superimposable, with signals corresponding to the pyridyl hydrogen atoms at 9.09, 8.29, 8.12, and 7.62 ppm, and a



signal corresponding to  $\text{CH}_3$  at 1.88 ppm. The  $^{13}\text{C}$ -NMR spectra for these complexes are also similar, with peaks at 196.5, 194.7, and 188.5 ppm corresponding to the carbonyl ligands. The characteristic C5 resonance at 166.1 ppm is also present, indicating co-planarity between the aryl and tetrazole rings is favoured, suggestive of chelation. There are also 7 remaining  $^{13}\text{C}$  resonances corresponding to the chelating ligand, with significant peaks at 68.4 and 29.2 ppm corresponding to  $(\text{CCH}_3)$  and  $(\text{CCH}_3)$ , respectively.



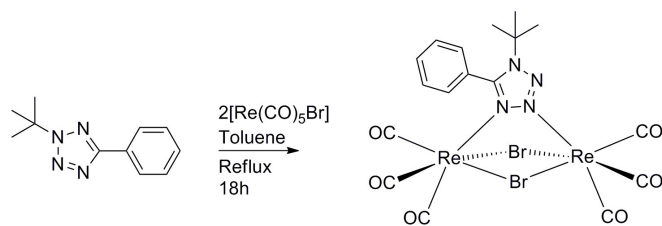
**Figure 2.8:** X-Ray crystal structures of  $[\text{Re}(\text{}^t\text{BuTzPy})\text{X}]$ , displacement ellipsoids drawn at 50 % probability. H atoms and solvent molecules are omitted for clarity. a)  $[\text{Re}(\text{}^t\text{BuTzPy})\text{Cl}]$ . b)  $[\text{Re}(\text{}^t\text{BuTzPy})\text{Br}]$ .

$[\text{Re}(\text{}^t\text{BuTzPy})\text{Cl}]$  and  $[\text{Re}(\text{}^t\text{BuTzPy})\text{Br}]$  crystallise in monoclinic space groups  $\text{P}2_1/\text{n}$  and  $\text{P}2_1/\text{c}$ , respectively (Figure 2.8). In both structures the Re(I) centre is in a slightly distorted octahedral geometry and the metal centre is chelated by the tetrazole ligand at the  $\text{N}_{(\text{py})}$  and  $\text{N}4_{(\text{tz})}$  positions. The carbonyl ligands are in the *facial* configuration and both structures appear virtually identical.

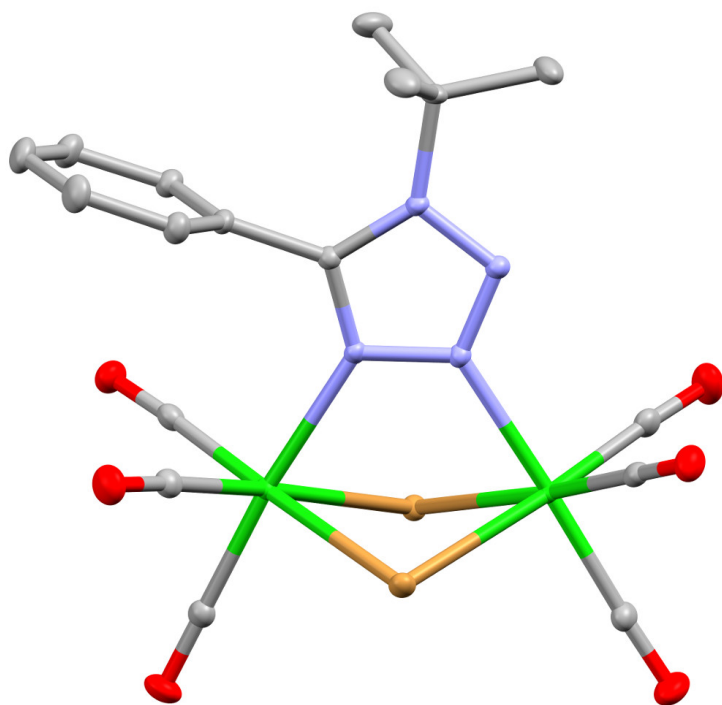
#### 2.4.2 Synthesis of Re(I) complex using ${}^t\text{BuTzPh}$

The next complex was formed by the combination of the ligand  ${}^t\text{BuTzPh}$  with  $[\text{Re}(\text{CO})_5\text{Br}]$  in toluene and stirred at reflux. The reaction did not produce a cyclometallated structure as proposed. The actual product was determined by crystallographic analysis (Figure 2.10), as bulk purification did not lead to a pure product.

This complex crystallises in the monoclinic space group  $\text{P}2_1/\text{n}$ , and illustrates that there are two Re(I) metal centres bridged by the tetrazole ligand at the N4



**Figure 2.9:** Reaction scheme for the synthesis of  $[\text{Re}_2(\text{}^t\text{BuTzPh})\text{Br}_2]$ .

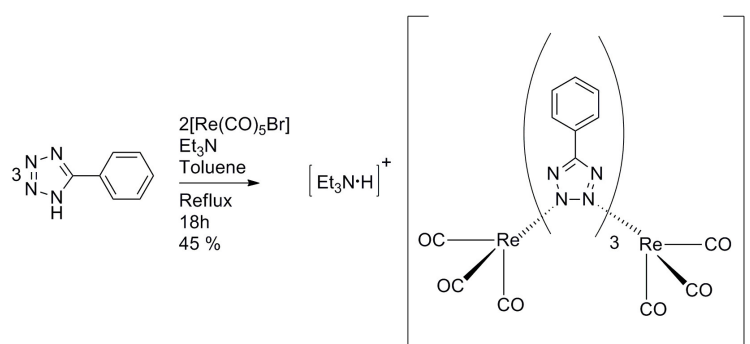


**Figure 2.10:** X-Ray crystal structure of  $[\text{Re}_2(\text{}^t\text{BuTzPh})\text{Br}_2]$ , where displacement ellipsoids are drawn at 50 % probability. H atoms and solvent molecules are omitted for clarity.

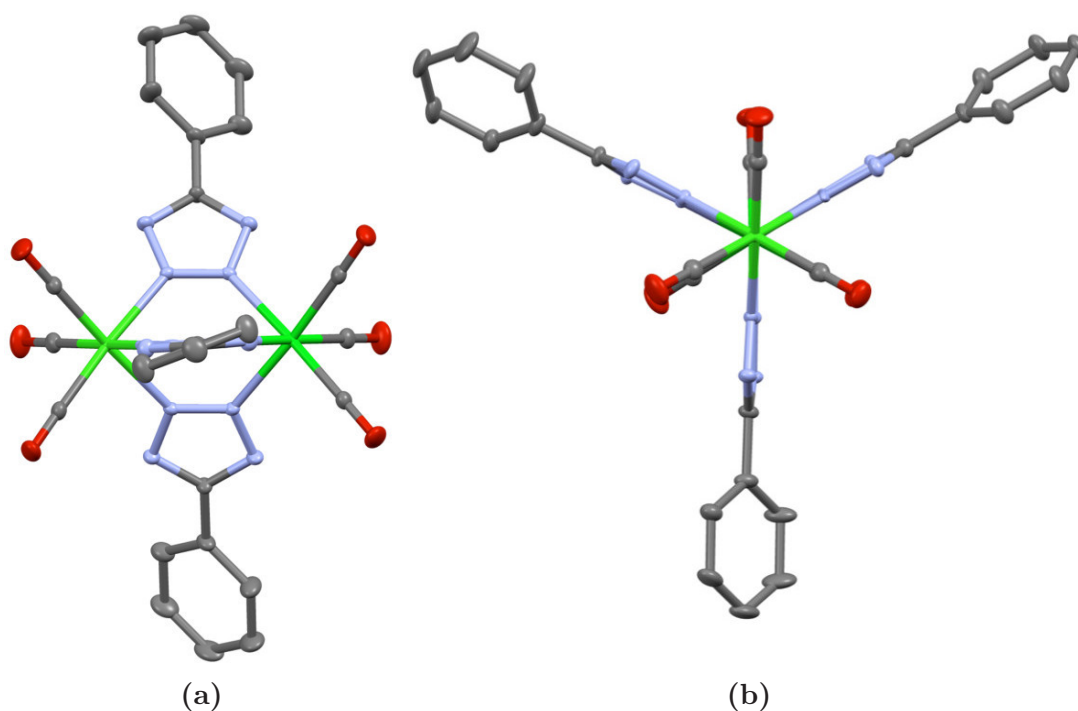
and N3 positions. The *tert*-butyl group has moved from the N2 to the N1 position. This compound could not be characterised further due to the inability to obtain it pure. This type of structure has been observed with diazine complexes of Re(I) in literature.<sup>54,113,231–236</sup>

### 2.4.3 Synthesis of Re(I) complex with HTzPh

The interesting result obtaining  $[\text{Re}_2(\text{}^t\text{BuTzPh})\text{Br}_2]$  prompted interest into the reaction of HTzPh with  $[\text{Re}(\text{CO})_5\text{X}]$  ( $\text{X} = \text{Cl}, \text{Br}$ ), as shown in Figure 2.11. The product of this synthesis,  $[\text{HNET}_3][\text{Re}_2(\text{TzPh})_3]$  (also referred to as  $[\text{Re}_2(\text{TzPh})_3]^-$ ), was a triethylammonium salt of a negatively charged dinuclear complex. This synthesis required the use of  $[\text{Re}(\text{CO})_5\text{Br}]$  in lieu of  $[\text{Re}(\text{CO})_5\text{Cl}]$  as a reagent, due to inability to isolate a product when using the latter.



**Figure 2.11:** Reaction scheme for the synthesis of  $[\text{HNEt}_3][\text{Re}_2(\text{TzPh})_3]$ .



**Figure 2.12:** X-Ray crystal structure of  $[\text{HNEt}_3][\text{Re}_2(\text{TzPh})_3]$ , with displacement ellipsoids drawn at 50 % probability. H atoms, counter-ions, and solvent molecules are omitted for clarity. a) view along pseudo  $C_2$  axis. b) View along pseudo  $C_3$  axis.

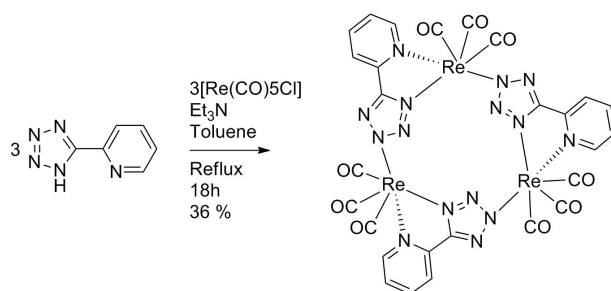
The structure of this complex was initially determined by crystallographic analysis and the crystal structure is shown in Figure 2.12. This complex crystallises in the monoclinic space group  $C2/c$ . It can be seen that the metal centres are bridged by three tetrazole ligands via the N2 and N3 atoms. The assembly possesses a  $C_3$  type rotation axis running through the two Re(I) centres and appears in a "propeller" arrangement seen down this axis. The CO ligands are seen to be in a *facial* conformation and the complex is in a pseudo  $D_{3h}$  point group. This type of structure has been observed in thiobenzoate complexes of manganese, rhenium, molybdenum, and tungsten.<sup>237,238</sup>

The IR spectrum for this complex has significant peaks at 2024 and 1901  $\text{cm}^{-1}$  for the carbonyl stretching frequencies. These frequencies correspond to the *facial* CO stretches. A peak at 1603  $\text{cm}^{-1}$  confirms the presence of the tetrazole.

The  $^1\text{H-NMR}$  spectrum for this complex matches the determined structure. Multiplets at 8.15 and 7.53 ppm, with integration ratios of 6 to 9 respectively, correspond to the phenyl protons. Signals at 3.42 and 1.39 ppm with integration ratios of 6 and 9 protons, respectively, correspond to the ethyl protons on the triethylammonium cation. The  $^{13}\text{C-NMR}$  spectrum display a signal at 196.6 ppm for the CO ligands, suggestive that the carbonyl ligands are equivalent.

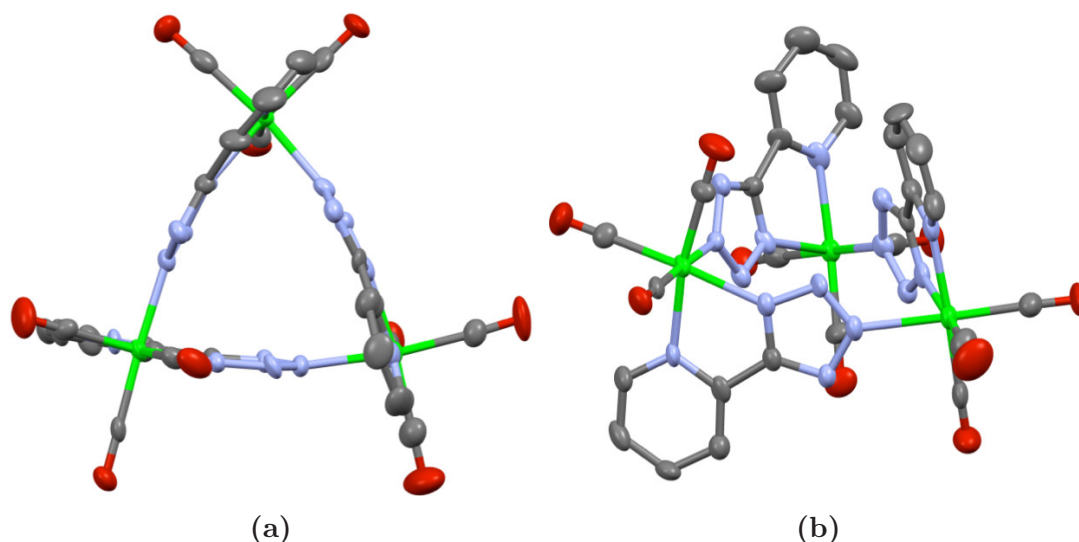
#### 2.4.4 Synthesis of Re(I) complex with HTzPy

The reaction of HTzPy with  $[\text{Re}(\text{CO})_5\text{X}]$  ( $\text{X} = \text{Cl}, \text{Br}$ ), as shown in Figure 2.13, gave a neutral complex that contains three Re(I) centres and three ligands in a triangular arrangement, as determined by X-Ray crystallography (Figure 2.14).

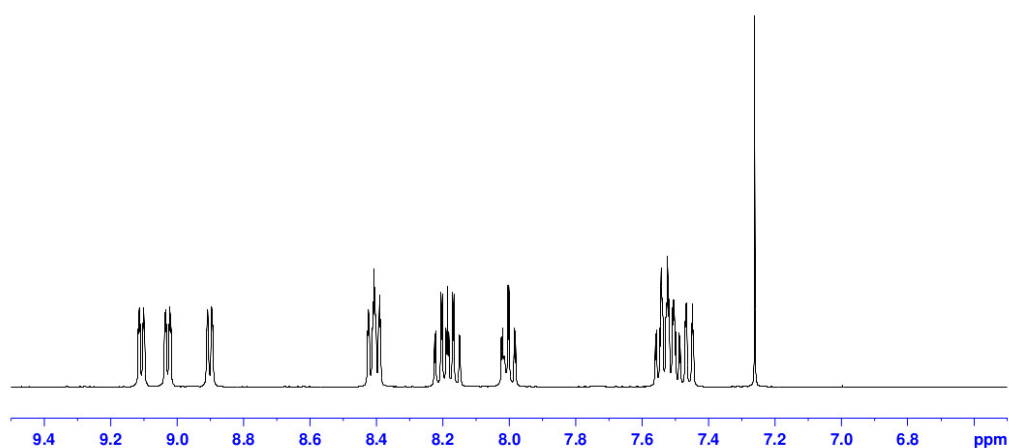


**Figure 2.13:** Reaction scheme for the synthesis of  $[\text{ReTzPy}]_3$ .

The complex crystallises in the monoclinic space group  $\text{P}2_1/\text{n}$  (Figure 2.14). The metal centres are arranged in a triangular type system bridged by three  $\text{TzPy}^-$  anions, and the ligands appear in a "partial cone" type conformation (*syn, syn, anti*), where one of the  $\text{TzPy}^-$  ligands is oriented on the opposite side to the other two.<sup>239</sup> The three CO ligands on each Re(I) centre are arranged in a *facial* configuration. The aromatic region of the  $^1\text{H-NMR}$  spectrum is shown in Figure 2.15, and the three doublets at 9.28, 9.23, and 9.13 ppm with integration of 1 are indicative of three non-equivalent  $\text{TzPy}^-$  environments. The other signals are convoluted, however, the overall integration of the aromatic region corresponds to 12 protons in agreement with three  $\text{TzPy}^-$  identities. The  $^{13}\text{C-NMR}$  spectrum for this complex also confirms three unique  $\text{TzPy}^-$  systems, revealed by signals at 166.8, 166.6, and 165.0 ppm corresponding to the three tetrazolic C5. There are overlapping peaks in the 198 - 192 ppm region of which only 6 could be clearly distinguished. This is consistent with the presence of multiple  $[\text{Re}(\text{CO})_3]$  cores. The IR spectrum has peaks at 2027 1916, and 1887  $\text{cm}^{-1}$  which



**Figure 2.14:** X-Ray crystal structure of  $[\text{ReTzPy}]_3$ , with thermal ellipsoids drawn at 50 % probability. H atoms and solvent molecules are omitted for clarity. a) View of cavity. b) Side view of crystal structure.



**Figure 2.15:**  $^1\text{H-NMR}$  spectrum of  $[\text{ReTzPy}]_3$  in  $\text{CDCl}_3$ .

are the stretching modes of the *facial* CO groups. The significant CO stretching frequency at  $2027\text{ cm}^{-1}$  is suggestive of a reduction in electron density on the metal centres with respect to other reported neutral Re(I) complexes bound to diimine ligands.

There have been multiple reports in literature of supramolecular motifs of Re(I) forming molecular polyhedra.<sup>18,240–245</sup> However the synthesis of  $[\text{ReTzPy}]_3$  appears to be a facile synthetic route to a photo-stable complex with a uniquely metallacalix[3]arene type structure, of which there is only one other known report by Coogan.<sup>246</sup>

## 2.5 Photophysical and computational investigation

### 2.5.1 Absorption and computational results

A summary of the photophysical properties of the complexes is reported in Table 2.1

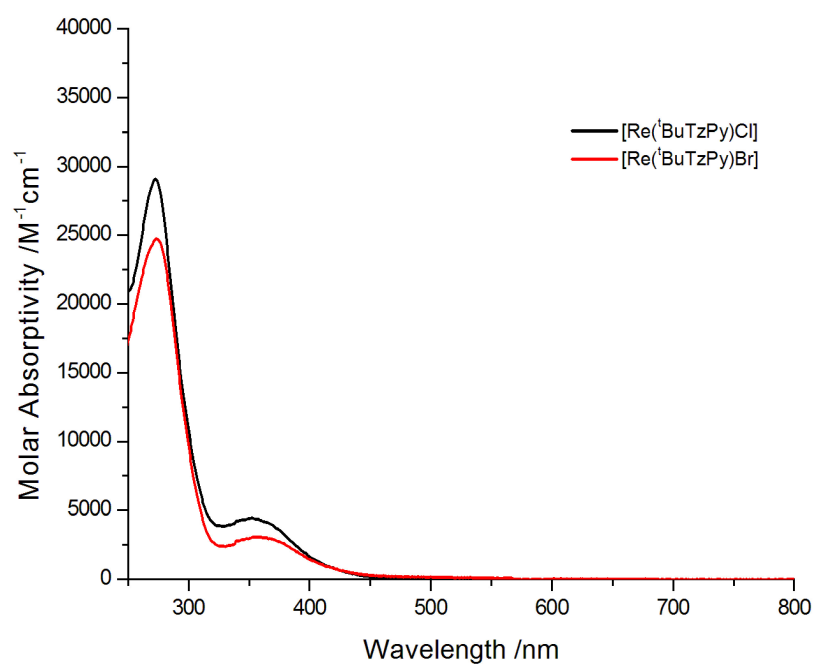
**Table 2.1:** Summary of the photophysical properties of dilute ( $10^{-5}$  M) DCM solutions of the reported complexes.

Complex	Absorption		Emission, 298 K				Emission, 77 K		
	$\lambda_{max}$ [nm]	$(10^4\epsilon)$ [M <sup>-1</sup> cm <sup>-1</sup> ]	$\lambda_{max}$ [nm]	$\tau^a$ [ns]	$\tau^b$ [ns]	$\phi^a$	$\phi^b$	$\lambda_{em}$ [nm]	$\tau$ [ $\mu$ s]
[Re( <sup>t</sup> BuTzPy)Cl]	271(2.90) 353(0.45)		574	167	291	0.033	0.077	510	5.81
[Re( <sup>t</sup> BuTzPy)Br]	268(2.48) 358(0.31)		568	177	323	0.024	0.058	508	6.28
[Re <sub>2</sub> (TzPh) <sub>3</sub> ] <sup>-</sup>	253(6.85) 312(0.60)		- <sup>c</sup>	- <sup>c</sup>	- <sup>c</sup>	- <sup>c</sup>	- <sup>c</sup>	474	4.30
[ReTzPy] <sub>3</sub>	252(5.26) 283(3.88) 310(2.01)		498	135	244	0.030	0.060	466	4.99

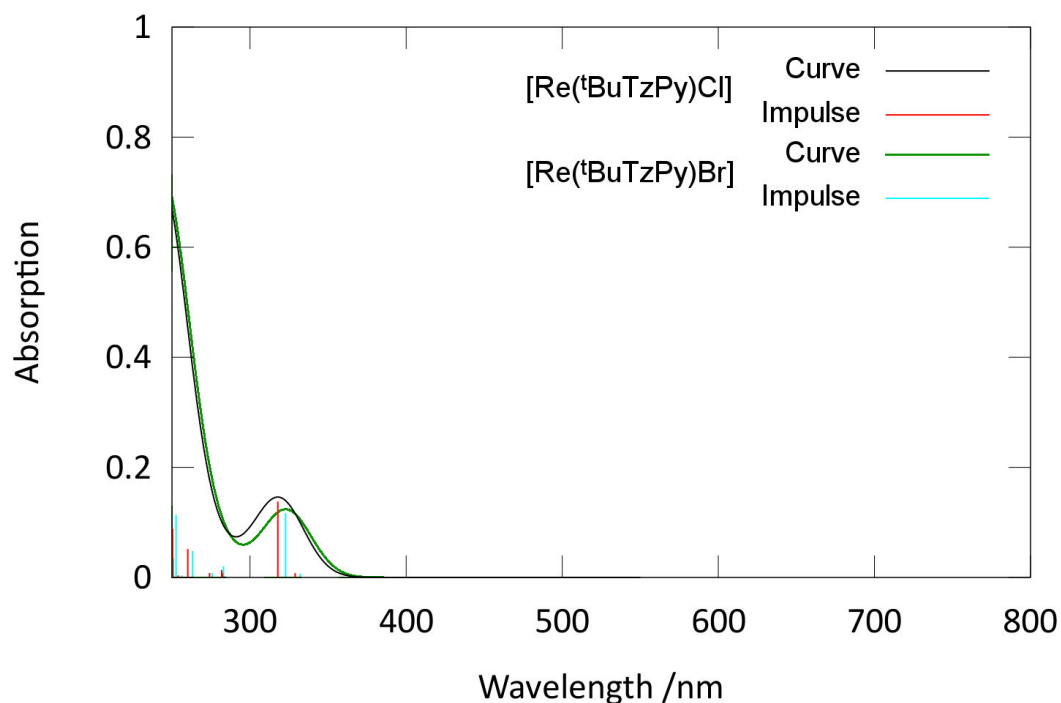
<sup>a</sup>Air-equilibrated solution, <sup>b</sup>deoxygenated solution.

<sup>c</sup>Emission of [Re<sub>2</sub>(TzPh)<sub>3</sub>]<sup>-</sup> at r.t. in solution was too weak to be accurately measured. Quantum yield values measured against an air-equilibrated aqueous solution of [Ru(bpy)<sub>3</sub>]Cl<sub>2</sub> ( $\phi = 0.028$ ).

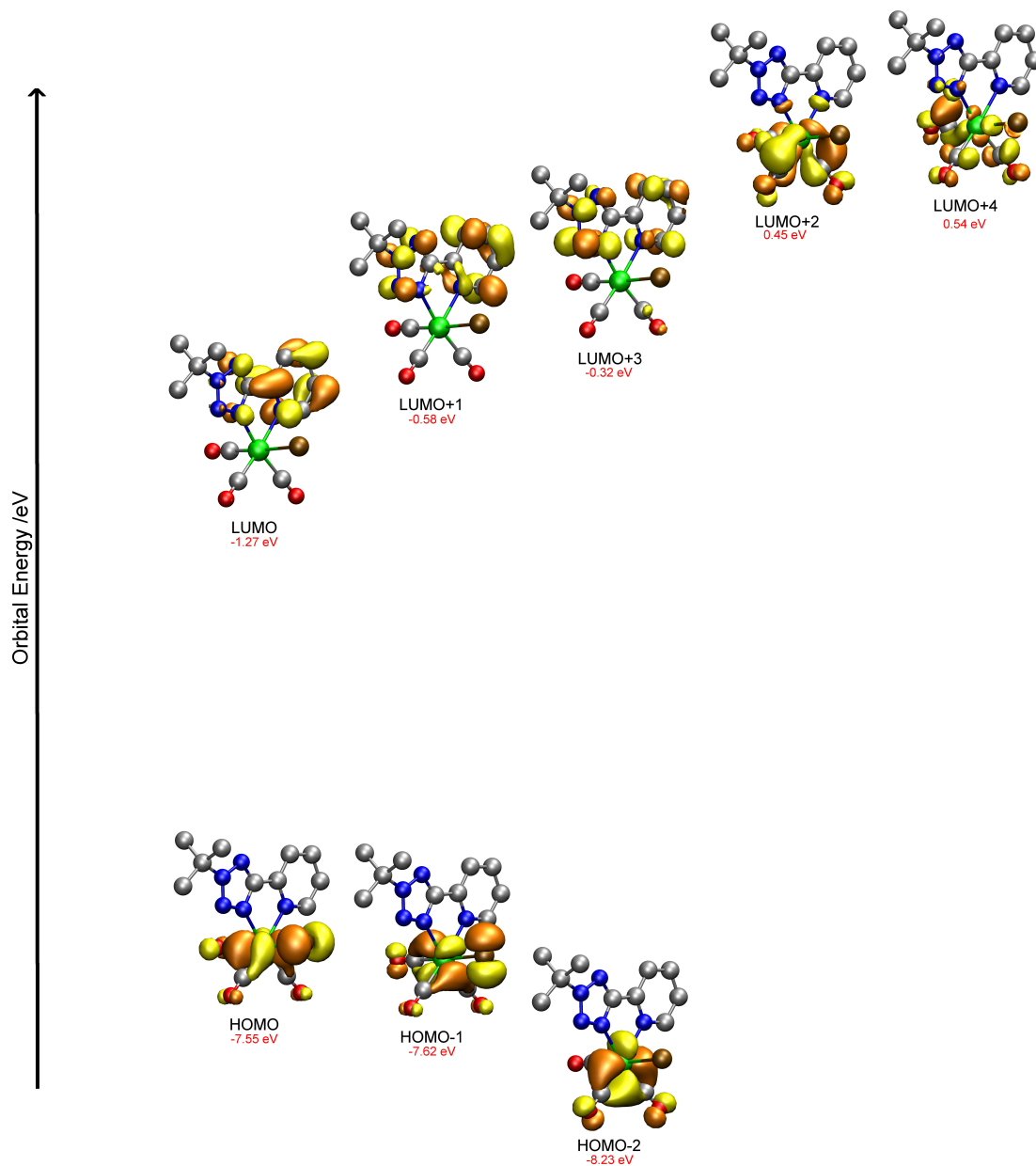
The absorption spectra of [Re(<sup>t</sup>BuTzPy)Cl] and [Re(<sup>t</sup>BuTzPy)Br] are shown in Figure 2.16. These absorption profiles appear very similar, as is expected considering the similarity of the structures. Both spectra have a high energy absorption band at ca. 270 nm, corresponding to the intra-ligand  $\pi$ - $\pi^*$  transition. There is also a peak at lower energy for each complex at 355 nm corresponding to the admixture of a metal-to-ligand charge transfer (from Re(I) to <sup>t</sup>BuTzPy) and ligand-to-ligand charge transfer (halide to <sup>t</sup>BuTzPy), as typically reported for Re(I) diimine complexes.<sup>247</sup>



**Figure 2.16:** Absorption spectra of dilute ( $10^{-5}$  M) DCM solutions of  $[\text{Re}(\text{}^t\text{BuTzPy})\text{Cl}]$  and  $[\text{Re}(\text{}^t\text{BuTzPy})\text{Br}]$ .



**Figure 2.17:** Simulated absorption spectra of  $[\text{Re}(\text{}^t\text{BuTzPy})\text{Cl}]$  and  $[\text{Re}(\text{}^t\text{BuTzPy})\text{Br}]$ . Limited to the 250 nm to 800 nm range. Impulses correspond to transitions listed in Table 2.2.



**Figure 2.18:** Simulated orbitals for  $[\text{Re}(t\text{BuTzPy})\text{Br}]$  corresponding to transitions listed in Table 2.2. Orbitals are spaced vertically relative to their energy and the HOMO-LUMO gap has been reduced for clarity.



**Table 2.2:** Table of overall transitions with oscillator strength  $\geq 0.05$ . Limited to the 250 nm to 800 nm range.

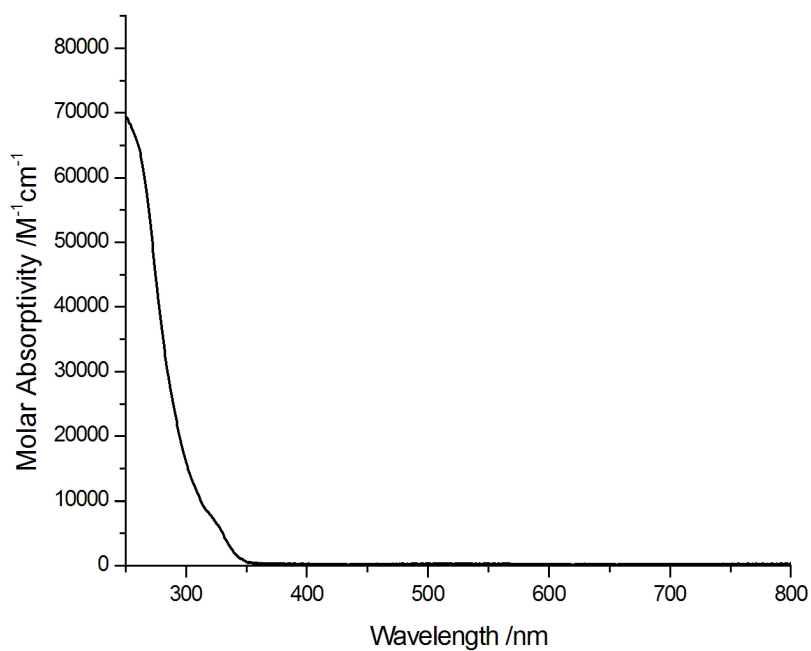
Species	Wavelength	Intensity	Levels	Character	Assignment
[Re( <sup>t</sup> BuTzPy)Cl]	317.83	0.14	HOMO-1 → LUMO	90 %	MLLCT
	260.18	0.05	HOMO-1 → LUMO+1	29 %	MLLCT
			HOMO-1 → LUMO+4	25 %	MLLCT + MC
[Re( <sup>t</sup> BuTzPy)Br]	322.82	0.12	HOMO-1 → LUMO	91 %	MLLCT
	263.23	0.05	HOMO-1 → LUMO+1	33 %	MLLCT
			HOMO-1 → LUMO+4	23 %	MLLCT + MC
			HOMO-2 → LUMO+3	29 %	MLLCT + MC
	252.61	0.11	HOMO-1 → LUMO+1	16 %	MLLCT

The simulated absorption spectra for complexes [Re(<sup>t</sup>BuTzPy)Cl] and [Re(<sup>t</sup>BuTzPy)Br] can be found in Figure 2.17, with relevant transitions listed in Table 2.2. The simulated orbital contours are located in Figure 2.18. Figure 2.18 contains only the simulated orbitals for [Re(<sup>t</sup>BuTzPy)Br]; the orbitals for [Re(<sup>t</sup>BuTzPy)Cl] are virtually identical, thus only one set is displayed.

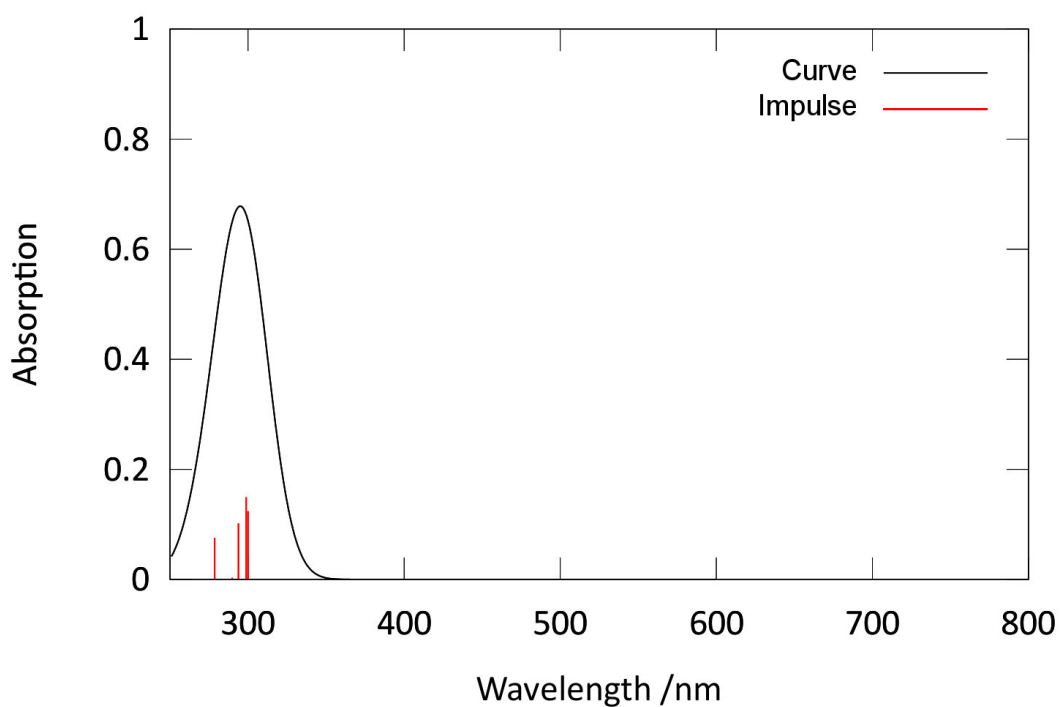
The simulated spectra for [Re(<sup>t</sup>BuTzPy)Cl] and [Re(<sup>t</sup>BuTzPy)Br] indicate that transitions of lowest energy (ca. 320 nm) primarily involve the HOMO-N (N = 1, 2) and LUMO+M (M = 0, 1). From Figure 2.18, these transitions are seen to be an admixture of MLCT and LLCT transitions, confirming the MLLCT assignment given for the absorption spectrum.

Further to this, the HOMO-N (N = 3 - 5) are localised on the <sup>t</sup>BuTzPy ligand. These orbitals are involved in transitions of higher energy than 250 nm and suggests that these transitions display IL character.

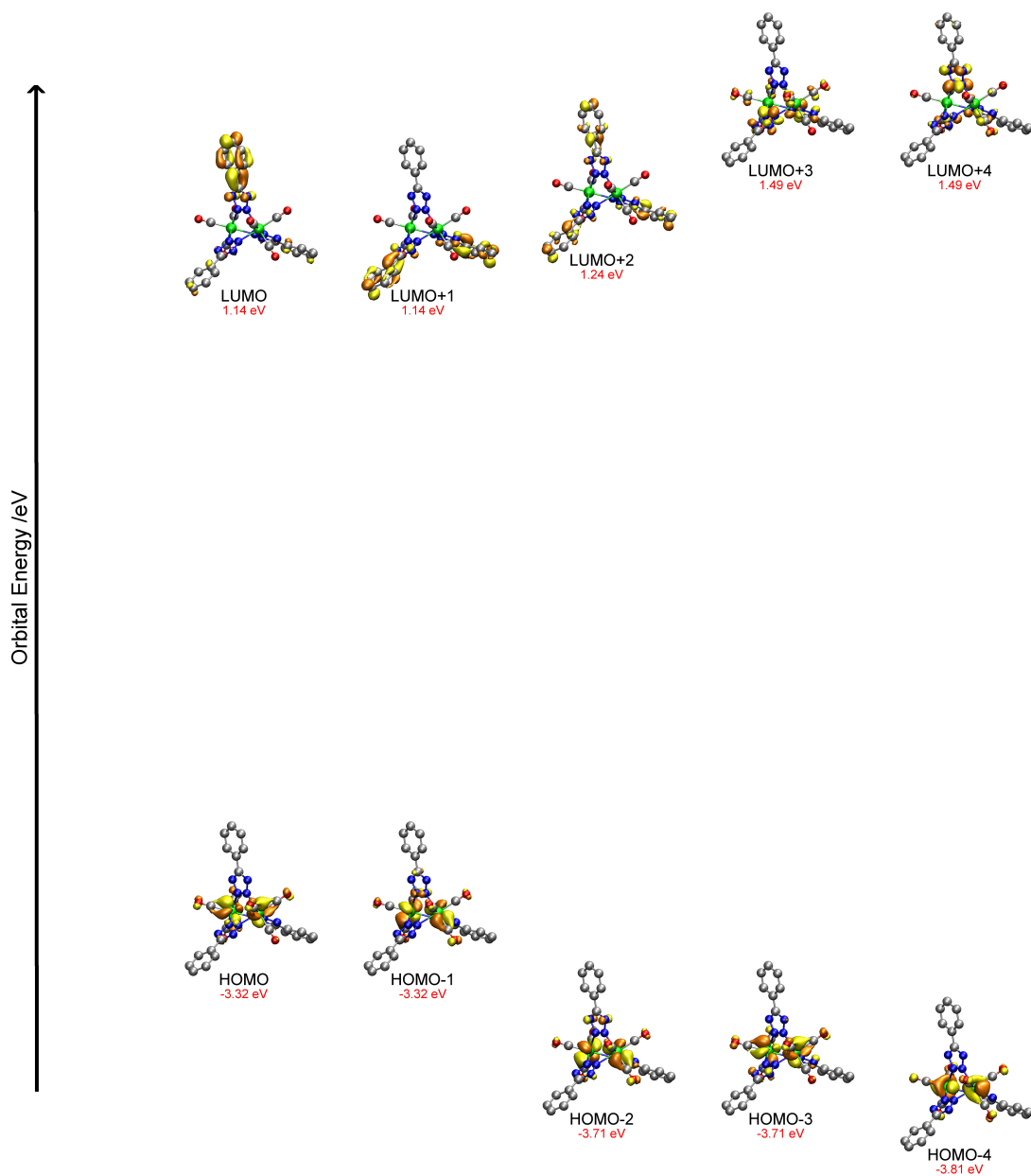
The absorption spectrum of [HNet<sub>3</sub>][Re<sub>2</sub>(TzPh)<sub>3</sub>] is shown in Figure 2.19 and displays a high energy band at ca. 253 nm that corresponds to the intra-ligand  $\pi$ - $\pi^*$  transition. There is also a peak of lower energy that appears to be partially hidden behind the  $\pi$ - $\pi^*$  transition at ca. 312 nm. This peak possibly corresponds to involvement of a metal-to-ligand charge transfer transition, from Re(I) to TzPh<sup>-</sup>.



**Figure 2.19:** Absorption spectrum of a dilute ( $10^{-5}$  M) DCM solution of  $[\text{Re}_2(\text{TzPh})_3]^-$ .



**Figure 2.20:** Simulated absorption spectrum for  $[\text{Re}_2(\text{TzPh})_3]^-$ . Limited to the 250 nm to 800 nm range. Impulses correspond to transitions listed in Table 2.3.



**Figure 2.21:** Simulated orbitals for  $[\text{Re}_2(\text{TzPh})_3]^-$  corresponding to transitions listed in Table 2.3. Orbitals are spaced vertically relative to their energy and the HOMO-LUMO spacing has been reduced for clarity.

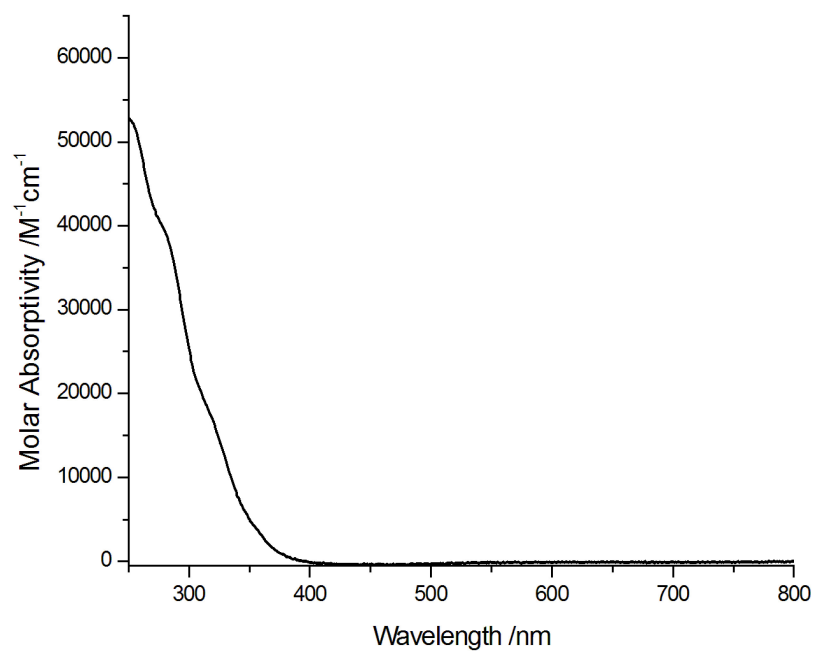
**Table 2.3:** Table of overall transitions with oscillator strength  $\geq 0.05$ . Limited to the 250 nm to 800 nm range.

Species	Wavelength	Intensity	Levels	Character	Assignment
$[\text{Re}_2(\text{TzPh})_3]^-$	299.99	0.12	HOMO-1 $\rightarrow$ LUMO+1	47 %	MLLCT
			HOMO $\rightarrow$ LUMO	47 %	MLLCT
	298.82	0.15	HOMO-1 $\rightarrow$ LUMO+4	41 %	MLLCT
			HOMO $\rightarrow$ LUMO+3	41 %	MLLCT
	293.87	0.10	HOMO $\rightarrow$ LUMO+2	98 %	MLLCT
	278.62	0.08	HOMO-4 $\rightarrow$ LUMO+3	43 %	MLLCT
			HOMO-3 $\rightarrow$ LUMO+3	23 %	MLLCT
			HOMO-2 $\rightarrow$ LUMO+4	23 %	MLLCT

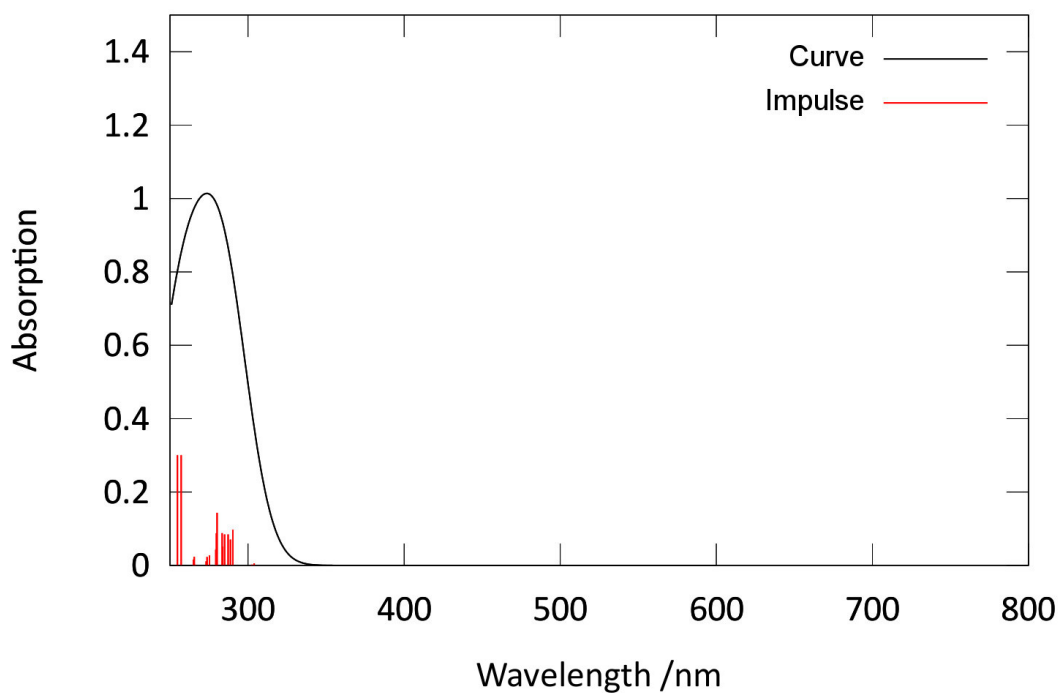
The simulated absorption spectra for  $[\text{Re}_2(\text{TzPh})_3]^-$  can be found in Figure 2.20, the relevant transitions are found in Table 2.3, and the simulated orbitals are located in Figure 2.21. The simulation for this complex was performed differently than other complexes due to the inability to optimise the geometry under the same conditions. Symmetry restrictions were used for the molecule and looser cutoffs were used to determine the minimised structure.

The impulses of highest oscillator strength involve transitions from HOMO-N ( $N = 0 - 2$ ), primarily localised on the Re(I) centres and CO ligands, to the LUMO+M ( $M = 0 - 4$ ), localised on the  $\text{TzPh}^-$  species. Figure 2.21 displays representative orbitals showing that the transitions are of MLLCT character, suggesting that the transitions observed in the absorption spectrum of  $[\text{Re}_2(\text{TzPh})_3]^-$  are likely to be of MLLCT character. This assignment appears to contradict that given to the experimental absorption spectrum, however, the restrictions used in the simulations may have yielded results that do not reflect the experiment well.

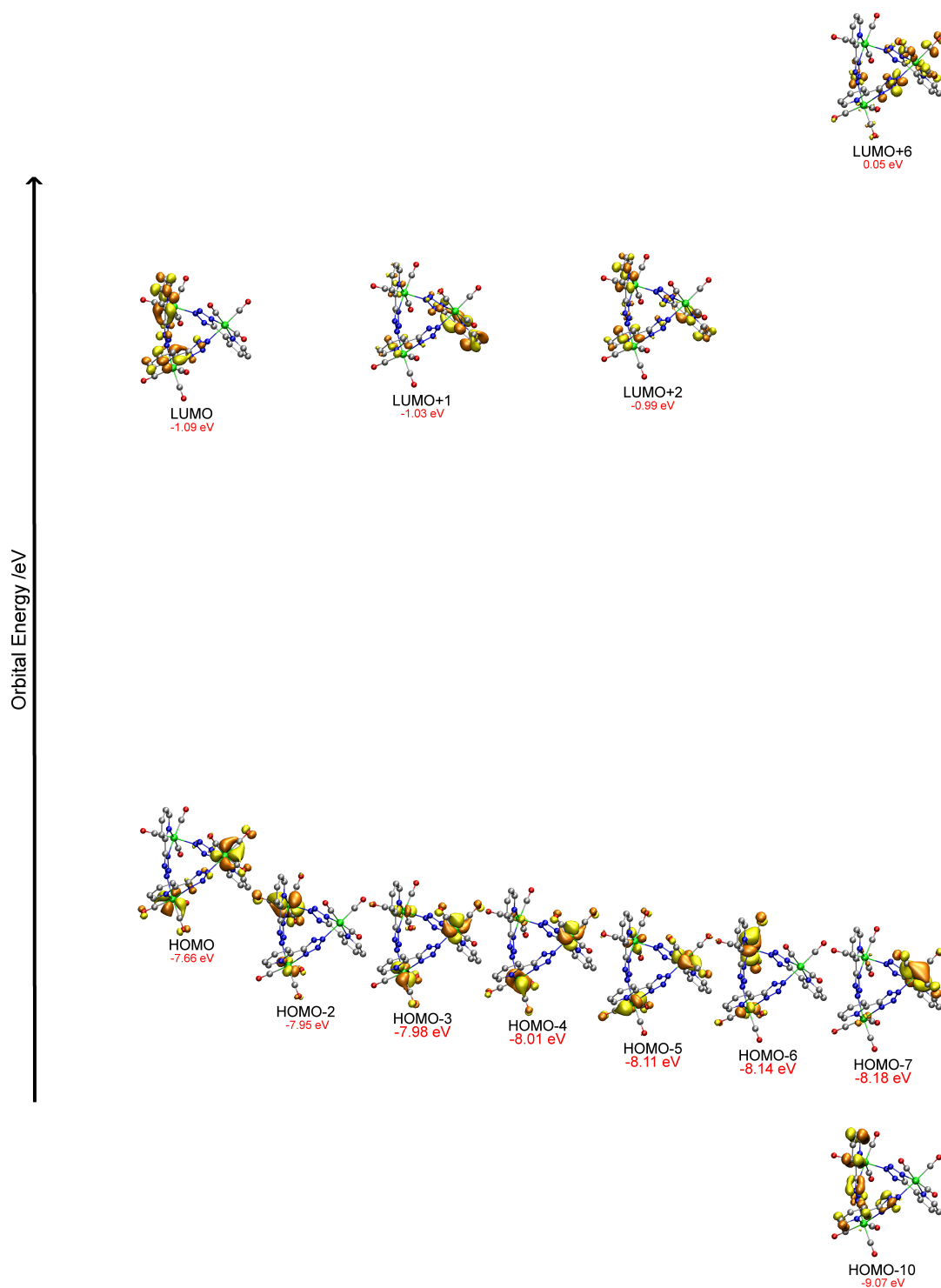
The absorption spectrum of  $[\text{ReTzPy}]_3$  is shown in Figure 2.22 and has a high energy absorption band at ca. 252 nm assigned to the intra-ligand  $\pi-\pi^*$  transition. There are also a series of peaks that appear as shoulders on the tail of this  $\pi-\pi^*$  transition at 283, 310, and 340-350 nm. It is difficult to deconvolute these peaks however they are tentatively attributed as a mixture of a set of MLLCT transitions that involve each of the Re(I) centres and the  $\text{TzPy}^-$  ligands.



**Figure 2.22:** Absorption spectrum of a dilute ( $10^{-5}$  M) DCM solution of  $[\text{ReTzPy}]_3$ .



**Figure 2.23:** Simulated absorption spectrum of  $[\text{ReTzPy}]_3$ . Limited to the 250 nm to 800 nm range. Impulses correspond to transitions listed in Table 2.4.



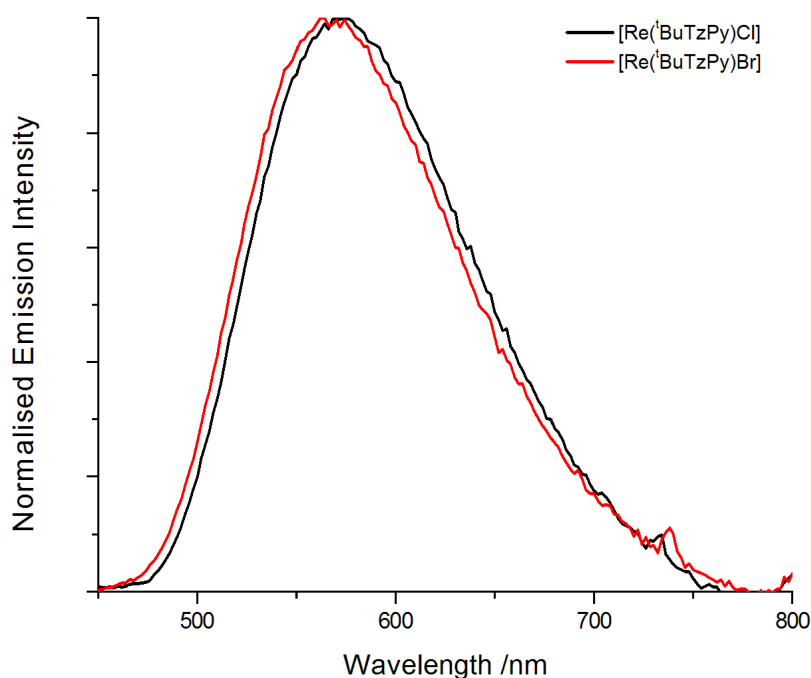
**Figure 2.24:** Simulated orbitals for  $[\text{ReTzPy}]_3$  corresponding to transitions listed in Table 2.4. Orbitals are spaced vertically relative to their energy and the HOMO-LUMO spacing has been reduced for clarity.

**Table 2.4:** Table of overall transitions with oscillator strength  $\geq 0.05$ . Limited to the 250 nm to 800 nm range.

Species	Wavelength	Intensity	Levels	Character	Assignment
[ReTzPy] <sub>3</sub>	290.28	0.10	HOMO-2 → LUMO	25 %	MLLCT
			HOMO-2 → LUMO+2	13 %	MLLCT
	287.23	0.08	HOMO-4 → LUMO+1	16 %	MLLCT
			HOMO-5 → LUMO+1	14 %	MLLCT
			HOMO-3 → LUMO+1	13 %	MLLCT
			HOMO-6 → LUMO+2	13 %	MLLCT
	280.19	0.14	HOMO-7 → LUMO+1	16 %	MLLCT
			HOMO → LUMO+6	15 %	MLLCT+IL
	257.17	0.30	HOMO-10 → LUMO	12 %	MLLCT+IL
			HOMO → LUMO	15 %	MLLCT

The simulated absorption spectrum for [ReTzPy]<sub>3</sub> can be found in Figure 2.23 and high oscillator strength ( $\geq 0.05$ ) transitions are found in Table 2.4. Representative orbital contours are located in Figure 2.24. [ReTzPy]<sub>3</sub> has many convoluted transitions that contribute to the overall absorption spectrum. The lower energy transitions  $\leq 287$  nm appear to be primarily MLLCT in character. Moving to higher energy transitions, the HOMO-N (N = 9 - 12) are localised on the TzPy<sup>-</sup> ligands, and the LUMO+M (M = 6 - 12) correspond to orbitals that are partly localised on the metal centre and TzPy<sup>-</sup> ligands. Thus some of the higher energy transitions may display IL character (280.19 and 257.17 nm).

## 2.5.2 Emission properties of the complexes



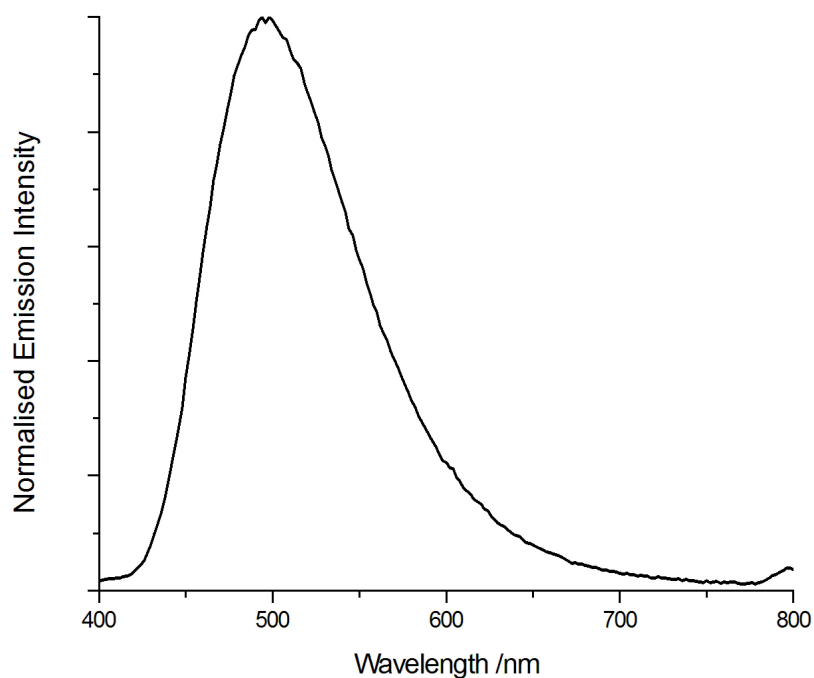
**Figure 2.25:** Emission spectra of dilute ( $10^{-5}$  M) DCM solutions of  $[\text{Re}(^t\text{BuTzPy})\text{Cl}]$  and  $[\text{Re}(^t\text{BuTzPy})\text{Br}]$  excited at 350 nm.

The emission of both  $[\text{Re}(^t\text{BuTzPy})\text{Cl}]$  and  $[\text{Re}(^t\text{BuTzPy})\text{Br}]$  appear similar, as shown in Figure 2.25, with peak maxima at 574 and 568 nm, respectively. The emission bands are broad and structureless indicating that the transitions are MLLCT in nature. The phosphorescent nature of the emission is supported by the change in lifetime and quantum yield when moving from air-equilibrated to deoxygenated solutions. The quantum yield and lifetime of  $[\text{Re}(^t\text{BuTzPy})\text{Cl}]$  and  $[\text{Re}(^t\text{BuTzPy})\text{Br}]$  are similar to that of previously reported Re(I) diimine complexes.

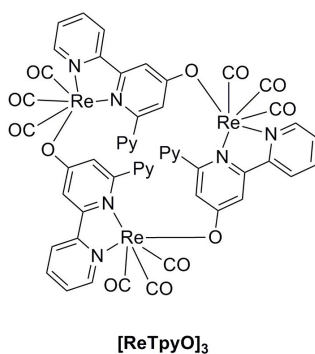
The emission of  $[\text{Re}_2(\text{TzPh})_3]^-$  at r.t. in solution is too weak to be distinguishable from the baseline and is not reported.

The emission of  $[\text{ReTzPy}]_3$  appears in Figure 2.26 with a single peak maximum at 498 nm. The emission band is broad and structureless indicating the transition is primarily MLLCT in nature. The assignment of phosphorescent emission is supported by the change in lifetime and quantum yield upon deoxygenation of the solution. The emission of this complex, at 498 nm, is significantly blue-shifted with respect to previously reported complexes and literature examples of neutral Re(I) complexes. In-fact, this complex to the best of our knowledge is the most *blue* emitting neutral Re(I) complex reported in literature to date. It can be compared to the only other photophysically characterised triangle of





**Figure 2.26:** Emission spectrum of a dilute ( $10^{-5}$  M) DCM solution of  $[\text{ReTzPy}]_3$  excited at 310 nm.



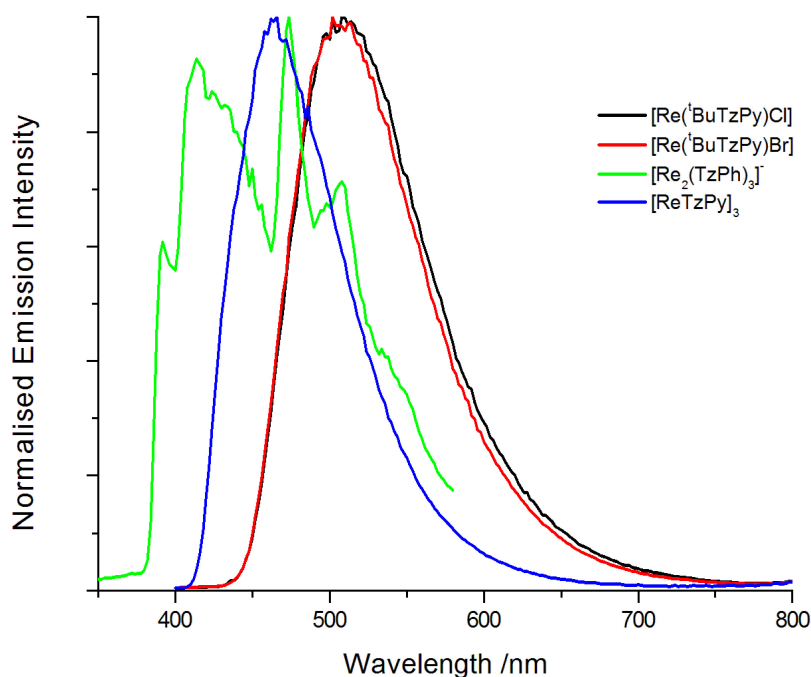
**Figure 2.27:** Structural representation of  $[\text{ReTpyO}]_3$ .<sup>246</sup>

Re(I),  $[\text{ReTpyO}]_3$ , reported by Coogan with emission wavelength at 557 nm.<sup>246</sup> The blueshift of the MLLCT transition for  $[\text{ReTzPy}]_3$  is possibly caused by a reduction of electron density on the Re(I) centre, this is suggested by a relatively higher CO stretching frequency at  $2027\text{ cm}^{-1}$  in comparison to  $2016\text{ cm}^{-1}$  for  $[\text{ReTpyO}]_3$ .

**Table 2.5:** Decay constants in deoxygenated solution.

Complex	$k_r [10^5 \text{s}^{-1}]$	$k_{nr} [10^5 \text{s}^{-1}]$
$[\text{ReTzPy}]_3$	2.45	38.52
$[\text{ReTpyO}]_3$	0.86	453.68

Comparing the overall photophysical performance of  $[\text{ReTzPy}]_3$  and  $[\text{ReTpyO}]_3$  indicates that the major difference is a reduction in the value of the non-radiative decay constant by a factor of almost 12.  $[\text{ReTzPy}]_3$  has a more rigid structure than  $[\text{ReTpyO}]_3$  which would reduce  $k_{nr}$  by removing vibrational modes of relaxation, and the higher energy gap would also reduce the non-radiative decay rate according to the energy gap law.



**Figure 2.28:** Emission spectra of complexes at 77 K. Excitations of 350 nm for  $[\text{Re}(^t\text{BuTzPy})\text{Cl}]$  and  $[\text{Re}(^t\text{BuTzPy})\text{Br}]$ , and 310 nm for  $[\text{Re}_2(\text{TzPh})_3]^-$  and  $[\text{ReTzPy}]_3$ .

Emission of these complexes at 77 K is shown in Figure 2.28. All complexes, except  $[\text{Re}_2(\text{TzPh})_3]^-$ , display a blue-shift relative to their solution state emission, this is ascribed to rigidochromism typical to transitions of CT character. The emission of  $[\text{Re}(^t\text{BuTzPy})\text{Cl}]$  and  $[\text{Re}(^t\text{BuTzPy})\text{Br}]$  is blue-shifted to 510 nm, while remaining broad and structureless, suggestive that the transition is of MLLCT character. The lifetime of this emission elongates to 5.81  $\mu\text{s}$  and 6.28  $\mu\text{s}$  for  $[\text{Re}(^t\text{BuTzPy})\text{Cl}]$  and  $[\text{Re}(^t\text{BuTzPy})\text{Br}]$ , respectively.

Contrary to measurements of dilute solution, the emission of  $[\text{Re}_2(\text{TzPh})_3]^-$  at 77 K, shown in Figure 2.28, can be measured. The structured emission is indicative of IL character. The lifetime of this emission is detectable at 4.30  $\mu\text{s}$ . The emission for  $[\text{ReTzPy}]_3$  blueshifts to 466 nm, remaining broad and structureless, as seen in Figure 2.28, and the decay lifetime increases to 4.99  $\mu\text{s}$  when frozen in rigid matrix at 77 K. This is consistent with a transition primarily MLLCT in character.

## 2.6 Electrochemical investigation

The electrochemical behaviour of the complexes was investigated using cyclic voltammetry, and a summary of the data can be found in Table 2.6. Peak mid-points, or maxima if peaks are irreversible, are listed as  $E_p$  and peak to peak separations are given as  $\Delta E_{pp}$ .

**Table 2.6:** Summary of electrochemical data for ca. 10 mmol/L solutions of complexes in C6mim[FAP]. Potentials are relative to ferrocene/ferrocinium<sup>+</sup> couple.

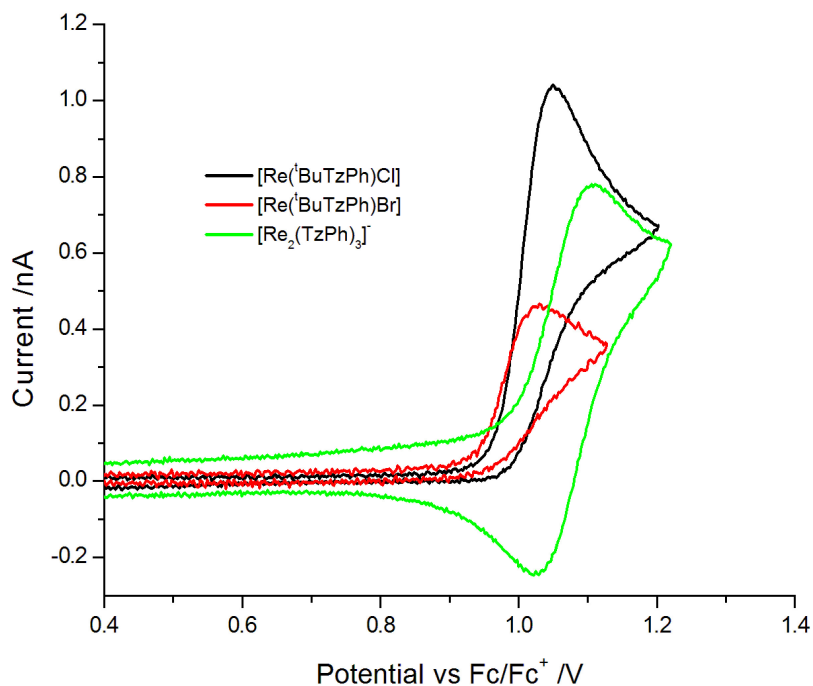
Complex	Oxidation		Reduction	
	$E_p$ vs Fc/Fc <sup>+</sup> (V)	$\Delta E_{pp}$ (mV)	$E_p$ vs Fc/Fc <sup>+</sup> (V)	$\Delta E_{pp}$ (mV)
[Re( <sup>t</sup> Bu-TzPy)Cl]	1.04	- <sup>a</sup>	-1.89	110
[Re( <sup>t</sup> Bu-TzPy)Br]	1.03	- <sup>a</sup>	-1.88	110
[Re <sub>2</sub> (TzPh) <sub>3</sub> ] <sup>-</sup>	1.10	80	-1.62	- <sup>a</sup>
[ReTzPy] <sub>3</sub>	1.21, 1.32, 1.47	87, 86, 90	-	-

<sup>a</sup>Could not be obtained due to irreversible nature.

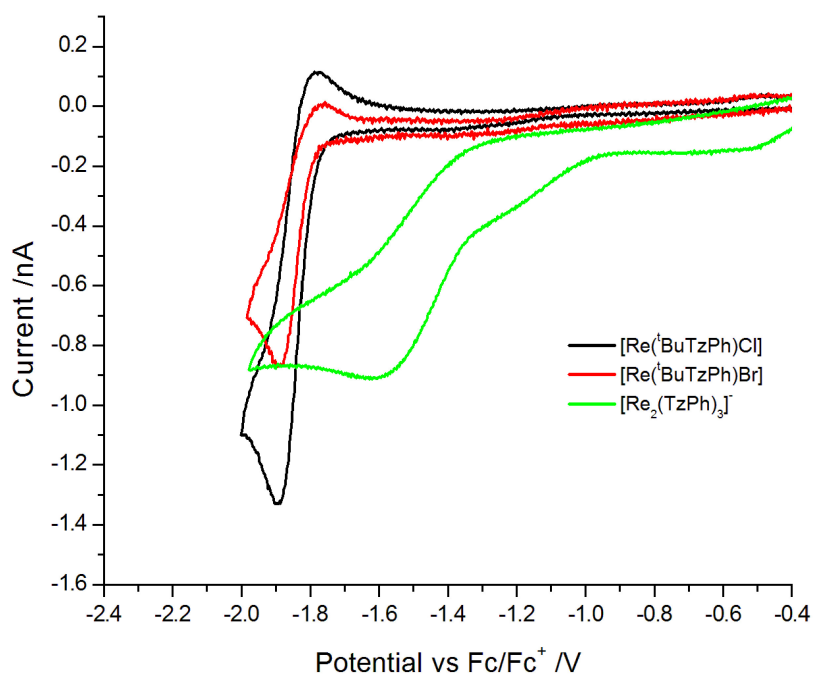
The voltammograms were recorded from solutions of the complexes dissolved in the ionic liquid 1-hexyl-3-methylimidazolium tris-(pentafluoroethyl) trifluorophosphate, [C6mim][FAP]. The advantages for this type of analysis have been previously described.<sup>2,248</sup>

The voltammograms for the oxidation and reduction regions of [Re(<sup>t</sup>BuTzPy)Cl], [Re(<sup>t</sup>BuTzPy)Br], and [Re<sub>2</sub>(TzPh)<sub>3</sub>]<sup>-</sup> are shown in Figure 2.29 and Figure 2.30, respectively.

The oxidation peaks for [Re(<sup>t</sup>BuTzPy)Cl] and [Re(<sup>t</sup>BuTzPy)Br] are at 1.04 and 1.03 V, respectively, and have no reversible character. From investigations involving other mononuclear Re(I) complexes,<sup>249</sup> this peak is attributed to oxidation occurring on the Re(I) centre as Re(I) → Re(II) + e<sup>-</sup>. The lack of reversibility indicates that any follow up chemistry occurring to these complexes is quite fast on the electrochemical timescale of 100 mVs<sup>-1</sup>. The fact that these oxidation peaks are very close to each other is in agreement with their compositional and structural similarity. The reduction peaks for [Re(<sup>t</sup>BuTzPy)Cl] and [Re(<sup>t</sup>BuTzPy)Br] can be seen at -1.89 and -1.88 V, respectively, and have minimal reversible character shown by the small height of the back peak current. This peak is ascribed to a reduction of the alkylated-pyridyl tetrazole ligand. The peak has slight reversible character, which indicates that the follow up chemistry after reduction is moderately fast on the electrochemical timescale of 100 mVs<sup>-1</sup>. The peak-to-peak separation of 110 mV is in line with a moderately fast electrochemical step in comparison to that of ferrocene of 90 mV, which has very



**Figure 2.29:** Oxidation region of voltammograms obtained for ca. 10 mmol/L solutions of complexes in C6mim[FAP]. Potentials are relative to Fc/Fc<sup>+</sup> couple.

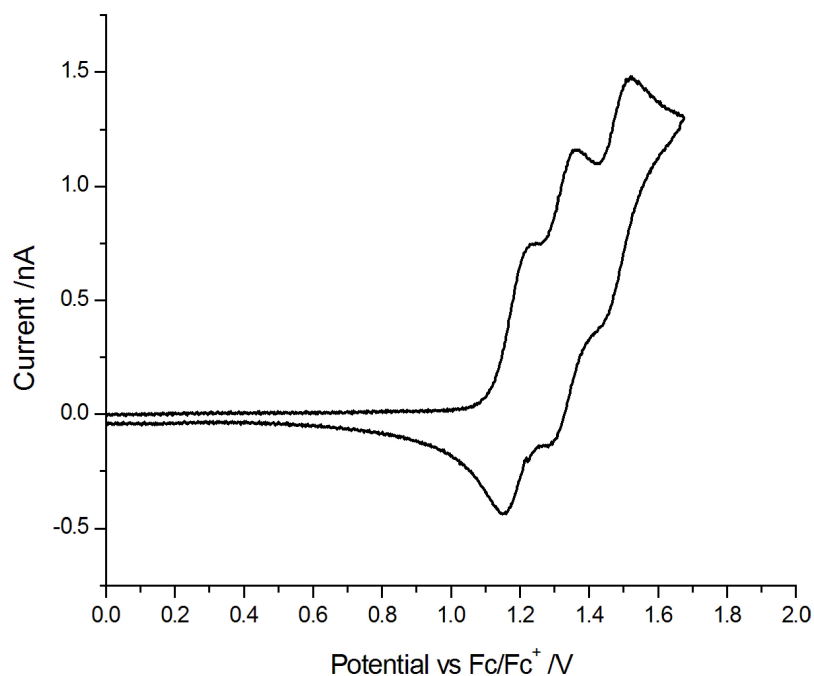


**Figure 2.30:** Reduction region of voltammograms obtained for ca. 10 mmol/L solutions of complexes in C6mim[FAP]. Potentials are relative to Fc/Fc<sup>+</sup> couple.

fast kinetics. The similarities of these complexes demonstrate that there is very little difference between the complexes when changing from the chlorine to the bromine group.

$[\text{Re}_2(\text{TzPh})_3]^-$  displays a single peak in the oxidation scan with a mid-point of 1.10 V, and a peak-to-peak separation of 80 mV. This oxidation peak is reversible, indicating fast electrochemical kinetics and that any follow up chemistry after electrochemical oxidation is relatively slow. It is also the only peak found within the electrochemical window of  $[\text{C}_6\text{mim}][\text{FAP}]$ . This is tentatively assigned to a two electron oxidation of the dinuclear species which has been seen in dinuclear complexes of Re(I) bridged by 1,2-diazine and halogen atoms.<sup>231</sup> To try to determine if in-fact this was a simultaneous two-electron oxidation, another CV experiment was run in a much less polar solvent, with the assumption that the ionic liquid was stabilizing the formation of the cationic species. Thus DCM was used as the solvent, however there was no additional distinguishable peak observed in this experiment. This lack of splitting is suggestive of minimal interaction between the two Re(I) centres.

The reduction scan for this complex can be seen in Figure 2.30 and has a broad peak suggesting very slow kinetics, and also appears to be quite irreversible. This is attributed to the reduction of the phenyl tetrazole ligand.



**Figure 2.31:** Oxidation region of cyclic voltammogram of  $[\text{ReTzPy}]_3$  in  $\text{C}_6\text{mim}[\text{FAP}]$  referenced to  $\text{Fc}/\text{Fc}^+$ . Concentration of approximately  $10 \text{ mmolL}^{-1}$  dependent on solubility.

The oxidation region of the voltammogram for  $[\text{ReTzPy}]_3$  shows different elec-

trochemical properties with respect to other complexes and is shown in Figure 2.31. The reduction scan for this complex showed no distinguishable reduction processes within the electrochemical window.

There are 3 subsequent redox couples in the oxidation region with midpoints located at 1.21, 1.32, and 1.47 V respectively. Each of the three couples appears to be reversible and have peak-to-peak separations of 87-90 mV, indicating very fast kinetics for the electrochemical step.

Comparing this complex to the closest mononuclear analogues

$[\text{Re-Tz}p\text{Py}]$  (+1.27 V),<sup>2</sup>  $[\text{Re}(^t\text{BuTzPy})\text{Cl}]$  (+1.04 V), and  $[\text{Re}(^t\text{BuTzPy})\text{Br}]$  (+1.03 V), the first oxidation potential appears to be at a much higher potential than that of  $[\text{Re}(^t\text{BuTzPy})\text{Cl}]$  and  $[\text{Re}(^t\text{BuTzPy})\text{Br}]$ , but at a similar potential to that of  $[\text{Re-Tz}p\text{Py}]$ . This indicates that the Re(I) centres of the trinuclear complex display a reduced electron density relative to  $[\text{Re}(^t\text{BuTzPy})\text{Cl}]$  and  $[\text{Re}(^t\text{BuTzPy})\text{Br}]$ .

The presence of three oxidation peaks for  $[\text{ReTzPy}]_3$  suggests that there may be three formal oxidations of each metal centre  $\text{Re(I)} \rightarrow \text{Re(II)} + e^-$ . The progression of the oxidation peaks indicate metal-metal interaction facilitated by the  $\text{TzPy}^-$  ligand.

The absence of a peak in the reduction scan indicates that the  $\text{PyTz}^-$  ligand that would be involved in this process is very difficult to reduce. This could be a contributing factor to the observed blue-shifted emission.

## 2.7 Conclusion

This chapter has initiated the investigation into diverse multinuclear complexes formed from the combination of an aryl-tetrazole and  $[\text{Re}(\text{CO})_5\text{X}]$ . It can be seen in Figure 2.32 that small alterations to the ligands give products with diverse structures.

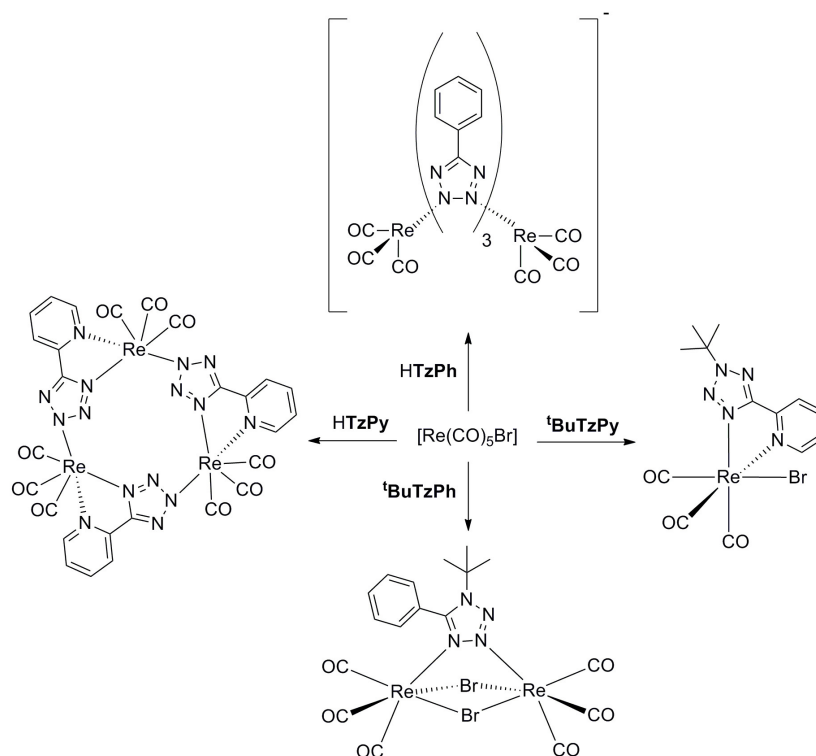
The combination of  $^t\text{BuTzPy}$  with  $[\text{Re}(\text{CO})_5\text{X}]$  results in complexes  $[\text{Re}(^t\text{BuTzPy})\text{Cl}]$  and  $[\text{Re}(^t\text{BuTzPy})\text{Br}]$  with structures resembling literature examples of Re(I) diimine complexes, with electronic properties that are also similar.

The combination of  $^t\text{BuTzPh}$  with  $[\text{Re}(\text{CO})_5\text{X}]$  resulted in a dinuclear complex where two metal centres are bridged by the two bromide ligands and a tetrazole ligand; this product could not be obtained pure and the electronic properties were not investigated.

The combination of  $\text{HTzPh}$  with  $[\text{Re}(\text{CO})_5\text{Br}]$  results in  $[\text{HNEt}_3][\text{Re}_2(\text{TzPh})_3]$ , an anionic propeller type structure which has poor solution state photophysical properties. The electronic properties showed a reversible

oxidation peak and irreversible reduction peak.

The combination of **HTzPy** with  $[\text{Re}(\text{CO})_5\text{X}]$  resulted in an unusual, metalla-calix[3]arene complex which contained three Re(I) centres and three tetrazoles. This complex has the *bluest* emission ( $\lambda_{\text{max}} = 490 \text{ nm}$ ) of a neutral Re(I) complex and has a lifetime and quantum yield greater than that of the only previously characterised Re(I) triangular structure. This complex also displays three reversible oxidation peaks, and no reduction peak could be identified in the electrochemical window.



**Figure 2.32:** Abridged set of synthesis schemes in this chapter

These results display that the structure and electronic properties of Re(I) complexes can be readily modified by simple alterations of the ligands, leading to the idea that if a terpyridine moiety could be attached to the *para* position of the aryl-tetrazole, bridging between multiple metal centres may be possible utilising the structures from this chapter. This may be particularly interesting in the case of the analogous  $[\text{ReTzPy}]_3$  complex.



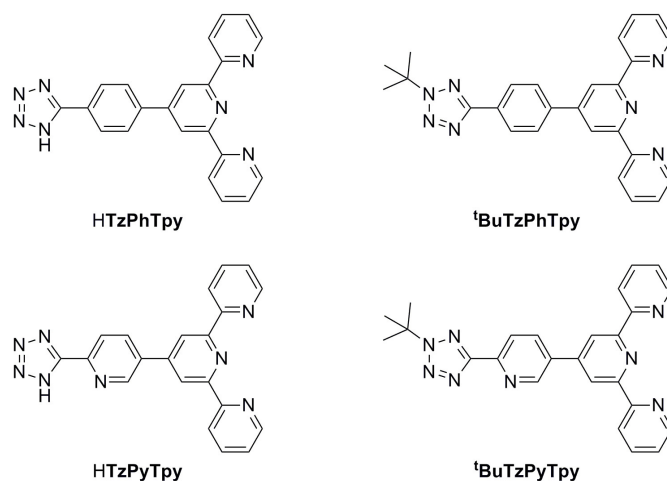


# Chapter 3

## Functionalisation of tetrazole ligands with terpyridine

### 3.1 Introduction

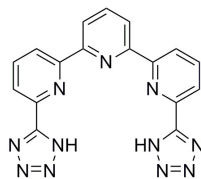
In a previous investigation into multinuclear complexes, 4-substituted aryl tetrazoles were utilised as bridging ligands between two rhenium centres.<sup>2</sup> The ligands were able to bridge between the two metals and facilitate charge delocalisation. Further to this, Chapter 1 demonstrated that modification of aryl tetrazole ligands resulted in a variety of coordination motifs. A further goal is to expand these investigations to utilise tetrazole containing ligands as a bridge between rhenium and lanthanides.



**Figure 3.1:** Structures of target ligands in this chapter.

The terpyridine moiety has a history of investigation into poly-pyridyl species in the fields of photophysics and catalysis.<sup>250–252</sup> It has been widely used in conjunction with lanthanides as it is a good chelator and sensitiser.<sup>253–256</sup> Terpyridine

ligands, such as those shown in Figure 3.2, have been combined with tetrazoles for investigations into lanthanide sensitization.<sup>173,174</sup>



**Figure 3.2:** Tetrazole functionalised terpyridine utilised for  $\text{Ln}^{3+}$  sensitisation.<sup>173,174</sup>

The terpyridine moiety itself, without the inclusion of a metal centre, also has uses in the field of photophysical applications as sensors and in luminescent devices.<sup>257–260</sup>

The target molecules illustrated in Figure 3.1 contain either a phenyl-tetrazole (**HTzPhTpy** and **<sup>t</sup>BuTzPhTpy**) or a pyridyl tetrazole (**HTzPyTpy** and **<sup>t</sup>BuTzPyTpy**). This set of ligands is similar to those utilised in Chapter 2, and when applied to metal complexes, these differences will allow the discrimination of properties based on the the positions of multiple chelation sites. As terpyridine containing molecules have multiple potential applications, this chapter will focus on the synthesis and properties of these ligands themselves.

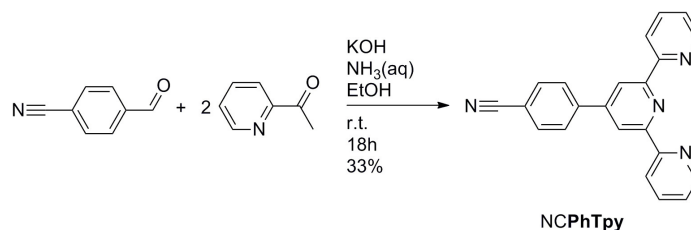
The synthesised molecules will also be used to form complexes with  $\text{Re(I)}$ , hopefully of similar structure to those formed in Chapter 2. If successful, these complexes will then be utilised to bridge a  $\text{Re(I)}$  centre to a lanthanide cation.

## 3.2 Synthesis of aryl-tetrazole functionalised terpyridines

The synthesis and modifications of 4'-aryl-substituted 2,2':6',2''-terpyridines has been a focused area of investigation due to simple preparation and diverse applications.<sup>261–263</sup> In this chapter, the synthesis outlined by Wang for the facile assembly of terpyridine ligands from 2-acetylpyridine and the appropriate aldehyde will be used.<sup>261</sup>

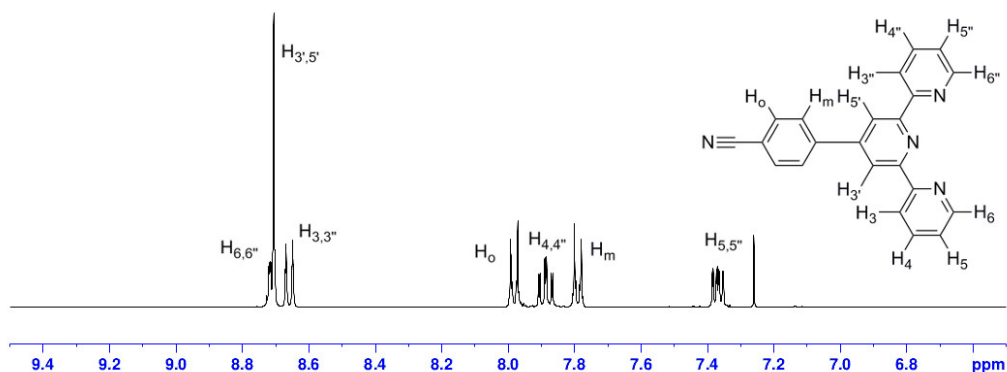
### 3.2.1 Phenyl-tetrazole functionalised terpyridine

To obtain the ligand **HTzPhTpy**, firstly the precursor nitrile **NCPhtpy** is synthesised by the combination of cyanobenzaldehyde and 2-acetylpyridine. The synthesised compound is shown in Figure 3.3. This terpyridine system has been previously reported and the characterisation data obtained were consistent with literature.<sup>261</sup>



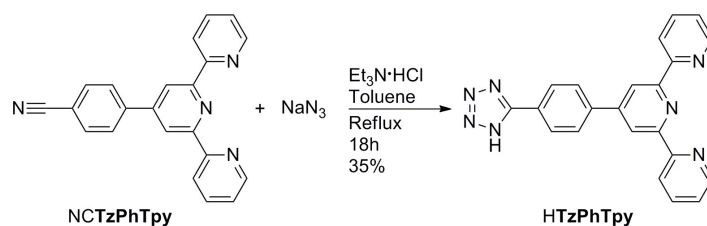
**Figure 3.3:** Reaction scheme for the formation of **NCPhtpy**.

The synthesised species was characterised by IR and NMR spectroscopy. The IR spectrum of **NCPhtpy** displays a sharp peak at  $2225\text{ cm}^{-1}$ , suggesting the presence of a nitrile group. Further to this, the lack of a carbonyl peak in the spectrum indicates the absence of starting material.

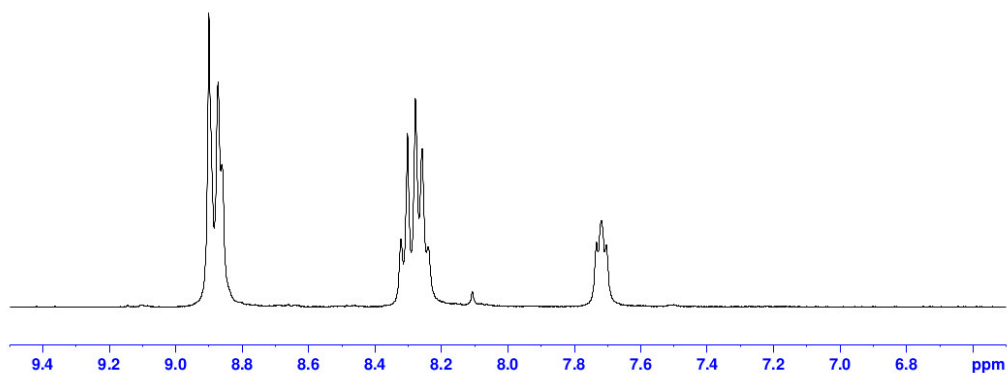


**Figure 3.4:**  $^1\text{H}$ -NMR spectrum of **NCPhtpy** in  $\text{CDCl}_3$ .

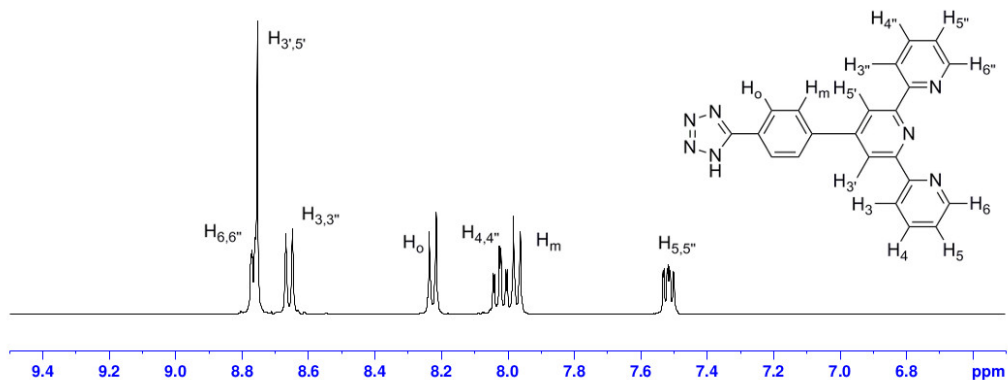
The  $^1\text{H-NMR}$  spectrum of **NCTzPhTpy** is displayed in Figure 3.4 and the peak assignments is also shown. The splitting patterns and peak positions are consistent with the proposed product. The pair of doublets at 7.98 and 7.79 ppm of integration ratios 2:2 corresponds to  $\text{H}_o$  and  $\text{H}_m$  positions. The convoluted singlet at 8.70 ppm corresponds to  $\text{H}_{3',5'}$ . The overall integration to 14 protons is consistent with the suggested structure and literature.<sup>261</sup> The  $^{13}\text{C-NMR}$  spectrum for this compound also displays 13 peaks in the aromatic region, corresponding to those expected for the proposed product. A resonance at 112.7 ppm confirms again the presence of a nitrile group.



**Figure 3.5:** Reaction scheme for the formation of **HTzPhTpy**.



(a)



(b)

**Figure 3.6:**  $^1\text{H-NMR}$  spectra of species in  $\text{DMSO-}d_6$ . a) **HTzPhTpy** alone. b)  $[\text{Et}_3\text{NH}][\text{TzPhTpy}]$ .

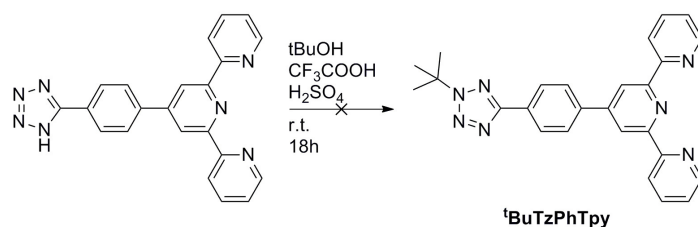
After obtaining **NCPHTpy**, the synthesis of **HTzPhTpy** was performed as shown in Figure 3.5, according to the method proposed by Koguro.<sup>148</sup> In this case, due to the difference from the previously reported **HTzPh** and **HTzPy**, the product is obtained by evaporation of the solvent and subsequent recrystallisations from water and DCM. This method removes the salts generated in the reaction and any unreacted **NCPHTpy**.

**HTzPhTpy** was characterised by IR, <sup>1</sup>H-NMR and <sup>13</sup>C-NMR spectroscopy. The IR spectrum displays a band at 1603 cm<sup>-1</sup>, corresponding to the C=N stretch of the tetrazole moiety, and the spectrum was absent of a peak at 2225 cm<sup>-1</sup> indicating that there is no nitrile present.

This compound is not very soluble in common polar and non-polar deuterated solvents and also displays acid-base equilibria. The <sup>1</sup>H-NMR spectrum of the bulk compound is therefore difficult to interpret as the peaks are broad and overlapping, as seen in Figure 3.6a. The <sup>1</sup>H-NMR in DMSO-*d*<sub>6</sub>, has broad signals between 8.80-8.95 ppm, 8.20-8.35 ppm, and 7.67-7.76 ppm with integration ratio of 6:6:2, respectively, which matches with the expected compound.

Excess triethylamine was added to the solution to promote the formation of the more soluble triethylammonium tetrazolate salt. The resulting <sup>1</sup>H-NMR spectrum is shown in Figure 3.6b, and has a similar appearance to that obtained for **NCPHTpy**, consistent with the proposed product. The <sup>13</sup>C-NMR spectrum for this compound exhibits 13 signals corresponding to those expected for the proposed product, in particular a resonance at 160.3 ppm corresponding to the C5 position of the tetrazole is suggestive of its formation. The peak present in the <sup>13</sup>C-NMR spectrum of **NCPHTpy** at 112.7 ppm was not observed for **HTzPhTpy** and is indicative that the nitrile is no longer present.

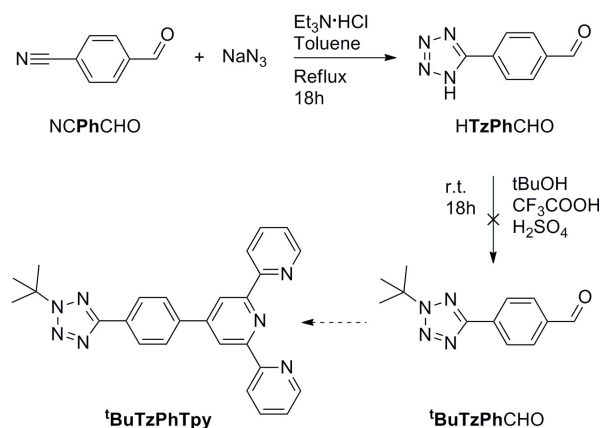
### 3.2.2 Alkylation of **HTzPhTpy**



**Figure 3.7:** First attempted reaction scheme for the formation of **<sup>t</sup>BuTzPhTpy**.

To maintain consistency with the previous species **<sup>t</sup>BuTzPh** and **<sup>t</sup>BuTzPy** synthesised in Chapter 1, a *tert*-butyl moiety was chosen as an alkylating group. However, the attempted synthesis of **<sup>t</sup>BuTzPhTpy**, as shown in Figure 3.7, was

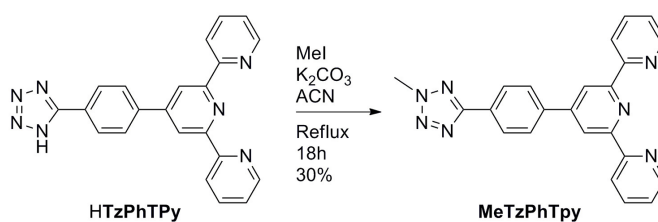
unsuccessful. The reaction was therefore altered such that formation of the tetrazole would occur first from **NCPHCHO**. Then, alkylation would follow to produce **<sup>t</sup>BuTzPhTpy** (Figure 3.8).



**Figure 3.8:** Second attempted reaction scheme for the formation of **<sup>t</sup>BuTzPhTpy**.

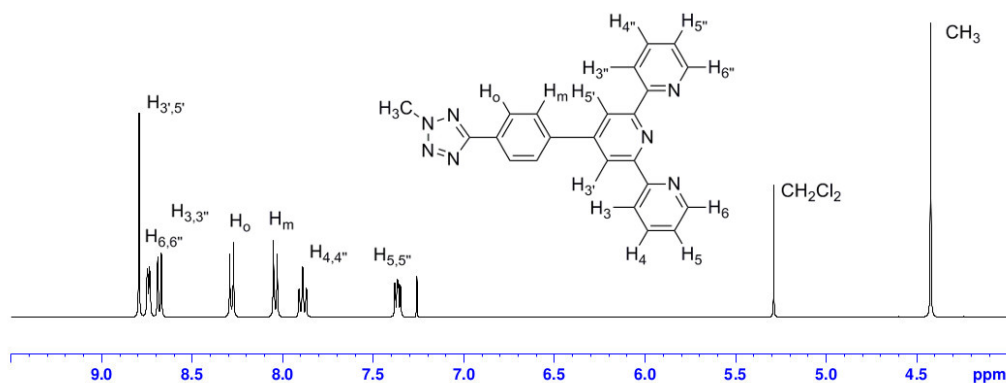
The synthesis of **HTzPhCHO** was performed following the method outlined by Koguro,<sup>148</sup> and the synthesised species was characterised by IR and NMR spectroscopy. The characterisation was consistent with literature for this compound.<sup>1</sup> The following alkylation method utilising **<sup>t</sup>BuOH** along with **CF<sub>3</sub>COOH** and **H<sub>2</sub>SO<sub>4</sub>** to obtain **<sup>t</sup>BuTzPhCHO** was performed as reported in literature.<sup>190</sup> However, the desired product could not be isolated from this reaction.

As an alkylated form of **TzPhTpy<sup>-</sup>** was the target in this synthesis, a methyl group was then chosen in lieu of the *tert*-butyl substituent. The synthesis of the methylated tetrazole is shown in Figure 3.9. The synthesis of **MeTzPhTpy** was



**Figure 3.9:** Reaction scheme for the formation of **MeTzPhTpy**, although two regioisomers are formed, only the N2 regioisomer is displayed.

carried out in acetonitrile with **HTzPhTpy**, methyl-iodide, and potassium carbonate. This reaction was performed at reflux due to the relatively low solubility of **HTzPhTpy**, similarly to literature reports of methylation of tetrazoles.<sup>194,264</sup> This reaction yielded both the N1 and N2 regioisomers of the methylated compound in a ratio of ca. 4:6 respectively, which were separated by flash chromatography.



**Figure 3.10:**  $^1\text{H-NMR}$  spectrum of **MeTzPhTpy** in  $\text{CDCl}_3$ .  $\text{CH}_2\text{Cl}_2$  corresponds to remaining dichloromethane after flash-chromatography.

The synthesised product was characterised by IR,  $^1\text{H-NMR}$ , and  $^{13}\text{C-NMR}$  spectroscopy. The IR spectrum displays a band at  $1601\text{ cm}^{-1}$  corresponding to tetrazole  $\text{C}=\text{N}$  stretch.

The  $^1\text{H-NMR}$  spectrum for **MeTzPhTpy**, shown in Figure 3.10, is similar to that for **HTzPhTpy** and **NCPHTpy** in terms of splitting and integration ratio. The presence of the singlet at 4.42 ppm with an integration ratio of 3, corresponding to the  $\text{CH}_3$  group, is confirmation of the methylated product. The  $^{13}\text{C-NMR}$  spectrum displays 14 signals corresponding to those expected for the proposed product and specifically the **C5** resonance at 165.0 ppm supports an **N2** substituted aryl tetrazole.<sup>224,227</sup>

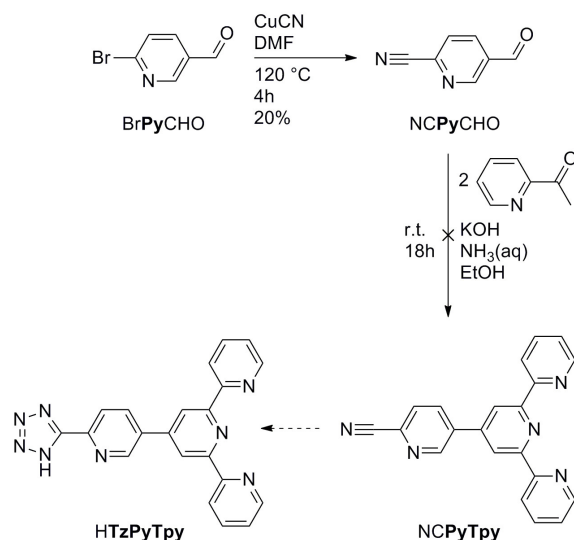
### 3.2.3 Pyridyl-tetrazole functionalised terpyridine

To obtain **HTzPyTpy**, an analogous reaction path to that shown in Figure 3.5 was attempted. The synthesis first attempted is shown in Figure 3.11.

Due to the relatively high cost of **NCPyCHO**, the first step in this scheme is to form it from cheaper precursors. This was achieved via the reaction of **BrPyCHO** with a source of cyanide, according to the Rosenmund-von Braun nitrile synthesis.<sup>265</sup>

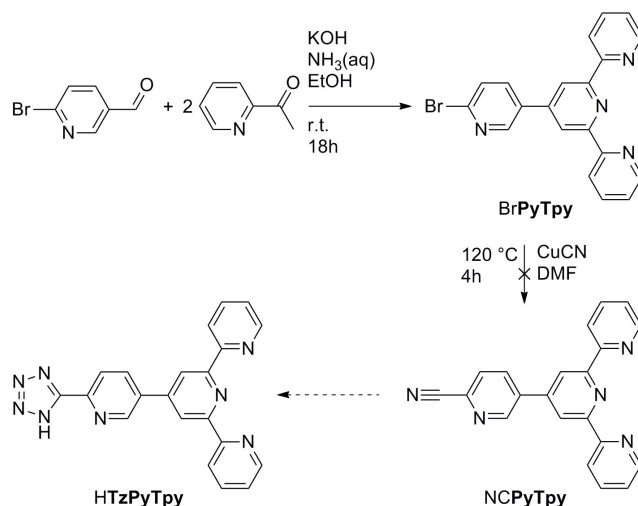
The synthesised product **NCPyCHO** was characterised by IR and NMR spectroscopy. The IR spectrum displays the presence of a band at  $2237\text{ cm}^{-1}$ , corresponding to a nitrile stretch, and a strong band at  $1710\text{ cm}^{-1}$ , corresponding to the carbonyl stretch of the aldehyde.

The  $^1\text{H-NMR}$  spectrum has a singlet at 10.19 ppm with integration for 1 proton corresponding to **CHO**, and the remaining signals also match those reported in literature.<sup>266</sup> The  $^{13}\text{C-NMR}$  spectrum has 7 signals corresponding to those expected for the proposed product. The presence of a nitrile resonance at 116.5



**Figure 3.11:** First reaction scheme attempted for the formation of HTzPyTpy.

ppm, and carbonyl resonance at 189.1 ppm are suggestive of the product formed. Subsequent to the substitution of the nitrile is the formation of the terpyridine moiety NCPyTpy, as seen in Figure 3.11. The product of this reaction, however, was not what was expected. The evidence in the  $^1\text{H-NMR}$  and  $^{13}\text{C-NMR}$  spectra of the synthesised compound suggests formation of a terpyridine moiety, by displaying signals resembling those in Figure 3.4. However, the absence of a nitrile band the IR spectrum and the presence a carbonyl peak at  $1650\text{ cm}^{-1}$ , are suggestive of conversion of the nitrile to a primary amide.

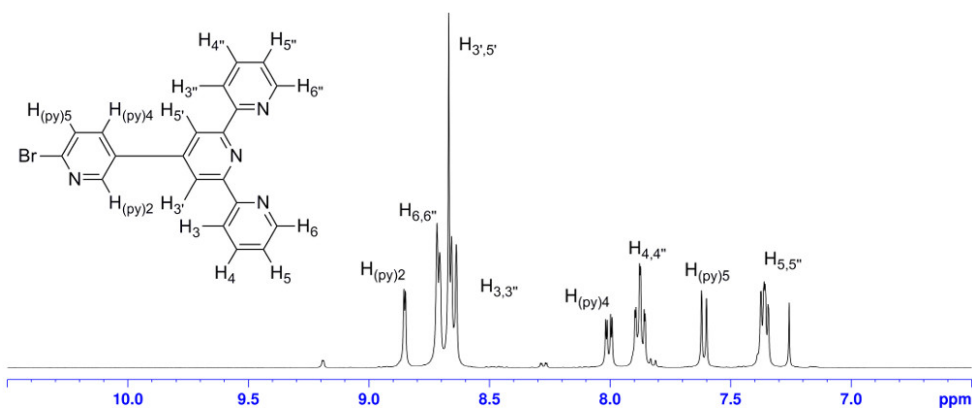


**Figure 3.12:** Second reaction scheme attempted for the formation of HTzPyTpy.

The second reaction scheme to obtain HTzPyTpy is shown in Figure 3.12. In this scheme, BrPyCHO is prepared, followed by substitution to form NCPyTpy



and cyclisation to form **HTzPyTpy**. **BrPyTpy** was formed following a literature procedure to synthesise terpyridines from acetyl-pyridine.<sup>261</sup> The product obtained was analysed by IR, <sup>1</sup>H-NMR and <sup>13</sup>C-NMR spectroscopy and was absent of carbonyl signals in the IR spectrum, suggestive of no remaining starting materials. In the <sup>1</sup>H-NMR spectrum, shown in Figure 3.13, an integration ratio of 2:1 for peaks **H**<sub>3',5'</sub>:**H**<sub>(py)2</sub> is consistent with the proposed product. The <sup>13</sup>C-NMR also has 13 signals corresponding to what would be expected for this product.

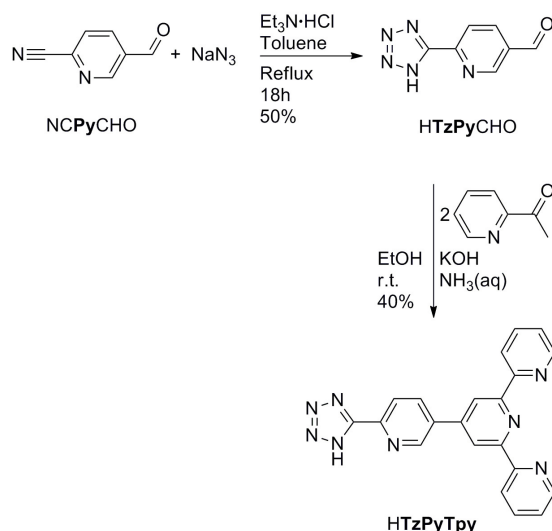


**Figure 3.13:** <sup>1</sup>H-NMR spectrum of **BrPyTpy** in CDCl<sub>3</sub>.

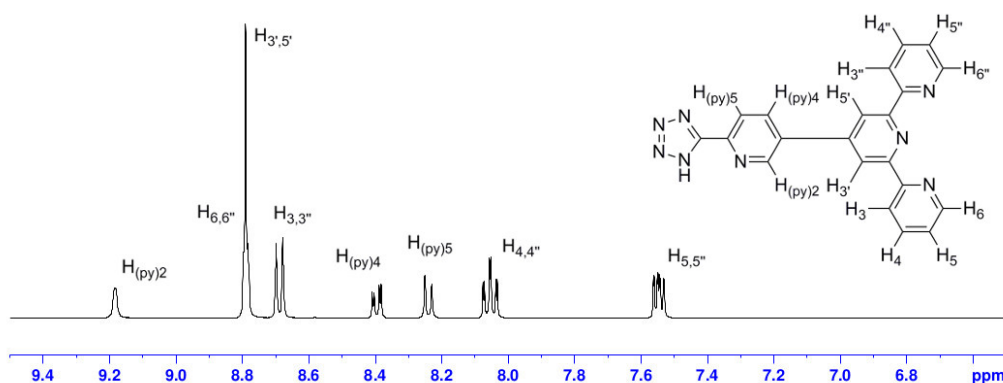
**BrPyTpy** was then used to substitute the nitrile group onto the molecule as shown in Figure 3.12. The procedure was followed as previously described for the synthesis of **NCPyCHO**. The product that was obtained was analysed by IR and <sup>1</sup>H-NMR. The <sup>1</sup>H-NMR spectrum matched the starting material **BrPyTpy**. This was an indication that no reaction had occurred, as the substitution to a nitrile group would be expected to cause a shift in signals for the **H**<sub>(py)2</sub>, **H**<sub>(py)4</sub>, and **H**<sub>(py)5</sub> protons. The infra-red spectrum was absent of a signal in the region of 2230 cm<sup>-1</sup> indicating the nitrile group was not present.

To obtain **HTzPyTpy**, another reaction scheme was followed and is outlined in Figure 3.14. In this scheme, **NCPyCHO** is formed first as shown previously (Figure 3.11). The tetrazole **HTzPyCHO** was then formed following literature methods.<sup>148</sup>

**HTzPyCHO** was analysed by IR, <sup>1</sup>H-NMR, and <sup>13</sup>C-NMR spectroscopy. The IR spectrum for this compound has important signals at 1704 cm<sup>-1</sup>, corresponding to the aldehyde group, and 1605 cm<sup>-1</sup> for the tetrazole C=N stretch. The <sup>1</sup>H-NMR spectrum for this complex matches the desired product, having a singlet at 10.20 ppm integrating to 1 proton and corresponding to **CHO**, and a singlet at 9.26 ppm with integration of 1 proton corresponding to **H**<sub>(py)2</sub>. Two doublets at 8.50 ppm and 8.42 ppm with integration to 1 proton each correspond to **H**<sub>(py)4,(py)5</sub>. The <sup>13</sup>C-NMR spectrum displays 7 signals consistent with the product, with noteworthy resonances at 191.8 ppm, corresponding to the aldehyde carbon, and



**Figure 3.14:** Successful reaction scheme for the formation of **HTzPyTpy**.



**Figure 3.15:**  $^1\text{H-NMR}$  spectrum of  $[\text{Et}_3\text{NH}][\text{TzPyTpy}]$  in  $\text{DMSO-}d_6$ .

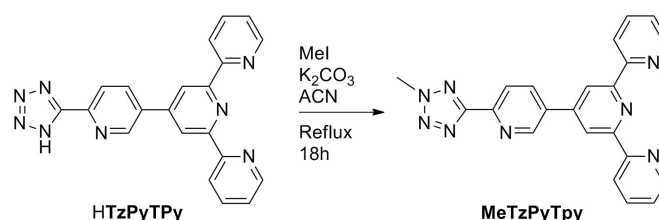
154.6 ppm, corresponding to the **C5** tetrazole signal.

The final step to prepare **HTzPyTpy**, as shown in Figure 3.14, is to form the terpyridine moiety. **HTzPyCHO** was combined with 2-acetylpyridine with two equivalents of **KOH**, one of which serves to deprotonate the tetrazole.

The product was characterised by IR spectroscopy and showed a signal at  $1597\text{ cm}^{-1}$ , corresponding to the tetrazole  $\text{C}=\text{N}$  stretch. The product was also characterised by  $^1\text{H-NMR}$  spectroscopy. The compound, similarly to **HTzPhTpy**, also required the addition of triethylamine to dissolve and resolve the signals. In the  $^1\text{H-NMR}$  spectrum, displayed in Figure 3.15, a singlet at 9.18 ppm with integration of 1 proton corresponds to  $\text{H}_{(\text{py})2}$ . The singlet at 8.79 ppm corresponding to  $\text{H}_{3',5'}$  overlaps with the doublet corresponding to  $\text{H}_{6,6''}$ , these signals integrated together have a ratio of 4 protons. The  $^{13}\text{C-NMR}$  spectrum displays 14 signals corresponding to those expected for the proposed product and specifically the **C5** resonance at 161.1 ppm corresponding to a deprotonated aryl tetrazole.<sup>224,227</sup>

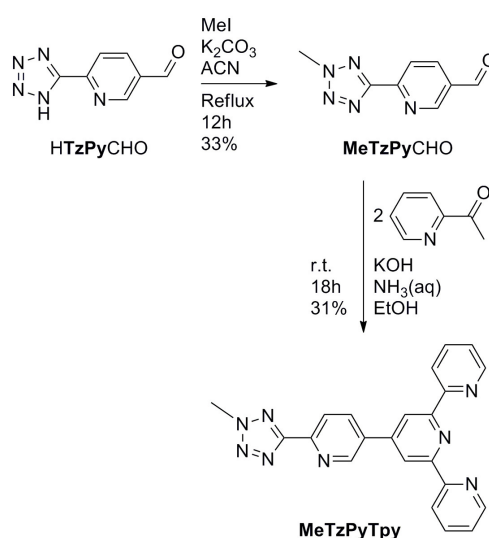
### 3.2.4 Alkylation of HTzPyTpy

Methylation of **HTzPyTpy**, shown in Figure 3.16, was then attempted to obtain the desired compound, as performed for **MeTzPhTpy**. This methylation was performed by combining **HTzPyTpy** with potassium carbonate and methyl iodide in acetonitrile. The product from this reaction was analysed by  $^1\text{H-NMR}$  and the signals in the aromatic region of the spectrum were convoluted. However, it was possible to distinguish sets of signals that correspond to terpyridine signals similar to those seen in Figure 3.15. There is also the presence of two singlets at 4.49 ppm and 4.56 ppm, which correspond to the methyl substituents of the N1 and N2 regioisomers in a ratio of ca. 6:4 respectively. Purification was not possible due to co-elution of both regioisomers during flash-chromatography.



**Figure 3.16:** Attempted reaction scheme for the formation of **MeTzPyTpy**, although two regioisomers are formed, only the N2 regioisomer is displayed.

Due to the difficulty in separating the products, the methylation of **HTzPyCHO** was performed first and the two regioisomers were separated before formation of **MeTzPyTpy**. The synthesis scheme is shown in Figure 3.17.

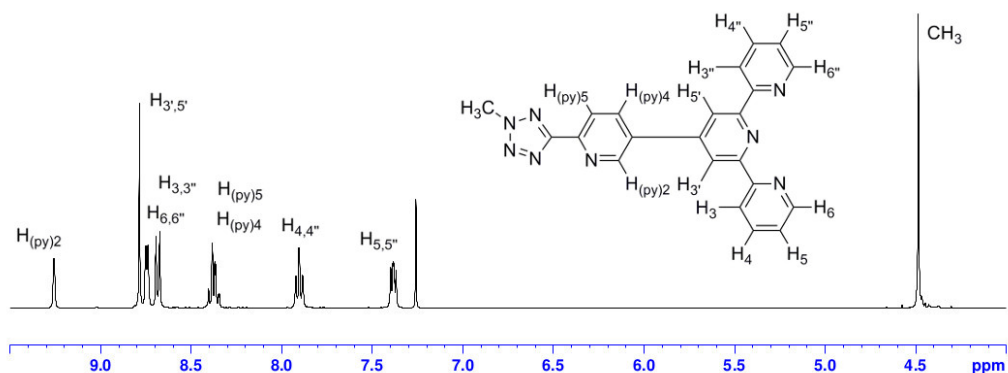


**Figure 3.17:** Successful reaction scheme for the formation of **MeTzPyTpy**. When synthesising **MeTzPyCHO** two regioisomers are formed, however, only the N2 regioisomer is displayed.

This methylation was performed by combining **HTzPyCHO** with potassium carbonate and methyl iodide in acetonitrile, yielding the N1 and N2 regioisomers in a ca. 4:6 ratio. The product was purified by flash-chromatography. The N2 regioisomer of **MeTzPyCHO** was separated and characterised by IR,  $^1\text{H-NMR}$ , and  $^{13}\text{C-NMR}$  spectroscopy. There were significant peaks in the IR spectrum at  $1690\text{ cm}^{-1}$  corresponding to the carbonyl group and  $1595\text{ cm}^{-1}$  corresponding to the tetrazole  $\text{C}=\text{N}$  stretch.

The  $^1\text{H-NMR}$  spectrum displays two noteworthy signals, the singlet at 10.18 ppm with integration of 1 proton corresponding to **CHO** and a singlet at 4.48 ppm with integration of 3 protons corresponding to **CH<sub>3</sub>**. The remaining signals are also consistent with the proposed structure. The  $^{13}\text{C-NMR}$  spectrum has 8 signals as expected for this compound with significant signals at 190.1 ppm for **CHO**, 164.1 ppm for the **C5** carbon, indicative of an N2 substituted aryl tetrazole.

Having isolated the N2 regioisomer of **MeTzPyCHO**, the terpyridine moiety was then formed as shown in Figure 3.17. The product **MeTzPyTpy** was characterised by IR,  $^1\text{H-NMR}$ , and  $^{13}\text{C-NMR}$  spectroscopy. There was a significant peak in the IR spectrum at  $1595\text{ cm}^{-1}$ , corresponding to the tetrazole  $\text{C}=\text{N}$  stretch. The absence of a carbonyl stretch suggests no starting material remained.



**Figure 3.18:**  $^1\text{H-NMR}$  spectrum of **MeTzPyTpy** in  $\text{CDCl}_3$ .

The  $^1\text{H-NMR}$  spectrum, as shown in Figure 3.18, has an overall integration of 16 protons. A singlet at 9.26 ppm corresponds to  $\text{H}_{(\text{py})2}$ , a singlet at 8.79 ppm corresponds to  $\text{H}_{3,5'}$ , and a singlet at 4.49 ppm corresponds to  $\text{CH}_3$ . The  $^{13}\text{C-NMR}$  spectrum has 15 signals as expected for this compound with significant signals at 164.8 ppm for the **C5** tetrazole carbon, also indicative of an N2 substituted aryl tetrazole, and a signal at 39.9 ppm corresponding to the methyl carbon.

### 3.3 Photophysical properties

A summary of the photophysical data in acetonitrile for the four species **HTzPhTpy**, **HTzPyTpy**, **MeTzPhTpy**, and **MeTzPyTpy** is shown in Table 3.1. The absorption and emission spectra are shown in Figure 3.19. Due to low solubility of **HTzPhTpy** and **HTzPyTpy**, 1 equivalent of triethylamine was added to promote dissolution.

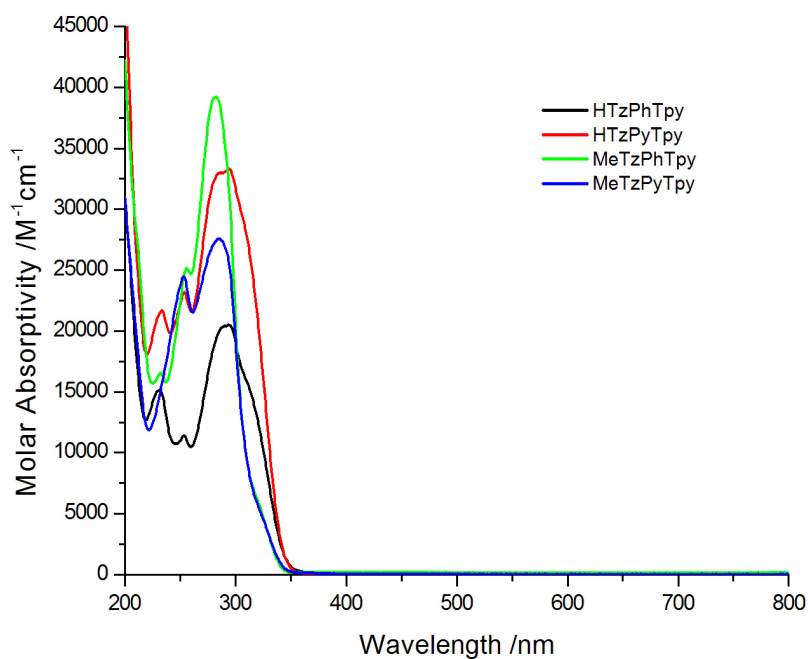
**Table 3.1:** Summary of photophysical properties for dilute ( $10^{-5}$  M) acetonitrile solutions.

Compound	Absorption		Emission, 298 K		
	$\lambda_{max}$ [nm]	$(10^4 \epsilon)$ [M <sup>-1</sup> cm <sup>-1</sup> ]	$\lambda_{em}$ [nm]	$\tau$ [ns]	$\phi^a$
<b>HTzPhTpy</b>	295	(2.06)	426	2.62	0.7688
	253	(1.15)			
	231	(1.51)			
<b>HTzPyTpy</b>	295	(3.32)	400	3.36	0.8524
	253	(2.31)			
	230	(2.16)			
<b>MeTzPhTpy</b>	283	(3.93)	356	2.84	0.316
	255	(2.51)			
	232	(1.66)			
<b>MeTzPyTpy</b>	282	(2.76)	362	2.76	0.2760
	253	(2.44)			

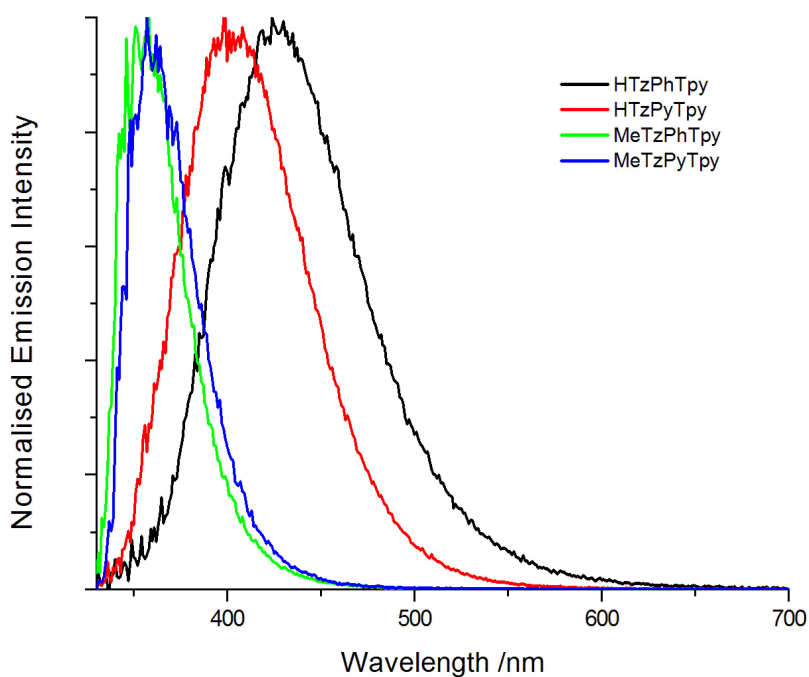
<sup>a</sup>Quantum yields measured against an air equilibrated aqueous 1 M H<sub>2</sub>SO<sub>4</sub> solution of quinine sulphate ( $\phi = 0.546$ ).

Each of the compounds display absorption peaks near 220-300 nm, with molar absorptivity values in the range of allowed  $\pi - \pi^*$  transitions for organic molecules. A shoulder also appears on the lower energy transition at 310 nm.

The emission spectra show that the two tetrazole salts, [Et<sub>3</sub>NH][**TzPhTpy**] and [Et<sub>3</sub>NH][**TzPyTpy**], exhibit a broad and structureless emission peak at 426 nm and 400 nm respectively. These compounds are expected to undergo acid/base equilibria in solution and it is noted that further addition of tetrabutylammonium hydroxide did not give appreciable changes to the spectra. The emission lifetime of these two ligands are in the expected range for fluorescence of organic molecules. The alkylated tetrazole ligands **MeTzPhTpy** and **MeTzPyTpy** both exhibit sharp emission at 356 nm and 362 nm, respectively, similarly ascribed to emission from a  $\pi - \pi^*$  excited state. Again, decay lifetime values are consistent with fluorescence.



(a)



(b)

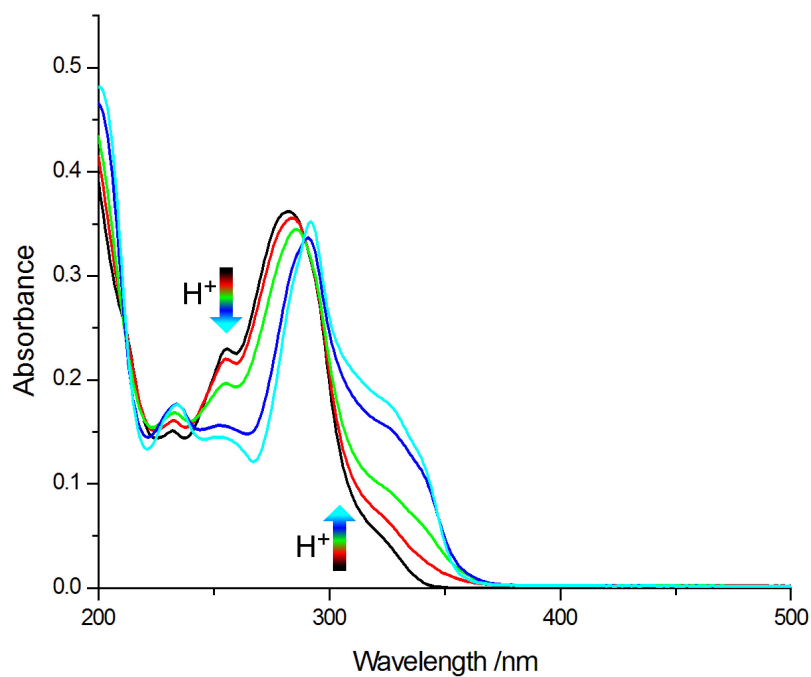
**Figure 3.19:** Absorption and emission spectra for dilute ( $10^{-5}$  M) acetonitrile solutions of labelled ligands. a) Absorption spectra. b) Emission spectra under excitation at 280 nm.

Comparison between the emission spectra of  $[\text{Et}_3\text{NH}][\text{TzPhTpy}]$  and **MeTzPhTpy** illustrates that the alkylated derivative display a blue-shifted emission in comparison to the tetrazolate salt. A similar difference is seen for  $[\text{Et}_3\text{NH}][\text{TzPyTpy}]$  and **MeTzPyTpy**. This is tentatively attributed to the negative charge of the tetrazolate salt destabilising the HOMO orbitals, thus reducing the energy gap of the emission.

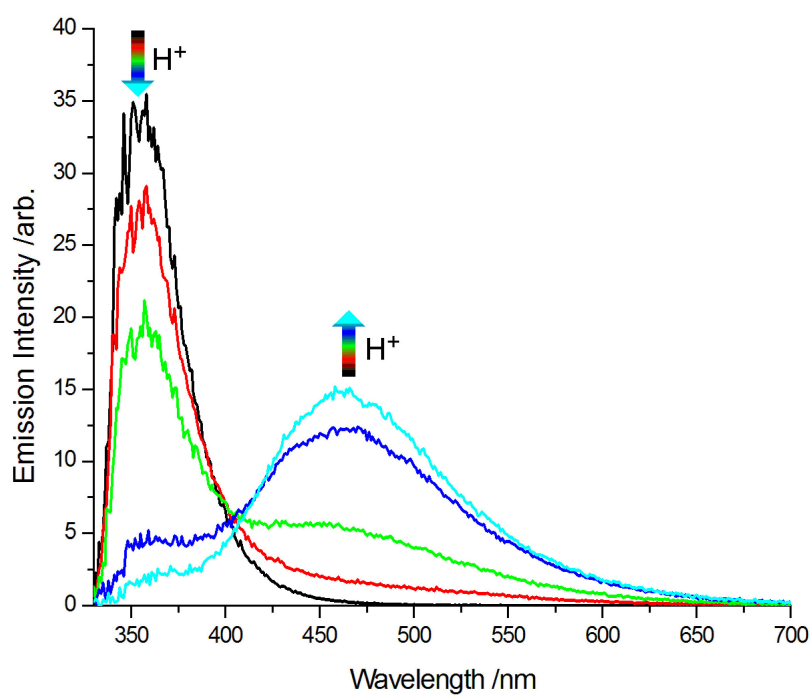
### 3.4 Modulation of the photophysical properties in acidic or alkali conditions

The ability of terpyridine containing molecules to behave as luminescent sensors and the differences observed in the emission spectra of deprotonated tetrazoles, and their alkylated derivatives, prompted an investigation into the modification of their photophysical properties with respect to addition of acids or bases.

Due to the more complex acid-base equilibria of **HTzPhTpy** and **HTzPyTpy** involving both the tetrazole and terpyridine groups, the alkylated derivatives **MeTzPhTpy** and **MeTzPyTpy** will be analysed first. For **MeTzPhTpy** and **MeTzPyTpy**, camphorsulphonic acid is added and the progression in absorption and emission are recorded. For **HTzPhTpy** and **HTzPyTpy** camphorsulphonic acid is added to the solution where 1 equivalent of tetrabutylammonium hydroxide was added with respect to the analyte.



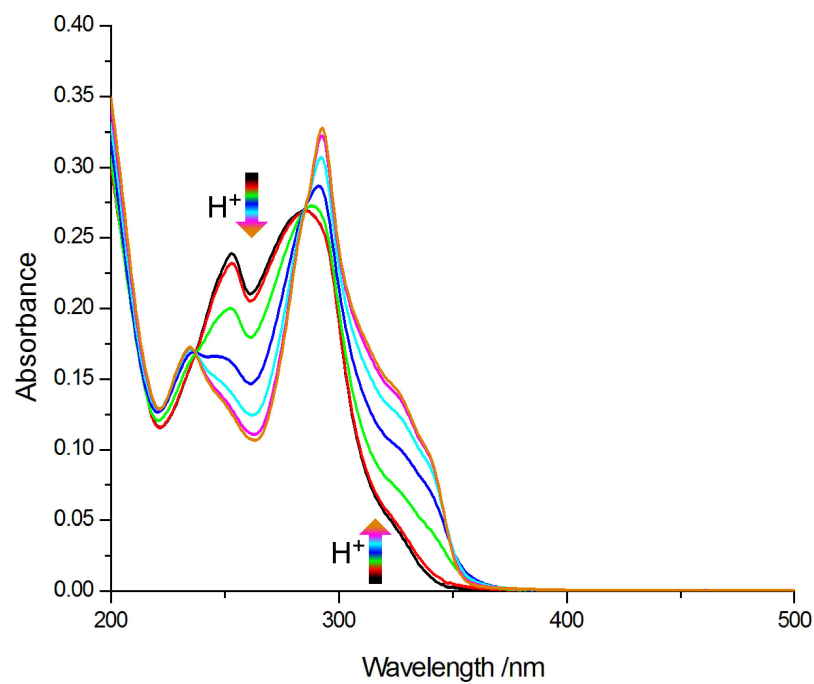
(a)



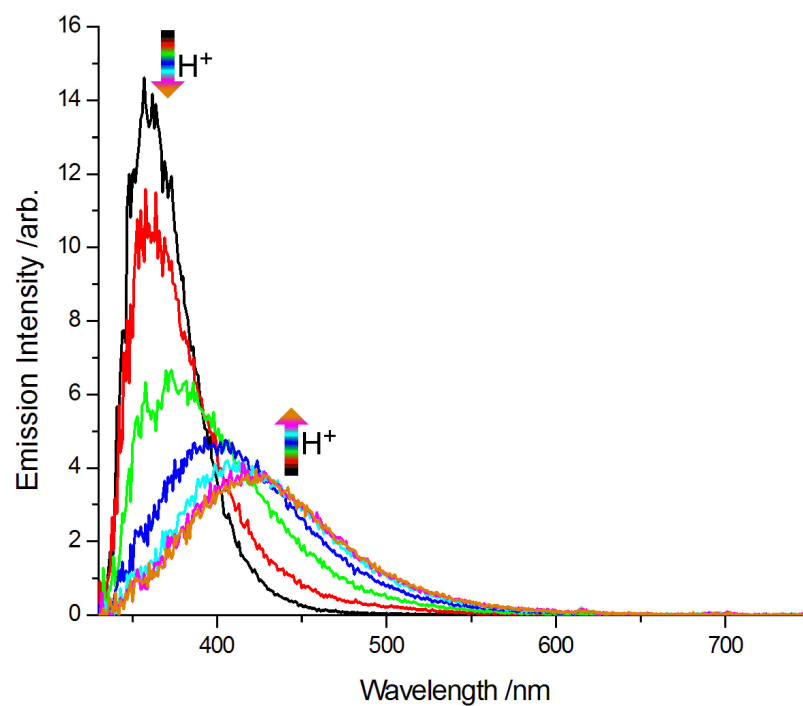
(b)

**Figure 3.20:** Absorption and emission spectra of **MeTzPhTpy** under progressive addition of acid. Each line represents the addition of  $\frac{1}{3}$  equivalent of camphorsulphonic acid. a) Absorption spectra. b) Emission spectra





(a)



(b)

**Figure 3.21:** Absorption and emission spectra of MeTzPyTpy under progressive addition of acid. Each line represents the addition of  $\frac{1}{3}$  equivalent of camphorsulphonic acid. a) Absorption spectra. b) Emission spectra

For **MeTzPhTpy** and **MeTzPyTpy**, the changes in absorption and emission spectra under the progressive addition of acid are shown in Figure 3.20 and Figure 3.21. The progressive addition begins as the black curve. Isosbestic points appear in the absorption spectra during the addition of acid at 240 nm and 290 nm and the progressions are similar. Importantly, a lower energy transition at 340-350 nm becomes prevalent as acid is progressively added. This is attributed to protonation of the terpyridine moiety which inhibits rotation of the pyridine rings. This results in an overall increase in the conjugation of the molecule and a lower HOMO-LUMO gap. In the case of **MeTzPyTpy** it was expected that the pyridyl-tetrazole may be able to be protonated, however, as the trend of the absorption spectrum of **MeTzPyTpy** resembles that of **MeTzPhTpy**, this species does not appear to contribute to the progression of the spectra.

The emission spectra for these compounds also display similar progression. The initial emission at 360 nm decreases in intensity, and a peak at 420-480 nm increases in intensity. The progression of these spectra also suggests that addition of acid protonates the terpyridine moiety resulting in a lower HOMO-LUMO gap. The emission spectra of the protonated form of **MeTzPyTpy** appears to be blue-shifted relative to the protonated form of **MeTzPhTpy**. Although the absorption spectra do not suggest this, there may be some contribution of protonation at the pyridyl-tetrazole site lowering the HOMO and increasing the energy gap.

In each case of absorption and emission, the progression of the spectra is reversible by addition of base.

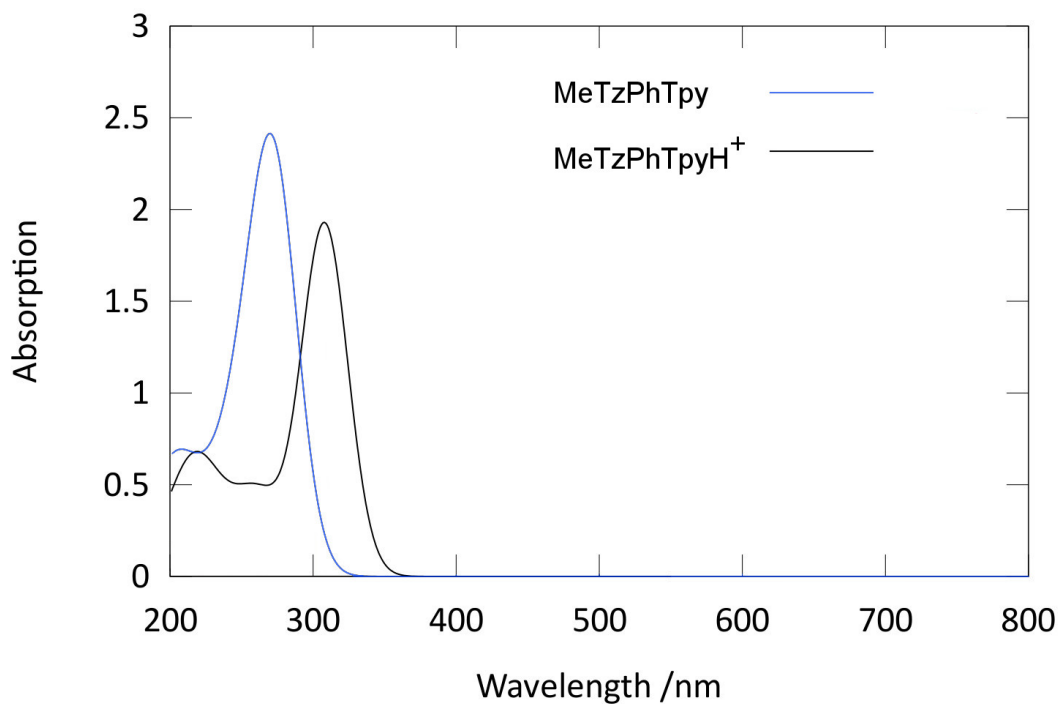


Figure 3.22: Simulated absorption spectra of derivatives of [MeTzPhTpy].

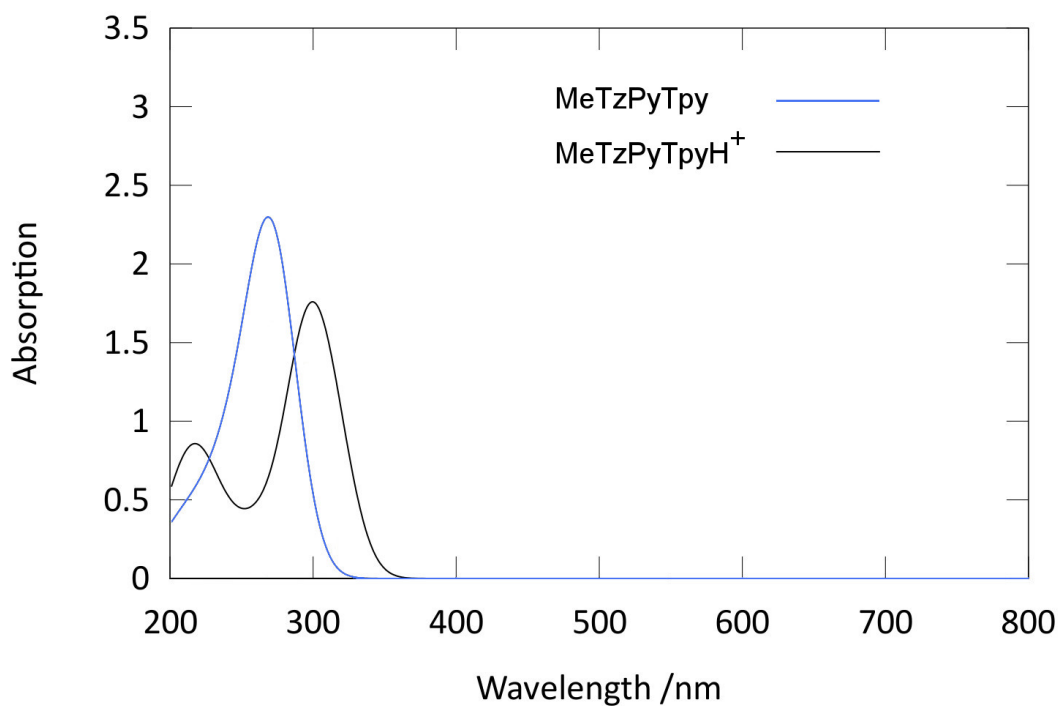
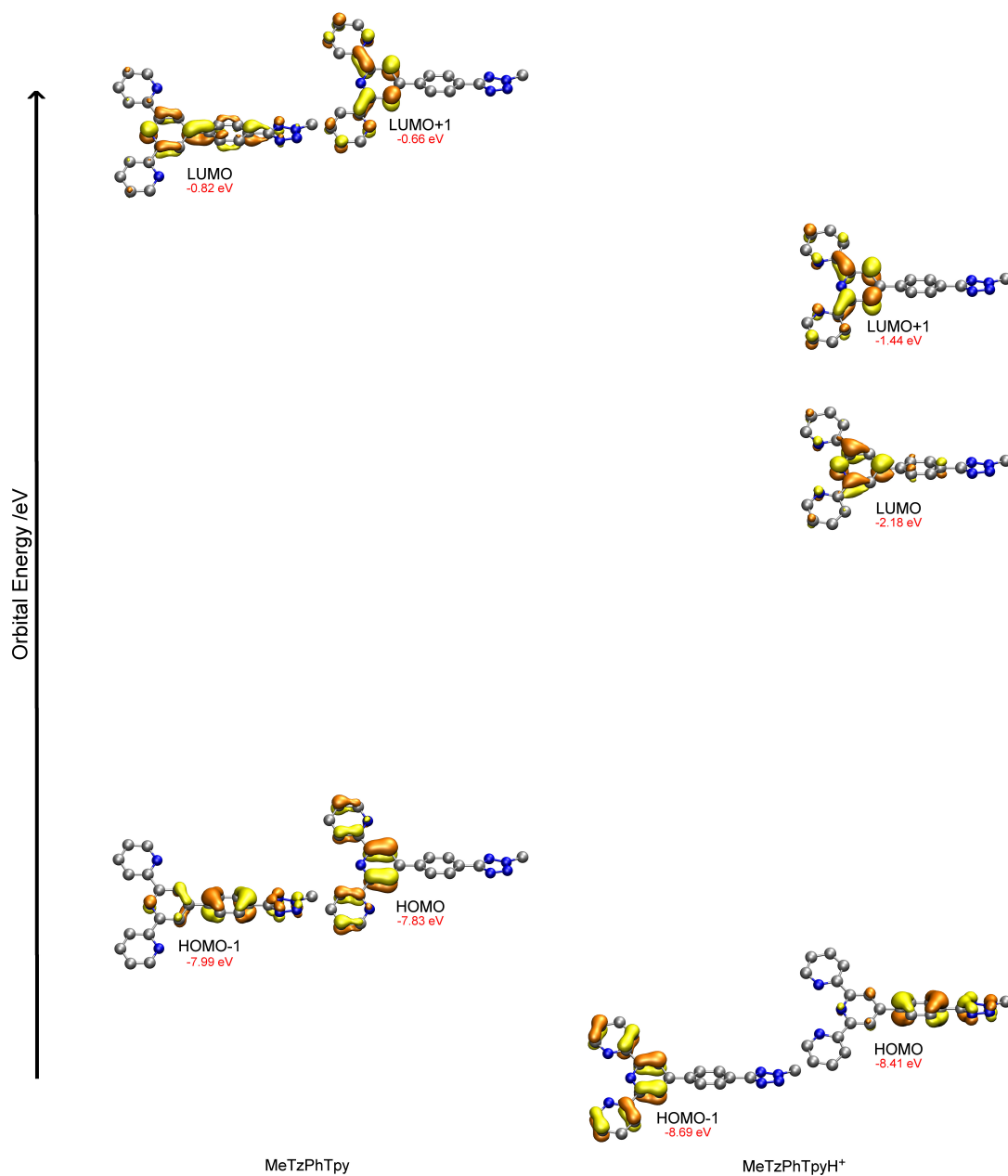
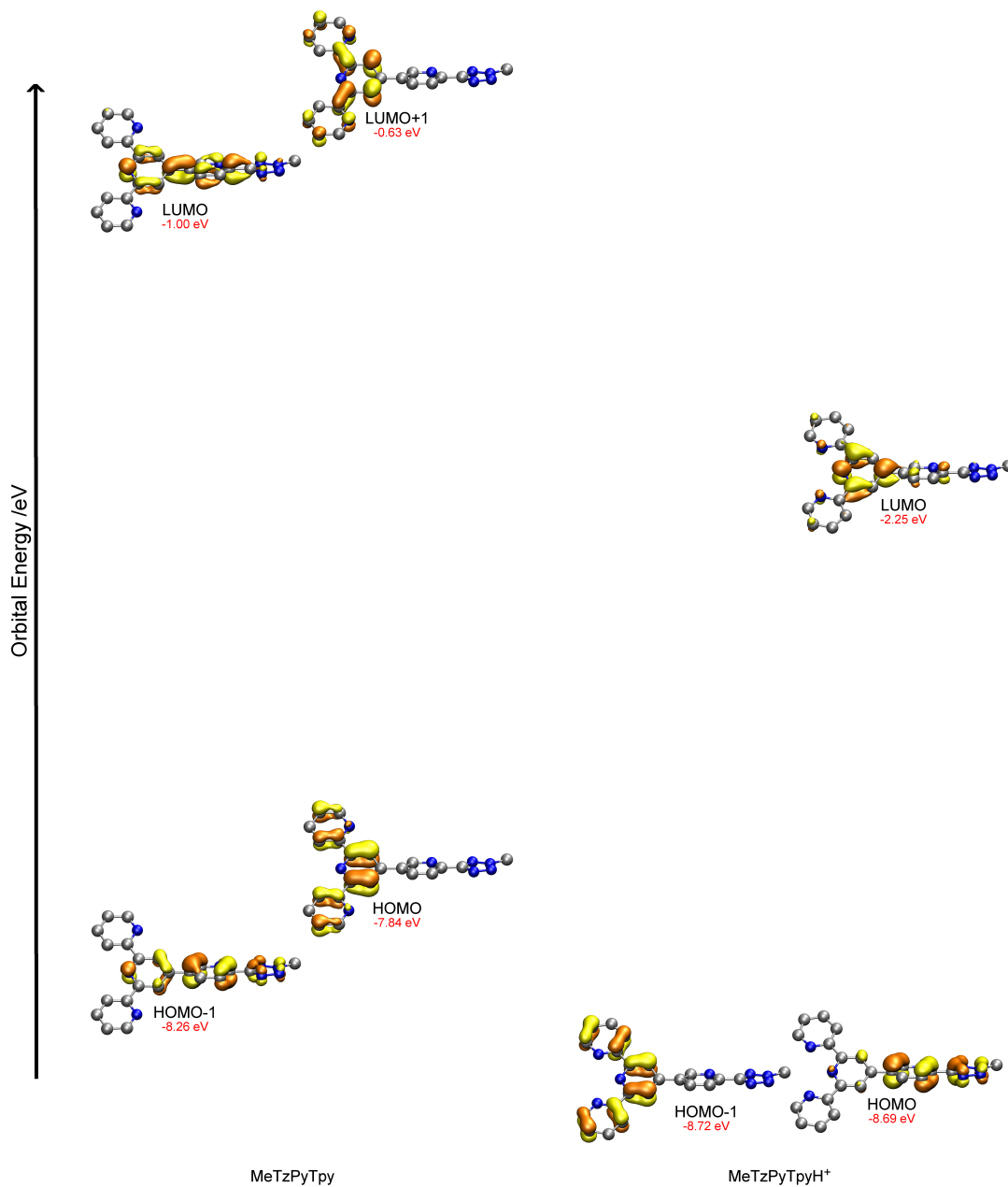


Figure 3.23: Simulated absorption spectra for derivatives of [MeTzPyTpy].



**Figure 3.24:** Simulated orbitals for derivatives of MeTzPhTpy corresponding to transitions listed in Table 3.2. Orbitals are spaced vertically relative to their energy and the HOMO-LUMO gap has been reduced for clarity.



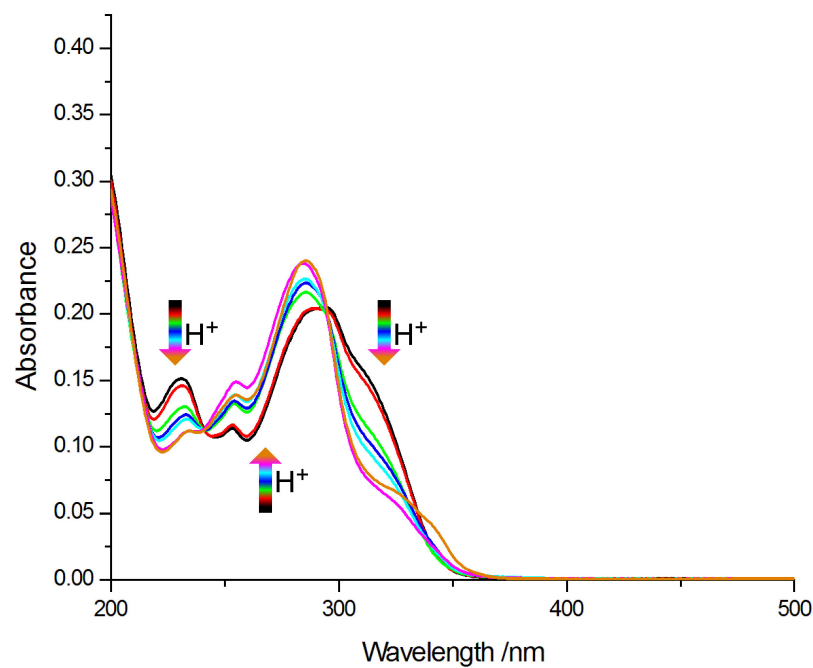
**Figure 3.25:** Simulated orbitals for derivatives of MeTzPhTpy corresponding to transitions listed in Table 3.2. Orbitals are spaced vertically relative to their energy and the HOMO-LUMO gap has been reduced for clarity.

**Table 3.2:** Transitions of relatively large oscillator strength, involved in absorption spectra, for species shown in Figure 3.22 and Figure 3.23.

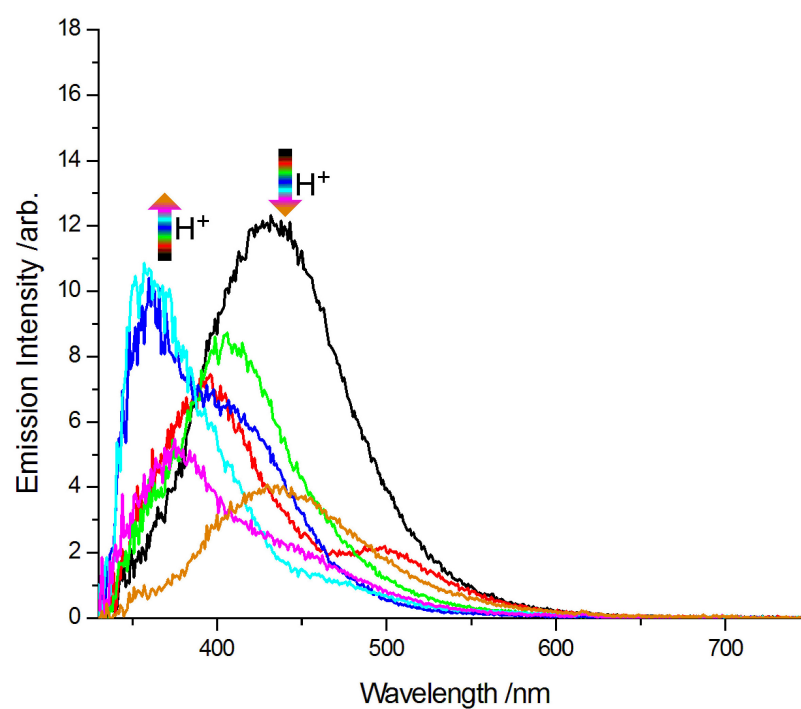
Species	Wavelength	Intensity	Levels	Character
<b>MeTzPhTpy</b>	281.58	0.516	HOMO $\rightarrow$ LUMO	79 %
	270.25	1.78	HOMO-1 $\rightarrow$ LUMO	59 %
			HOMO $\rightarrow$ LUMO+1	24 %
<b>MeTzPhTpyH<sup>+</sup></b>	313.09	0.705	HOMO-1 $\rightarrow$ LUMO	90 %
	305.19	1.28	HOMO $\rightarrow$ LUMO	85 %
<b>MeTzPyTpy</b>	282.84	0.51	HOMO $\rightarrow$ LUMO	75 %
	269.27	1.61	HOMO-1 $\rightarrow$ LUMO	47 %
			HOMO $\rightarrow$ LUMO+1	30 %
<b>MeTzPyTpyH<sup>+</sup></b>	314.8	0.708	HOMO-1 $\rightarrow$ LUMO	89 %
	294.9	1.36	HOMO $\rightarrow$ LUMO	81 %

To verify the explanation given, theoretical calculations were performed on the proposed species in solution. As the progression of absorption and emission spectra appears to follow a single path, and addition of acid beyond 10 equivalents does not yield significant change, it was expected that only the terpyridine moiety would be protonated in each case. Hence **MeTzPhTpyH<sup>+</sup>** and **MeTzPyTpyH<sup>+</sup>** were chosen as the protonated derivatives, and the simulated absorption spectra are found in Figure 3.22 and Figure 3.23.

The simulated spectra display an analogous trend where the lowest energy transition initially at 260 nm for the neutral species shifts to 310 nm for the protonated system. The theoretical absorbance spectra shown in Figure 3.22 suggest that this red-shift of the lowest energy transition agrees with the protonation of the terpyridine moiety to form **MeTzPhTpyH<sup>+</sup>**. The agreement between the experimental and theoretical absorbance spectra progression is also seen for **MeTzPyTpy** in Figure 3.23. Table 3.2 gives the lowest energy transitions that correspond to the simulated absorbance spectra in Figure 3.22, and the relevant orbitals and their relative energies are displayed in Figure 3.24 and Figure 3.25. The orbitals for **MeTzPyTpy** and **MeTzPyTpyH<sup>+</sup>** display a similar change to those in Figure 3.30 as seen in Figure 3.25. The computational results suggest that upon protonation of **MeTzPhTpy** the HOMO and LUMO are stabilised by 0.58 eV and 1.36 eV respectively. The overall effect of this stabilisation is a smaller HOMO-LUMO gap.

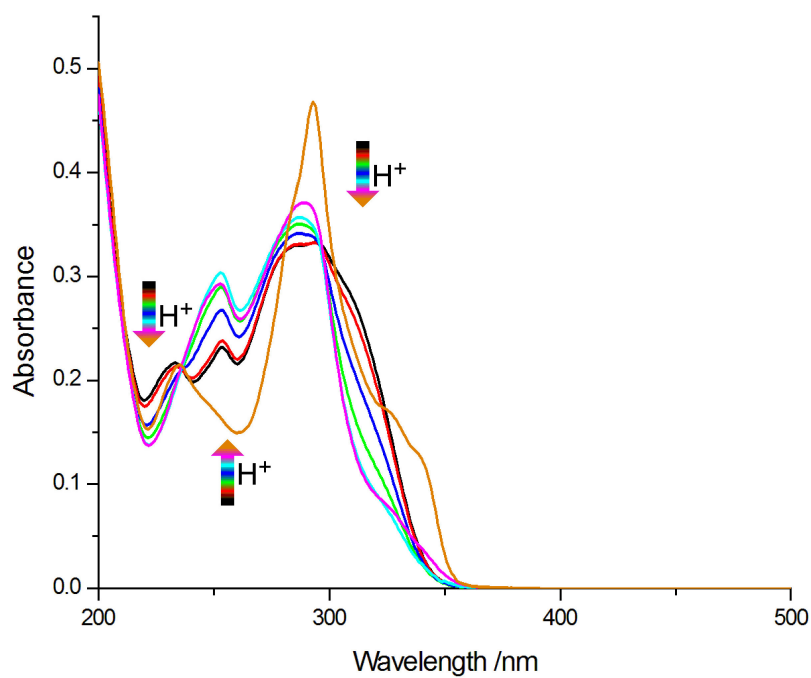


(a)

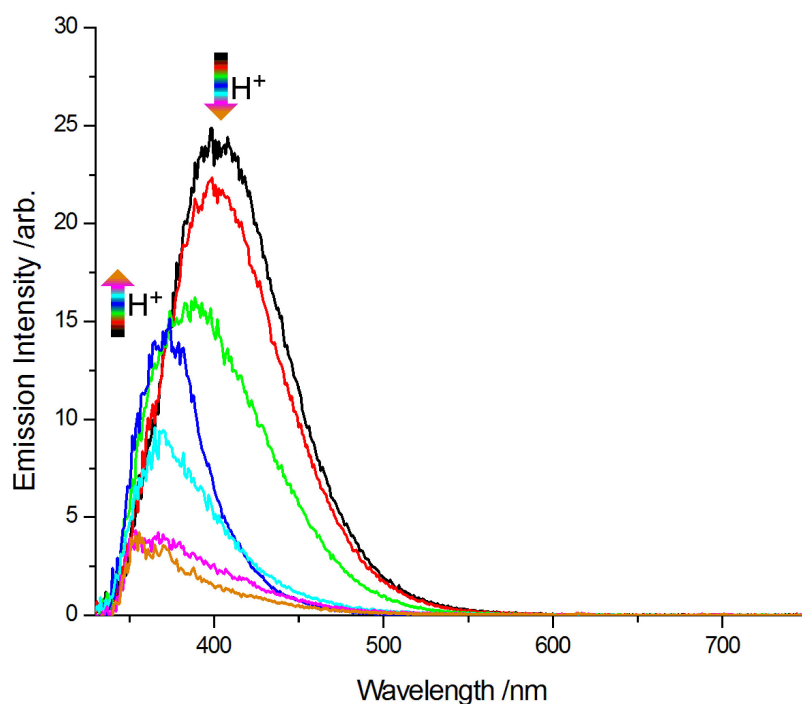


(b)

**Figure 3.26:** Absorption and emission spectra of  $\text{TzPhTpy}^-$  under progressive addition of acid. Each line represents the addition of  $\frac{1}{3}$  equivalent of camphorsulphonic acid. The orange line represents the addition of ca. 5 equivalents of acid. a) Absorption spectra. b) Emission spectra.



(a)



(b)

**Figure 3.27:** Absorption and emission spectra of  $\text{TzPyTpy}^-$  under progressive addition of acid. Each line represents the addition of  $\frac{1}{3}$  equivalent of camphorsulphonic acid. The orange line represents the addition of ca. 10 equivalents of acid. a) Absorption spectra. b) Emission spectra.



The progression of absorption and emission profiles under addition of acid for **TzPhTpy**<sup>-</sup> and **TzPyTpy**<sup>-</sup> are shown in Figure 3.26 and Figure 3.27, respectively. Two isobestic points can be identified in the progression of each of the absorption spectra, Figure 3.26a (295 nm and 240 nm) and Figure 3.27a (290 nm and 230 nm). As acid is added progressively to the solutions, the absorption peaks at 320 and 235 nm reduce in intensity, and the peaks at 280 and 260 nm increase in intensity. This trend continues until ca. 2 equivalents of acid have been added. Under further addition of acid to ca. 5 equivalents, a band at 345 nm increases in intensity shown for the magenta and orange curves. This band was observed in the absorption spectra of **MeTzPhTpy** and **MeTzPyTpy** implying protonation at the terpyridine moiety.

Moving to the changes in emission profiles, the emission spectra of **TzPhTpy**<sup>-</sup>, Figure 3.26b, begins with a single peak at 420 nm. As acid is progressively added, this peak decreases in intensity and a peak at 365 nm increases in intensity until ca. 2 equivalents of acid has been added. As acid is added further, as seen for the magenta and orange curves, the peak at 365 nm reduces in intensity and a peak at 410 nm increases in intensity. Further addition of acid does not appreciably change the emission spectrum. In the emission spectra of **TzPyTpy**<sup>-</sup>, Figure 3.27b, progressive addition of acid causes a reduction in intensity of the 400 nm emission and a new peak at 360 nm develops. Addition of acid beyond ca. 2 equivalents does not lead to the development of an emission peak at 420 nm as seen for **TzPhTpy**<sup>-</sup>.

In each case of absorption and emission, the progression of the spectra is reversible by addition of an appropriate amount of base.

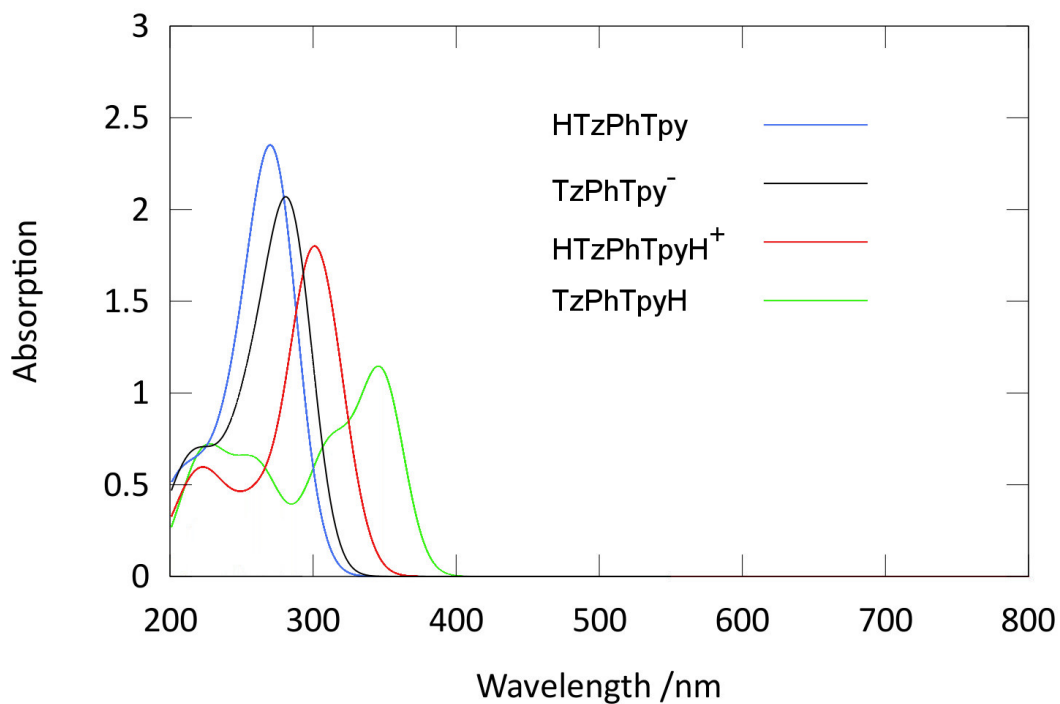


Figure 3.28: Simulated absorption spectra for derivatives of HTzPhTpy.

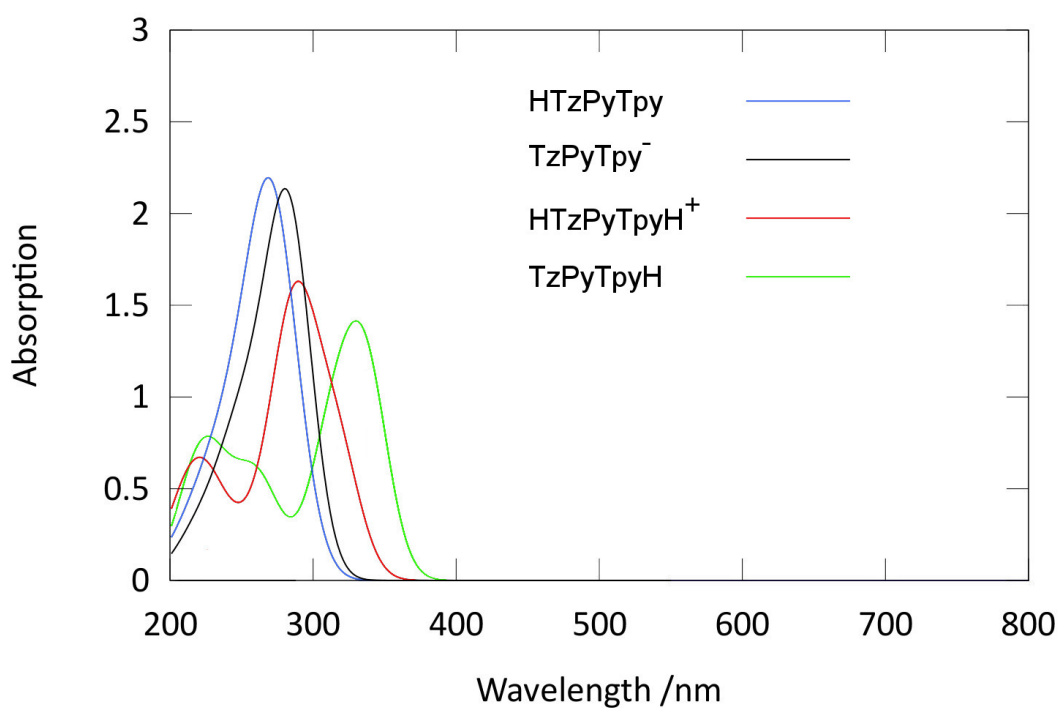
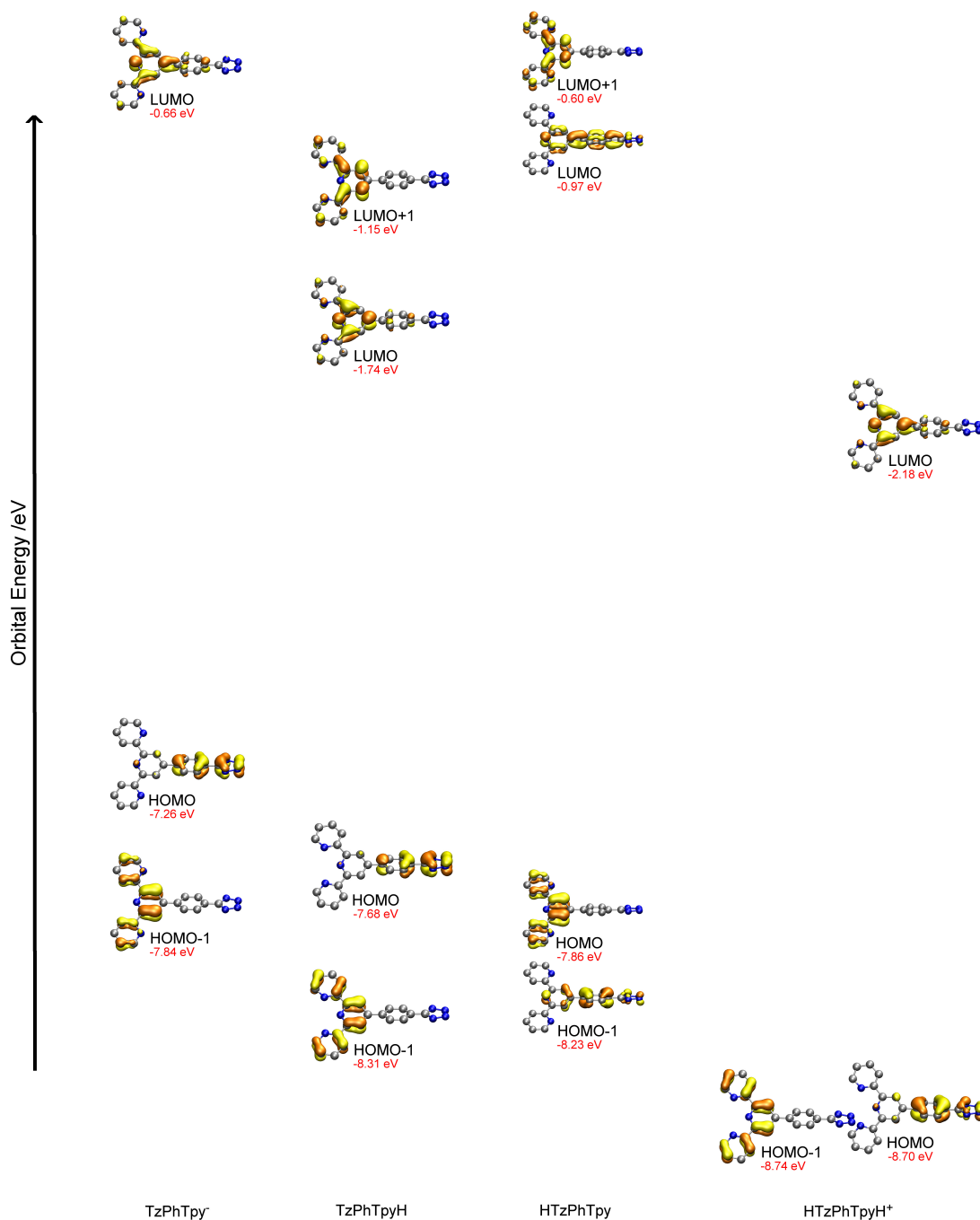
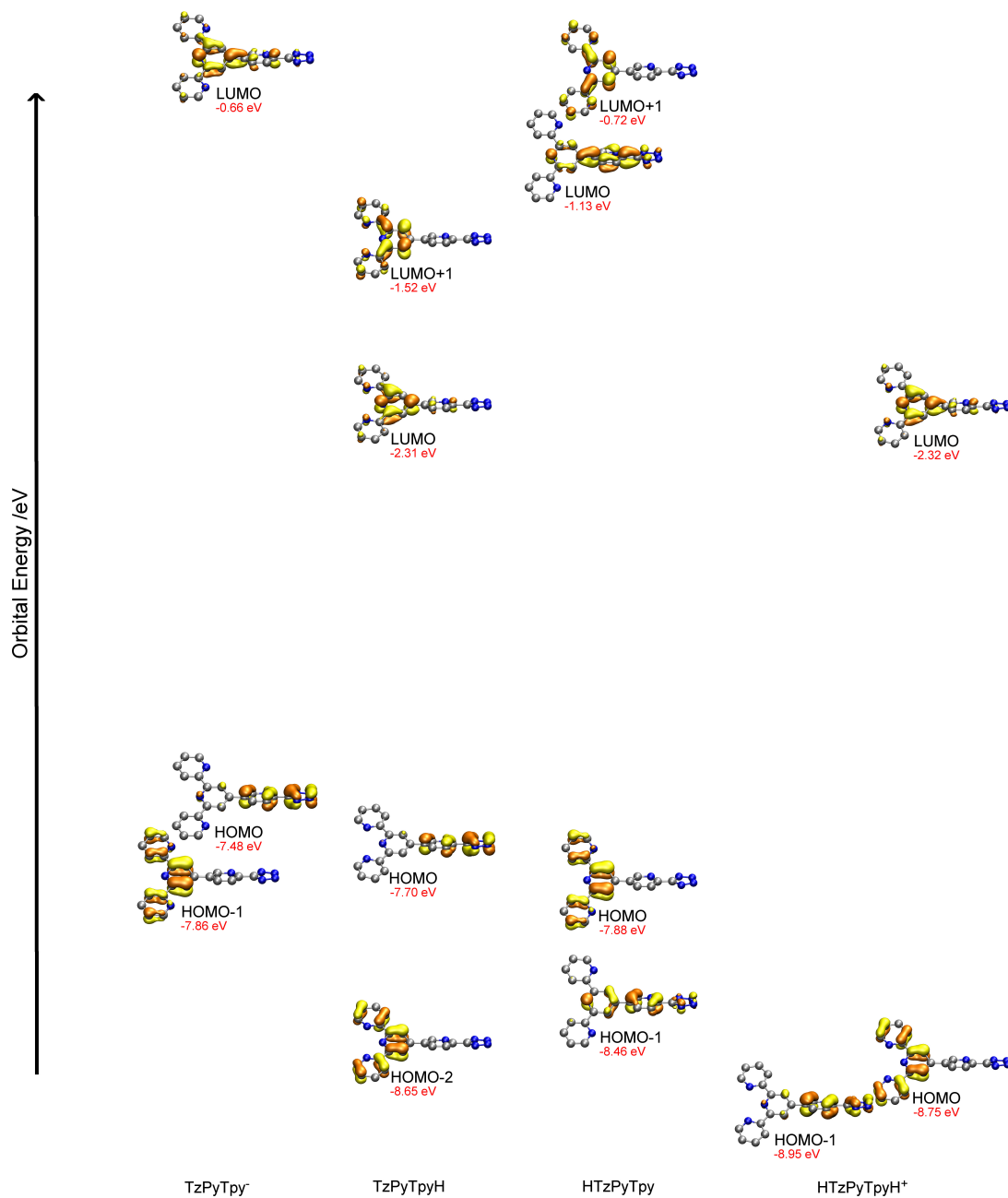


Figure 3.29: Simulated absorption spectra for derivatives of HTzPyTpy.



**Figure 3.30:** Simulated orbitals for derivatives of HTzPhTpy corresponding to transitions listed in Table 3.3. Orbitals are spaced vertically relative to their energy and the HOMO-LUMO gap has been reduced for clarity.



**Figure 3.31:** Simulated orbitals for derivatives of HTzPyTpy corresponding to transitions listed in Table 3.3. Orbitals are spaced vertically relative to their energy and the HOMO-LUMO gap has been reduced for clarity.

**Table 3.3:** Transitions of relatively large oscillator strength involved in simulated absorption spectra, for species shown in Figure 3.28 and Figure 3.29.

Species	Wavelength	Intensity	Levels	Character
<b>TzPhTpy<sup>-</sup></b>	285.85	1.38	HOMO → LUMO	74 %
	280.23	0.47	HOMO-1 → LUMO	80 %
<b>TzPhTpyH</b>	347.57	1.09	HOMO → LUMO	85 %
	310.94	0.67	HOMO-1 → LUMO	86 %
	260.43	0.48	HOMO-1 → LUMO+1	67 %
<b>HTzPhTpy</b>	283.52	0.50	HOMO → LUMO	74 %
	270.40	1.77	HOMO-1 → LUMO	60 %
			HOMO → LUMO+1	25 %
<b>HTzPhTpyH<sup>+</sup></b>	314.76	0.70	HOMO-1 → LUMO	89 %
	296.47	1.35	HOMO → LUMO	84 %
<b>TzPyTpy<sup>-</sup></b>	284.04	1.42	HOMO → LUMO	70 %
	280.53	0.52	HOMO-1 → LUMO	81 %
<b>TzPyTpyH</b>	336.30	1.13	HOMO → LUMO	83 %
	312.21	0.70	HOMO-2 → LUMO	88 %
	261.31	0.44	HOMO-2 → LUMO+1	67 %
<b>HTzPyTpy</b>	285.05	0.48	HOMO → LUMO	70 %
	269.45	1.56	HOMO-1 → LUMO	42 %
			HOMO → LUMO+1	30 %
<b>HTzPyTpyH<sup>+</sup></b>	316.47	0.71	HOMO → LUMO	89 %
	287.46	1.43	HOMO-1 → LUMO	80 %

To rationalise the progression of absorption spectra of **TzPhTpy<sup>-</sup>** and **TzPyTpy<sup>-</sup>**, theoretical studies have been performed on four hypothesised derivatives of **TzPhTpy<sup>-</sup>** and **TzPyTpy<sup>-</sup>**. It was assumed that the spectra started from a fully deprotonated system when 1 equivalent of base was added. This assumption was validated when addition of strong base (ca. 70 equivalents) to the prepared solutions did not yield an appreciable change in spectra. It was also assumed that after addition of sufficient amount of acid, the species would be protonated at both the tetrazole site and the terpyridine site. Thus the cationic species **HTzPhTpyH<sup>+</sup>** and **HTzPhTpyH<sup>+</sup>** were modelled. It was expected that the terpyridine moiety would behave as the strongest base, hence the zwitterionic species (**TzPhTpyH** and **TzPhTpyH**) were modelled. Equilibration of the zwitterionic species with **HTzPhTpy** and **HTzPhTpy** was expected, hence these species were also modelled. In the case of **HTzPyTpy**, the pyridyl-tetrazole moiety may be protonated at the pyridine site, however, simulation of **HTzPyTpy**, which places the proton proximal to the pyridine ring was considered to be sufficient for modelling.

The simulated absorption spectra for each of these species are illustrated in Fig-

ure 3.28 and Figure 3.29 for the derivatives of **HTzPhTpy** and **HTzPyTpy**, respectively. Table 3.3 lists transitions for each of the species with lower energy and relatively high oscillator strength, and Figures 3.30 and 3.31 display the associated orbital contours.

As seen in Figure 3.26a, the initial addition of acid to **TzPhTpy**<sup>-</sup> leads to a blue-shift of the lowest energy transition. Theoretical absorbance spectra shown in Figure 3.28 suggest that this blue-shift may be a result of the relative abundance of **TzPhTpy**<sup>-</sup> which equilibrates with other species in solution. This blue-shift comes as a result of stabilisation of the frontier orbitals as seen in Figure 3.31, where the HOMO has been reduced in energy to a greater extent. Under further addition of acid, beyond ca. 2 equivalents, the peak at 330 nm becomes prominent. The simulated absorption spectra suggests this may be due to the formation of and equilibration between **HTzPhTpyH**<sup>+</sup> and **TzPhTpyH**. In these two cases, the localisation of a proton at the terpyridine moiety results in further stabilisation of the frontier orbitals, where relatively greater stabilisation of the LUMO occurs. This overall progression is observed similarly for **TzPyTpy**<sup>-</sup>, and the rationalisation is the same as that given for **TzPhTpy**<sup>-</sup>. The progression of emission spectra for **HTzPhTpy** and **HTzPyTpy** is more convoluted and significantly more difficult to precisely rationalise.

## 3.5 Conclusion

This chapter has extended the ligand library from Chapter 2 to include the tetrazole functionalised terpyridines, **HTzPhTpy** and **HTzPyTpy**. Their methylated derivatives **MeTzPhTpy** and **MeTzPyTpy** were also successfully synthesised. The deprotonated ligands **TzPhTpy**<sup>-</sup> and **TzPyTpy**<sup>-</sup> display high luminescence efficiencies, and each of the synthesised ligands display photophysical properties in solution that are sensitive to the addition of acids or bases. This implies that these ligands could also be applied as fluorescent sensors to detect changes in solutions.

The synthesised ligands will be used to form complexes of Re(I) analogous to **[Re(<sup>t</sup>BuTzPy)Cl]** and **[ReTzPy]<sub>3</sub>**, analysed in Chapter 1, and to form new complexes analogous to literature reports of Re(I) tetrazolato complexes.<sup>1,2</sup> These mononuclear and multinuclear complexes will then be investigated for their ability to sensitize lanthanides.





# Chapter 4

## Terpyridine-functionalised Re(I) tricarbonyl tetrazolato complexes

### 4.1 Introduction

Previous investigations of luminescent Re(I) tetrazolato complexes have utilised aryl tetrazoles as an ancillary ligand, and have demonstrated the modulation of their photophysical properties by chemical modification of these ligands.<sup>1,2,196</sup> Further, the investigation performed in Chapter 2 illustrates that interesting coordination modes are obtainable when combining  $[\text{Re}(\text{CO})_5\text{X}]$  ( $\text{X} = \text{Cl}, \text{Br}$ ) with tetrazole containing ligands. This chapter will attempt to introduce the tetrazole functionalised terpyridines synthesised in Chapter 3 to the luminescent motifs discovered in Chapter 2. Further, the tetrazole functionalised terpyridines will also be used as ancillary ligands in Re(I) complexes, analogous to those reported in literature.<sup>1</sup>

The extension of these Re(I) complexes to include a terpyridine moiety is motivated primarily by their potential ability to bind to, and sensitise, a lanthanide cation. This chapter focuses on the synthesis and properties of these metal complexes to then determine if they may behave as suitable antennae for lanthanide sensitisation. The library of complexes were chosen as they will allow us to probe the relationship between binding site, energy of excited states, and sensitisation efficiency. The target complexes are shown in Figure 4.1.

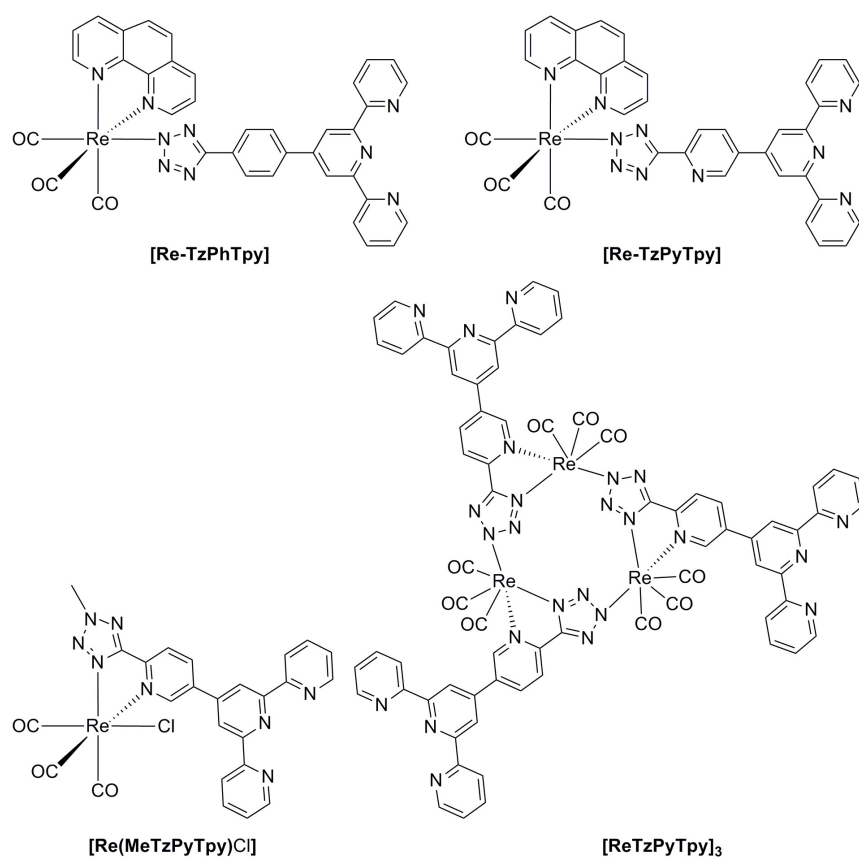
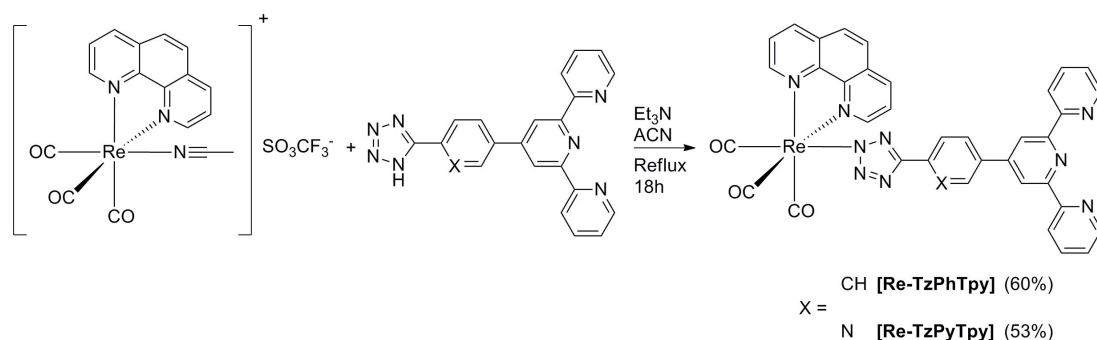


Figure 4.1: Structures of target complexes in this Chapter.

## 4.2 Synthesis of the target complexes

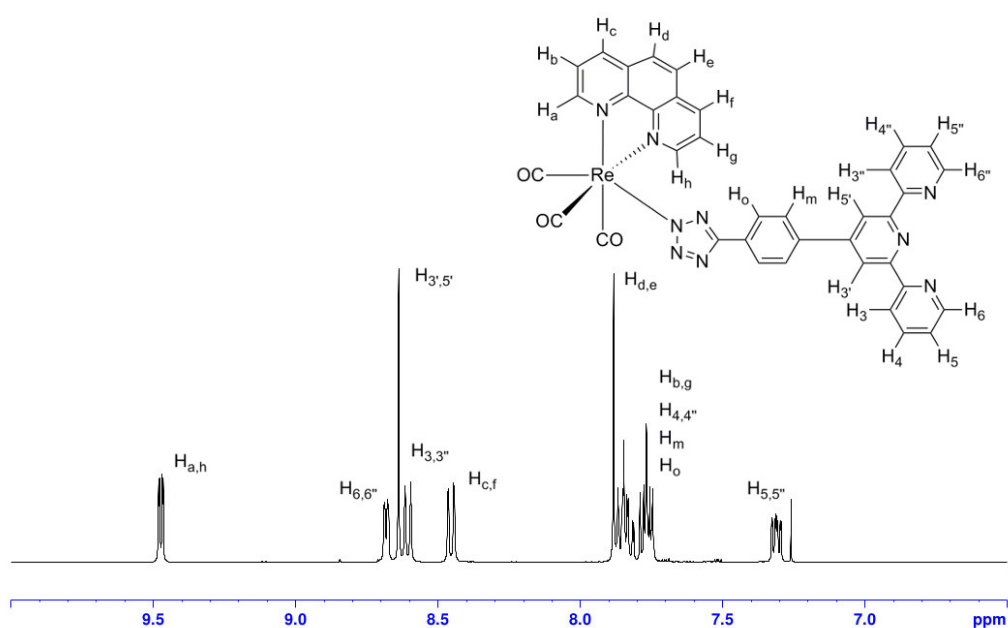
### 4.2.1 Synthesis of [Re-TzPhTpy] and [Re-TzPyTpy]

The synthesis of [Re-TzPhTpy] and [Re-TzPyTpy], via a previously reported method,<sup>1</sup> utilises the labile intermediate [Re(CO)<sub>3</sub>(phen)(NCCH<sub>3</sub>)]<sup>+</sup>[SO<sub>3</sub>CF<sub>3</sub>]<sup>-</sup> to encourage ligand substitution, as shown in Figure 4.2.



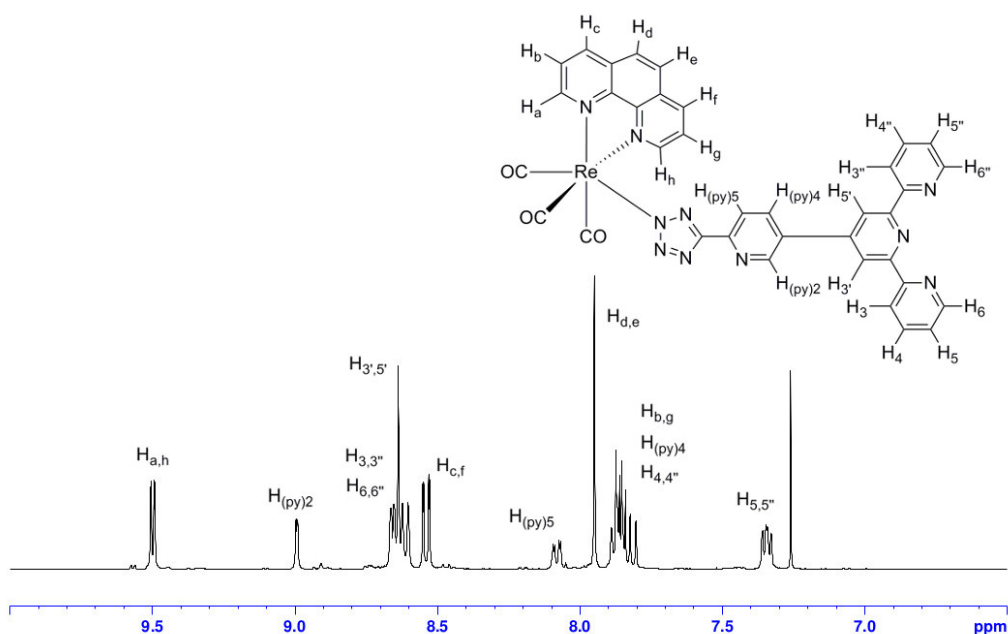
**Figure 4.2:** Reaction scheme for the synthesis of [Re-TzPhTpy] and [Re-TzPyTpy].

[Re-TzPhTpy] and [Re-TzPyTpy] are characterised by IR, <sup>1</sup>H-NMR and <sup>13</sup>C-NMR spectroscopy. The IR spectra display peaks at approximately 2022 cm<sup>-1</sup> (A'(1)) and 1894 cm<sup>-1</sup> (A'(2), A'') indicative of the *facial* configuration of the carbonyl ligands. These values are consistent with previously reported neutral rhenium tetrazolato complexes.<sup>1</sup>



**Figure 4.3:** <sup>1</sup>H-NMR spectrum of [Re-TzPhTpy] in CDCl<sub>3</sub>.

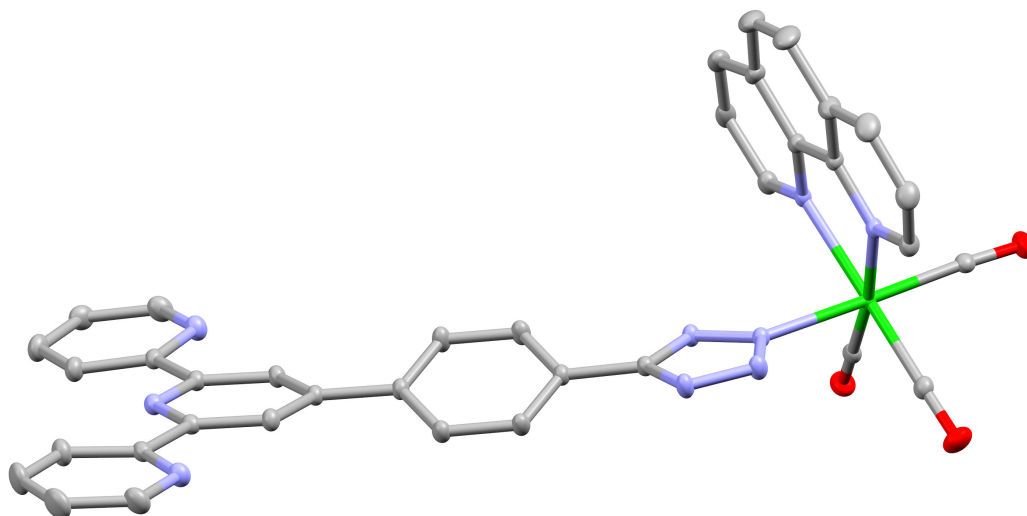
The  $^1\text{H-NMR}$  spectrum of **[Re-TzPhTpy]**, as shown in Figure 4.3, displays a set of signals consistent with the structure. The doublet at 9.47 ppm with an integration of 2 protons corresponds to  $\mathbf{H}_{a,h}$ . A singlet at 8.64 ppm with an integration of 2 protons corresponds to  $\mathbf{H}_{3',5'}$  and gives a ratio of 1:1 for 1,10-phenanthroline and aryl-tetrazole functionalised terpyridine. The equivalence of the  $\mathbf{H}_n$  and  $\mathbf{H}_{n''}$  ( $n = 3 - 6$ ) positions is also indicative that the terpyridine moiety has not chelated to Re(I). An overall integration to 22 protons is also confirmation of the given structure. The  $^{13}\text{C-NMR}$  spectrum for this compound displays 19 peaks in the aromatic region, corresponding to those expected for the proposed product. The resonance at 162.9 ppm corresponds to the C5 tetrazolic carbon and indicates a N2 coordination mode. The signals at 196.7 ppm and 193.7 ppm correspond to the carbonyl ligands.



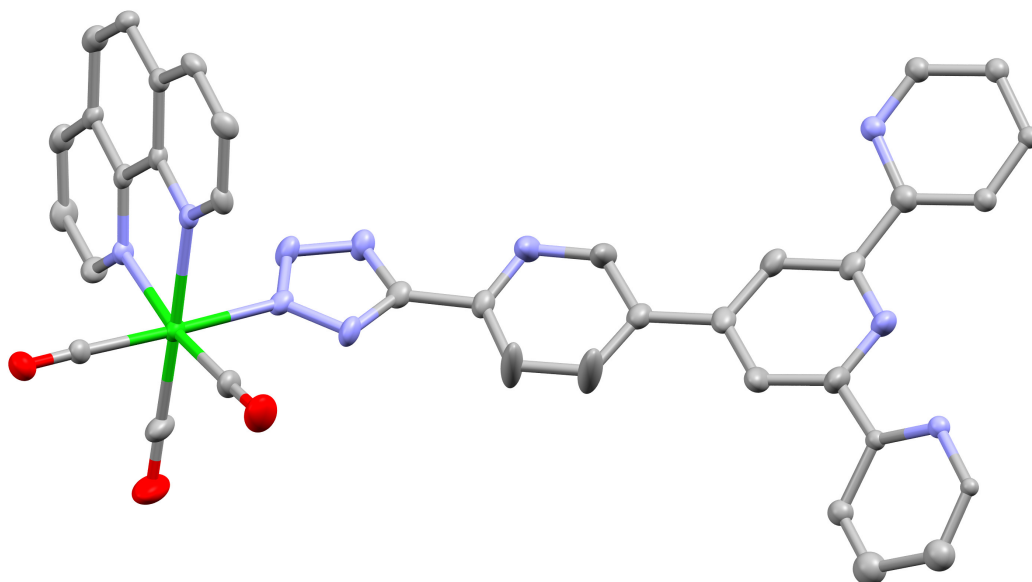
**Figure 4.4:**  $^1\text{H-NMR}$  spectrum of **[Re-TzPyTpy]** in  $\text{CDCl}_3$ .

The  $^1\text{H-NMR}$  spectrum for **[Re-TzPyTpy]**, as shown in Figure 4.4, displays signals in agreement with the proposed product. Specific signals in a ratio of 2:1:2 are a doublet at 9.50 ppm corresponding to  $\mathbf{H}_{a,h}$ , a singlet at 8.99 ppm with an integration of 1 proton corresponding to  $\mathbf{H}_{(py)2}$ , and a multiplet from 7.36 ppm to 7.33 ppm corresponding to  $\mathbf{H}_{5,5''}$ . These signals indicate the presence of 1,10-phenanthroline and the aryl-tetrazole functionalised terpyridine in a ratio of 1:1, and the equivalence of the  $\mathbf{H}_n$  and  $\mathbf{H}_{n''}$  ( $n = 3 - 6$ ) positions is also indicative that the terpyridine moiety has not chelated to Re(I). The overall integration of the spectrum gives 21 protons consistent with the proposed structure. The  $^{13}\text{C-NMR}$  spectrum for this compound also has 19 peaks in the aromatic region, corresponding to those expected for the proposed product. Specific resonance at

163.6 ppm for the C5 tetrazolic carbond indicates N2 coordination.



**Figure 4.5:** X-Ray crystal structure of **[Re-TzPhTpy]** with displacement ellipsoids drawn at 50 % probability, H atoms and solvent molecules are omitted for clarity.



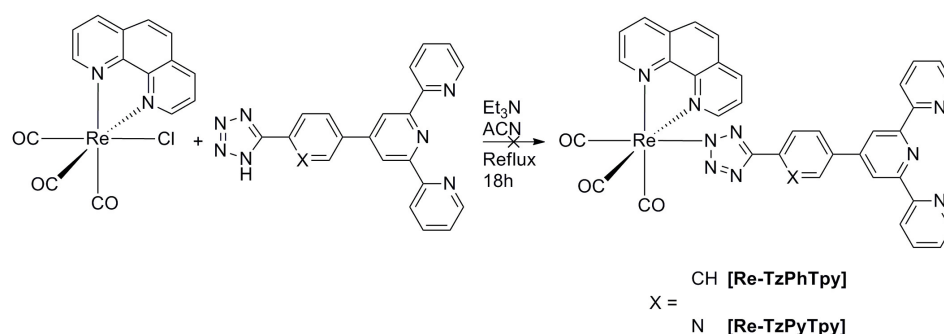
**Figure 4.6:** X-Ray crystal structure of **[Re-TzPyTpy]** with displacement ellipsoids drawn at 50 % probability, H atoms and solvent molecules are omitted for clarity..

Crystal structures of **[Re-TzPhTpy]** and **[Re-TzPyTpy]** were obtained and are shown in Figure 4.5 and Figure 4.6, respectively. Both complexes crystallise in the triclinic space group  $P\bar{1}$  with Re(I) centres in a slightly distorted octahedral

geometry. The three carbonyl ligands are in *facial* configuration and the Re(I) centre is coordinated to the N2 position of the tetrazole in agreement with the spectroscopic data. In the case of **[Re-TzPhTpy]**, the angle between the planes of the tetrazole and terpyridine rings is 2° and that of the planes of the tetrazole and phenyl rings is 18°. The nitrogen atoms on the appending pyridyl rings are shown to be *anti* to the nitrogen on the central pyridyl ring. In the case of **[Re-TzPyTpy]**, it can be seen that there is some disorder in the planes of each of the pyridyl rings. In this structure, the nitrogen atoms on the appending pyridyl rings are configured to have one *syn* and one *anti* relative to the central pyridyl ring.

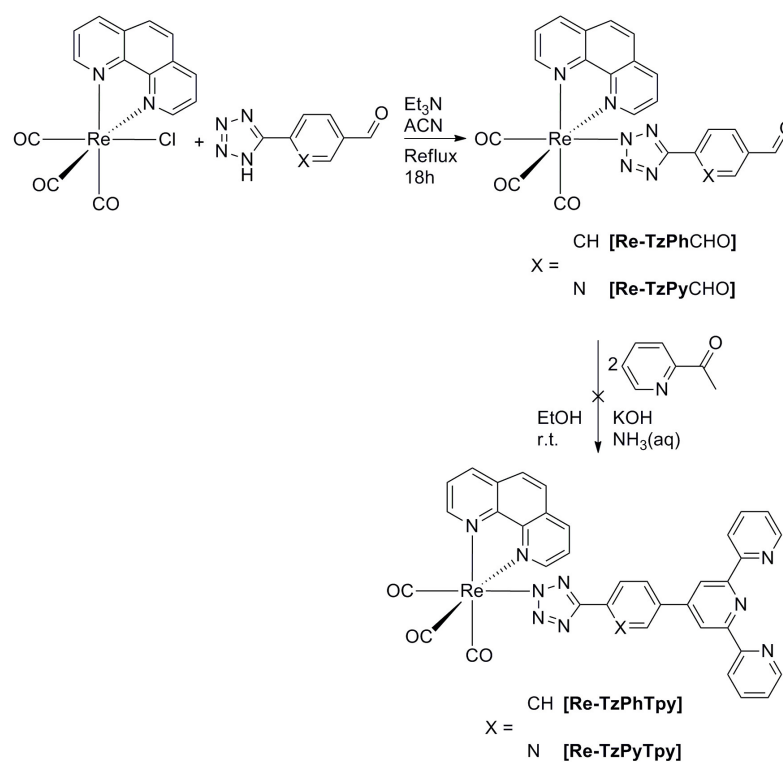
Other attempts to synthesise **[Re-TzPhTpy]** and **[Re-TzPyTpy]** by direct reaction of **HTzPhTpy** with **[Re(CO)<sub>3</sub>(phen)Cl]** in the presence of triethylamine, Figure 4.7, which avoids waste of the **[Re(CO)<sub>3</sub>(phen)Cl]** starting material were unsuccessful. Only the starting material **[Re(CO)<sub>3</sub>(phen)Cl]** was recovered via flash chromatography.

In another attempted method, displayed in Figure 4.8, the synthesis of **[Re-TzPhCHO]** and **[Re-TzPyCHO]** was performed first, and then followed by formation of the terpyridine moiety. The spectroscopic data obtained for **[Re-TzPyCHO]** is consistent with literature and the data for **[Re-TzPhCHO]** displays similar characteristics with relevant differences for the pyridyl ring.<sup>1</sup> After forming **[Re-TzPhCHO]** and **[Re-TzPyCHO]**, they are combined with with 2-acetylpyridine to obtain **[Re-TzPhTpy]** and **[Re-TzPyTpy]**, respectively. However, from these reactions only starting materials were recovered.



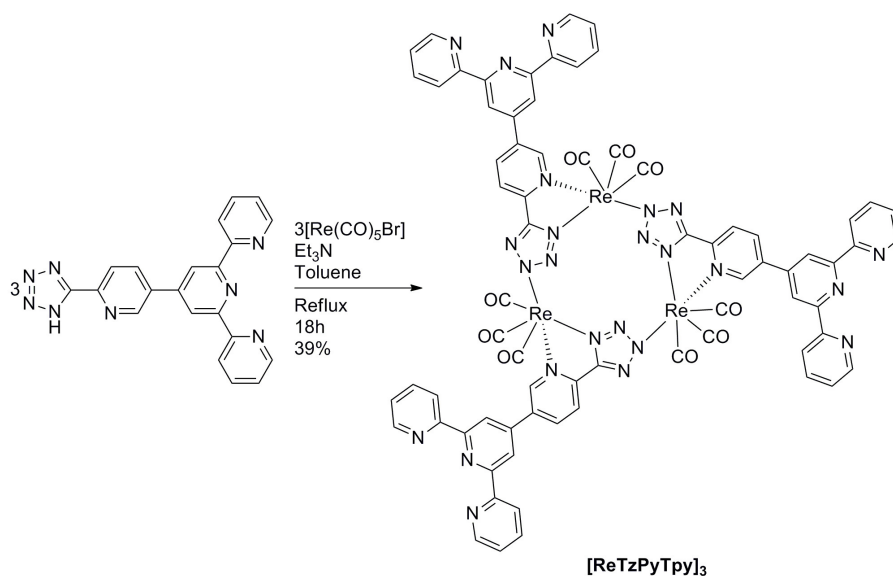
**Figure 4.7:** Attempted direct reaction scheme for the synthesis of **[Re-TzPhTpy]** and **[Re-TzPyTpy]**.

## 4.2 Synthesis of the target complexes



**Figure 4.8:** Second attempted direct reaction scheme for the synthesis of  $[\text{Re-TzPhTpy}]$  and  $[\text{Re-TzPyTpy}]$ .

### 4.2.2 Synthesis of $[\text{ReTzPyTpy}]_3$



**Figure 4.9:** Reaction scheme for the synthesis of  $[\text{ReTzPyTpy}]_3$ .

The synthesis of  $[\text{ReTzPyTpy}]_3$  is illustrated in Figure 4.9 and utilises similar conditions to those for the synthesis of  $[\text{ReTzPy}]_3$ , seen in Chapter 2. The synthesised species is characterised by IR,  $^1\text{H-NMR}$ , and  $^{13}\text{C-NMR}$  spectroscopy. Bands in the IR spectrum appear at approximately  $2029$  and  $1901\text{ cm}^{-1}$  for the carbonyl stretching modes, and a band at  $1605\text{ cm}^{-1}$  indicates the presence of the tetrazole  $\text{C}=\text{N}$  stretch.

The  $^1\text{H-NMR}$  spectrum, as shown in Figure 4.10, is consistent with the proposed product with three singlets at  $9.54\text{ ppm}$ ,  $9.43\text{ ppm}$ , and  $9.33\text{ ppm}$  with an integration of 1 proton each corresponding to  $\text{H}_{(\text{py})2}$  for each of the three unique  $\text{TzPyTpy}^-$  moieties. The remaining signals are convoluted and cannot be precisely assigned, however, the overall integration to 39 protons matches with what is expected for this molecule. This splitting of signals is very similar to that found for the previously reported  $[\text{ReTzPy}]_3$  in Chapter 2. The  $^{13}\text{C-NMR}$  spectrum was not obtained as the solubility of this compound was too low in deuterated solvents and the signals were not resolvable.

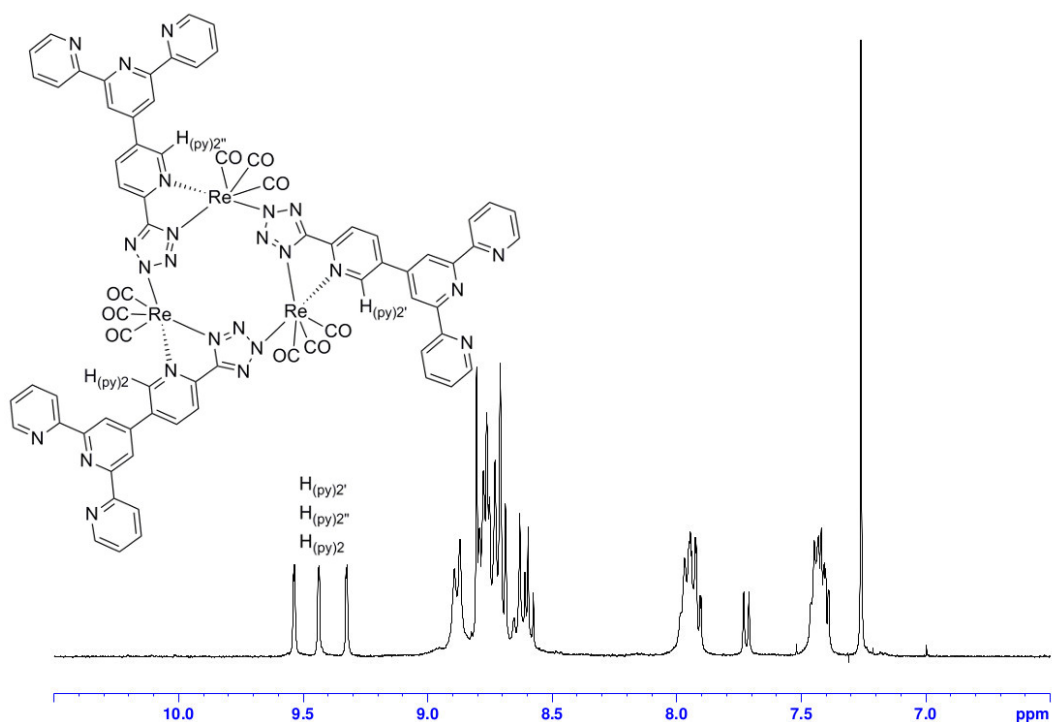
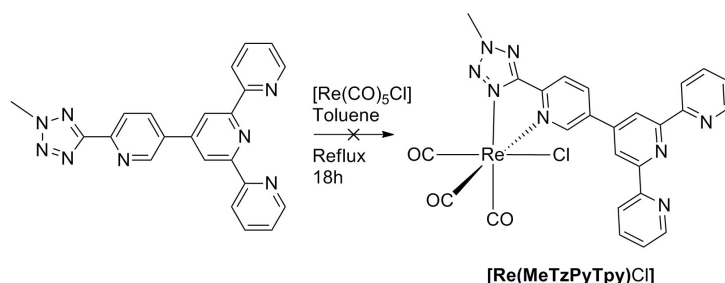


Figure 4.10:  $^1\text{H-NMR}$  spectrum of  $[\text{ReTzPyTpy}]_3$  in  $\text{CDCl}_3$ .

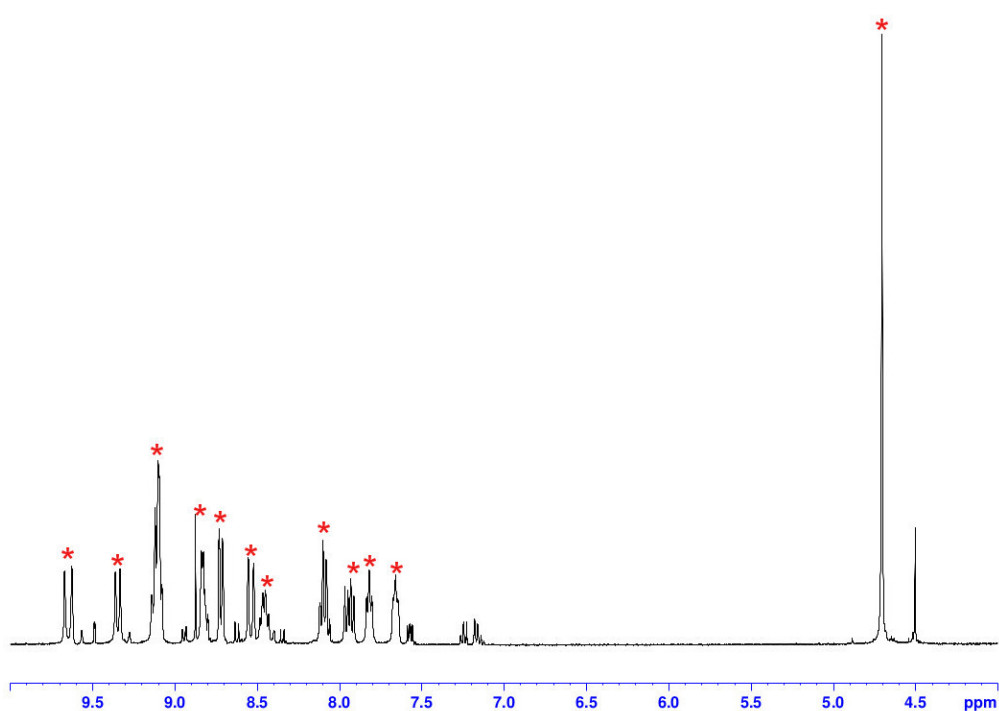


### 4.2.3 Synthesis of $[\text{Re}(\text{MeTzPyTpy})\text{Cl}]$

To obtain the complex  $[\text{Re}(\text{MeTzPyTpy})\text{Cl}]$ , the synthesis scheme outlined in Figure 4.11 was attempted.



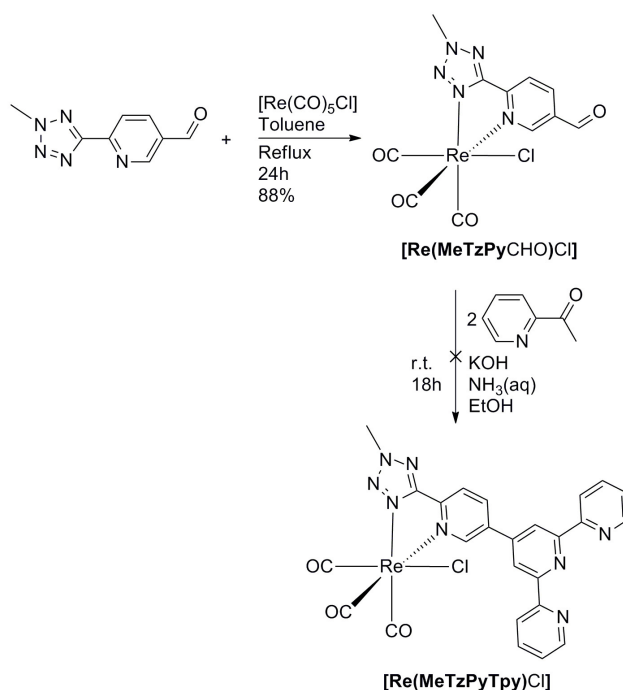
**Figure 4.11:** Reaction scheme for the synthesis of  $[\text{Re}(\text{MeTzPyTpy})\text{Cl}]$ .



**Figure 4.12:**  $^1\text{H}$ -NMR spectrum of the product obtained by the reaction outlined in Figure 4.11 in  $\text{CDCl}_3$ .

The product of this reaction was only slightly soluble in DMSO. IR analysis of the product gave bands at 2042, 2025, 1958, 1929, 1897, and 1879  $\text{cm}^{-1}$ . This is indicative of potentially multiple Re(I) centres, and the band at 2042  $\text{cm}^{-1}$  is indicative of a cationic species. The  $^1\text{H}$ -NMR spectrum, shown in Figure 4.12, further suggests the presence of multiple Re(I) complexes. The methyl group at 4.71 ppm with an integration of 3 was taken as the standard to integrate the aromatic signals. The signals illustrated by a star integrate to 1 relative to the

methyl group, also highlighted. The sum of all these values with the methyl group corresponds to 16 protons, which indicates that the ligand is present, however the protons of the terpyridine moiety are no longer equivalent. This splitting of each proton into an individual environment suggests that the terpyridine might have chelated the metal centre. The chelation of rhenium tris-carbonyl species by terpyridine moieties is supported by multiple reports in literature.<sup>44,45,246,267–269</sup> It was not possible to purify the reaction mixture any further.



**Figure 4.13:** Reaction scheme for the synthesis of  $[\text{Re}(\text{MeTzPyCHO})\text{Cl}]$ .

Failing to obtain the pure target compound via the scheme shown in Figure 4.11, the synthetic route shown in Figure 4.13 was attempted. The synthesised species  $[\text{Re}(\text{MeTzPyCHO})\text{Cl}]$  is characterised by IR,  $^1\text{H-NMR}$  and  $^{13}\text{C-NMR}$  spectroscopy. The presence of sharp peaks in the IR spectrum at approximately  $2024$  and  $1882\text{ cm}^{-1}$  is indicative of the *facial* conformation of the carbonyl ligands. There is also a band at  $1618\text{ cm}^{-1}$ , corresponding to the tetrazole  $\text{C}=\text{N}$  stretch. The presence of the following signals in the  $^1\text{H-NMR}$  spectrum is indicative of the desired structure. A singlet at  $10.23\text{ ppm}$  corresponds to  $\text{CHO}$ , a singlet at  $9.46\text{ ppm}$  corresponds to  $\text{H}_{(\text{py})2}$ , and a singlet at  $4.62\text{ ppm}$  with integration of 3 corresponds to  $\text{CH}_3$ .

The  $^{13}\text{C-NMR}$  spectrum for this compound also displays 8 peaks corresponding to those expected for the proposed product with specific resonances at  $187.0\text{ ppm}$  for  $\text{CHO}$ ,  $42.0\text{ ppm}$  for  $\text{CH}_3$ , and  $166.2\text{ ppm}$  for  $\text{C5}$ , indicating coplanarity of the tetrazole and pyridyl rings.

Although the precursor **[Re(MeTzPyCHO)Cl]** was successfully isolated, the subsequent reaction to form the terpyridine moiety did not yield the desired product and only the starting material was recovered.

### 4.3 Photophysical and computational investigation

A summary of the photophysical properties of the synthesised complexes in dichloromethane is shown in Table 4.1.

**Table 4.1:** Summary of photophysical properties of dilute ( $10^{-5}$  M) DCM solutions.

Complex	Absorption		Emission, 298 K				Emission, 77 K		
	$\lambda_{max}$ [nm]	$(10^4\epsilon)$ [M <sup>-1</sup> cm <sup>-1</sup> ]	$\lambda_{max}$ [nm]	$\tau^a$ [ns]	$\tau^b$ [ns]	$\phi^a$	$\phi^b$	$\lambda_{em}$ [nm]	$\tau$ [ $\mu$ s]
<b>[Re-TzPhTpy]</b>	278(4.81) 360(0.49)		585	266	607	0.018	0.054	532	4.49
<b>[Re-TzPyTpy]</b>	276(4.23) 360(0.39)		583	283	564	0.022	0.053	513	3.97
<b>[ReTzPyTpy]<sub>3</sub></b>	280(8.80) 325(3.77)		518	507	2430	0.0782	0.216	475	34.37 (59 %) 0.92 (41 %)
<b>[Re(MeTzPyCHO)Cl]</b>	288(2.62) 403(0.37)		645	33.5	92	- <sup>c</sup>	- <sup>c</sup>	564	0.48 (88 %) 0.12 (12 %)

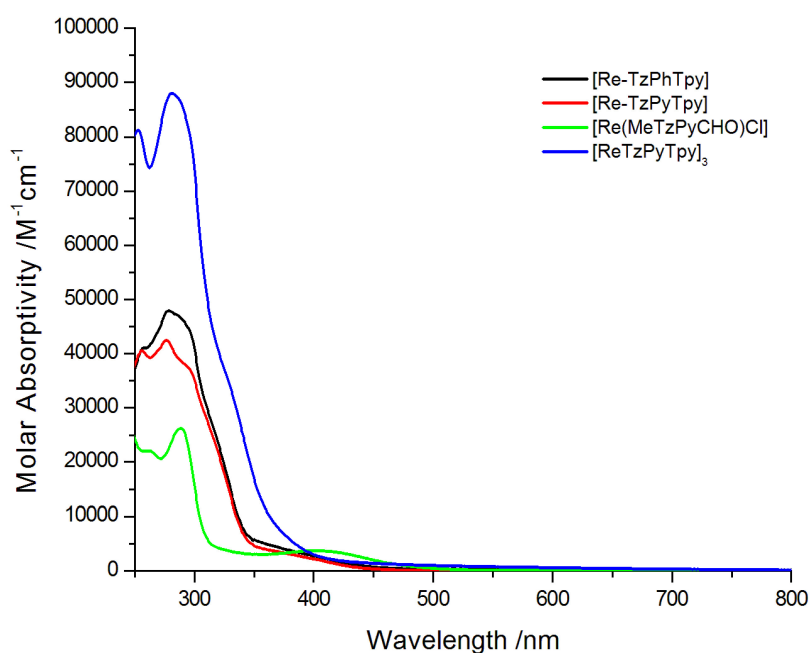
<sup>a</sup>Air-equilibrated solution, <sup>b</sup>Deoxygenated solution, <sup>c</sup>The emission of **[Re(MeTzPyCHO)Cl]** was too weak for accurate quantum yield determination. Quantum yield values measured against an air-equilibrated aqueous solution of **[Ru(bpy)<sub>3</sub>Cl<sub>2</sub>]** ( $\phi = 0.028$ ).

Absorption plots for **[Re-TzPhTpy]** and **[Re-TzPyTpy]**, Figure 4.14, display a high energy band at ca. 280 nm. This peak is assigned to the intra-ligand  $\pi-\pi^*$  transition that would occur on the phenanthroline and terpyridine moieties. A peak also appears on the tail of this  $\pi-\pi^*$  band at 350-450 nm attributed to MLLCT transitions.

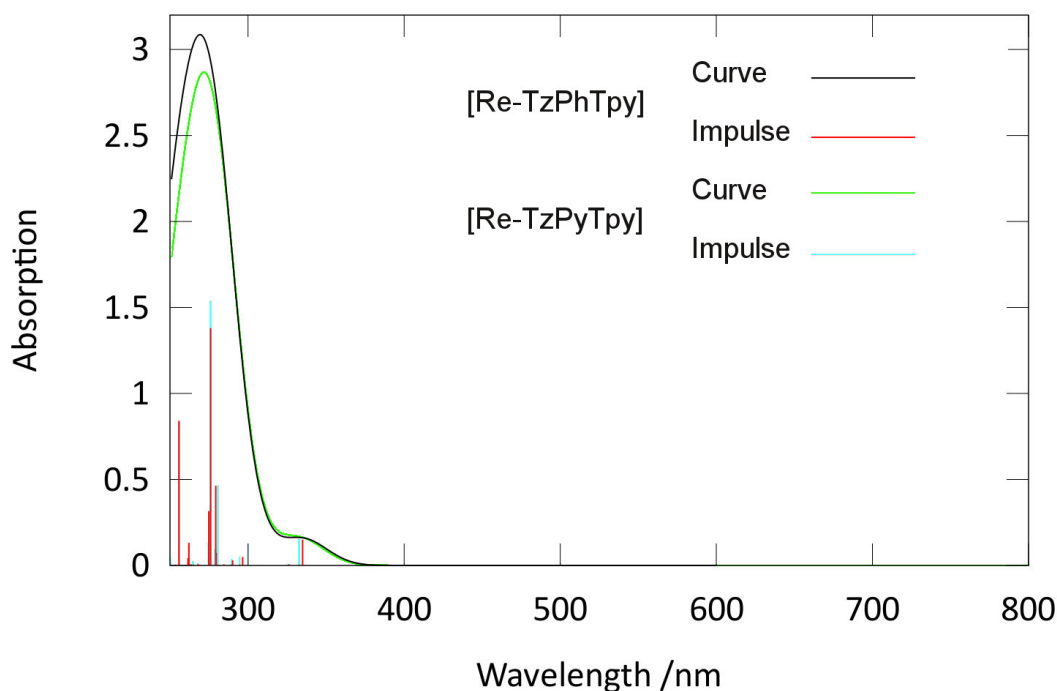
**[Re(MeTzPyCHO)Cl]** is assigned similarly, showing a  $\pi-\pi^*$  band at 288 nm and an MLLCT band appearing at 403 nm. The MLLCT transition for this compound is red-shifted by 40 nm in comparison to **[Re(<sup>t</sup>BuTzPy)Cl]**. In comparison to its analogous complex synthesised in Chapter 2, **[Re(<sup>t</sup>BuTzPy)Cl]**, the structural difference is the presence of an aldehyde group on the chelating ligand. The aldehyde increases the overall conjugation of the ligand and withdraws electron density from the pyridyl ring, thereby stabilising the LUMO.

The absorption spectrum of **[ReTzPyTpy]<sub>3</sub>** has a high energy band at ca. 280 nm and a shoulder on the tail of this  $\pi-\pi^*$  transition appears at ca. 325 nm.

This lower energy peak is tentatively assigned to a mixing of the intra-ligand  $\pi$ - $\pi^*$  transition that would occur on the terpyridine ligand and and MLLCT transitions. The convolution of the MLLCT with the  $\pi$ - $\pi^*$  transition is suggestive that the MLLCT is of higher energy than those of the other complexes. This is an analogous result to that seen for  $[\text{ReTzPy}]_3$



**Figure 4.14:** Absorption spectra of dilute  $10^{-5}\text{M}$  DCM solutions of labelled species.

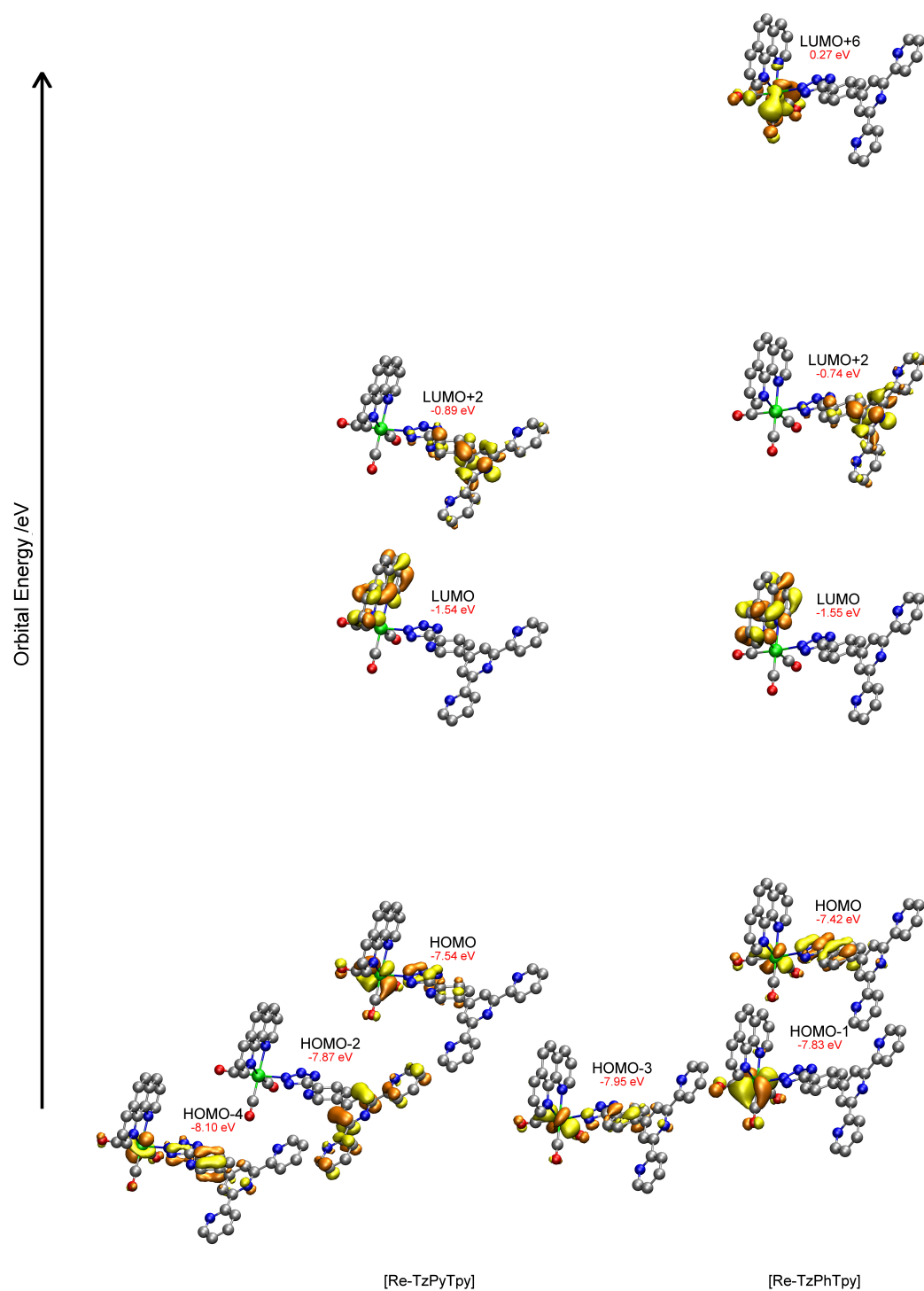


**Figure 4.15:** Simulated absorption spectra for **[Re-TzPhTpy]** and **[Re-TzPyTpy]**. Limited to the 250 nm to 800 nm range. Impulses correspond to transitions listed in Table 4.2.

**Table 4.2:** Simulated transitions with relatively large oscillator strength for **[Re-TzPhTpy]** and **[Re-TzPyTpy]**.

Species	Wavelength	Intensity	Levels	Character	Assignment	
<b>[Re-TzPhTpy]</b>	335.00	0.15	HOMO → LUMO HOMO-3 → LUMO	69 % 27 %	MLLCT(Re → phen) MLLCT(Re → phen)	
	276.03	1.38	HOMO → LUMO+2 HOMO-1 → LUMO+6 HOMO-3 → LUMO+2	38 % 21 % 14 %	MLLCT(Re → TzPhTpy) + IL(TzPhTpy) MLLCT(Re → (CO)) MLLCT(Re → TzPhTpy) + IL(TzPhTpy)	
	<b>[Re-TzPyTpy]</b>	332.70	0.15	HOMO → LUMO	81 %	MLLCT(Re → phen)
		280.54	0.46	HOMO-2 → LUMO+2	80 %	IL(TzPyTpy)
275.98		1.54	HOMO → LUMO+2 HOMO-4 → LUMO+2	31 % 23 %	MLLCT(Re → TzPyTpy) + IL(TzPyTpy) MLLCT(Re → TzPyTpy) + IL(TzPyTpy)	

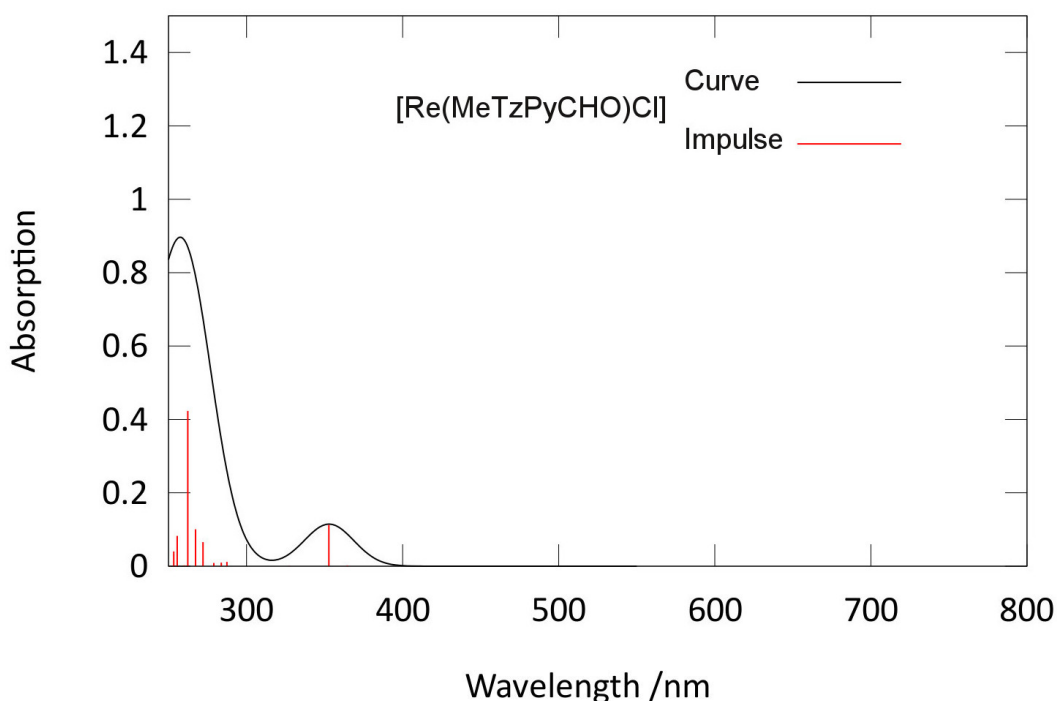
Figure 4.15 overlays the simulated absorption spectra for **[Re-TzPhTpy]** and **[Re-TzPyTpy]**. The impulses show the relative oscillator strength of the electronic transitions and their wavelength. Comparing these simulated spectra to the experimental absorption spectra (Figure 4.14) shows agreement with the shape and peak positions. Table 4.2 describes each of the impulses seen in Figure 4.15 giving details for each of the transitions, the orbitals involved, and the percentage character. Contours of each of the orbitals involved in the transitions are also shown in Figure 4.16.



**Figure 4.16:** Simulated orbitals for [Re-TzPyTpy] and [Re-TzPhTpy] corresponding to transitions listed in Table 4.2. Orbitals are spaced vertically relative to their energy and the HOMO-LUMO spacing has been reduced for clarity.

For both  $[\text{Re-TzPhTpy}]$  and  $[\text{Re-TzPyTpy}]$ , the lowest energy band at 335 nm involves the transition from the HOMO to the LUMO. From Figure 4.16 it can be seen that the HOMO is localised on the metal centre and on the tetrazole. The LUMO is shown to be localised on the phenanthroline ligand. This transition is characterised as a MLLCT. This is in concordance with previous investigations into rhenium tetrazolato complexes.<sup>1,2</sup> The higher energy band is the result of a mixture of an MLLCT from Re(I) to  $\text{TzPhTpy}/\text{TzPyTpy}$  and an IL ( $\pi - \pi^*$ ) localised on the terpyridine moiety.

For  $[\text{Re}(\text{TzPyCHO})\text{Cl}]$ , the simulated absorption spectrum can be found in Figure 4.17 and Table 4.3 contains calculated transition data.

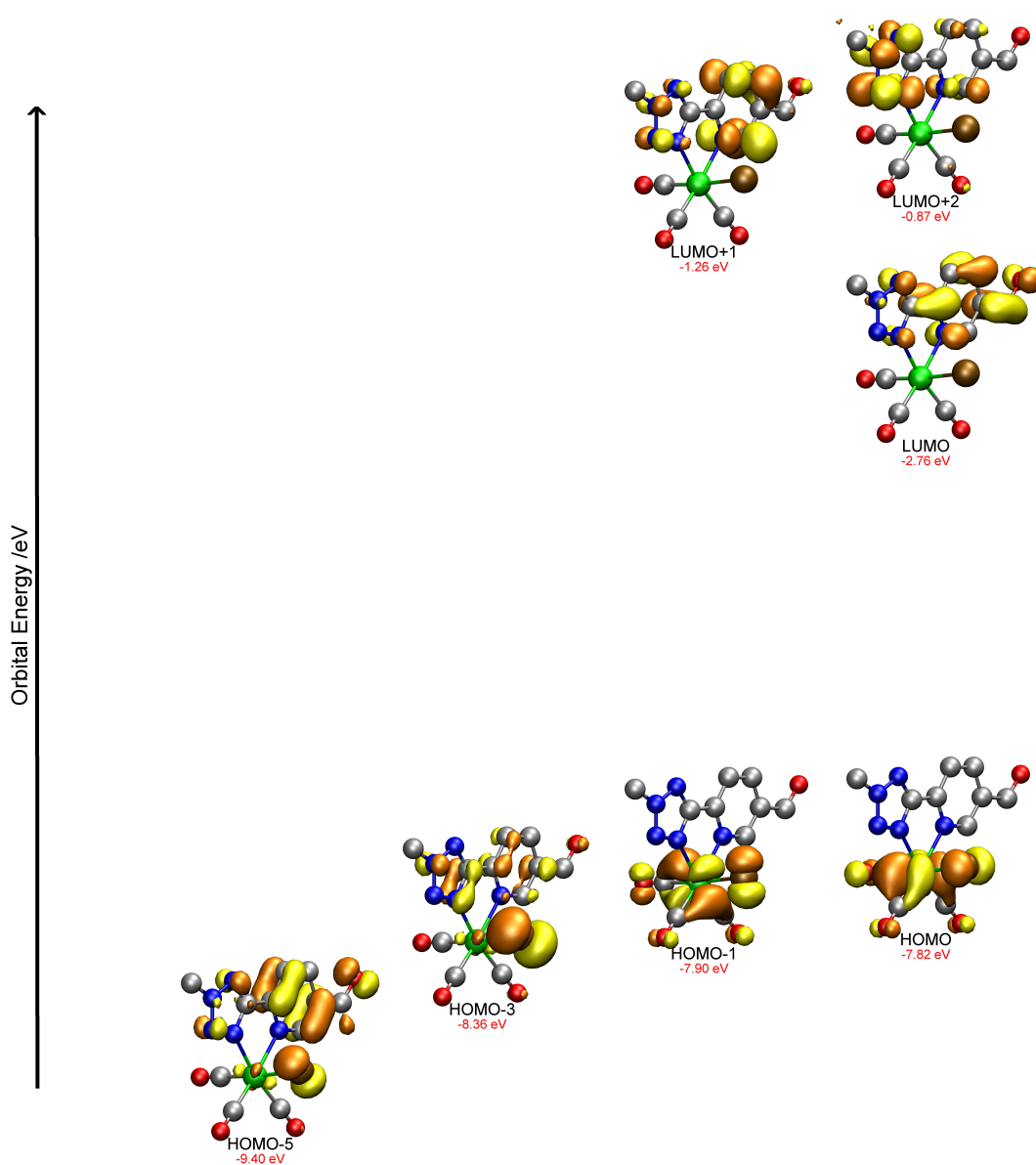


**Figure 4.17:** Simulated absorption spectrum of  $[\text{Re}(\text{MeTzPyCHO})\text{Cl}]$ . Limited to the 250 nm to 800 nm range. Impulses correspond to transitions listed in Table 4.3.

**Table 4.3:** Simulated transitions with relatively large oscillator strength for  $[\text{Re}(\text{TzPyCHO})\text{Cl}]$ .

Species	Wavelength	Intensity	Levels	Character	Assignment
$[\text{Re}(\text{MeTzPyCHO})\text{Cl}]$	352.77	0.113	HOMO-1 $\rightarrow$ LUMO	91 %	MLLCT (Re $\rightarrow$ $\text{TzPyCHO}$ )
	262.38	0.423	HOMO-3 $\rightarrow$ LUMO	27 %	MLLCT(Re $\rightarrow$ $\text{TzPyCHO}$ ) + IL( $\text{TzPyCHO}$ )
			HOMO $\rightarrow$ LUMO+1	24 %	MLLCT(Re $\rightarrow$ $\text{TzPyCHO}$ )
			HOMO-5 $\rightarrow$ LUMO	19 %	MLLCT(Re $\rightarrow$ $\text{TzPyCHO}$ ) + IL( $\text{TzPyCHO}$ )

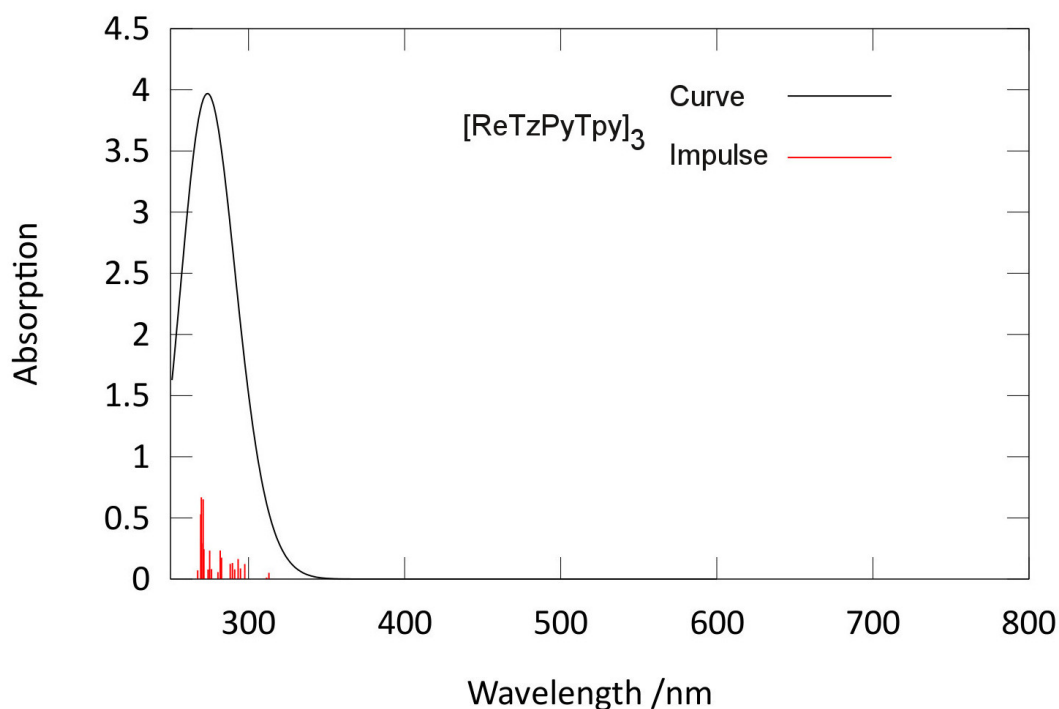
Figure 4.17 agrees with the experimentally obtained absorption spectrum (Figure 4.14) and displays two prominent bands, the first at 353 nm corresponds to a single impulse, and the second at 260 nm corresponds to the mixture of several



**Figure 4.18:** Simulated Orbitals for  $[\text{Re}(\text{MeTzPyCHO})\text{Cl}]$  corresponding to transitions listed in Table 4.3. Orbitals are spaced vertically relative to their energy and the HOMO-LUMO spacing has been reduced for clarity.

impulses. Comparison of the data in Table 4.3 to the orbitals seen in Figure 4.18 indicates the lowest energy transition at 353 nm is an MLLCT transition and the high energy band is a mixture of  $\pi$ - $\pi^*$  and MLLCT transitions. The 353 nm band highlights the relatively low energy of this transition in comparison to  $[\text{Re}(\text{tBuTzPy})\text{Cl}]$ , and relative orbital energies shown in Figure 4.18 imply that this is primarily a result of the stabilisation of the LUMO.





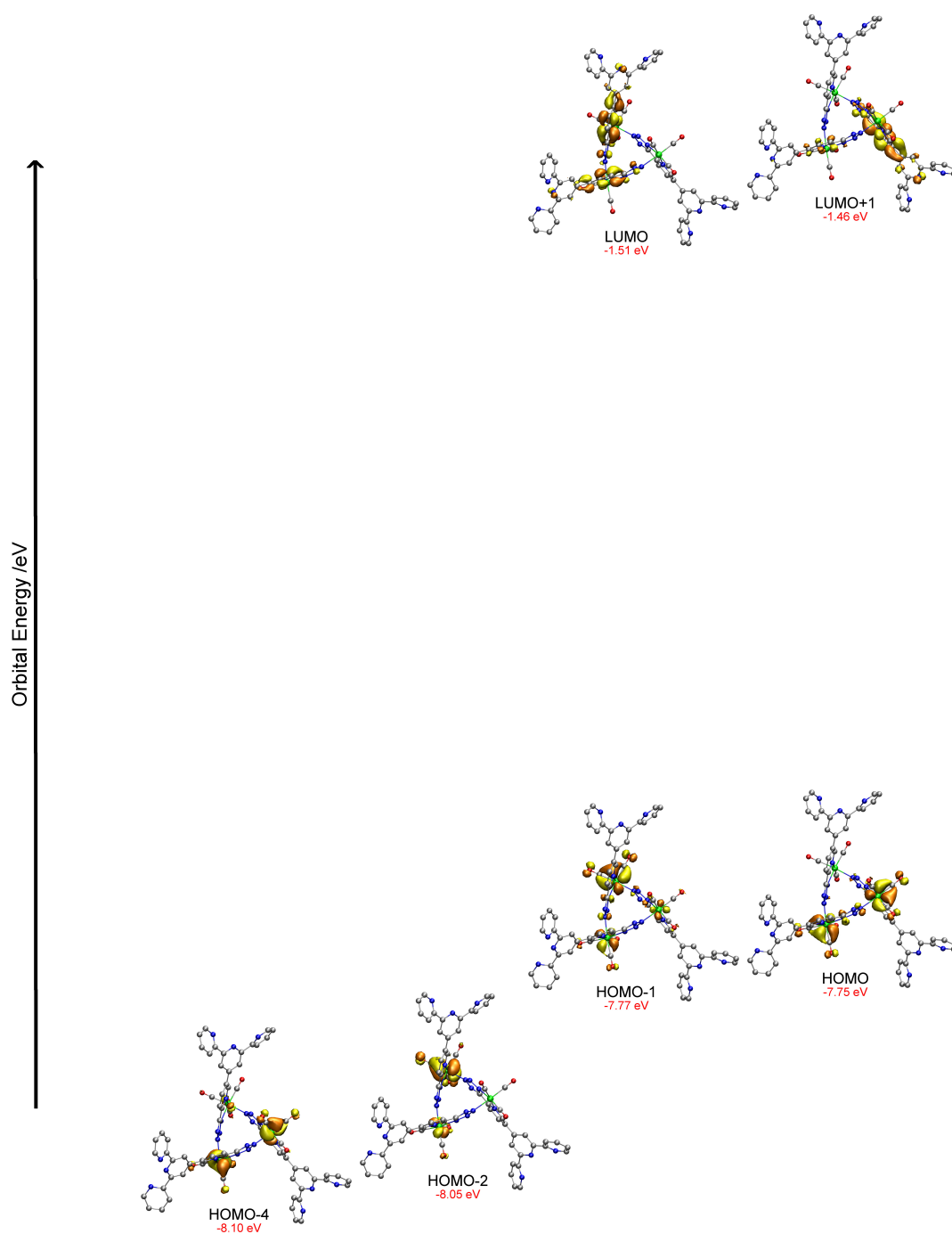
**Figure 4.19:** Simulated absorption spectrum for  $[\text{ReTzPyTpy}]_3$ . Limited to the 250 nm to 800 nm range. Impulses correspond to transitions listed in Table 4.3.

**Table 4.4:** Simulated transitions with relatively large oscillator strength for  $[\text{Re}(\text{TzPyTpy})]_3$ .

Species	Wavelength	Intensity	Levels	Character	Assignment
$[\text{Re}(\text{TzPyTpy})]_3$	313.08	0.05	HOMO-1 $\rightarrow$ LUMO	44 %	MLLCT <sup>a</sup>
	297.58	0.124	HOMO-2 $\rightarrow$ LUMO	31 %	MLLCT <sup>a</sup>
	293.33	0.164	HOMO-4 $\rightarrow$ LUMO+1	25 %	MLLCT <sup>a</sup>
	291.15	0.079	HOMO-6 $\rightarrow$ LUMO	28 %	MLLCT <sup>a</sup>
	288.29	0.125	HOMO-9 $\rightarrow$ LUMO+1	37 %	IL <sup>a</sup>
	282.70	0.176	HOMO $\rightarrow$ LUMO+12	26 %	MLLCT <sup>a</sup>
	280.42	0.057	HOMO-1 $\rightarrow$ LUMO+14	27 %	MLLCT <sup>a</sup>
	269.90	0.293	HOMO-7 $\rightarrow$ LUMO+1	28 %	IL <sup>a</sup>
	269.36	0.529	HOMO-10 $\rightarrow$ LUMO	22 %	MLLCT <sup>a</sup>
	269.34	0.442	HOMO-8 $\rightarrow$ LUMO	28 %	IL <sup>a</sup>

<sup>a</sup>Assignments for  $[\text{ReTzPyTpy}]_3$  are labelled as generic MLLCT and IL, as orbitals are dispersed across multiple metal centres and  $\text{TzPyTpy}^-$  ligands.

For  $[\text{ReTzPyTpy}]_3$ , the simulated absorption spectrum can be found in Figure 4.19 and Table 4.4 contains calculated transition data. Figure 4.19 shows a series of impulses that convolute to give what appears to be a broad absorption band, which displays agreement with the experimental absorption spectrum (Figure 4.14). The simulated absorption spectrum indicates that the absorption band is a mixture of many different MLLCT and IL transitions, which involve the



**Figure 4.20:** Simulated orbitals for  $[\text{ReTzPyTpy}]_3$  corresponding to lower energy ( $\geq 293$  nm) transitions listed in Table 4.4. Orbitals are spaced vertically relative to their energy and the HOMO-LUMO spacing has been reduced for clarity.

three Re(I) centres and three tetrazolato ligands. For the lower energy transitions ( $\lambda \geq 293$  nm) the contours of the orbitals involved are illustrated in Figure 4.20. These frontier orbitals for  $[\text{ReTzPyTpy}]_3$  are shown to have a larger gap than for  $[\text{Re-TzPhTpy}]$  and  $[\text{Re-TzPyTpy}]$ , this is in agreement with the blue-

shifted MLLCT transition. In comparison to the orbital energies of  $[\text{ReTzPy}]_3$ ,  $[\text{ReTzPyTpy}]_3$  exhibits a stabilisation of the HOMO and LUMO levels, with the extended conjugation of the ligand lowering the LUMO energy to a relatively greater extent. This reduced energy gap is consistent with the red-shifted MLLCT transition of  $[\text{ReTzPyTpy}]_3$  compared to  $[\text{ReTzPy}]_3$ .

The emission spectra of  $[\text{Re-TzPhTpy}]$  and  $[\text{Re-TzPyTpy}]$ , shown in Figure 4.21a, demonstrate similar emission bands centred at 585 nm. The emission bands are broad and structureless, indicating that the transition is primarily MLLCT in character. The increase in emission lifetime and quantum yield going from air-equilibrated to degassed conditions (Table 4.1) suggests phosphorescent emission. The identical properties of  $[\text{Re-TzPhTpy}]$  and  $[\text{Re-TzPyTpy}]$  is in agreement with the calculations. This indicates that changing between a phenyl and pyridyl group in the ligand has no significant effect on the HOMO, and hence the MLLCT transitions are the same.

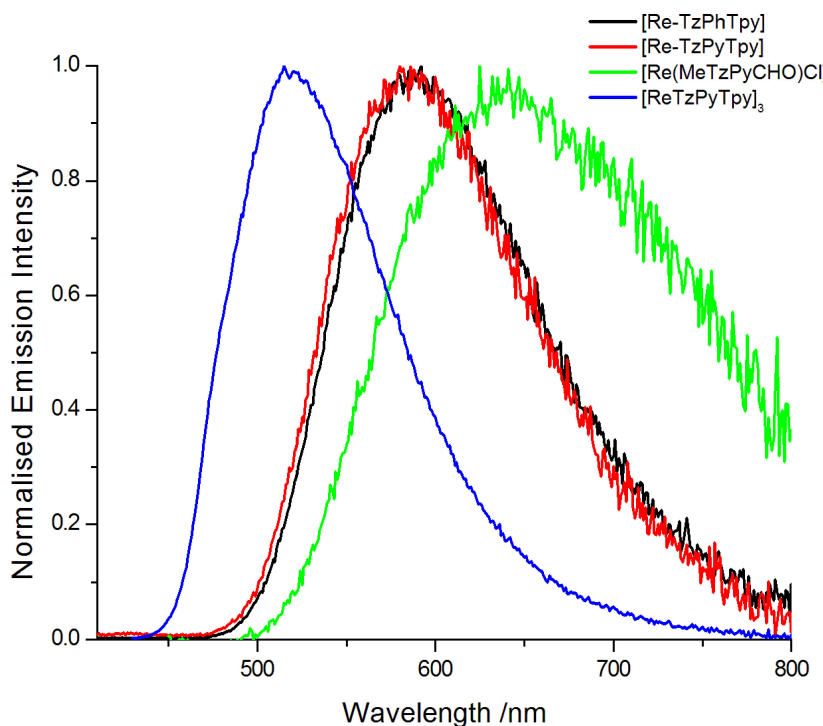
The emission spectrum of  $[\text{Re}(\text{MeTzPyCHO})\text{Cl}]$  displays a broad and structureless band centred at 645 nm, consistent with a MLLCT transition. This MLLCT is red-shifted by ca. 50 nm in comparison to  $[\text{Re}(\text{tBuTzPy})\text{Cl}]$ . The lifetime of this complex is 92 ns in degassed solution and the quantum yield of the emission is very low. The short lifetime and low quantum yield for this red-shifted emitting complex are consistent with the energy gap law.

The emission spectrum of  $[\text{ReTzPyTpy}]_3$  displays a structureless MLLCT band centred at 518 nm, with a quantum yield and lifetime of 0.216 and 2430 ns, respectively. The decay constants are shown in Table 4.5 and illustrate that in comparison to that of  $[\text{ReTzPy}]_3$ , the non-radiative decay has reduced by a factor of ca. 10 and the emission has red-shifted by 20 nm. The reduction in non-radiative decay could suggest that the emissive state of  $[\text{ReTzPy}]_3$  may be affected by thermally accessible quenching states, possibly of MC nature.<sup>270,271</sup>

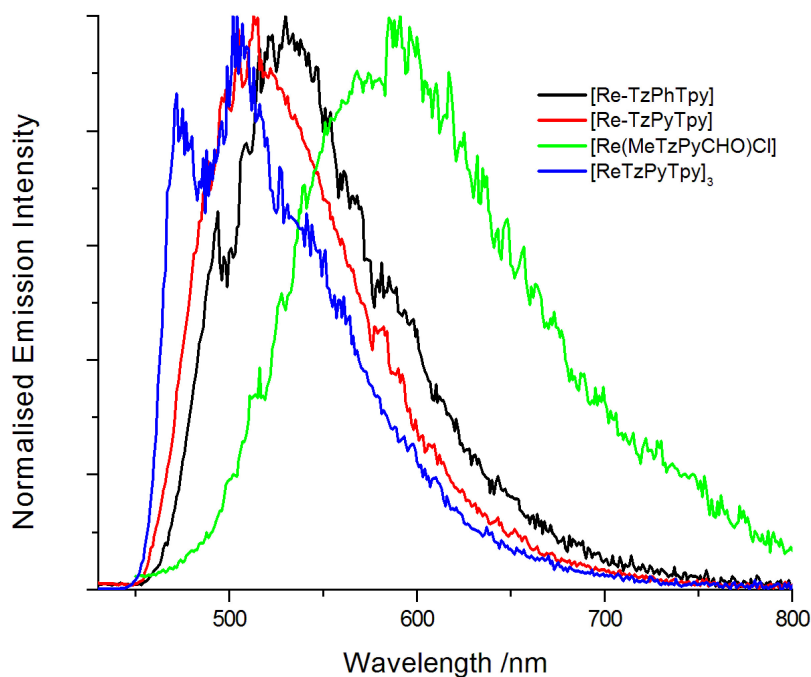
**Table 4.5:** Decay constants of the emission for complexes in degassed DCM solutions.

Complex	$k_r/10^5[\text{s}^{-1}]$	$k_{nr}/10^5[\text{s}^{-1}]$
$[\text{ReTzPyTpy}]_3$	0.89	3.23
$[\text{ReTzPy}]_3$	2.45	38.5

All complexes display a blue-shifted emission at 77 K, a behaviour that is ascribed to rigidochromism. The emission profiles of  $[\text{Re-TzPhTpy}]$  and  $[\text{Re-TzPyTpy}]$  remain broad and structureless, and the decay lifetime values increase to 4.99 and 3.97  $\mu\text{s}$ , respectively. This is consistent with the ascribed MLLCT nature of the transition involved and the broadness implies that there is minimal mixing of IL character with the charge transfer transition. The emission



(a)



(b)

**Figure 4.21:** Emission spectra of dilute ( $10^{-5}$  M) DCM solution excited at 375 nm. a) r.t. solutions. b) 77 K frozen solutions.

of  $[\text{Re}(\text{MeTzPyCHO})\text{Cl}]$  also remains broad and structureless, and the decay lifetime becomes biexponential and increases with components of  $0.48 \mu\text{s}$  (88 %) and  $0.12 \mu\text{s}$  (12%). On the other hand, the emission of  $[\text{ReTzPyTpy}]_3$  at 77

K has become structured, indicating some involvement of IL transitions. The emission lifetime has elongated and become biexponential with components of 34.37  $\mu\text{s}$  (59 %) and 0.92  $\mu\text{s}$  (41 %).

## 4.4 Electrochemical properties of the synthesised complexes

A summary of the electrochemical properties of the complexes, obtained in C6mim[FAP], are shown in Table 4.6 and voltammograms displaying oxidation and reduction regions are shown in Figure 4.22.

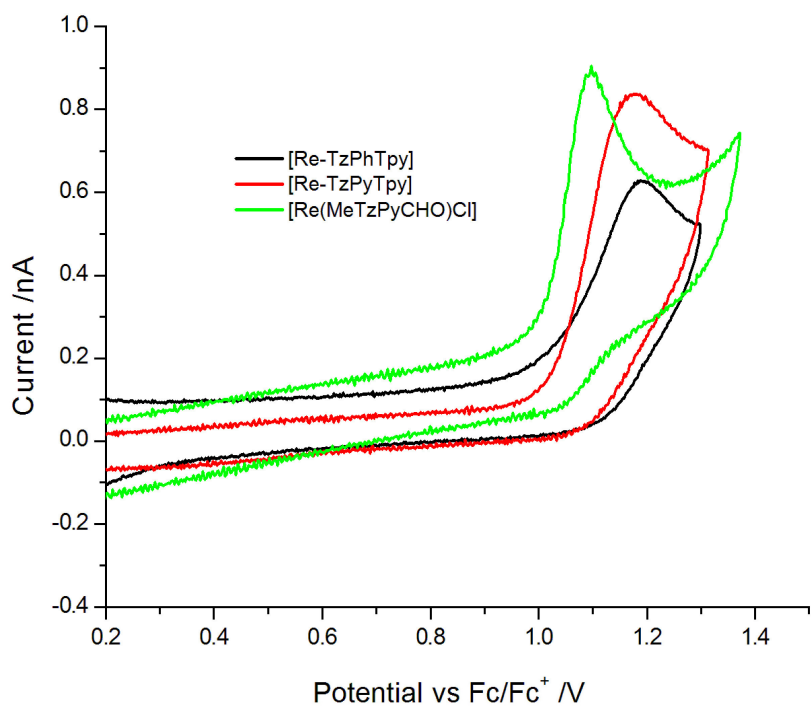
**Table 4.6:** Summary of electrochemical data for ca. 10 mmol/L solutions of complexes in C6mim[FAP]. Potentials are relative to ferrocene/ferrocinium<sup>+</sup> couple.

Complex	Oxidation		Reduction	
	$E_p$ vs Fc/Fc <sup>+</sup> (V)	$\Delta E_{pp}$ (mV)	$E_p$ vs Fc/Fc <sup>+</sup> (V)	$\Delta E_{pp}$ (mV)
[Re-TzPhTpy]	1.19	<sup>a</sup>	-1.60	70
[Re-TzPyTpy]	1.18	<sup>a</sup>	-1.60	72
[Re(MeTzPyCHO)Cl]	1.10	<sup>a</sup>	-0.88	<sup>a</sup>

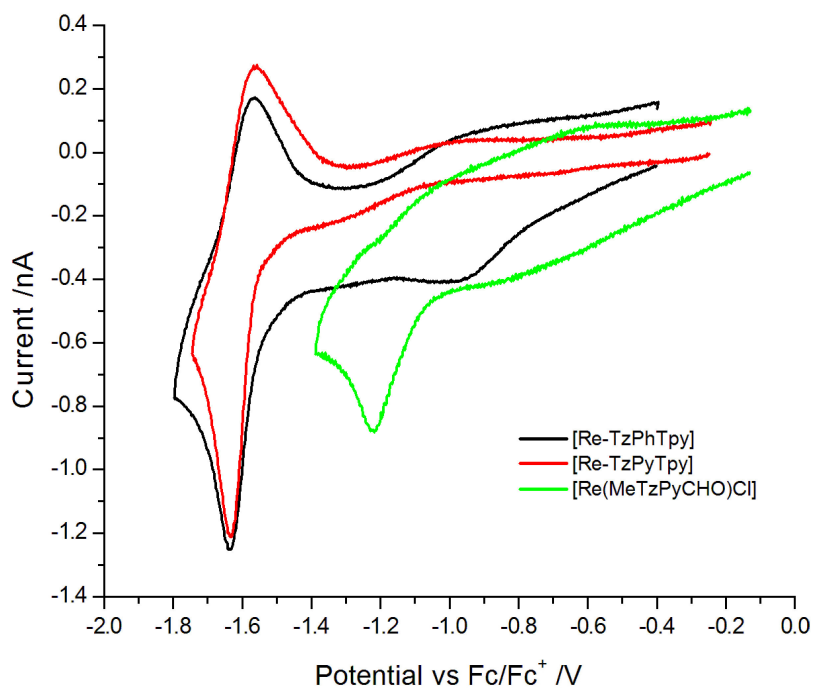
<sup>a</sup>Could not be obtained due to irreversible nature.

The oxidation peaks for [Re-TzPhTpy] and [Re-TzPyTpy] are at 1.04 and 1.03 V, respectively, and have no reversible character. From investigations involving other mononuclear *fac*-[Re(CO)<sub>3</sub>(phen)L] complexes,<sup>249</sup> this peak is attributed to oxidation occurring on the Re(I) centre as Re(I) → Re(II) + e<sup>-</sup>. The lack of reversibility indicates that any follow-up chemistry occurring to these complexes is relatively fast on the electrochemical timescale of 100 mVs<sup>-1</sup>. The reduction peaks for [Re-TzPhTpy] and [Re-TzPyTpy] are at -1.61 and -1.60 V, respectively, and display reversible character. This is assigned to a reduction of the diimine ligand, and the reversible character indicates that follow-up chemistry after reduction is slow on the electrochemical timescale of 100 mVs<sup>-1</sup>. The peak-to-peak separation of 110 mV is in line with a moderately fast electrochemical step in comparison to that of ferrocene of 90 mV, which has very fast kinetics. The similarities of [Re-TzPhTpy] and [Re-TzPyTpy] demonstrate that there is very little difference in the complexes when changing the ancillary ligand between TzPhTpy<sup>-</sup> and TzPyTpy<sup>-</sup>. The negligible difference in electrochemical behaviour of [Re-TzPhTpy] and [Re-TzPyTpy] is well reflected in the photophysical and computational investigations.

[Re(MeTzPyCHO)Cl] displays an oxidation peak at 1.10 V and reduction at -0.88 V, both of which are irreversible. This indicates that the follow-up chem-



(a)



(b)

**Figure 4.22:** Voltammograms of ca.  $10^{-3}$  M solutions of complexes in C6mim[FAP] with potentials reported relative to Fc/Fc<sup>+</sup> couple. a) Oxidation region of voltammogram. b) Reduction region of voltammogram.

istry of the oxidised/reduced compound is relatively fast on the electrochemical timescale. The reduction peak appears relatively lower than that seen for  $[\text{Re}(\text{}^t\text{BuTzPy})\text{Cl}]$ , suggestive that the LUMO is lower in energy. This is in agreement with the conclusions drawn from the computationally derived orbital energies and the red-shift in the MLLCT transition.

Attempts to obtain voltammograms of  $[\text{ReTzPyTpy}]_3$  were not successful, as it was not sufficiently soluble in ionic liquids and voltammograms in common polar solvents did not give reproducible results, attributed to fouling at the surface of the electrode.

## 4.5 Conclusion

In this chapter, the successful syntheses of  $[\text{Re-TzPhTpy}]$ ,  $[\text{Re-TzPyTpy}]$ ,  $[\text{ReTzPyTpy}]_3$ , and  $[\text{Re}(\text{MeTzPyCHO})\text{Cl}]$  were reported.  $[\text{Re-TzPhTpy}]$  and  $[\text{Re-TzPyTpy}]$  demonstrate the use of tetrazole functionalised terpyridines as ancillary ligands, similar to previous literature reports of Re(I) tetrazolato complexes.<sup>1</sup> The successful synthesis of  $[\text{ReTzPyTpy}]_3$  illustrates that the triangular metallacalix[3]arene structure is conserved when changing the ligand from HTzPy to HTzPyTpy.  $[\text{Re}(\text{MeTzPyTpy})\text{Cl}]$  could not be synthesised in this investigation.

The photophysical and electrochemical properties of the mononuclear complexes,  $[\text{Re-TzPhTpy}]$  and  $[\text{Re-TzPyTpy}]$ , were similar to previously reported Re(I) tetraolato complexes.<sup>1,2</sup>  $[\text{ReTzPyTpy}]_3$  displayed properties similar to that of  $[\text{ReTzPy}]_3$  in terms of emission wavelength, however, there has been a significant increase in quantum yield (0.06 to 0.22) and lifetime (244 ns to 2430 ns) of the <sup>3</sup>MLCT emission.

The next stage in the investigation is to employ the synthesised complexes and ligands as sensitisers for lanthanides, to determine if they can be utilised for such an application.





# Chapter 5

## Sensitisation of red-emitting Eu<sup>3+</sup> and NIR-emitting Yb<sup>3+</sup>

### 5.1 Introduction

#### 5.1.1 f-block metals

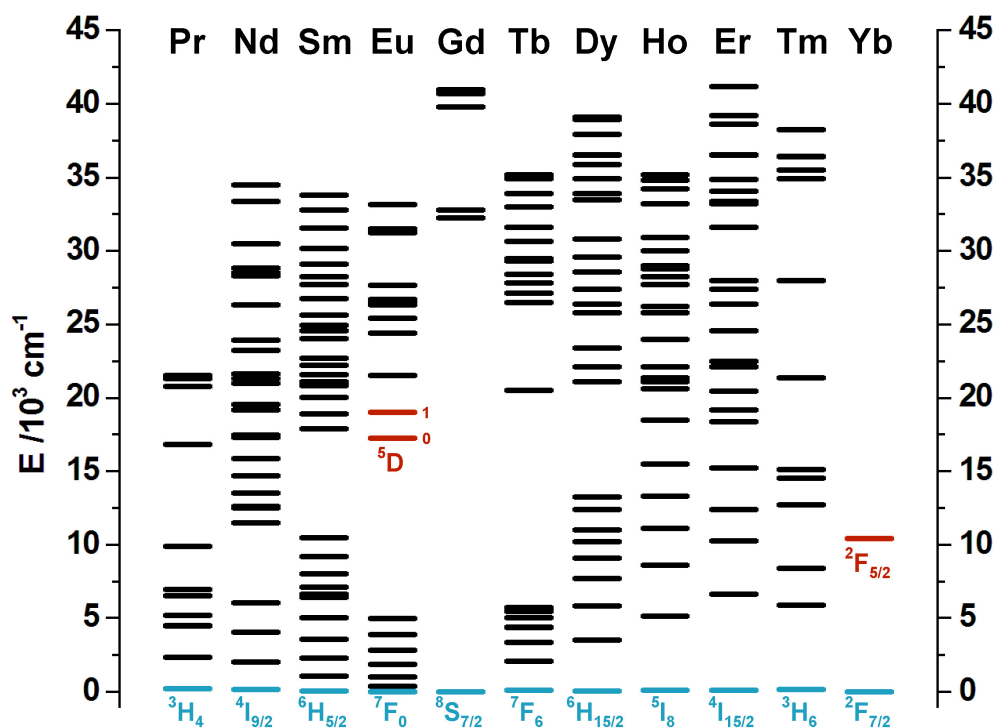
Since the discovery of the optical properties of lanthanides (Ln) in the 1800s,<sup>272</sup> the investigations into their luminescent properties quickly became a vast and intricate field of research.<sup>273</sup> Such investigations led to the discovery that the trivalent lanthanide ions are luminescent, except La<sup>3+</sup> and Lu<sup>3+</sup>, and each of them has a characteristic line-like spectrum that is largely independent of the surrounding ligand environment. The knowledge gained about the spectroscopic and chemical nature of the Ln<sup>3+</sup> cations has resulted in applications in the fields of light emitting devices, lasers, optical glasses, and biological probes.<sup>123,272,274–277</sup>

#### 5.1.2 Photophysical properties and spectra of trivalent lanthanide ions

The 4f-orbitals of Ln<sup>3+</sup> ions are considered "inner-core" as they are well shielded from external interactions by the 5s<sup>2</sup>5p<sup>6</sup> electrons.<sup>80</sup> The electrons in the 4f<sup>*n*</sup> shell are those involved in the electronic transitions of Ln<sup>3+</sup> ions, and this shielding causes the emission spectra of the lanthanide ions to remain consistent in different coordination environments.

Lanthanides can also potentially undergo 4f-5d transitions and ligand to metal charge transfer (LMCT) transitions, which are affected by changes in the ligand field.<sup>80</sup> In this chapter only the 4f-4f transitions are of significance and will be discussed primarily.

A free Ln<sup>3+</sup> ion can be described spectroscopically according to the number and



**Figure 5.1:** Energy level diagram for  $\text{Ln}^{3+}$  aqueous ions, data taken from Carnall *et al.*<sup>278–281</sup>

arrangement of electrons in the 4f-orbitals. The terms that describe the various configurations of electrons within these orbitals, known as the spectroscopic terms, are given as  $^{2S+1}\Gamma_J$ .  $S$  represents the total spin number,  $\Gamma$  represents the combined orbital angular momenta number which takes on a character (S, P, D, F, ...) corresponding to the value of  $L$ .  $J$  represents the total angular momentum number ranging from  $|L + S|$ ,  $|L + S - 1|$ , down to  $|L - S|$ . The ground term for a lanthanide is determined by Hund's rules:

1. Highest multiplicity ( $2S + 1$ )
2. For the terms with highest multiplicity, the largest orbital angular momentum ( $\Gamma$ )
3. For an electronic sub-shell less than half filled
  - (a) The total angular momentum ( $J$ ) is taken as  $J = J_{\min} = |L - S|$
4. For an electronic sub-shell more than half filled
  - (a) The total angular momentum ( $J$ ) is taken as  $J = J_{\max} = |L + S|$

In Figure 5.1, the ground terms are given for each of the lanthanides and the excited states of interest for  $\text{Eu}^{3+}$  and  $\text{Yb}^{3+}$  are highlighted in red. Each of

these terms can further be split into a maximum of  $2J+1$  states by the effective ligand/electrostatic field.<sup>272</sup> This splitting is known as the Stark effect and is not illustrated in Figure 5.1.

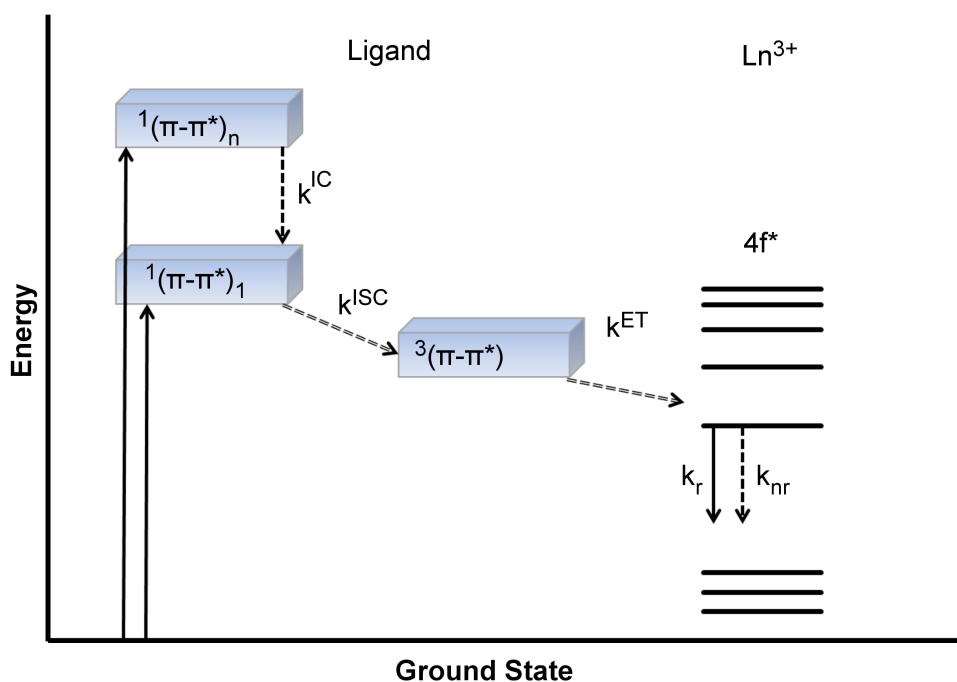
The 4f-4f transitions occur between states of the same parity, and are considered to be forbidden as described by *Laporte's* selection rule. This selection rule can be relaxed under the influence of the ligand-field, perturbing the system from a centrosymmetric environment. Further to *Laporte's* selection rule, the spin selection rule forbids some lanthanide transitions when they result in a change in spin multiplicity, i.e. the  $^5D_0 \rightarrow ^7F_J$  transition of  $\text{Eu}^{3+}$ . This selection rule is somewhat relaxed by the heavy atom effect, originating from the  $\text{Ln}^{3+}$  cation itself. Importantly for these lanthanides, these selection rules mean that direct excitation of the lanthanides is highly inefficient (e.g.  $\epsilon$  values  $\leq 10 \text{ M}^{-1}\text{cm}^{-1}$  with very few exceptions).<sup>272</sup> Therefore a different approach to obtaining emissive lanthanides is needed.

### 5.1.3 Sensitisation of lanthanides

To circumvent the forbidden nature of direct lanthanide excitations, energy transfer mechanisms from appropriate ligands have been utilised.<sup>173,272,276,282</sup> The energy transfer to lanthanides from ligated chromophores is known as the "antenna effect", and a simple illustration of this effect is shown in the Jablonski diagram in Figure 5.2.

In Figure 5.2, a typical case is presented where an organic chelator with  $\pi - \pi^*$  transitions is utilised to undergo energy transfer to the lanthanide. In this mechanism, the ligand absorbs incident photons and is excited to the manifold of singlet excited states  $^1(\pi - \pi^*)_1 \dots ^1(\pi - \pi^*)_n$ . The ligand will quickly relax to the lowest excited state via internal conversion, according to Kasha's rule.<sup>71</sup> The presence of the lanthanide ion increases the rate of inter-system crossing (ISC) and the ligand relaxes to the triplet excited state,  $^3(\pi - \pi^*)$ . From this state, energy transfer occurs to the lanthanide, which then decays to the ground state via emission of the characteristic spectrum and non-radiative deactivation. This is the generally accepted mechanism for lanthanide sensitisation, however the singlet excited state can also undergo energy transfer to the lanthanide ion.<sup>72,272,283</sup> The energy transfer mechanism can be Förster (dipole-dipole)<sup>131</sup> or Dexter (electron-exchange).<sup>131,272</sup>

As can be seen in Figure 5.2, the energy level of the sensitising state,  $^3(\pi - \pi^*)$ , must be higher than the accepting state of the  $\text{Ln}^{3+}$  cation. Importantly, research into the cases of  $\text{Eu}^{3+}$  and  $\text{Tb}^{3+}$  has shown that the optimum energy gap between the donating and accepting excited states is 2,500 to 3,000  $\text{cm}^{-1}$ .<sup>133,140</sup> This is due



**Figure 5.2:** Generalised sensitisation pathways for lanthanides via the antenna effect.

to the competition of two pathways, the rate of energy transfer to the lanthanide and the rate of back transfer to the  $^3(\pi - \pi^*)$ . Hence, the sensitising state must be sufficiently far to reduce the rate of back transfer, but be sufficiently close to enable fast forward energy transfer.

High energy vibrations are a potential problem for lanthanide luminescence, as multi-phonon deactivation by NH and OH for visible emitters, and also CH for near infra-red (NIR) emitters, can lead to a reduction of the quantum yield. Therefore, coordinated molecules such as a sensitizer or solvent that place such groups in close proximity to the lanthanide will enhance the non-radiative decay of the lanthanide.

The ratio of the number of photons absorbed by the chromophore to those emitted by the lanthanide is known as the overall quantum yield ( $\phi_{Ln}^L$ ) and is given by Equation 5.1 (under the assumption of a photophysical mechanism displayed in Figure 5.2, where emission originates solely from the lanthanide).

$$\phi_{Ln}^L = \frac{\text{photons emitted}}{\text{photons absorbed}} \quad (5.1)$$

The overall quantum yield ( $\phi_{Ln}^L$ ) relates to the intrinsic quantum yield of the lanthanide ( $\phi_{Ln}^{Ln}$ ) by Equation 5.2, where  $\eta_{sens}$  is the sensitisation efficiency of the

ligand.

$$\phi_{Ln}^L = \eta_{sens} \phi_{Ln}^{Ln} \quad (5.2)$$

The intrinsic quantum yield is obtained from the ratio of the experimentally observed lifetime ( $\tau_{obs}$ ) and the radiative lifetime ( $\tau_{rad}$ ), via Equation 5.3.

$$\phi_{Ln}^{Ln} = \frac{\tau_{obs}}{\tau_{rad}} \quad (5.3)$$

Judd-Ofelt theory enables the calculation of the radiative lifetime of a lanthanide in a given electronic field from the emission spectrum.<sup>272,284</sup> For  $\text{Eu}^{3+}$ , the  ${}^5D_0 \rightarrow {}^7F_1$  transition has pure magnetic dipole origin and allows a simple calculation of  $\tau_{rad}$  by Equation 5.4,

$$\frac{1}{\tau_{rad}} = A_{MD,0} \cdot n^3 \left( \frac{I_{tot}}{I_{MD}} \right) \quad (5.4)$$

where  $\tau_{rad}$  is the radiative lifetime,  $A_{MD,0}$  is a constant of  $14.65 \text{ s}^{-1}$ ,  $n$  is the refractive index of the solvent, and  $(I_{tot}/I_{MD})$  is the ratio of the total integrated emission spectrum from the  ${}^5D_0$  level to the  ${}^7F_J$  manifold ( $J = 0 - 6$ ) to the integrated intensity of the magnetic dipole transition  ${}^5D_0 \rightarrow {}^7F_1$ .

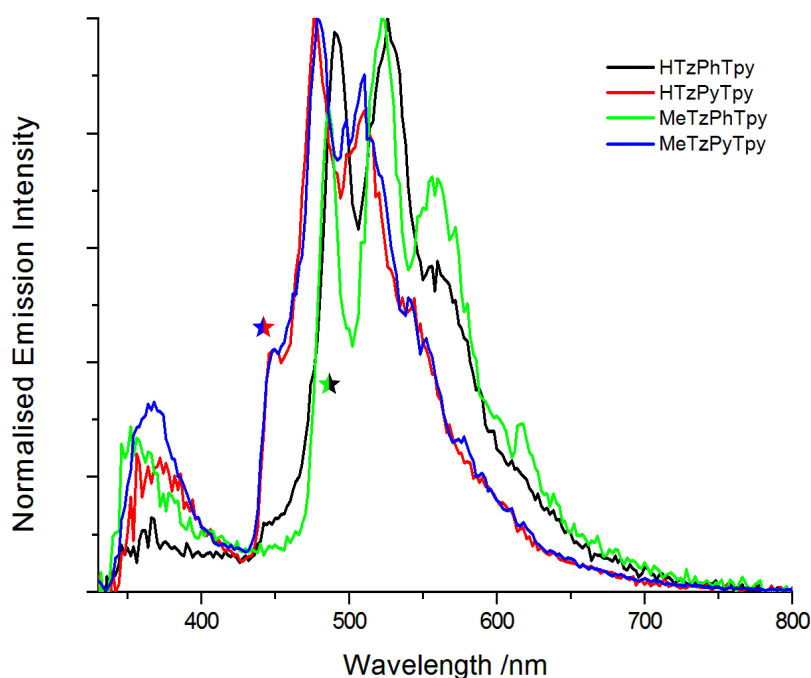
#### 5.1.4 Methodology for the assessment of $\text{Eu}^{3+}$ and $\text{Yb}^{3+}$ sensitisation.

Changes in the photophysical properties of the investigated  $\text{Re(I)}$  complexes will be firstly performed in the presence of  $\text{Gd}^{3+}$ , which will also be useful to estimate the energy of the triplet sensitising state. Then, the addition of  $\text{Eu}^{3+}$  or  $\text{Yb}^{3+}$  will allow observation of any occurring sensitisation. Optically dilute solutions of the complexes ( $A_{375} \leq 0.05$ ) and ligands ( $A_{310} \leq 0.05$ ) will be used with an excess of the chosen  $\text{Ln}^{3+}$  as DMSO solvated nitrate salts  $[\text{Ln}(\text{NO}_3)_3(\text{DMSO})_n]$ . The addition of excess  $\text{Ln}^{3+}$  is expected to result in occupation of all available chelating sites, as the addition of insufficient lanthanide will result in the presence of multiple species which would complicate the energy transfer study. This method was chosen to favour the formation of  $[\text{Ln}(\text{NO}_3)_3(\text{N}^{\wedge}\text{N}^{\wedge}\text{N})]$  where  $(\text{N}^{\wedge}\text{N}^{\wedge}\text{N})$  represents the chelating ligand.

## 5.2 Photophysical properties of ligands in the presence of $\text{Ln}^{3+}$

### 5.2.1 Emission from ligands in the presence of $\text{Gd}^{3+}$

The preliminary step in the investigation of the sensitisation of lanthanides is to determine the triplet energy level of the sensitising ligand. To enhance emission from the triplet state,  $\text{Gd}^{3+}$  is added. The excited state of  $\text{Gd}^{3+}$  ( ${}^6P_{7/2}$ ) is too high in energy ( $32,000 \text{ cm}^{-1}$ ) to be sensitised by the ligands, which will be prompted to emit from their  ${}^3(\pi - \pi^*)$  excited state.



**Figure 5.3:** Emission of dilute ( $10^{-5} \text{ M}$ ) acetonitrile solutions of ligands with excess  $\text{Gd}^{3+}$  frozen at 77 K, excited at 310 nm. Point of curves taken for  ${}^3(\pi - \pi^*)_1$  0-0 transition are denoted by a star.  $\text{CH}_3\text{CN}$  was utilised as the solvent due to poor solubility of compounds in ethers and alcohols.

Figure 5.3 illustrates the emission from the ligands in the presence of  $\text{Gd}^{3+}$  at 77 K in acetonitrile. In each case, an emission peak is observed at approximately 370 nm. However, the most intense emission occurs in the range 430 - 700 nm. The emission at 370 nm is attributed to residual fluorescence from the singlet excited state of the ligands. This is determined on comparison with the emission spectra at room temperature of the free ligands, shown in Chapter 2. The emission peak 430 - 700 nm is considered to be from the  ${}^3(\pi - \pi^*)$  state.

**Table 5.1:** Estimation of <sup>3</sup>( $\pi - \pi^*$ ) 0-0 energy of the ligands and energy gap to Eu<sup>3+</sup>(<sup>5</sup>D<sub>0</sub>) and Yb<sup>3+</sup>(<sup>2</sup>F<sub>5/2</sub>).

Ligand + Gd <sup>3+</sup>	$\lambda_{3(0-0)}$ [cm <sup>-1</sup> ]	$\Delta\lambda_{(3(0-0)-5D_0)}$ [cm <sup>-1</sup> ]	$\Delta\lambda_{(3(0-0)-2F_{5/2})}$ [cm <sup>-1</sup> ]
<b>HTzPhTpy</b>	21,052	3,552	10,652
<b>HTzPyTpy</b>	22,222	4,722	11,822
<b>MeTzPhTpy</b>	21,052	3,552	10,652
<b>MeTzPyTpy</b>	22,222	4,722	11,822

Table 5.1 displays the estimated energy of the <sup>3</sup>( $\pi - \pi^*$ ) state and a comparison of the <sup>3</sup>( $\pi - \pi^*$ ) 0-0 transition of the ligands to the lowest excited state of Eu<sup>3+</sup> and Yb<sup>3+</sup>. The 0-0 transition is taken for **HTzPhTpy** and **MeTzPhTpy** at 475 nm, and for **HTzPyTpy** and **MeTzPyTpy** at 448 nm. These values are higher than the required 17,500 cm<sup>-1</sup> for the <sup>7</sup>F<sub>0</sub> → <sup>5</sup>D<sub>0</sub> excitation of europium. The energy of the <sup>3</sup>( $\pi - \pi^*$ ) excited state is also much higher than the required 10,400 cm<sup>-1</sup> for the <sup>2</sup>F<sub>7/2</sub> → <sup>2</sup>F<sub>5/2</sub> excitation of ytterbium.

### 5.2.2 Sensitisation of Eu<sup>3+</sup> emission by the ligands.

**Table 5.2:** Summary of photophysical properties of dilute (10<sup>-5</sup> M) air-equilibrated acetonitrile solutions of ligands with Eu<sup>3+</sup>.

Ligand + Eu <sup>3+</sup>	Absorption	Emission, 298 K					
	$\lambda_{max}$ (10 <sup>4</sup> ε) [nm][M <sup>-1</sup> cm <sup>-1</sup> ]	$\lambda_{max}$ [nm]	$\tau_{obs}^a$ [ms]	$\phi_{Ln}^L$	$\tau_{rad}^b$ [ms]	$(\phi_{Ln}^{Ln})^c$	$\eta_{sens}^d$
<b>HTzPhTpy</b>	290(2.19)	580, 590, 618,	1.225	0.239	2.802	0.437	0.545
	327(0.99)	650, 690-720					
<b>HTzPyTpy</b>	290(3.21)	580, 590, 618,	1.194	0.208	2.749	0.434	0.478
	327(1.10)	650, 690-720					
<b>MeTzPhTpy</b>	280(3.45)	580, 590, 618,	1.087	0.249	2.747	0.396	0.630
	310(2.34)	650, 690-720					
<b>MeTzPyTpy</b>	280(2.80)	580, 590, 618,	1.263	0.214	2.806	0.450	0.476
	327(1.10)	650, 690-720					

<sup>a</sup>Lifetime measured at  $\lambda_{em} = 618$  nm. <sup>b</sup>Calculated according to Equation 5.4.

<sup>c</sup>Calculated according to Equation 5.3. <sup>d</sup>Calculated according to Equation 5.2.

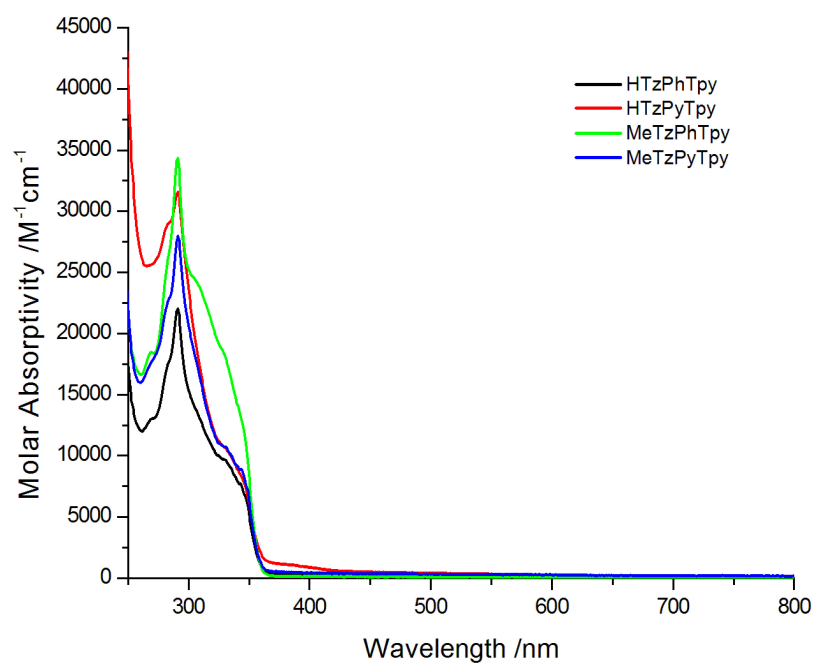
Quantum yield measured against an air-equilibrated aqueous solution of [Ru(**bpy**)<sub>3</sub>]Cl<sub>2</sub> ( $\phi = 0.028$ ).

From the absorption spectra in Figure 5.4, it can be seen that, after the addition of Eu<sup>3+</sup> or Yb<sup>3+</sup>, a new band at 320 nm appears. This lower energy transition is similar to that observed during acid addition to the free ligand, and is suggestive that the terpyridine moiety has chelated the Ln<sup>3+</sup> ion. This causes the ring system to become coplanar, giving access to red-shifted  $\pi - \pi^*$  transitions.

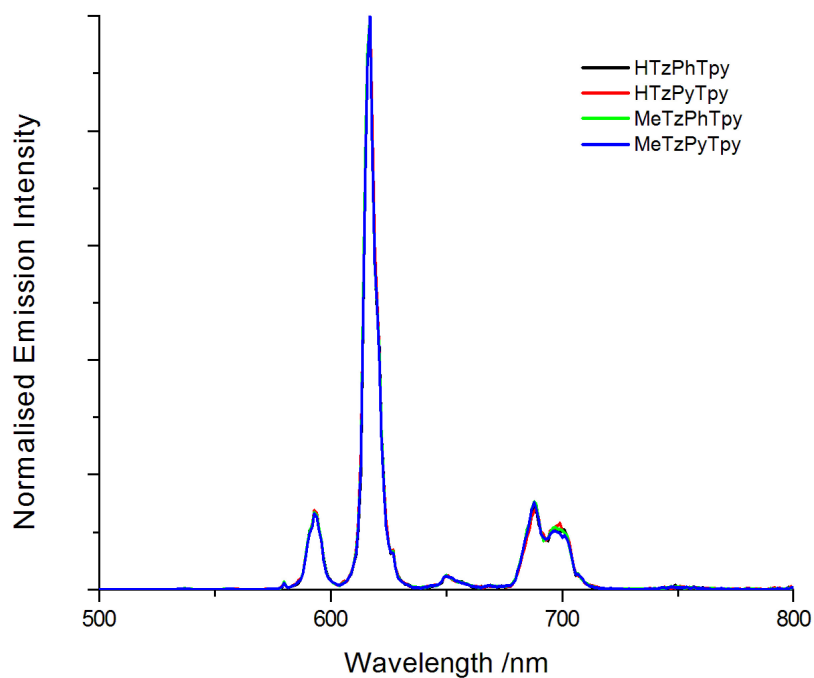
The emission spectra of the ligands in solution with europium is shown in Figure 5.5. Each of the ligands successfully sensitises europium and the spectra are superimposable. Residual emission from the ligand is not observed. The emission peak values of europium appear in Table 5.2 and correspond to the  ${}^5D_0 \rightarrow {}^7F_J$  ( $J = 0 - 4$ ) transitions. The  ${}^5D_0 \rightarrow {}^7F_0$  transition is visible in these spectra and information about the coordination sphere of  $\text{Eu}^{3+}$  can be obtained from it. The  ${}^5D_0 \rightarrow {}^7F_0$  peaks are superimposable. The peaks are symmetrical, and the full width half maximum for each of these peaks is  $\leq 59 \text{ cm}^{-1}$ . These properties are suggestive of similar emitting  $\text{Eu}^{3+}$  species.<sup>285</sup>

Utilising Equation 5.2, 5.3, and 5.4, the radiative lifetime of  $\text{Eu}^{3+}$ , the intrinsic quantum yield, and the sensitisation efficiency of each of the ligands have been determined. The values are shown in Table 5.2, and the overall quantum yield ( $\phi_{Ln}^L$ ) and observed lifetime are similar to those reported for terpyridine complexes of  $\text{Eu}^{3+}$ .<sup>173,274,275,286,287</sup> The intrinsic quantum yield values are all very similar, indicating that the non-radiative decay pathways for  $\text{Eu}^{3+}$  in these environments are very similar. The data seems to suggest that, in all the solutions, the emissive species is  $[(\mathbf{RTpy})\text{Eu}(\text{NO}_3)_3]$  ( $\mathbf{R} = \mathbf{MeTzPh}, \mathbf{MeTzPy}, \mathbf{HTzPh}, \mathbf{HTzPy}$ ).





**Figure 5.4:** Absorption of dilute ( $10^{-5}$  M) acetonitrile solutions of ligands with addition of excess  $\text{Ln}^{3+}$  (Ln = Eu, Yb).



**Figure 5.5:** Emission spectra of dilute ( $10^{-5}$  M) acetonitrile solutions of ligands in the presence of excess  $\text{Eu}^{3+}$ , under excitation at 310 nm.

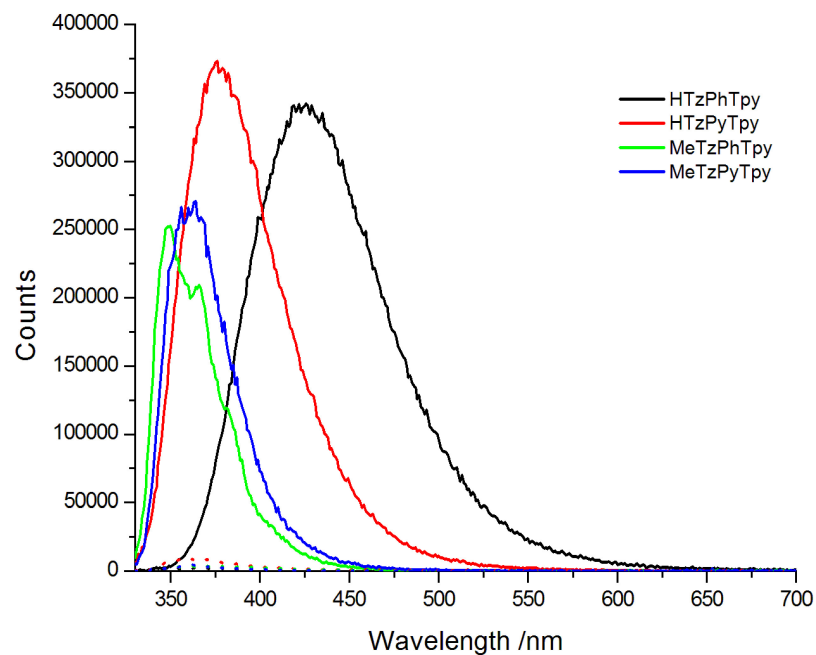
### 5.2.3 Sensitisation of $\text{Yb}^{3+}$ by the synthesised ligands.

The synthesised ligands **HTzPhTpy**, **HTzPyTpy**, **MeTzPhTpy**, and **MeTzPyTpy** were also tested for their sensitising ability in solution with  $\text{Yb}^{3+}$ .

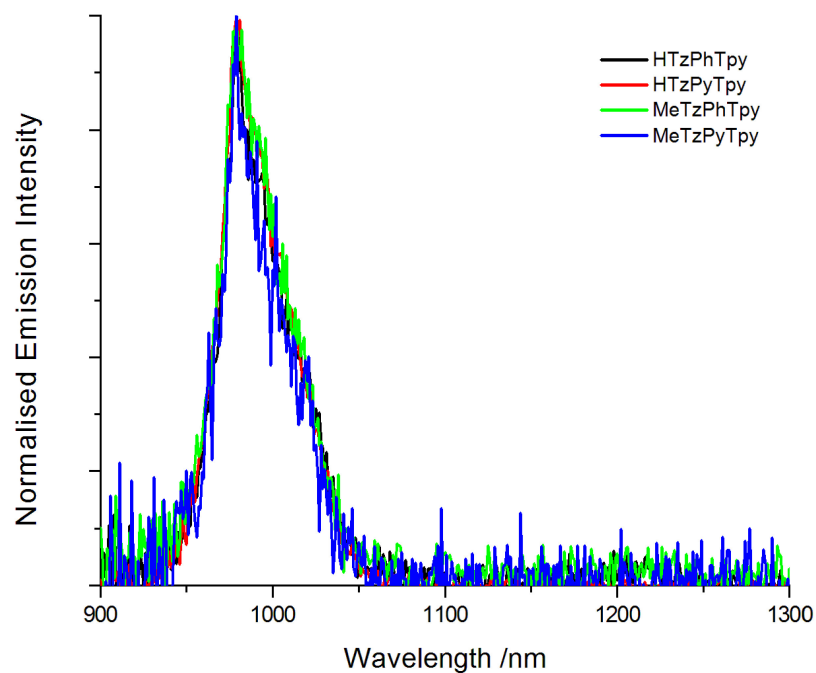
**Table 5.3:** Summary of photophysical properties of dilute ( $10^{-5}$  M) air-equilibrated acetonitrile solutions of ligands in the presence of excess  $\text{Yb}^{3+}$ .

Ligand + $\text{Yb}^{3+}$	Emission, 298 K	
	$\lambda_{max}$ [nm]	$\tau_{obs}$ [ $\mu\text{s}$ ]
<b>HTzPhTpy</b>	980	10.07
<b>HTzPyTpy</b>	980	10.62
<b>MeTzPhTpy</b>	980	9.64
<b>MeTzPyTpy</b>	980	8.48

The changes seen for the absorption spectra shown in Figure 5.4 are analogous to those for the addition of  $\text{Yb}^{3+}$ , as expected by the similar coordination properties of  $\text{Ln}^{3+}$  ions. The addition of excess  $\text{Yb}^{3+}$  causes the emission profiles of the ligands to drastically decrease in intensity (Figure 5.6). The reduction in intensity implies that the ligands are possibly being quenched via energy transfer to  $\text{Yb}^{3+}$ . Although the energy difference between the  ${}^3(\pi - \pi^*)$  and  ${}^2F_{5/2}$  excited states is quite high (Table 5.1), sensitisation of  $\text{Yb}^{3+}$  by organic chromophores with  ${}^3(\pi - \pi^*)$  excited states of similar energy have been reported in literature.<sup>39</sup> The  $\text{Yb}^{3+}$  excited state may also be populated via electron transfer or through a LMCT state.<sup>72,128,288,289,290</sup> Figure 5.7 shows the emission profiles in the 900 to 1300 nm range and illustrates that the spectra are superimposable. Each spectrum displays a peak at 980 nm for the  ${}^2F_{5/2} \rightarrow {}^2F_{7/2}$  transition of  $\text{Yb}^{3+}$ . Importantly, there is no observed peak at 1275 nm corresponding to emission from  ${}^1\text{O}_2$ , this is suggestive that the  $\text{Yb}^{3+}$  excited state is populated rapidly. The emission lifetime in each case is ca. 10  $\mu\text{s}$ , Table 5.3. This value is slightly lower than many reported excited state lifetime of  $\text{Yb}^{3+}$  in solution chelated by N-donor ligands (ca. 15  $\mu\text{s}$ ).<sup>39,134,291</sup> The excited state lifetimes of  $\text{Yb}^{3+}$  with **HTzPhTpy** or **HTzPyTpy** are very similar. This is also seen with **MeTzPhTpy** or **MeTzPyTpy**. This illustrates a similar environment for  $\text{Yb}^{3+}$  in each case, as observed previously for  $\text{Eu}^{3+}$ .<sup>272</sup>



**Figure 5.6:** Visible emission (normalised according to absorbance value) of dilute ( $10^{-5}$  M) acetonitrile solutions, without  $\text{Yb}^{3+}$  (solid line), with  $\text{Yb}^{3+}$  (dashed).



**Figure 5.7:** NIR emission of dilute ( $10^{-5}$  M) acetonitrile solutions in the presence of excess  $\text{Yb}^{3+}$ , excitation at 310 nm.

## 5.3 Photophysical properties of the $\text{Re}(\text{I})$ complexes in the presence of $\text{Ln}^{3+}$

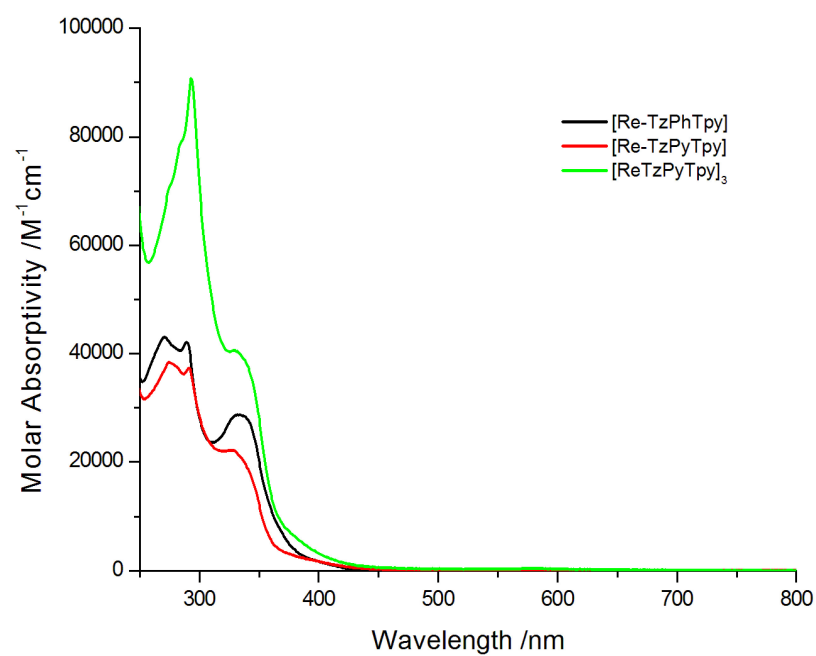
### 5.3.1 Absorption and emission properties of the synthesised complexes in the presence of $\text{Gd}^{3+}$ .

Table 5.4 lists the photophysical properties for each of the complexes before and after the addition of gadolinium. Figure 5.8 illustrates the absorption spectra of solution of complexes  $[\text{Re-TzPhTpy}]$ ,  $[\text{Re-TzPyTpy}]$ , and  $[\text{ReTzPyTpy}]_3$  in the presence of  $\text{Gd}^{3+}$ . It can be seen that the major difference between the spectra of the free complexes and those with  $\text{Gd}^{3+}$  is the appearance of an absorption band at 340 nm, similar to the case for the free ligands. Each of the complexes still appear to exhibit an absorption band at 360 – 440 nm, attributed to the MLLCT absorption.

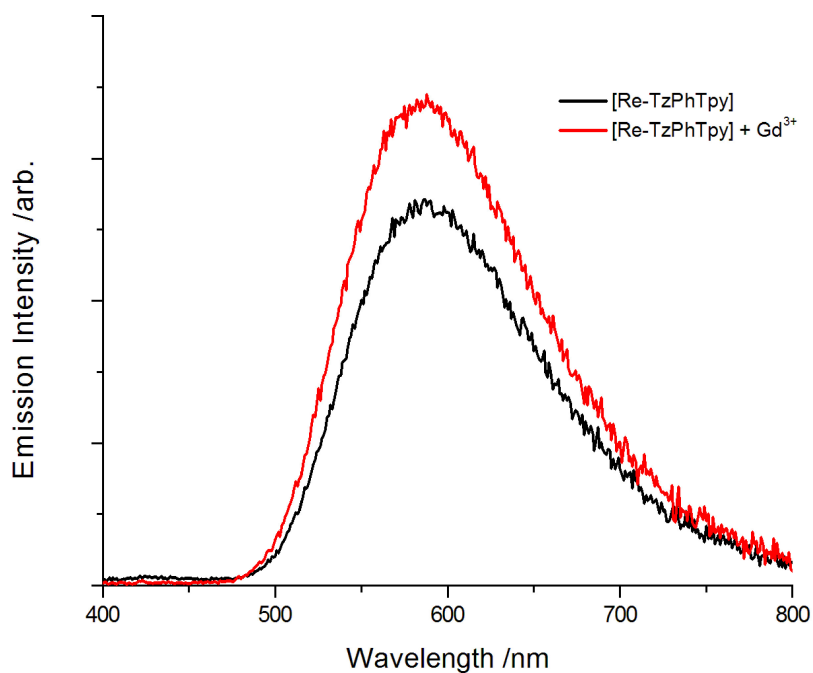
**Table 5.4:** Summary of photophysical properties of dilute ( $10^{-5}$  M) DCM solutions.

Species	Absorption	Emission, 298 K				
	$\lambda_{max}(10^4\epsilon)[\text{nm}][\text{M}^{-1}\text{cm}^{-1}]$	$\lambda_{max}[\text{nm}]$	$\tau_{MLLCT}^a[\text{ns}]$	$\phi_{MLLCT}^a$	$\tau_{MLLCT}^b[\text{ns}]$	$\phi_{MLLCT}^b$
$[\text{Re-TzPhTpy}]$	278(4.81) 360(0.49)	587	252	0.026	607	0.054
$[\text{Re-TzPhTpy}] + \text{Gd}^{3+}$	290(4.22) 333(2.88) 375(0.53)	590	276	0.029	764	0.069
$[\text{Re-TzPyTpy}]$	276(4.23) 360(0.39)	580	284	0.025	564	0.053
$[\text{Re-TzPyTpy}] + \text{Gd}^{3+}$	291(3.73) 326(2.21) 375(0.32)	560	519	0.048	923	0.093
$[\text{ReTzPyTpy}]_3$	280(8.80) 325(3.77)	520	524	0.039	2430	0.216
$[\text{ReTzPyTpy}]_3 + \text{Gd}^{3+}$	293(9.10) 330(4.07)	570	238	0.033	295	0.036

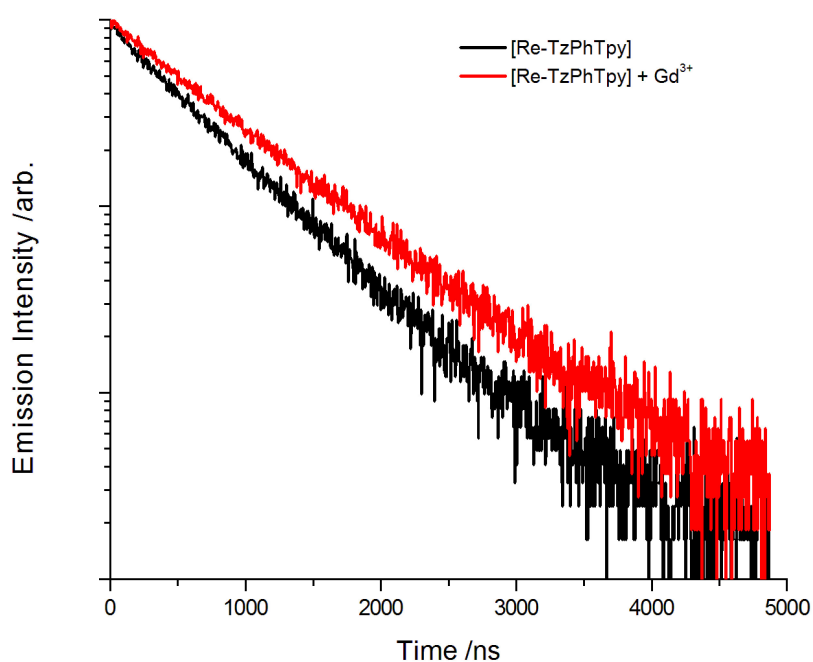
<sup>a</sup>Air-equilibrated solution. <sup>b</sup>Deoxygenated solution. Quantum yield measured against an air-equilibrated aqueous solution of  $[\text{Ru}(\text{bpy})_3]\text{Cl}_2$  ( $\phi = 0.028$ ).



**Figure 5.8:** Absorption spectra of dilute (ca.  $10^{-5}$  M) DCM solutions with excess  $\text{Ln}^{3+}$  ( $\text{Ln} = \text{Gd}, \text{Eu}, \text{Yb}$ ).

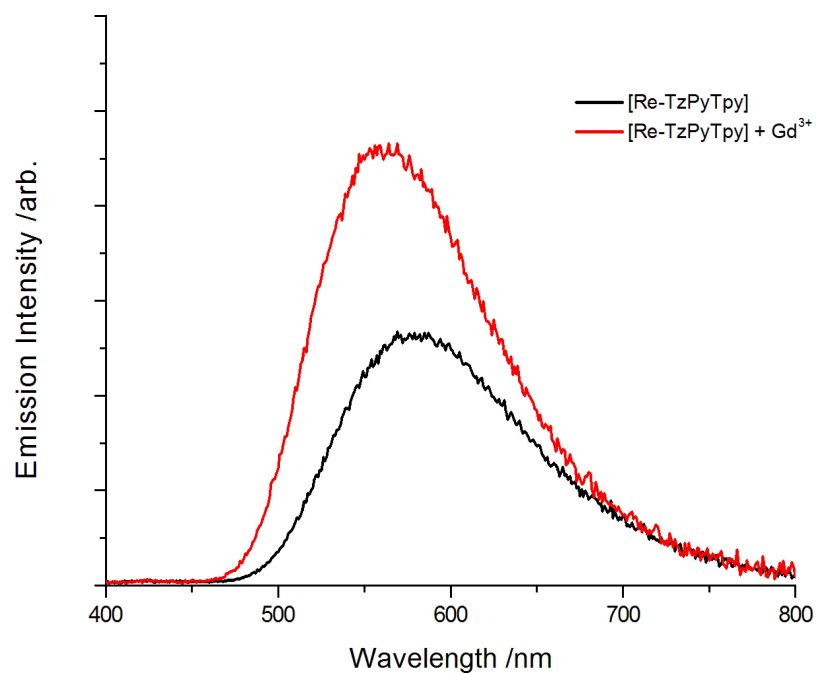


(a)

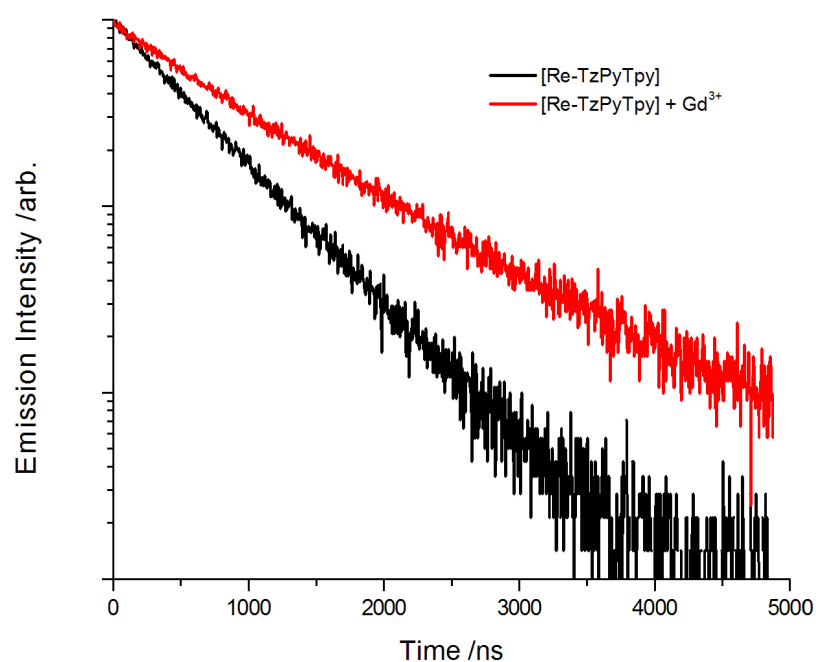


(b)

**Figure 5.9:** Emission properties of a deoxygenated DCM solution (ca.  $10^{-5}$  M) of [Re-TzPhTpy] alone and in the presence of excess  $\text{Gd}^{3+}$  under 375 nm excitation. a) Emission spectra normalised to absorbance value, under excitation at 375 nm. b) TCSPC decay of  $^3\text{MLLCT}$  emission, excited at 375 nm.



(a)



(b)

**Figure 5.10:** Emission properties of a deoxygenated DCM solution (ca.  $10^{-5}$  M) of [Re-TzPyTpy] alone and in the presence of excess Gd<sup>3+</sup> under 375 nm excitation. a) Emission spectra normalised to absorbance value, under excitation at 375 nm. b) TCSPC decay of <sup>3</sup>MLLCT emission, excited at 375 nm.

Figure 5.9 illustrates the difference in emission profiles between deoxygenated solutions of **[Re-TzPhTpy]** alone and in the presence of excess  $\text{Gd}^{3+}$ . The peak maximum does not change position upon the addition of  $\text{Gd}^{3+}$  indicating that its presence does not significantly alter the energy level of the emissive  $^3\text{MLLCT}$  state. The quantum yield slightly increases in comparison to **[Re-TzPhTpy]**, and the decay of the emission at 590 nm under 375 nm excitation for the complex alone and in the presence of  $\text{Gd}^{3+}$  is shown in Figure 5.9b. The two decay profiles appear similar, where the lifetime has slightly increased after the addition of  $\text{Gd}^{3+}$ . This can potentially be ascribed to increased rigidity by chelation of  $\text{Gd}^{3+}$  at the terpyridine site, as also suggested by the slight decrease in  $k_{nr}$  upon addition of  $\text{Gd}^{3+}$  (Table 5.5).

**Table 5.5:** Decay constants in deoxygenated solution.

Species	$k_r [10^5 \text{s}^{-1}]$	$k_{nr} [10^5 \text{s}^{-1}]$
<b>[Re-TzPhTpy]</b>	0.89	15.57
<b>[Re-TzPhTpy]</b> + $\text{Gd}^{3+}$	0.90	12.18

Figure 5.10a illustrates the difference in emission properties of a deoxygenated solution of **[Re-TzPyTpy]** in the absence and presence of excess  $\text{Gd}^{3+}$ . The peak maximum has blue-shifted by ca. 20 nm to 560 nm and the quantum yield has increased from 0.025 to 0.048, as seen in Table 5.4. The decay profiles for the emission from **[Re-TzPyTpy]** with and without  $\text{Gd}^{3+}$  are shown in Figure 5.10b and illustrates an increase in lifetime from 564 to 923 ns.

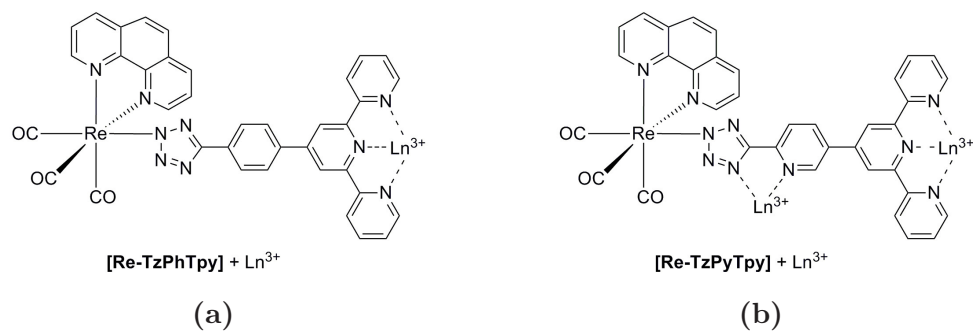
**Table 5.6:** Decay constants in deoxygenated solution.

Species	$k_r [10^5 \text{s}^{-1}]$	$k_{nr} [10^5 \text{s}^{-1}]$
<b>[Re-TzPyTpy]</b>	0.95	16.77
<b>[Re-TzPyTpy]</b> + $\text{Gd}^{3+}$	1.01	9.82

Table 5.6 shows the calculated decay constants for **[Re-TzPyTpy]** after the addition of  $\text{Gd}^{3+}$ . The combination of the blue-shift of emission, elongated lifetime, increase quantum yield and decrease in non-radiative decay is consistent with the energy gap law.<sup>36</sup>

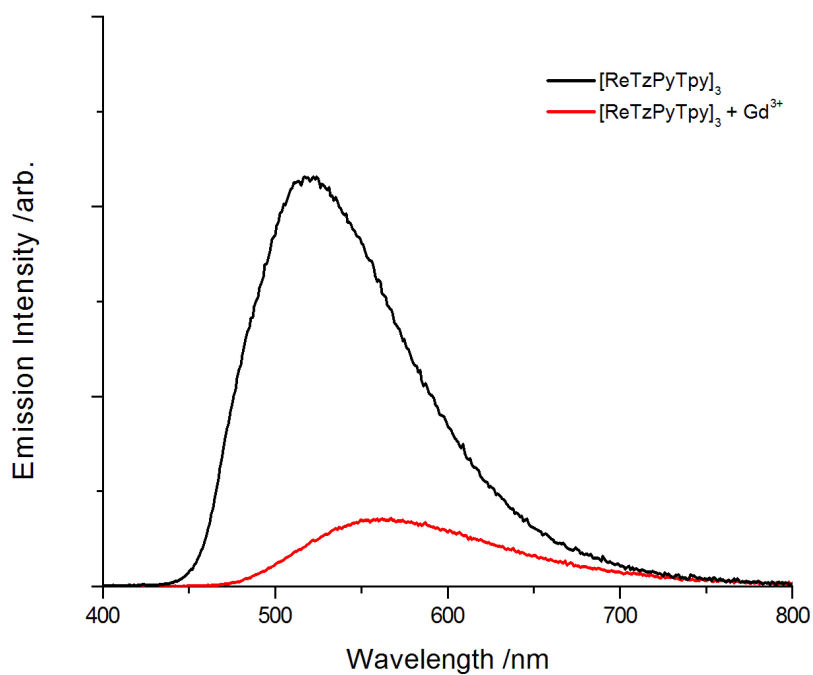
Comparison of the structures of **[Re-TzPhTpy]** and **[Re-TzPyTpy]** indicates that, in the case of **[Re-TzPyTpy]**, there is a second site available for the coordination of  $\text{Gd}^{3+}$ , as shown in Figure 5.11. It can be seen that the  $\text{Gd}^{3+}$  cation can coordinate to the 5-(2-pyridyl)-tetrazolate site. At this position, the Lewis acidity of  $\text{Gd}^{3+}$  would reduce the  $\sigma$  donation strength of the tetrazole, and hence stabilise the 5d orbitals. This results in the stabilisation of the HOMO and the net effect is an increase in the energy of the MLLCT transition. This effect has



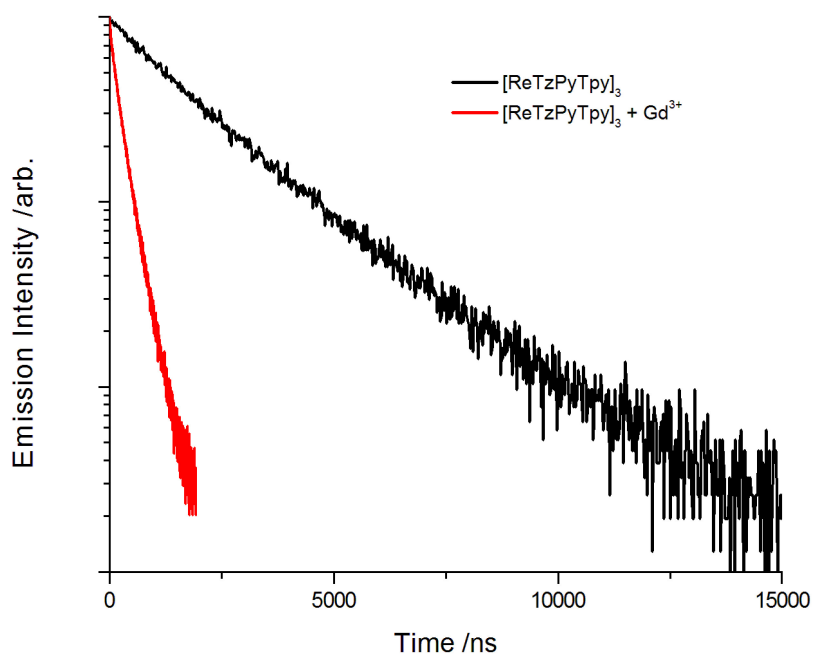


**Figure 5.11:** Chelation sites available for  $\text{Ln}^{3+}$  ions for complexes. a)  $[\text{Re-TzPhTpy}]$ . b)  $[\text{Re-TzPyTpy}]$ .

been observed in other research efforts into the protonation and methylation of similar rhenium tetrazolato complexes, where a positively charged electrophile is attached to the N4 atom of the tetrazolate ligand.<sup>196,292</sup> This is further suggestive that the  $\text{Gd}^{3+}$  species is localising at the tetrazolate moiety inducing a similar change in the electronic properties.



(a)



(b)

**Figure 5.12:** Emission properties of a DCM solution (ca.  $10^{-5}$  M) of  $[\text{ReTzPyTpy}]_3$  alone and in the presence of excess  $\text{Gd}^{3+}$  under 375 nm excitation. a) Emission spectra normalised to absorbance value, under excitation at 375 nm. b) TCSPC decay of  $^3\text{MLLCT}$  emission, excited at 375 nm.

Figure 5.12 illustrates the change in emission properties for **[ReTzPyTpy]<sub>3</sub>** after the addition of Gd<sup>3+</sup>. The emission maximum has red-shifted by 50 nm to 570 nm, the quantum yield of this emission has decreased by six-fold as shown in Table 5.4. The decay profile for the emission from **[ReTzPyTpy]<sub>3</sub>** with and without the presence of Gd<sup>3+</sup>, under 375 nm excitation, is shown in Figure 5.12b and illustrates a decrease in lifetime from 2.4  $\mu$ s to 295 ns as given in Table 5.4.

**Table 5.7:** Decay constants in deoxygenated solution.

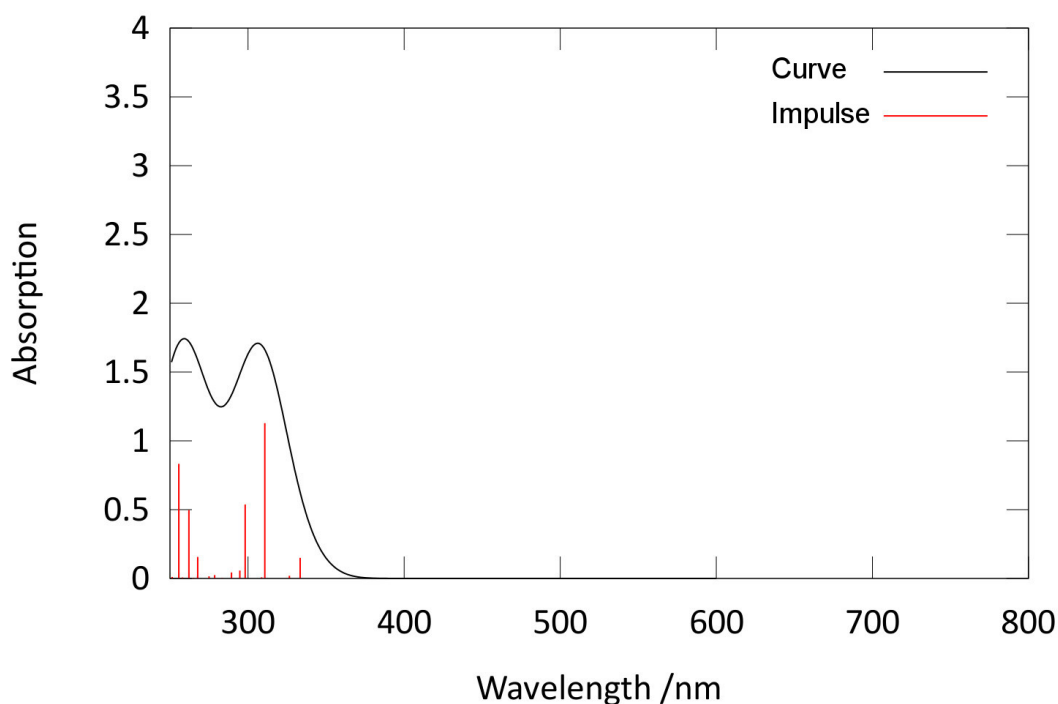
Species	$k_r [10^5 \text{s}^{-1}]$	$k_{nr} [10^5 \text{s}^{-1}]$
<b>[ReTzPyTpy]<sub>3</sub></b>	0.89	3.23
<b>[ReTzPyTpy]<sub>3</sub> + Gd<sup>3+</sup></b>	1.21	32.68

The calculated decay constants for **[ReTzPyTpy]<sub>3</sub>** with and without the presence of Gd<sup>3+</sup> are shown in Table 5.7 and illustrate that the non-radiative decay constant has increased by a factor of 10.

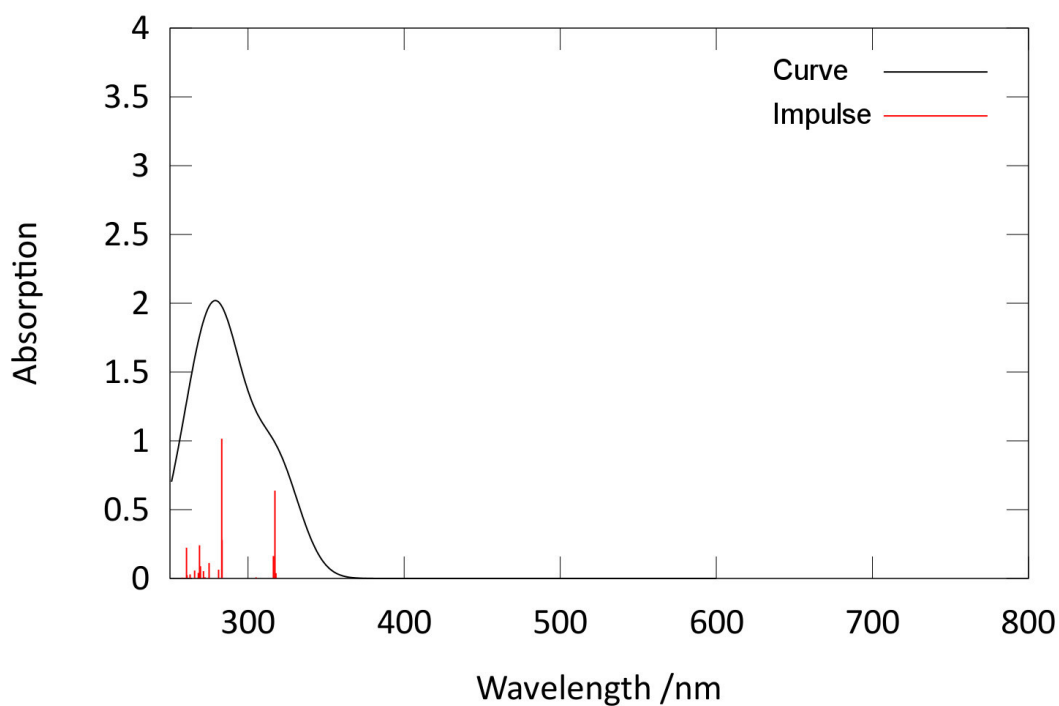
Gd<sup>3+</sup> is likely to localise at the terpyridine moieties of **[ReTzPyTpy]<sub>3</sub>** as there are no other chelation sites available in the molecule. This localisation of Gd<sup>3+</sup> will likely increase the conjugation of the terpyridine ligand, by locking it into a planar configuration, and stabilising the  $\pi^*$  system of the ligand. These effects lower the LUMO in the MLLCT transition, causing a red-shift of the emission and increase of the non-radiative decay constant, consistent with the energy gap law.

### 5.3.2 Computational Investigation

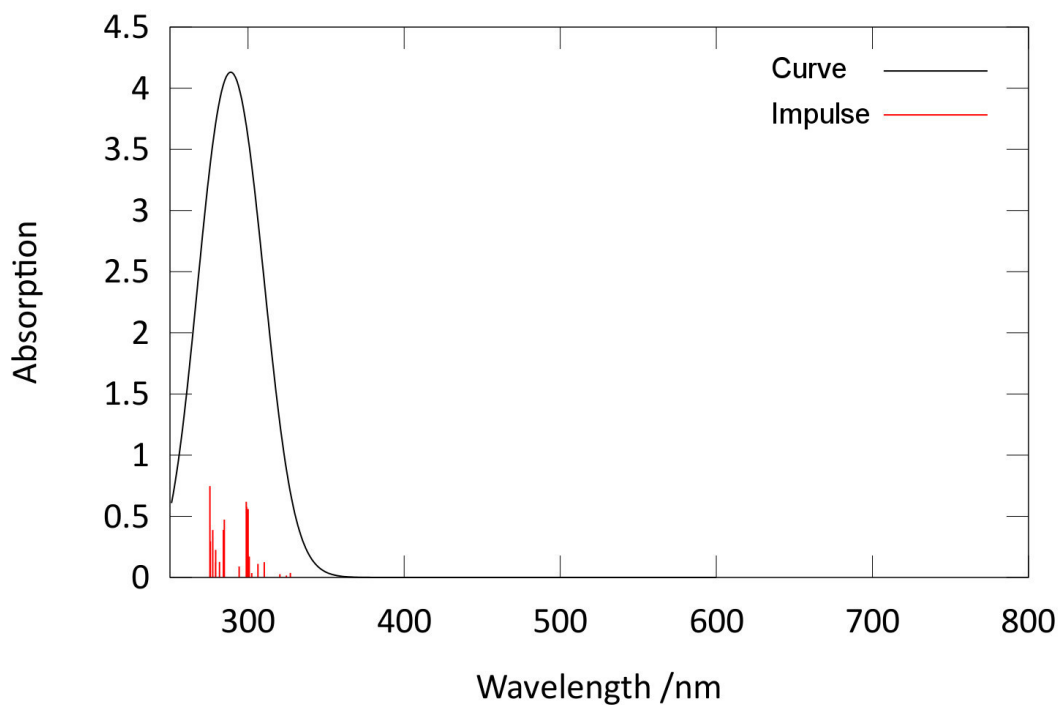
To gain further information about changes to energy levels upon  $\text{Ln}^{3+}$  addition, a computational investigation was performed using the complexes  $[\text{Re-TzPhTpy}]$  and  $[\text{ReTzPyTpy}]_3$  chelating  $\text{Ca}^{2+}$  at the terpyridine site, and  $[\text{Re-TzPyTpy}]$  chelating  $\text{H}^+$  at the terpyridine and tetrazole sites. These models were chosen as they will simulate the presence of a Lewis acid at the chelation sites.  $\text{Ca}^{2+}$  and  $\text{H}^+$  were chosen as Lewis acids as simulations attempted with heavier Lewis acids (e.g.  $\text{Ln}^{3+}$ ) did not lead to optimised geometries.



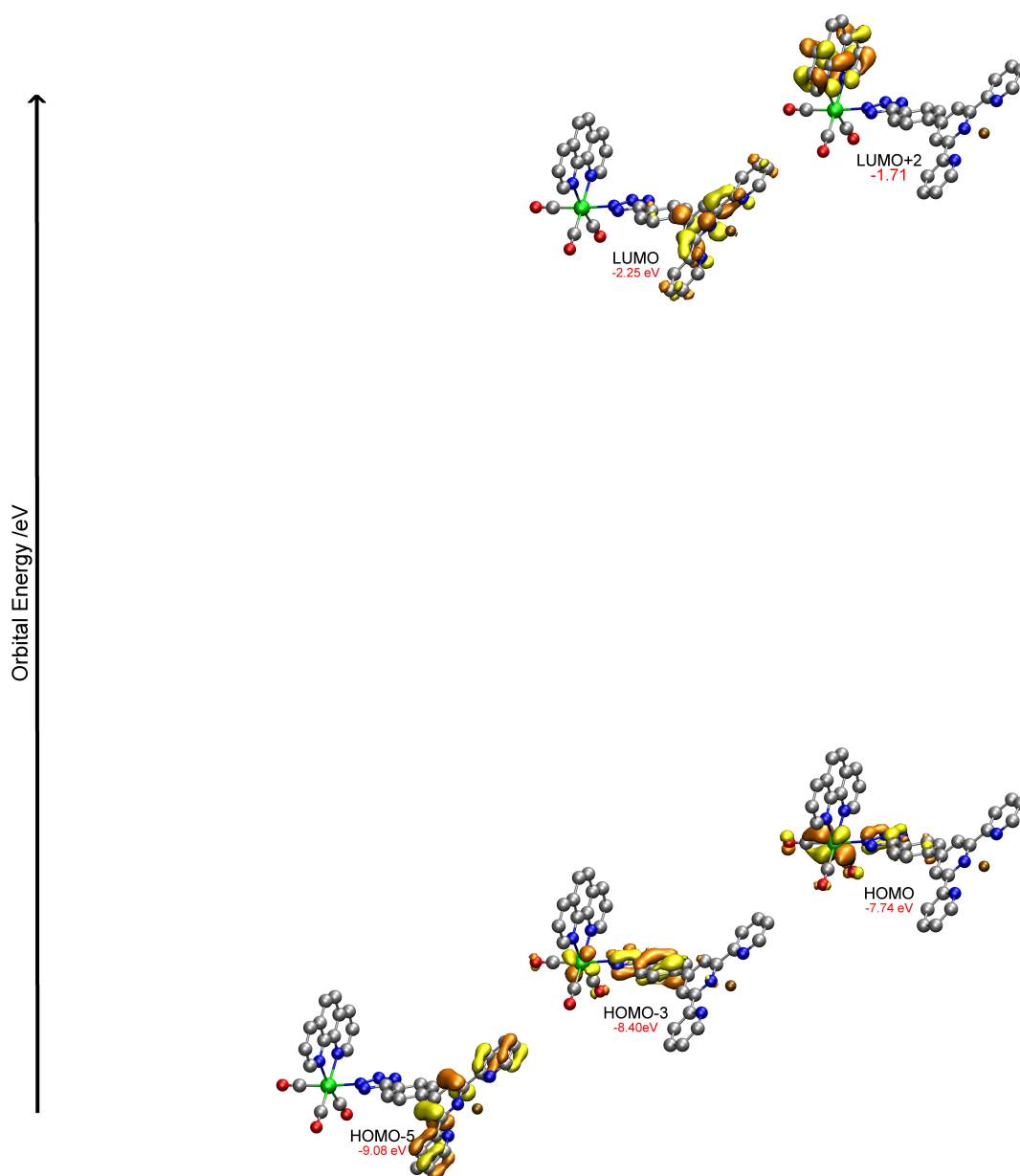
**Figure 5.13:** Simulated absorption spectrum for  $[\text{Re-TzPhTpyCa}]^{2+}$ . Limited to the 250 nm to 800 nm range. Impulses correspond to transitions listed in Table 5.8.



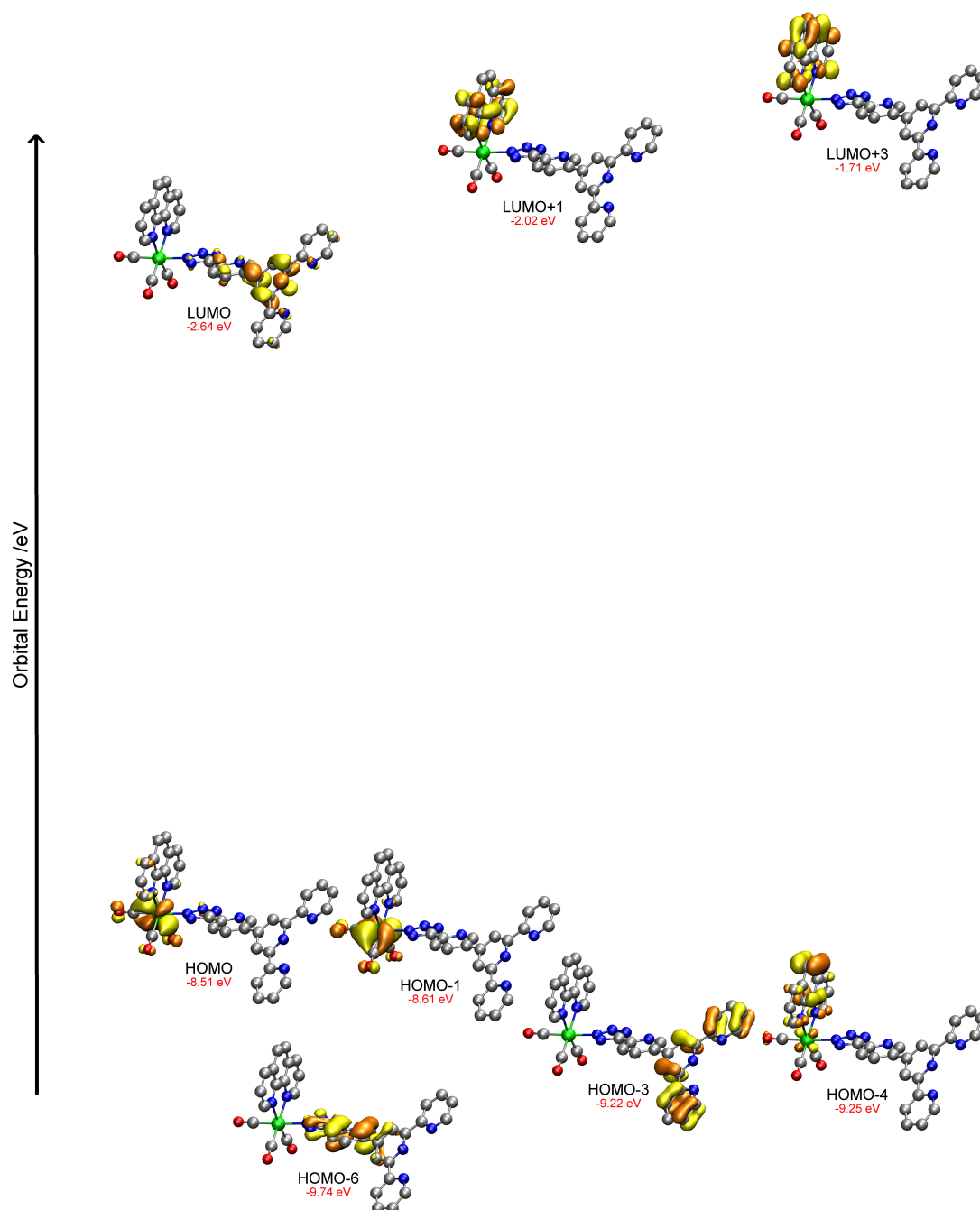
**Figure 5.14:** Simulated absorption spectrum of  $[\text{Re-TzPyHTpyH}]^{2+}$ . Limited to the 250 nm to 800 nm range. Impulses correspond to transitions listed in Table 5.8.



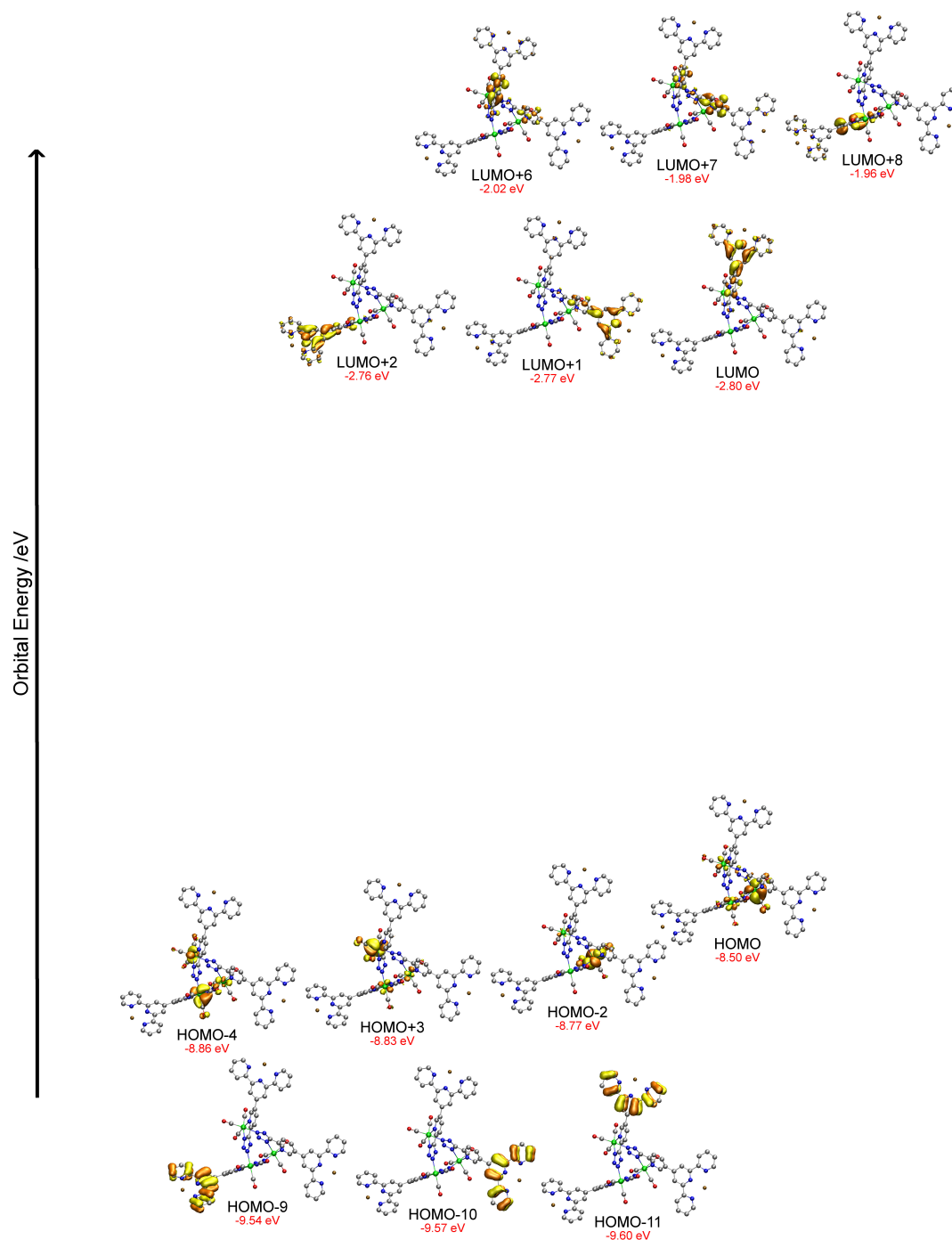
**Figure 5.15:** Simulated absorption spectrum for  $[\text{ReTzPyTpyCa}]_3^{6+}$ . Limited to the 250 nm to 800 nm range. Impulses correspond to transitions listed in Table 5.8.



**Figure 5.16:** Simulated orbitals for  $[\text{Re-TzPhTpyCa}]^{2+}$  corresponding to transitions listed in Table 5.8. Orbitals are spaced vertically relative to their energy and the HOMO-LUMO gap has been reduced for clarity.



**Figure 5.17:** Simulated orbitals for [Re-TzPyHTpyH]<sup>2+</sup> corresponding to transitions listed in Table 5.8. Orbitals are spaced vertically relative to their energy and the HOMO-LUMO gap has been reduced for clarity.



**Figure 5.18:** Simulated orbitals for  $[\text{ReTzPyTpyCa}]_3^{6+}$  corresponding to transitions listed in Table 5.8. Orbitals are spaced vertically relative to their energy and the HOMO-LUMO gap has been reduced for clarity.



**Table 5.8:** Simulated transitions with relatively large oscillator strength.

Species	Wavelength [nm]	Intensity	Levels	Character	Assignment
[Re-TzPhTpyCa] <sup>2+</sup>	333.41	0.15	HOMO → LUMO+2	84 %	MLLCT(Re → <b>phen</b> )
	310.47	1.12	HOMO-3 → LUMO	33 %	MLLCT(Re → <b>TzPhTpy</b> ) + IL( <b>TzPhTpy</b> )
			HOMO → LUMO	43 %	
[Re-TzPyHTpyH] <sup>2+</sup>	298.18	0.54	HOMO-5 → LUMO	84 %	IL ( <b>TzPhTpy</b> )
	317.90	0.04	HOMO-1 → LUMO+1	53 %	MLLCT(Re → <b>phen</b> )
			HOMO → LUMO+1	39 %	MLLCT(Re → <b>phen</b> )
	317.24	0.64	HOMO-3 → LUMO	86 %	IL( <b>TzPyTpy</b> )
	316.23	0.16	HOMO-1 → LUMO+1	39 %	MLLCT(Re → <b>phen</b> )
			HOMO → LUMO+1	52 %	MLLCT(Re → <b>phen</b> )
	283.35	0.28	HOMO-4 → LUMO+1	42 %	MLLCT(Re → <b>phen</b> ) + IL( <b>phen</b> )
			HOMO-1 → LUMO+3	19 %	
			283.17	1.02	HOMO-6 → LUMO
	[ReTzPyTpyCa] <sub>3</sub> <sup>6+</sup>	310.37	0.12	HOMO-2 → LUMO+1	31%
HOMO-2 → LUMO+7				24 %	MLLCT <sup>a</sup>
HOMO-2 → LUMO+6				12 %	MLLCT <sup>a</sup>
306.35		0.11	HOMO-3 → LUMO	26 %	MLLCT <sup>a</sup>
			HOMO-3 → LUMO+6	20 %	MLLCT <sup>a</sup>
300.81		0.17	HOMO-4 → LUMO+2	21 %	MLLCT <sup>a</sup>
			HOMO-4 → LUMO+8	23 %	MLLCT <sup>a</sup>
300.03		0.56	HOMO-9 → LUMO+2	75 %	IL <sup>a</sup>
299.09		0.58	HOMO-10 → LUMO+1	63 %	IL <sup>a</sup>
298.86	0.62	HOMO-11 → LUMO	68 %	IL <sup>a</sup>	

<sup>a</sup>Assignments for [ReTzPyTpyCa]<sub>3</sub><sup>6+</sup> are labelled as generic MLLCT and IL, as orbitals are dispersed across multiple metal centres and TzPyTpy<sup>-</sup> ligands.

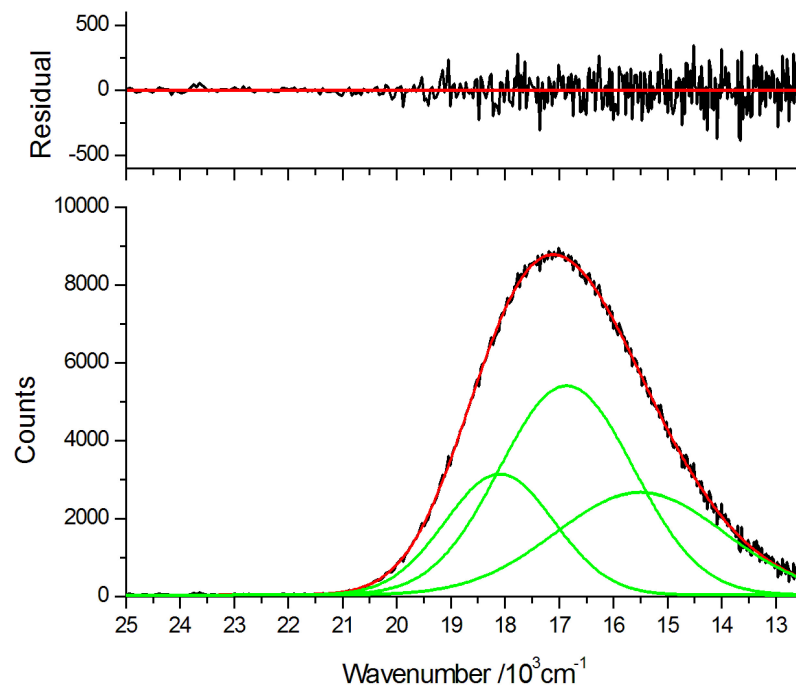
Figure 5.13, Figure 5.14, and Figure 5.15 show the simulated absorption spectra for  $[\text{Re-TzPhTpyCa}]^{2+}$ ,  $[\text{Re-TzPyHTpyH}]^{2+}$ , and  $[\text{ReTzPyTpyCa}]_3^{6+}$ , respectively. The relevant simulated orbitals are found in Figure 5.16, Figure 5.17, and Figure 5.18. Table 5.8 shows the significant transitions observed in the simulated absorbance plots.

It can be seen that in comparison to the neutral complex  $[\text{Re-TzPhTpy}]$ ,  $[\text{Re-TzPhTpyCa}]^{2+}$  displays a larger peak at 330 nm. The orbital contours show that the LUMO is now localised on the terpyridine system. The simulated spectrum agrees well with what is seen in Figure 5.8, with a significantly pronounced peak at 330 nm, which is attributed to mixing of  $\text{IL}(\text{TzPhTpy})$  transitions with the  $\text{MLCT}(\text{Re} \rightarrow \text{TzPhTpy})$ . Table 5.8 illustrates that the energy of the  $\text{MLLCT}(\text{Re} \rightarrow \text{phen})$  transition has not been significantly altered by the presence of a Lewis acid, and remains the lowest energy transition of appreciable oscillator strength, in agreement with the photophysical investigation.

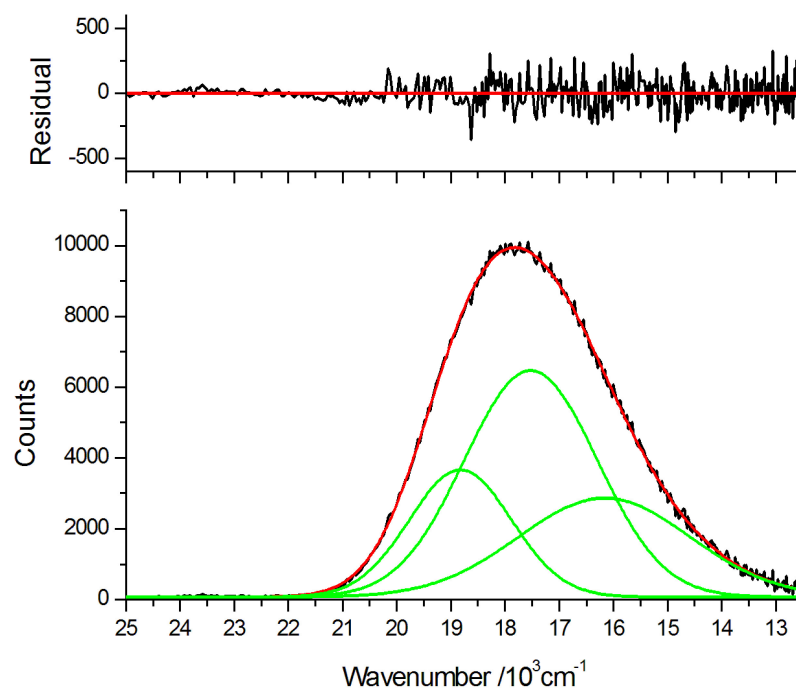
In the case of  $[\text{Re-TzPyHTpyH}]^{2+}$ , the simulated absorption spectrum (Figure 5.14) agrees well with the experimental spectrum of  $[\text{Re-TzPyTpy}]$  in the presence of  $\text{Gd}^{3+}$ . It can be seen that there is overlap of low energy  $\text{MLLCT}(\text{Re} \rightarrow \text{phen})$  (317.90 nm) with an  $\text{IL}(\text{TzPyHTpyH})$  (317.24 nm) transition. In relation to the transitions seen for  $[\text{Re-TzPyTpy}]$ , the  $\text{MLLCT}(\text{Re} \rightarrow \text{phen})$  remains the lowest energy transition, however, it has blue-shifted, as a result of the stabilisation of the HOMO, and a red-shift of the  $\text{IL}(\text{TzPyHTpyH})$  transition, caused by increased conjugation and stabilisation of the  $\pi^*$  orbitals. This is in agreement with the observed blue-shift of the  ${}^3\text{MLLCT}$  emission band under the addition of  $\text{Gd}^{3+}$ .

In the case of  $[\text{ReTzPyTpyCa}]_3^{6+}$ , the overall absorption band is seen to red-shift in comparison to  $[\text{ReTzPyTpy}]_3$ . The localisation of  $\text{Ca}^{2+}$  causes stabilisation of the  $\pi^*$  orbitals with a net effect of lowering the HOMO-LUMO gap. Further to this, the  $\text{IL}$  transitions become lower in energy and are overlapping with the  $\text{MLLCT}$  transitions in the 290 - 310 nm region. This is in agreement with the experimentally observed shoulder which appears in the absorption spectrum and the red-shift of the  ${}^3\text{MLLCT}$  emission band.

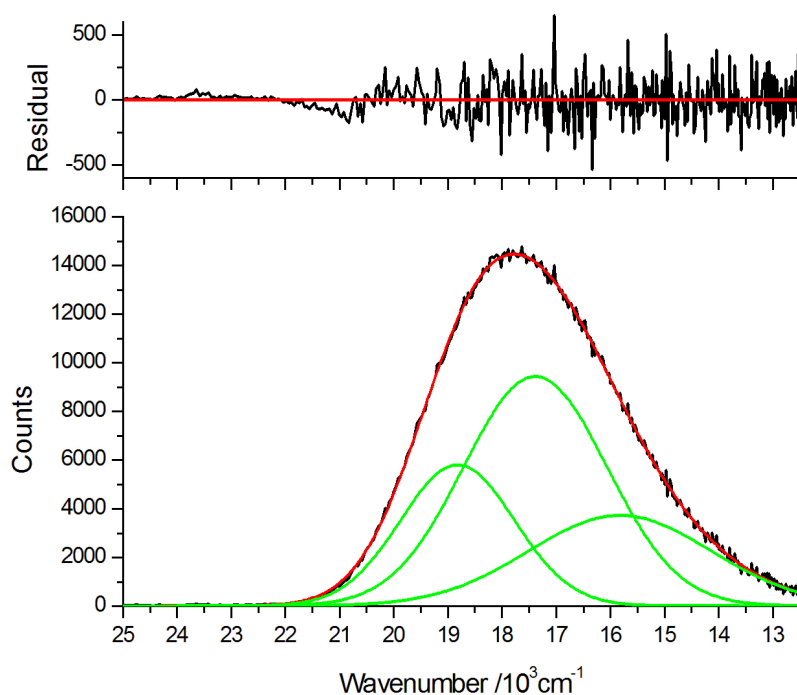
### 5.3.3 Determination of triplet state energy of the complexes in the presence of Gd<sup>3+</sup>



**Figure 5.19:** Gaussian fit for <sup>3</sup>MLLCT emission from [Re-TzPhTpy] with Gd<sup>3+</sup>.



**Figure 5.20:** Gaussian fit to the <sup>3</sup>MLLCT emission from [Re-TzPyTpy] with Gd<sup>3+</sup>.



**Figure 5.21:** Gaussian fit for  ${}^3\text{MLLCT}$  emission from  $[\text{ReTzPyTpy}]_3$  with  $\text{Gd}^{3+}$ .

**Table 5.9:** Gaussian analysis of complexes with  $\text{Gd}^{3+}$  and energy gap to  $\text{Eu}^{3+}({}^5D_0)$  and  $\text{Yb}^{3+}({}^2F_{5/2})$  excited states.

Complex + $\text{Gd}^{3+}$	$\lambda_{3\text{MLLCT}(0-0)}[\text{cm}^{-1}]$	$\text{Eu}^{3+} \Delta (\lambda_{3\text{MLLCT}(0-0)} - \lambda_{5D_0})[\text{cm}^{-1}]$	$\text{Yb}^{3+} \Delta (\lambda_{3\text{MLLCT}(0-0)} - \lambda_{2F_{5/2}})$
$[\text{Re-TzPhTpy}]$	18,096	596	7,696
$[\text{Re-TzPyTpy}]$	18,823	1,323	8,423
$[\text{ReTzPyTpy}]_3$	18,821	1,322	8,421

For each of the emission spectra, deconvolution with Gaussian functions has been performed to determine the approximate energy of the 0-0 transition and are shown in Figure 5.19, Figure 5.20 and Figure 5.21. The Gaussian function that corresponds to the higher wavenumber for each fitting is taken as the energy of the 0-0 transition and labelled as  ${}^3\text{MLLCT}(0-0)$  in Table 5.9. The energy difference between the  ${}^3\text{MLLCT}(0-0)$  and the  ${}^5D_0$  state of  $\text{Eu}^{3+}$  indicates that energy back transfer to the  ${}^3\text{MLLCT}$  excited state might be expected. The energy gap between the  ${}^3\text{MLLCT}(0-0)$  and the  ${}^2F_{5/2}$  state of  $\text{Yb}^{3+}$  is sufficiently high for energy transfer. However, the sensitisation of  $\text{Yb}^{3+}$  may occur via a proposed LMCT pathway, forming  $\text{Yb}^{2+}$ .<sup>290,293</sup>

### 5.3.4 Sensitisation of Eu<sup>3+</sup> by the Re(I) complexes.

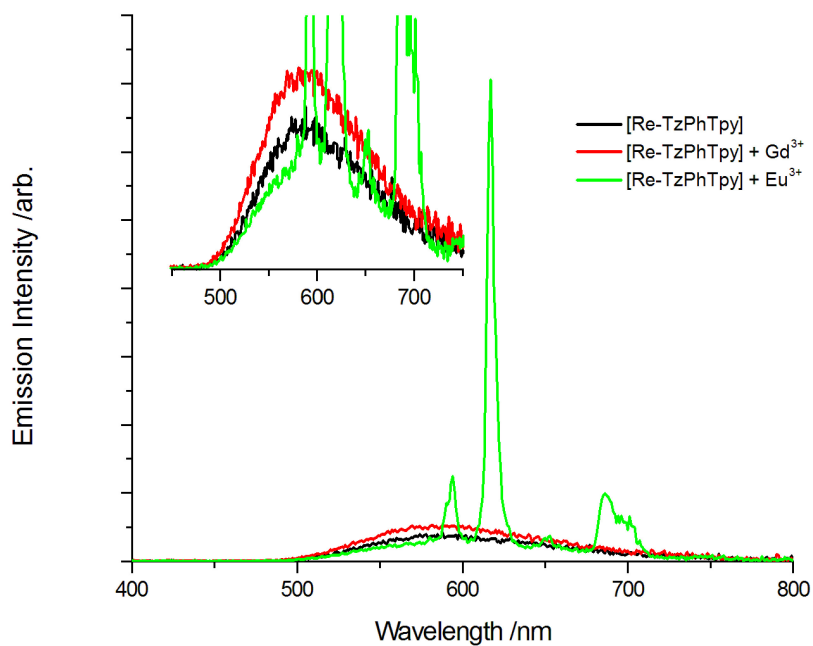
**Table 5.10:** Summary of photophysical properties of dilute (10<sup>-5</sup> M) DCM solutions.

Species	$\lambda_{max}$ [nm]	$\tau_{3MLLCT}^a$ [ns]	Emission, 298 K				
			$\phi^a$	$\tau_{3MLLCT}^b$ [ns]	$\phi^b$	$\tau_{Eu}^a$ [ms]	$\tau_{Eu}^b$ [ms]
[Re-TzPhTpy] + Gd <sup>3+</sup>	590	276	0.029	764	0.069		
[Re-TzPhTpy] + Eu <sup>3+</sup>	590, 618 650, 690	244	0.080	473	0.102	1.38	1.40
[Re-TzPyTpy] + Gd <sup>3+</sup>	560	519	0.048	923	0.093		
[Re-TzPyTpy] + Eu <sup>3+</sup>	560, 590 618, 650 690	388	0.088	682	0.153	1.26	1.34
[ReTzPyTpy] <sub>3</sub> + Gd <sup>3+</sup>	570	238	0.033	295	0.036		
[ReTzPyTpy] <sub>3</sub> + Eu <sup>3+</sup>	560, 590 618, 650, 690	27	0.204	29	0.275	1.37	1.49

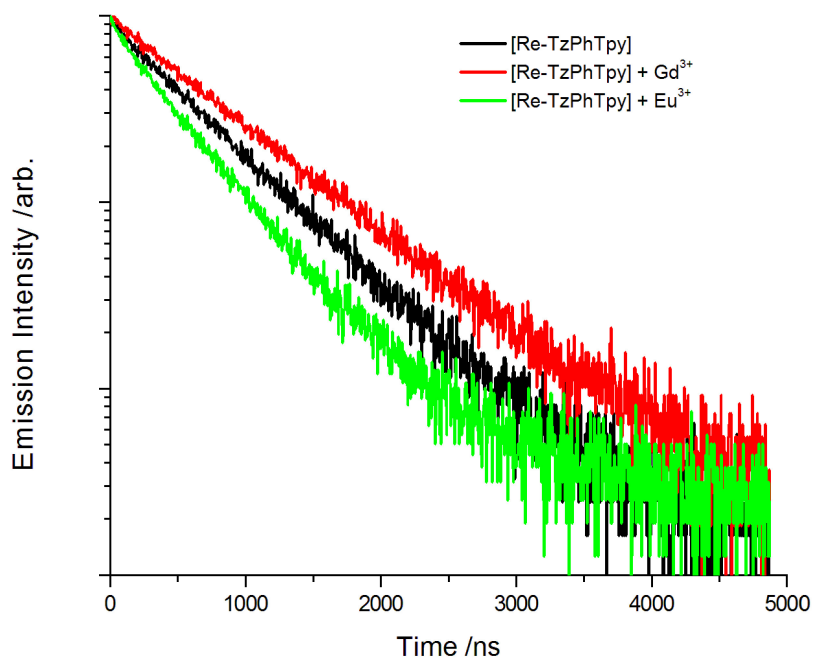
<sup>a</sup>Air-equilibrated solution, <sup>b</sup>deoxygenated solution, Gd<sup>3+</sup> data taken from Table 5.4 for reference. Quantum yield values for entire emission spectrum (400 - 800 nm) measured against an air-equilibrated aqueous solution of [Ru(**bpy**)<sub>3</sub>]Cl<sub>2</sub> ( $\phi = 0.028$ ).

Changes in the absorption spectra of the complexes after addition of Eu<sup>3+</sup> are analogous to those observed in Figure 5.8, indicating complexation of Eu<sup>3+</sup> at the terpyridine site.

Figure 5.22a illustrates the difference in emission spectra in dichloromethane of [Re-TzPhTpy] alone and with the addition of Eu<sup>3+</sup> or Gd<sup>3+</sup>. Comparing the spectra of [Re-TzPhTpy] with and without Eu<sup>3+</sup> shows that the emission from the <sup>3</sup>MLLCT has not shifted, and the emission intensity is similar when normalised to the absorbance. This effect is similarly seen under the addition of Gd<sup>3+</sup>. Accurate calculation of the intrinsic quantum yield, radiative lifetime, and sensitisation efficiency of Eu<sup>3+</sup> cannot be performed due to convolution of the <sup>3</sup>MLLCT emission and the <sup>5</sup>D<sub>0</sub> → <sup>7</sup>F<sub>J</sub> (*J* = 0 – 4) transitions. The emission decay at 560 nm in deoxygenated solution was measured to compare the lifetime for [Re-TzPhTpy] alone and with Gd<sup>3+</sup> or Eu<sup>3+</sup> (Figure 5.22b). The decay lifetime alters from 764 ns with Gd<sup>3+</sup> to 473 ns with Eu<sup>3+</sup>. This change might suggest the presence of energy transfer occurring from the <sup>3</sup>MLLCT to Eu<sup>3+</sup>. The data for air-equilibrated solutions, when moving from Gd<sup>3+</sup> to Eu<sup>3+</sup>, display a relatively smaller change of lifetime. This may suggest that the rate of quenching in the presence of <sup>3</sup>O<sub>2</sub> is competing with the rate of energy transfer, from the <sup>3</sup>MLLCT to Eu<sup>3+</sup>.

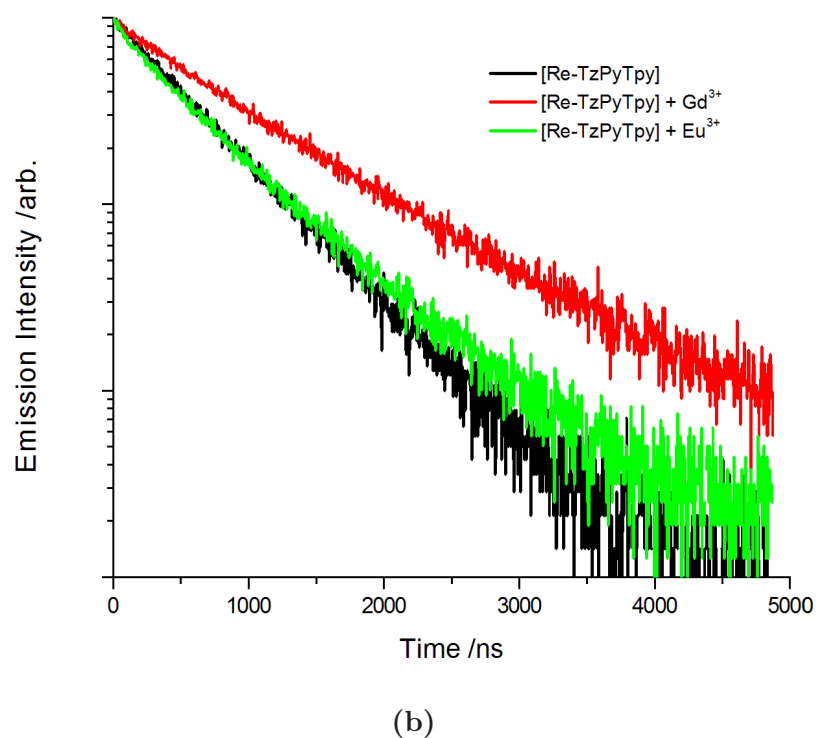
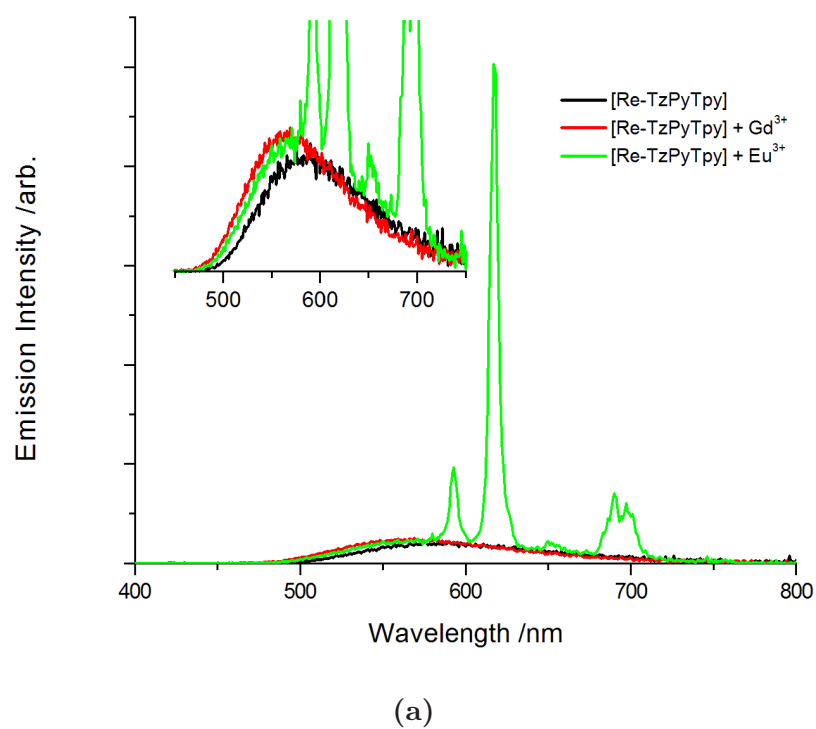


(a)



(b)

**Figure 5.22:** Emission properties of a deoxygenated DCM solution (ca.  $10^{-5}$  M) of [Re-TzPhTpy] alone and in the presence of  $\text{Eu}^{3+}$  under 375 nm excitation. a) Emission spectra normalised to absorbance value, under excitation at 375 nm. b) TCSPC decay of  $^3\text{MLLCT}$  emission, excited at 375 nm.

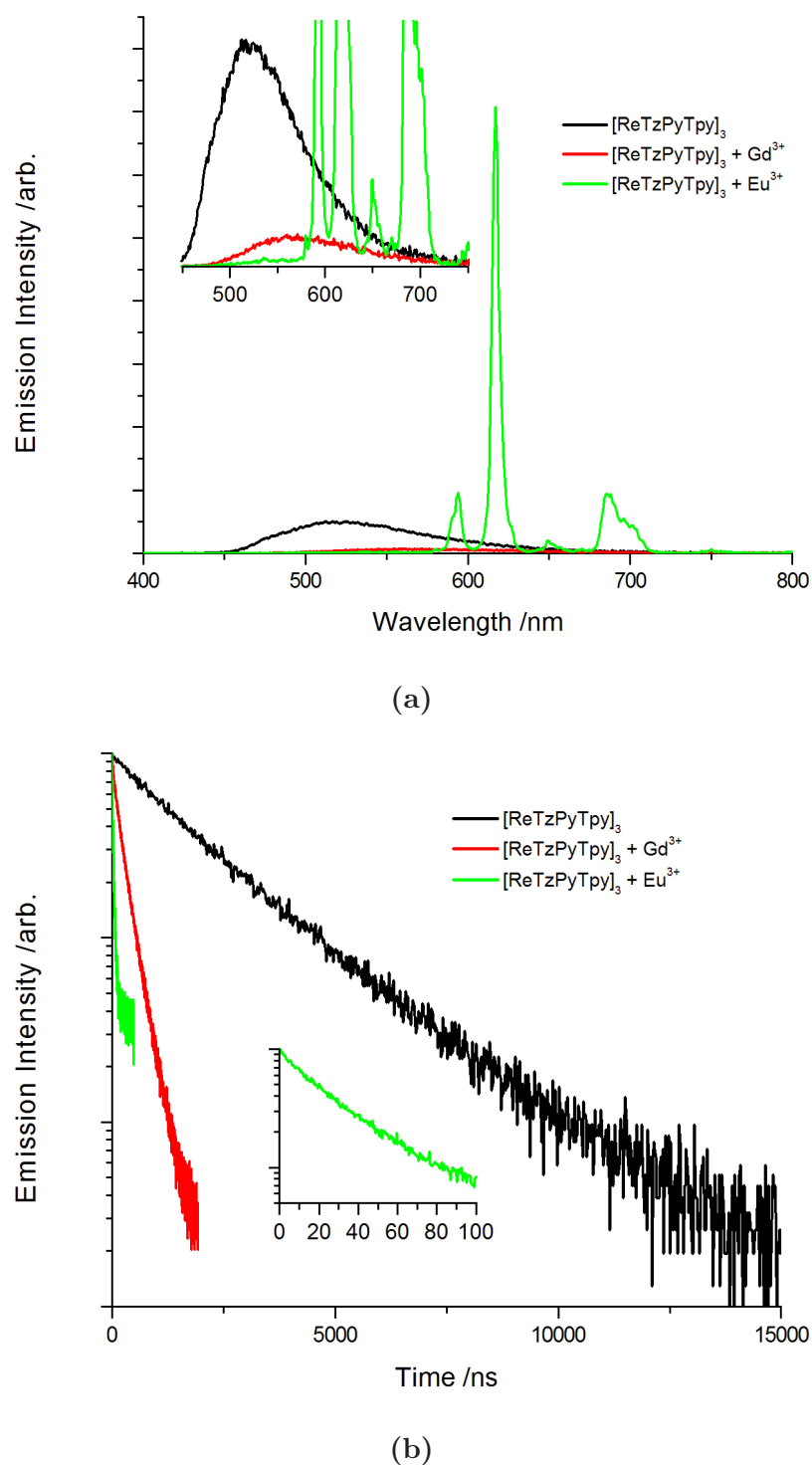


**Figure 5.23:** Emission properties of a deoxygenated DCM solution (ca.  $10^{-5}$  M) of [Re-TzPyTpy] alone and in the presence of Eu<sup>3+</sup> under 375 nm excitation. a) Emission spectra normalised to absorbance value, under excitation at 375 nm. b) TCSPC decay of <sup>3</sup>MLLCT emission, excited at 375 nm.

In the case of [**Re-TzPyTpy**] (Figure 5.23), the emission wavelength has blue-shifted from 580 nm to 560 nm when  $\text{Eu}^{3+}$  is added, as seen in Figure 5.23a. This effect is similar to the addition of  $\text{Gd}^{3+}$ , where the pyridyl-tetrazole moiety is also complexed. In deoxygenated solutions, the lifetime of the  $^3\text{MLLCT}$  emission changes from 923 ns with  $\text{Gd}^{3+}$  to 682 ns with  $\text{Eu}^{3+}$ . This change might suggest the presence of energy transfer occurring from the  $^3\text{MLLCT}$  to  $\text{Eu}^{3+}$ . The data for air-equilibrated solutions illustrates there is a significant change in  $^3\text{MLLCT}$  decay lifetime when moving from  $\text{Gd}^{3+}$  (923 ns) to  $\text{Eu}^{3+}$  (682 ns). This may suggest that the rate of energy transfer from the  $^3\text{MLLCT}$  of [**Re-TzPyTpy**] to the  $^5D_0$  state of  $\text{Eu}^{3+}$  is competing more efficiently with the rate of quenching by  $^3\text{O}_2$ , than in the case of [**Re-TzPhTpy**].

It would be expected in the case of [**Re-TzPyTpy**] that having two  $\text{Eu}^{3+}$  ions available for sensitisation the emission of  $\text{Eu}^{3+}$  would exhibit a bi-exponential decay, however, a mono-exponential decay was recorded for this complex. Further analysis would be required to accurately determine the speciation in solution and also determine the nature of the emission from  $\text{Eu}^{3+}$ .





**Figure 5.24:** Emission properties of a deoxygenated DCM solution (ca.  $10^{-5}$  M) of  $[\text{ReTzPyTpy}]_3$  alone and in the presence of  $\text{Eu}^{3+}$  under 375 nm excitation. a) Emission spectra normalised to absorbance value, under excitation at 375 nm. b) TCSPC decay of  $^3\text{MLLCT}$  emission, excited at 375 nm.

Figure 5.24a shows the difference in emission profiles of  $[\text{ReTzPyTpy}]_3$  alone and with the addition of  $\text{Eu}^{3+}$  or  $\text{Gd}^{3+}$ . With the addition of  $\text{Eu}^{3+}$ , the  $^3\text{MLLCT}$  emission is significantly reduced in intensity, even further than that measured in the presence of  $\text{Gd}^{3+}$ , and red-shifted by 50 nm. The lifetime decay in deoxygenated solutions at 560 nm was also measured (Figure 5.24b). With the addition of  $\text{Eu}^{3+}$ , the lifetime of the  $^3\text{MLLCT}$  reduces by a factor of 10 from 295 ns, with  $\text{Gd}^{3+}$ , to 29 ns in the presence of  $\text{Eu}^{3+}$ . This change seems to suggest efficient energy transfer to the  $^5D_0$  excited state of  $\text{Eu}^{3+}$ . Looking at the  $^3\text{MLLCT}$  decay lifetime in air-equilibrated solutions, it can be seen that there is a similar reduction in lifetime when moving from  $\text{Gd}^{3+}$  (295 ns) to  $\text{Eu}^{3+}$  (29 ns). This may suggest that the rate of energy transfer, from the  $^3\text{MLLCT}$  of  $[\text{ReTzPyTpy}]_3$  to the  $^5D_0$  state of  $\text{Eu}^{3+}$ , is significantly faster than quenching by  $^3\text{O}_2$ .

The rate of energy transfer ( $k_{EnT}$ ) and the quantum efficiency of energy transfer ( $\phi_{EnT}$ ) can be calculated according to Equation 5.5 and Equation 5.6, respectively:

$$k_{EnT} = 1/\tau_q - 1/\tau_u \quad (5.5)$$

$$\phi_{EnT} = 1 - \tau_q/\tau_u \quad (5.6)$$

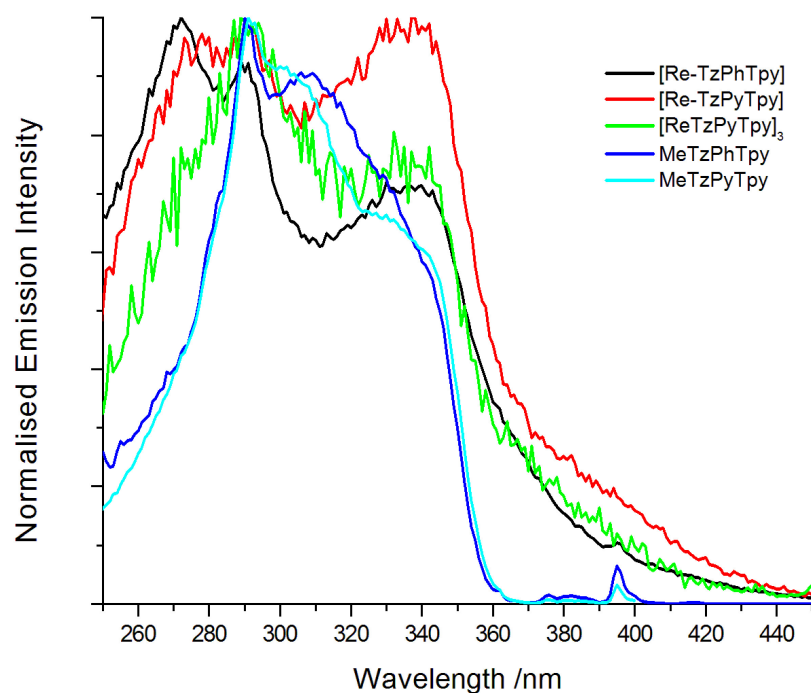
where  $\tau_q$  is the  $^3\text{MLLCT}$  decay lifetime in the presence of a quencher ( $\text{Eu}^{3+}$ ), and  $\tau_u$  is the  $^3\text{MLLCT}$  decay lifetime in the absence of a quencher, which is assumed to be very similar to that of the analogous  $\text{Gd}^{3+}$  complex in the same condition.<sup>118,119,124,131,146</sup> The rate of energy transfer may contain a deduction for energy back transfer due to the energy difference between the  $^3\text{MLCT}$  and the  $\text{Eu}^{3+}$  ( $^5D_0$ ) excited state.

**Table 5.11:** Rate and quantum efficiency of energy transfer of complexes to  $\text{Eu}^{3+}$ .

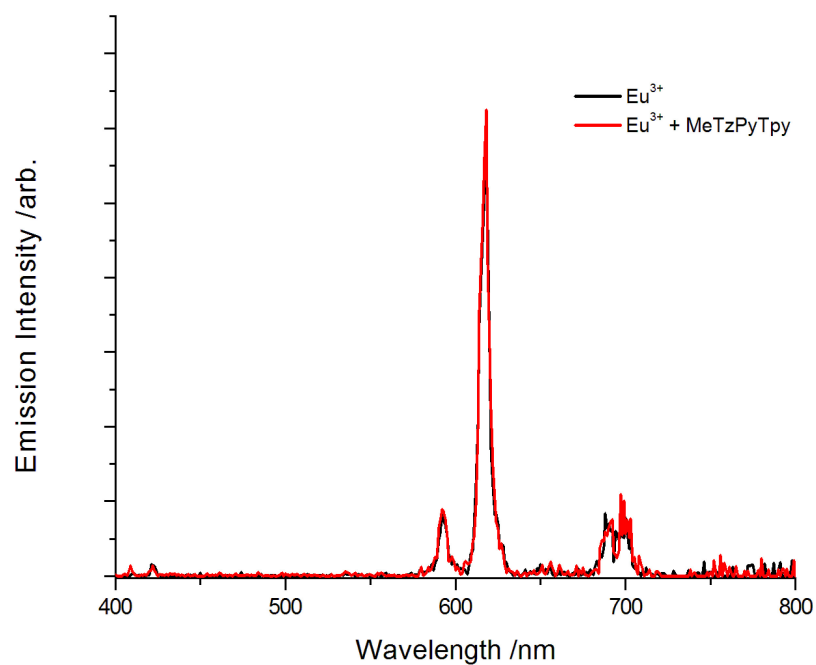
Sensitiser	$\tau_u^a$ [ns]	$\tau_q^b$ [ns]	$k_{EnT}$ [ $10^5\text{s}^{-1}$ ]	$\phi_{EnT}$
$[\text{Re-TzPhTpy}]$	764	473	8.05	0.381
$[\text{Re-TzPyTpy}]$	923	682	3.83	0.261
$[\text{ReTzPyTpy}]_3$	295	27	336.47	0.908

Lifetime data taken from Table 5.10 for deoxygenated solutions in the presence of  $^a\text{Gd}^{3+}$  and  $^b\text{Eu}^{3+}$ .

Table 5.11 illustrates the energy transfer rate and energy transfer quantum efficiency for the sensitisation of  $\text{Eu}^{3+}$ . The rate and quantum efficiency of energy transfer ( $^3\text{MLLCT} \rightarrow \text{Eu}^{3+}$ ) appears to decrease in the following order,  $[\text{ReTzPyTpy}]_3 \gg [\text{Re-TzPhTpy}] > [\text{Re-TzPyTpy}]$ . Interestingly, this result suggests that energy transfer from  $[\text{ReTzPyTpy}]_3$  to  $\text{Eu}^{3+}$  is very efficient.



**Figure 5.25:** Excitation spectra of Eu<sup>3+</sup> (617 nm) emission in dilute (10<sup>-5</sup> M) DCM solutions.



**Figure 5.26:** Emission spectra of acetonitrile solutions of Eu<sup>3+</sup>, alone and in presence of MeTzPyTpy, under excitation at 375 nm.

The excitation scans of the  ${}^5D_0 \rightarrow {}^7F_2$  emission from  $\text{Eu}^{3+}$  are shown in Figure 5.25. The similarity of the excitation spectra to the absorption spectra is suggestive that the sensitisation of  $\text{Eu}^{3+}$  is occurring from the  ${}^3\text{MLLCT}$  excited state of the  $\text{Re(I)}$  complex. There appears to be a contribution from the  $\text{MLLCT}$  excitation (375 nm) to the emission from  $\text{Eu}^{3+}$ . This may indicate involvement of the  $\text{MLLCT}$  in sensitisation of  $\text{Eu}^{3+}$ . However, it may also reflect the presence of residual  ${}^3\text{MLLCT}$  emission at 618 nm.

Figure 5.26 displays the emission spectra of  $\text{Eu}^{3+}$ , as a DMSO solvated nitrate salt, alone and in the presence of **MeTzPyTpy**. As can be seen at 375 nm excitation, the emission of  $\text{Eu}^{3+}$  in solution alone and in the presence of **MeTzPyTpy** are almost identical. This suggests that 375 nm wavelength excitation does not access ( $\pi - \pi^*$ ) excited states of the ligand and emission from  $\text{Eu}^{3+}$  is the result of direct excitation. The comparison of these spectra, and the evidence from excitation spectra, may suggest that when  $\text{Eu}^{3+}$  is in the presence of the synthesised complexes, excitation at 375 nm results in population of primarily the  $\text{MLLCT}$  excited state, with some possible minor contribution from direct excitation to the higher energy excited states ( ${}^5G_4$ ,  ${}^5G_6$ ) of  $\text{Eu}^{3+}$ .

### 5.3.5 Sensitisation of Yb<sup>3+</sup> by the synthesised complexes.

**Table 5.12:** Summary of photophysical properties in dilute (10<sup>-5</sup> M) DCM solutions.

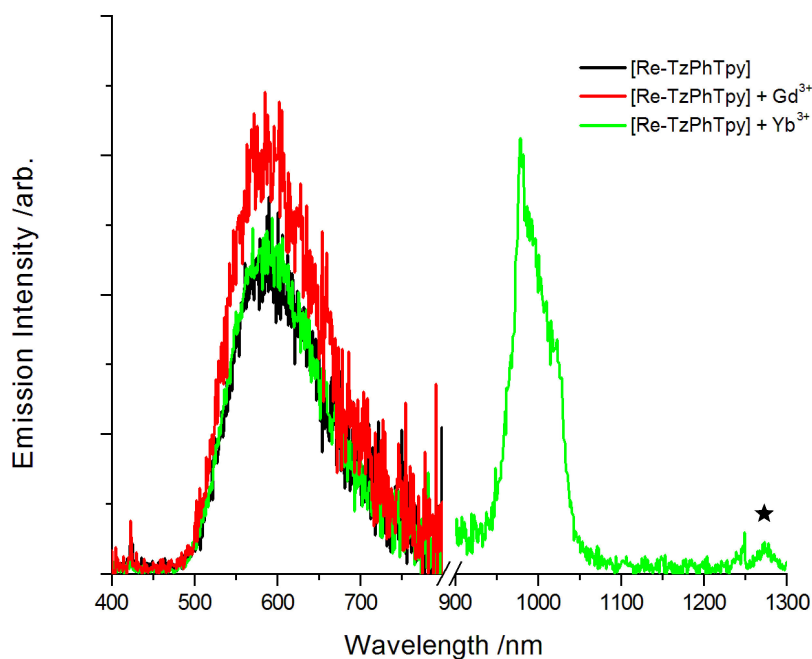
Species	Emission, 298 K						
	$\lambda_{max}$ [nm]	$\tau_{MLLCT}^a$ [ns]	$\phi_{MLLCT}^a$	$\tau_{MLLCT}^b$ [ns]	$\phi_{MLLCT}^b$	$\tau_{Yb}^a$ [ $\mu$ s]	$\tau_{Yb}^b$ [ $\mu$ s]
[ <b>Re-TzPhTpy</b> ] + Gd <sup>3+</sup>	590	276	0.029	764	0.069		
[ <b>Re-TzPhTpy</b> ] + Yb <sup>3+</sup>	588, 980	274	0.036	530	0.051	11.28	11.26
[ <b>Re-TzPyTpy</b> ] + Gd <sup>3+</sup>	560	519	0.048	923	0.093		
[ <b>Re-TzPyTpy</b> ] + Yb <sup>3+</sup>	565, 980	491	0.053	883	0.105	13.08	10.91
[ <b>ReTzPyTpy</b> ] <sub>3</sub> + Gd <sup>3+</sup>	570	238	0.033	295	0.036		
[ <b>ReTzPyTpy</b> ] <sub>3</sub> + Yb <sup>3+</sup>	580, 980	24	0.006	24	0.006	10.61	10.27

<sup>a</sup>Air-equilibrated solution, <sup>b</sup>deoxygenated solution, Gd<sup>3+</sup> data taken from Table 5.4 for reference. Quantum yield values for visible emission spectrum (400 - 800 nm) measured against an air-equilibrated aqueous solution of [Ru(**bpy**)<sub>3</sub>]Cl<sub>2</sub> ( $\phi = 0.028$ ).

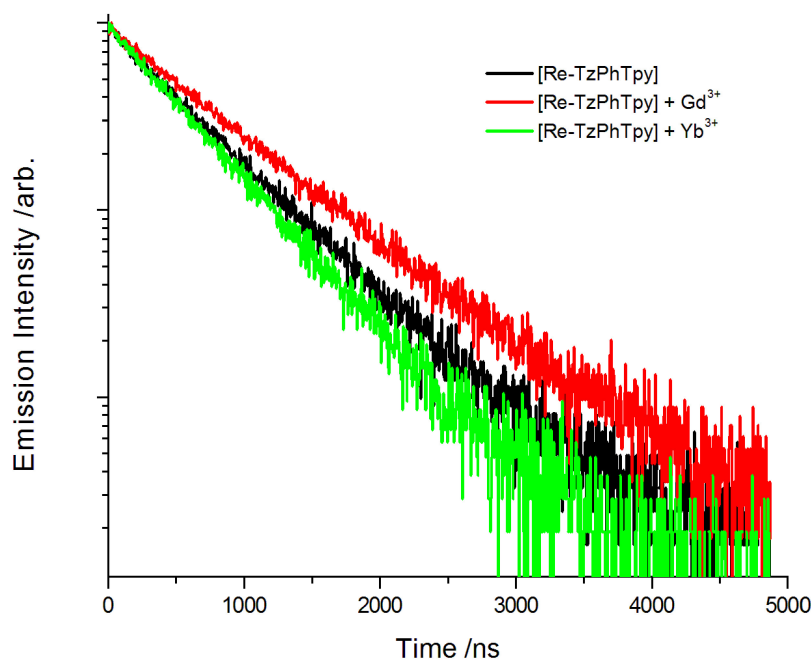
The addition of Yb<sup>3+</sup> to solutions containing the different Re(I) complexes causes analogous changes to the absorption spectra, as those observed in Figure 5.8.

The emission for these complexes is separated into two regions based on the detector used, the visible region (400 - 800 nm) to detect <sup>3</sup>MLLCT emission and the near infra-red (NIR) region (900 - 1300 nm) to detect emission from Yb<sup>3+</sup>. The spectra in the visible region are normalised to reflect the quantum yield of the <sup>3</sup>MLLCT emission. The emission intensity of the NIR region is arbitrarily normalised.

The visible and NIR emission spectra for [**Re-TzPhTpy**] alone and with Gd<sup>3+</sup> or Yb<sup>3+</sup>, are shown in Figure 5.27a. In comparison to the solution with Gd<sup>3+</sup>, the <sup>3</sup>MLLCT has reduced in quantum yield from 0.069 to 0.051, and the lifetime has reduced from 764 to 530 ns in deoxygenated conditions. This is suggestive that there may be partial energy transfer from the <sup>3</sup>MLLCT to the <sup>2</sup>F<sub>5/2</sub> or LMCT excited states of Yb<sup>3+</sup>. In air-equilibrated solutions, the <sup>3</sup>MLLCT lifetime decay does not change significantly when in the presence of Gd<sup>3+</sup> or Yb<sup>3+</sup>. Further to this, the NIR spectrum in air-equilibrated conditions displays a peak at 1275 nm corresponding to emission from <sup>1</sup>O<sub>2</sub>. This may suggest that the rate of sensitisation of Yb<sup>3+</sup> emission is competing with quenching by <sup>3</sup>O<sub>2</sub>.

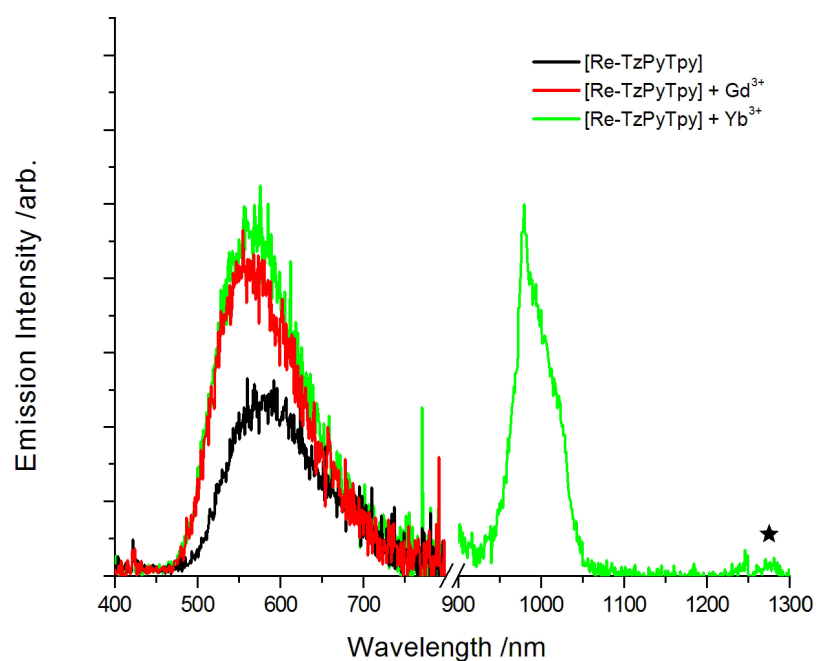


(a)

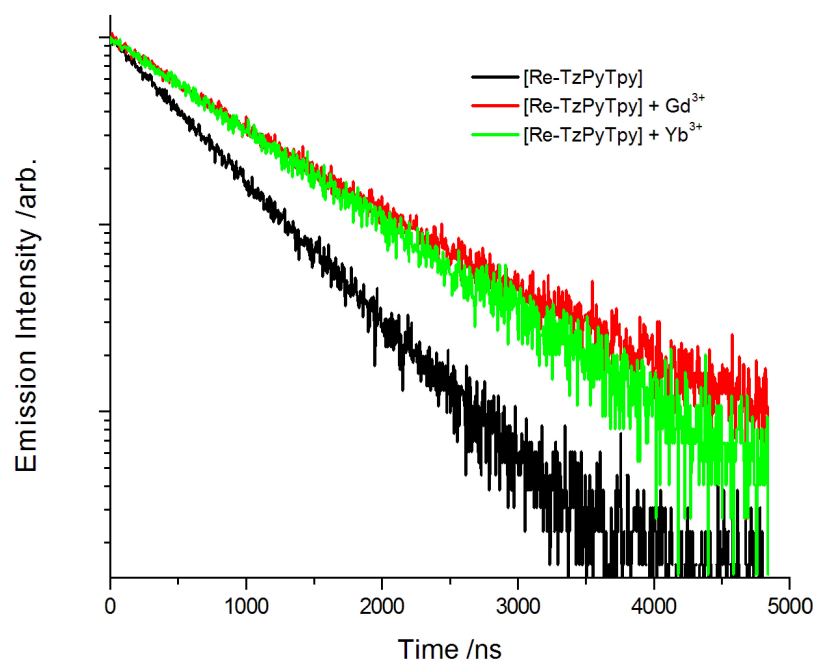


(b)

**Figure 5.27:** Emission properties of DCM solutions (ca.  $10^{-5}$  M) of [Re-TzPhTpy] alone and in the presence of  $\text{Yb}^{3+}$  under 375 nm excitation. a) Visible (deoxygenated) and NIR (air-equilibrated) emission spectra under excitation at 375 nm. Visible spectra normalised to absorbance value, NIR spectra arbitrarily normalised. Peak corresponding to emission from  $^1\text{O}_2$  denoted by a star. b) TCSPC decay of  $^3\text{MLLCT}$  emission, excited at 375 nm.



(a)



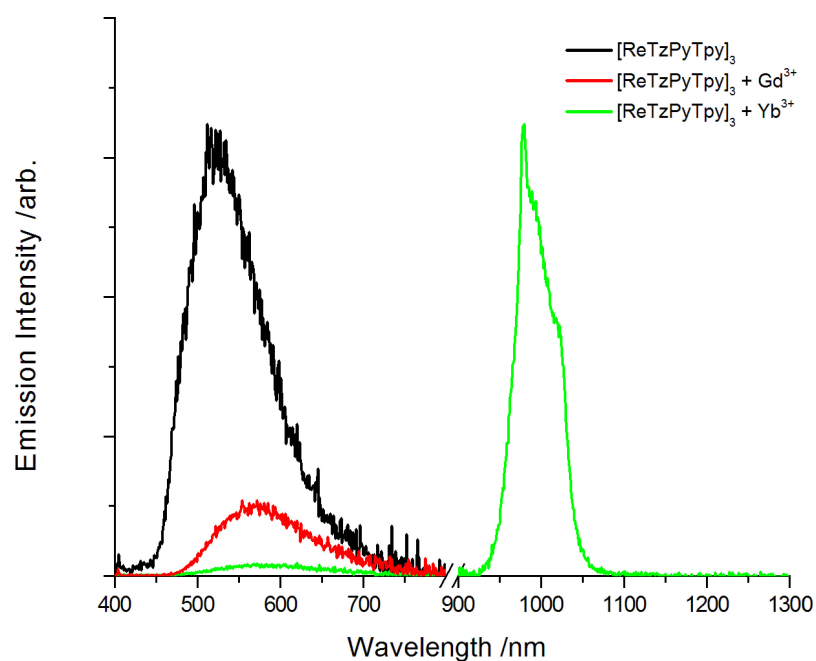
(b)

**Figure 5.28:** Emission properties of DCM solutions (ca.  $10^{-5}$  M) of [Re-TzPyTpy] alone and in the presence of Yb<sup>3+</sup> under 375 nm excitation. a) Visible (deoxygenated) and NIR (air-equilibrated) emission spectra under excitation at 375 nm. Visible spectra normalised to absorbance value, NIR spectra arbitrarily normalised. Peak corresponding to emission from <sup>1</sup>O<sub>2</sub> denoted by a star. b) TCSPC decay of <sup>3</sup>MLLCT emission, excited at 375 nm.

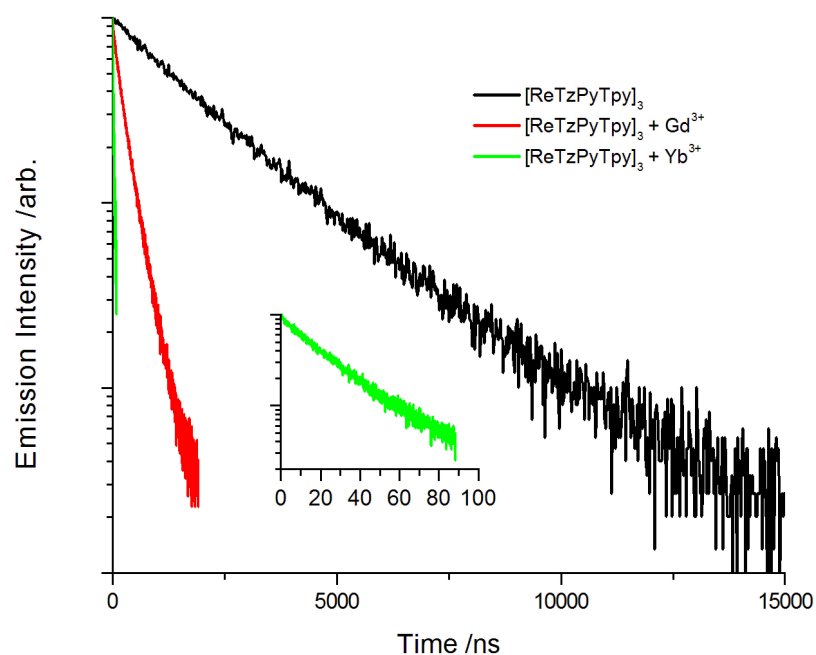
The emission spectra for [**Re-TzPyTpy**] alone and with  $\text{Gd}^{3+}$  or  $\text{Yb}^{3+}$  is shown in Figure 5.28a, and the decay profiles are shown in Figure 5.28b. It can be seen that, upon the addition of  $\text{Yb}^{3+}$ , the quantum yield and lifetime change to resemble those under the addition of  $\text{Gd}^{3+}$ , as shown in Table 5.12. This similarity is rationalised again by the energy gap law. This complex is still able to sensitise  $\text{Yb}^{3+}$ , however, the  $^3\text{MLLCT}$  does not appear to be an efficient sensitiser as the emission decay lifetime and quantum yield have not appreciably changed. In air-equilibrated solution, the NIR emission from this complex also displays a band of low intensity at 1275 nm corresponding to emission from  $^1\text{O}_2$ . This is suggestive that quenching of the  $^3\text{MLLCT}$  excited state by  $^3\text{O}_2$  is competing efficiently with the rate of sensitisation of  $\text{Yb}^{3+}$ .

It is noted for [**Re-TzPhTpy**] and [**Re-TzPyTpy**] that quenching by  $^3\text{O}_2$  is competing with the energy transfer process. There are occurrences of  $^3\text{O}_2$  dependent lanthanide luminescence reported in literature.<sup>72,125</sup> This may suggest these complexes can be exploited as ratiometric sensors for the presence of  $^3\text{O}_2$ . This aspect will require further investigation.





(a)



(b)

**Figure 5.29:** Emission properties of DCM solutions (ca.  $10^{-5}$  M) of [ReTzPyTpy]<sub>3</sub> alone and in the presence of Yb<sup>3+</sup> under 375 nm excitation. a) Visible (deoxygenated) and NIR (air-equilibrated) emission spectra under excitation at 375 nm. Visible spectra normalised to absorbance value, NIR spectra arbitrarily normalised. N.B. absence of peak at 1275 nm for emission from <sup>1</sup>O<sub>2</sub>. b) TCSPC decay of <sup>3</sup>MLLCT emission (deoxygenated), excited at 375 nm.

$[\text{ReTzPyTpy}]_3$  displays dramatically different emission properties when  $\text{Yb}^{3+}$  is added to the solution. Figure 5.29a shows that, in the presence of  $\text{Yb}^{3+}$ , the emission from the complex red-shifts to approximately 580 nm, analogous to the addition of  $\text{Gd}^{3+}$ , and decreases significantly in intensity. The emission lifetime of the  $^3\text{MLLCT}$  reduces from 295 ns ( $\text{Gd}^{3+}$ ) to 24 ns ( $\text{Yb}^{3+}$ ), as illustrated in Figure 5.29b. This dramatic reduction in lifetime and quantum yield suggests there is quenching of the  $^3\text{MLLCT}$  excited state for the sensitisation of  $\text{Yb}^{3+}$ . The lifetime and quantum yield of  $^3\text{MLCT}$  emission in air-equilibrated solutions change significantly when moving from the presence of  $\text{Gd}^{3+}$  to the presence of  $\text{Yb}^{3+}$ . The rate of energy transfer  $^3\text{MLLCT} \rightarrow \text{Yb}^{3+} ({}^2F_{5/2})/\text{LMCT}$  appears to be dominating over the rate of quenching by  $^3\text{O}_2$ . This is further suggested when measurements are taken in air-equilibrated solution, a band at 1275 nm, corresponding to emission from  $^1\text{O}_2$ , is absent in the NIR emission spectrum of  $[\text{ReTzPyTpy}]_3$ .

**Table 5.13:** Rate and quantum efficiency of energy transfer of complexes to  $\text{Yb}^{3+}$ .

Sensitiser	$\tau_u^a$ [ns]	$\tau_q^b$ [ns]	$k_{EnT}[10^5\text{s}^{-1}]$	$\phi_{EnT}$
$[\text{Re-TzPhTpy}]$	764	530	5.77	0.306
$[\text{Re-TzPyTpy}]$	923	883	- <sup>c</sup>	- <sup>c</sup>
$[\text{ReTzPyTpy}]_3$	295	24	382.77	0.919

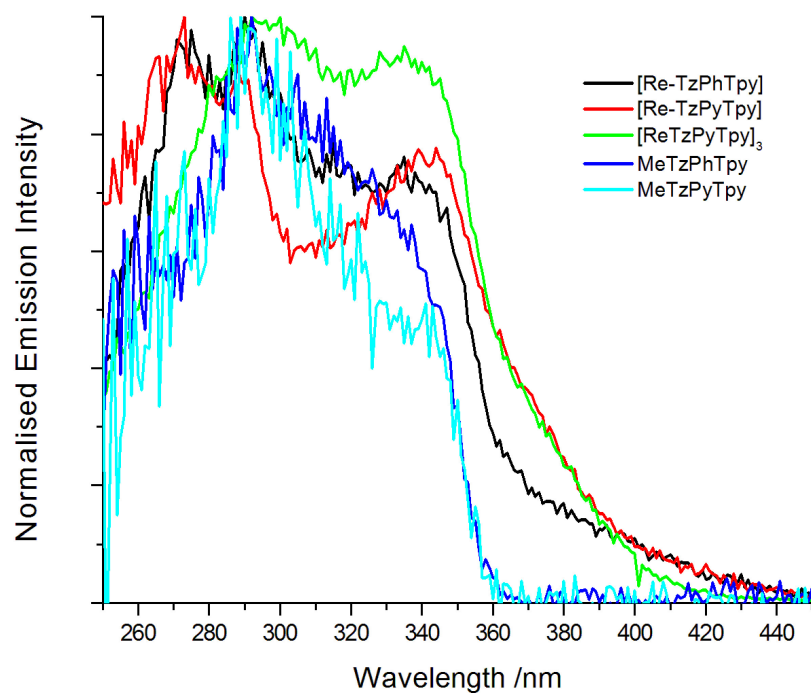
Lifetime data taken from Table 5.12 for deoxygenated solutions in the presence of  $^a\text{Gd}^{3+}$  and  $^b\text{Yb}^{3+}$ . <sup>c</sup>Values could not be accurately determined as lifetime values are within instrument uncertainty of  $\pm 8\%$ .

Table 5.13 illustrates the energy transfer rate and quantum efficiency for the complexes, calculated from Equation 5.5 and Equation 5.6. The rate and quantum efficiencies of energy transfer for  $[\text{Re-TzPhTpy}]$  to  $\text{Yb}^{3+}$  appear similar to those seen in Table 5.11 for  $\text{Eu}^{3+}$ .

The quenching of the lifetime of  $[\text{Re-TzPyTpy}]$  in the presence of  $\text{Yb}^{3+}$  is too low for accurate calculation of energy transfer rate and efficiency. Previously reported data (Table 5.11) suggested that sensitisation of  $\text{Eu}^{3+}$  by  $[\text{Re-TzPyTpy}]$  involves the  $^3\text{MLLCT}$  excited state. The sensitisation of  $\text{Yb}^{3+}$  by  $[\text{Re-TzPhTpy}]$  appears to involve the  $^3\text{MLLCT}$  (Table 5.13), which suggests that  $[\text{Re-TzPyTpy}]$  may perform similarly. Literature reports the sensitisation of  $\text{Yb}^{3+}$  can occur via the triplet excited state of the donor depending on Förster and Dexter overlaps or via the singlet excited state of the donor depending on the thermodynamic feasibility of the associated redox mechanism.<sup>288,289,293</sup> It is speculated that the low rate and quantum efficiency of the  $(^3\text{MLLCT}) \rightarrow \text{Yb}^{3+} ({}^2F_{5/2})$  energy transfer, from  $[\text{Re-TzPyTpy}]$ , may be due to the presence of two

chelated Yb<sup>3+</sup> ions reducing the Förster or Dexter overlap.

The rate of energy transfer by **[ReTzPyTpy]<sub>3</sub>** is 10 times slower than literature examples of the sensitisation of Yb<sup>3+</sup> by Re(I) diimine complexes ( $k_{EnT} = 3 \times 10^8 \text{ s}^{-1}$ ). However, in comparison to such literature reports, this complex appears to be the highest in quantum efficiency, where typical reports are (ca. 0.3).<sup>124,129,141,142,144–147,294</sup>



**Figure 5.30:** Excitation of Yb<sup>3+</sup> (980 nm) emission in dilute (10<sup>-5</sup> M) DCM solutions.

The excitation spectra of Yb<sup>3+</sup> (980 nm emission) in solution with the complexes and alkylated tetrazole containing ligands are shown in Figure 5.30. The excitation spectra for Yb<sup>3+</sup> in the presence of HTzPhTpy and HTzPyTpy are similar to MeTzPhTpy and MeTzPyTpy and are not shown for clarity. The spectra illustrate that the excitation of Yb<sup>3+</sup> in the presence of each of the metal complexes **[Re-TzPhTpy]**, **[Re-TzPyTpy]**, and **[ReTzPyTpy]<sub>3</sub>** contains the MLLCT excitation band at (370 - 440 nm). This is indicative that, for each complex, excitation to the <sup>1</sup>MLLCT results in a sensitisation process. This is an interesting result for **[Re-TzPyTpy]**, where excitation to the <sup>1</sup>MLLCT results in sensitisation of Yb<sup>3+</sup>, however, the <sup>3</sup>MLLCT does not appear to sensitise Yb<sup>3+</sup>. These results suggest that sensitisation of Yb<sup>3+</sup> by **[Re-TzPyTpy]** may be occurring directly from the <sup>1</sup>MLLCT excited state. This is in agreement with literature reports by Faulkner *et al* where this mechanism is also suggested.<sup>124</sup>

## 5.4 Conclusion

In this chapter, the previously synthesised terpyridine containing ligands and complexes have been shown to sensitise  $\text{Eu}^{3+}$  and  $\text{Yb}^{3+}$ . The complexes **[Re-TzPhTpy]** and **[Re-TzPyTpy]** appear to sensitise  $\text{Eu}^{3+}$  via the  $^3\text{MLLCT}$ , where **[Re-TzPhTpy]** appears to be the more efficient sensitiser. In the case of sensitisation of  $\text{Yb}^{3+}$ , **[Re-TzPhTpy]** appears to involve the  $^3\text{MLLCT}$  to a similar rate and quantum efficiency as for the sensitisation of  $\text{Eu}^{3+}$ . However, in the case of **[Re-TzPyTpy]** the sensitisation of  $\text{Yb}^{3+}$  via the  $^3\text{MLLCT}$  appears to be negligible, which may be a result of multiple chelation sites inhibiting the sensitisation process. Both **[Re-TzPhTpy]** and **[Re-TzPyTpy]** appear to sensitise  $\text{Eu}^{3+}$  at a faster rate and with greater efficiency than  $\text{Yb}^{3+}$ .

It would appear that **[ReTzPyTpy]<sub>3</sub>** is the best performer of the metal complexes. It is able to sensitise both  $\text{Eu}^{3+}$  and  $\text{Yb}^{3+}$  efficiently via the  $^3\text{MLLCT}$  excited state. It also appears that the rate (ca.  $3 \times 10^7$ ) and quantum efficiency (ca. 0.90) of the energy transfer processes are very similar for  $\text{Eu}^{3+}$  and  $\text{Yb}^{3+}$ . Literature reports of  $\text{Yb}^{3+}$  sensitisation by Re(I) complexes have sensitisation efficiencies ca. 0.30 with few at ca. 0.74, placing **[ReTzPyTpy]<sub>3</sub>** among the most efficient. The large value for quantum efficiency of sensitisation of  $\text{Eu}^{3+}$  by **[ReTzPyTpy]<sub>3</sub>** (0.908) suggests that  $\text{Eu}^{3+}$  sensitisation by Re(I) complexes may be an important avenue of research. In fact, this study reports the first investigation of mononuclear and multinuclear Re(I) complexes as sensitisers for  $\text{Eu}^{3+}$ .

# Chapter 6

## Conclusions and future work

The research presented in this thesis was intended to explore the properties of a variety of mononuclear and multinuclear Re(I) tetrazolato complexes where the chelating ligand was an aryl-tetrazole, then modify the ligand structure so that analogous complexes would coordinate  $\text{Ln}^{3+}$  cations in an attempt to sensitise their emission. This aim follows some interesting structures published recently around Re(I) tetrazolato complexes, and also the recent series of investigations into sensitisation of  $\text{Ln}^{3+}$  cations by Re(I) complexes. This type of investigation is of interest as inorganic complexes can be electronically excited by photons of energy in the visible region, making them very attractive in optical imaging.

The synthesis of Re(I) complexes with various aryl-tetrazole ligands appear to indicate that simple ligand modification can produce diverse structures. Of the synthesised complexes, a triangular structure was obtained from the combination of Re(I) with 5-(2-pyridyl)-1H-tetrazole which displayed emission at 490 nm. This interesting result was expanded on by forming an analogous triangular structure by using 4'-(5-(tetrazol-5-yl)-2-pyridyl)-2,2':6'2''-terpyridine as the ligand. This complex displayed a slightly red-shifted  $^3\text{MLCT}$  transition (510 nm) which was accompanied by a large increase in luminescence quantum yield and lifetime. Although there is precedence in literature of self-assembled multi-nuclear complexes of Re(I), these results suggests that diimine type ligands which contain anionic groups (e.g.  $\text{TzPy}^-$  and  $\text{TzPyTpy}^-$ ) will form neutral triangular complexes of Re(I) with relatively blue-shifted emission in comparison to most literature examples of neutral Re(I) complexes. This type of structure also appears to be rigid, which could contribute to the improved photophysical properties.

The synthesised triangular complex  $[\text{ReTzPyTpy}]_3$  successfully sensitises luminescence of both  $\text{Eu}^{3+}$  and  $\text{Yb}^{3+}$  with rates of ca.  $3 \times 10^7$  and quantum efficiencies of ca. 0.91. Although the rate is not as high as some literature examples of  $\text{Ln}^{3+}$  sensitisation by Re(I), the efficiency appears relatively high in comparison, which typical efficiencies range from 0.20 to 0.95. The ability to sensitise  $\text{Eu}^{3+}$  by

a Re(I) complex, let alone a multinuclear Re(I) complex, has not been reported previously in literature. This may indicate that some reported complexes of Re(I) which sensitise NIR-emitting lanthanides, particularly those with emission  $\leq 560$  nm may display a similar sensitisation of visible emitting lanthanides.

Mononuclear Re(I) complexes with ***t*BuTzPy** as a chelating ligand were successfully formed, and their photophysical properties were found to be similar to literature reports of neutral Re(I) diimine complexes.<sup>60</sup> However, when attempting to form an analogous complex with **MeTzPyTpy**, the presence of the terpyridine moiety may have competed for chelation, and hence the target complex could not be formed this way. During the attempt to form a terpyridine containing analogue of **[Re(*t*BuTzPy)Cl]**, which was unsuccessful, **[Re(MeTzPyCHO)Cl]** was formed. This complex displayed a red-shifted emission ( $\lambda_{em} = 645$  nm) along with low quantum yield and lifetime in comparison to **[Re(*t*BuTzPy)Cl]**.

The expansion of the ligand library successfully formed tetrazole functionalised 4'-aryl-2,2':6'2''-terpyridines and their alkylated derivatives. These ligands on their own displayed fluorescent properties which responded to changes to the acidity/alkalinity of their environment, and successfully sensitise emission from  $\text{Eu}^{3+}$  and  $\text{Yb}^{3+}$  in solution.

The expansion of previously reported Re(I) tetrazolato complexes to attach the synthesised tetrazole functionalised 4'-aryl-2,2':6'2''-terpyridine ligands was successful, and the photophysical properties of these new Re(I) complexes appear similar to the literature examples.<sup>1,2</sup>

The sensitisation of  $\text{Eu}^{3+}$  and  $\text{Yb}^{3+}$  in solution was observed for all synthesised terpyridine containing complexes. Although it was expected that sensitisation of  $\text{Yb}^{3+}$  would be more efficient than  $\text{Eu}^{3+}$  due to the relative energies of the excited states, this only proved true for **[ReTzPyTpy]<sub>3</sub>**. It is interesting to note that the sensitisation of  $\text{Eu}^{3+}$  by **[Re-TzPhTpy]** and **[Re-TzPhTpy]** appears to have similar efficiency and energy transfer rate to some reports of  $\text{Yb}^{3+}$  sensitisation by Re(I) complexes ( $\phi_{EnT} \approx 0.30$ ).<sup>124,147</sup> Further, sensitisation of  $\text{Yb}^{3+}$  by **[Re-TzPyTpy]** does not appear to involve the <sup>3</sup>MLLCT excited state, however, excitation to the <sup>1</sup>MLLCT excited state ( $\lambda_{ex} = 375$  nm) sensitises emission from  $\text{Yb}^{3+}$ . These results indicates that pursuing research to understand this <sup>3</sup>MLCT  $\rightarrow$   $\text{Ln}^{3+}$  sensitisation mechanism may be very important, particularly in the case of  $\text{Yb}^{3+}$ . Although this study focused only on solution state sensitisation in the presence of excess  $\text{Eu}^{3+}$  and  $\text{Yb}^{3+}$  by three Re(I) complexes, the results may suggest that limiting investigations to sensitising only NIR-emitting  $\text{Ln}^{3+}$  cations by Re(I) complexes should be avoided, as it is possible there is much more to discover.

The diverse structures obtained in Chapter 2 suggest further investigation is nec-

essary. This study was limited to two aryl-tetrazoles and their N2 alkylated derivatives, there may be many more diverse structures obtainable with modifications of these ligands. Slight modifications to the ligands are possible, such as utilising pyrimidine or pyrazine groups instead of pyridine. These ligand modifications may also result in other interesting structures with electronic properties that can be investigated.

The results obtained when synthesising complexes utilising derivatives of 5-(2-pyridyl)-1H-tetrazole suggest that ligands containing this moiety have versatile uses. The alkylated derivative  ${}^t\text{BuTzPy}$  readily chelated Re(I) to form mononuclear complexes, of which further derivatisation of the ligand may yield interesting properties, or potential applications. The 5-(2-pyridyl)-1H-tetrazole moiety appears to encourage the formation of triangular structures with "blue" emission and high quantum yields and lifetimes. Further investigation is warranted to discover how photophysical properties can be modulated in this type of structure and its potential applications. It may be particularly interesting to investigate application in light emitting devices as the thermal stability of this complex may indicate that vacuum sublimation is possible. The pyridyl group can also be substituted for pyrazine or pyrimidine groups to determine how more chelation sites may alter structures and properties.

The interesting structures formed with  $\text{TzPh}^-$  and  ${}^t\text{BuTzPh}$  may require further investigation. This study was limited to pursue stable complexes that displayed interesting photophysical properties. Stable Re(I) diazine complexes have been reported in literature, and this may suggest a similar capacity could be obtained with Re(I) complexes of  ${}^t\text{BuTzPh}$  derivatives.<sup>236</sup> The "propeller" type complex,  $[\text{Re}_2(\text{TzPh})_3]^-$ , may also be exploited in some electrochemical process due to the presence of a reversible oxidation peak, substitution on the phenyl ring may lead to the formation of metallo-organic framework type structures, and further substitutions to obtain luminescent derivatives of this type of structure may lead to compounds usable in electrochemiluminescent devices.

Re(I) complexes utilising alkylated tetrazole ligands as chelating groups also have room for investigation. Substitution of other functional groups may lead to interesting tuning properties, as seen for  $[\text{Re}(\text{MeTzPyCHO})\text{Cl}]$ .

The use of terpyridine containing ligands to detect cations in solution is also an area of interest. Literature progress has suggested that functionalised 2,2':6',2"-terpyridines can be fluorescent sensors of different cations in solution.<sup>260</sup> The investigations in this thesis suggested that the synthesised tetrazole functionalised terpyridines may behave as fluorescent sensors of acidic or alkali conditions of solutions. Although this investigation only explored acidic and alkali conditions, the presence of multiple chelation sites in ligands such as  $\text{TzPyTpy}^-$  may en-

able selective sensing of specific cations, or multiple cations in solution. Further investigations into the sensing ability for these ligands should be performed by monitoring the UV-vis and emission spectra during titration with cations such as zinc, calcium, cadmium, and nickel. Further, combinations of such cations would also determine if ratiometric sensing is possible.

The synthesised complexes that have shown an ability to sensitise luminescence of  $\text{Ln}^{3+}$  cations may also have further interesting properties. The terpyridine moiety has been established as a possible sensor for cations in solution,<sup>260</sup> and Re(I) tetrazolato complexes of 5-(2-pyridyl)-1H-tetrazole have luminescent responses to dissolved species.<sup>46</sup> The investigation in this thesis did not explore the use of these complexes as chemosensors, thus expanding the research into cation recognition utilising [**Re-TzPhTpy**] and [**Re-TzPyTpy**] may be of interest.

Sensitisation of  $\text{Ln}^{3+}$  cations was achieved by the synthesised mononuclear and multinuclear complexes containing terpyridine ligands. The extension of the study area to include the full emissive  $\text{Ln}^{3+}$  library may help understand the sensitisation mechanisms. Further, there may be multiple different changes that are possible in future studies. Modification of the ligands to include derivatives of 1,3,5-triazine, or ligands containing  $\beta$ -diketone structures may lead to different sensitisation capabilities. These modifications could be applied to the chelating ligand in mononuclear complexes, the ancillary ligand in mononuclear complexes, the bridging ligand in multinuclear complexes, and charged versions of these species. The results in this thesis also suggest that further research efforts could include sensitisation of  $\text{Eu}^{3+}$  as efficient sensitisation of  $\text{Eu}^{3+}$  by an Re(I) complexes appears to be possible. Further research into the difference in sensitisation when a  $\text{Ln}^{3+}$  cation coordinates to a chelating or ancillary ligand of Re(I) could help to further elucidate sensitisation mechanisms. Further, this investigation could be extended to include solid state studies, where crystallisation experiments could help elucidate coordination sites of  $\text{Ln}^{3+}$  cations, and photophysical studies may help investigate potential applications in light emitting devices.



# Chapter 7

## Experimental

### General experimental

All reagents and solvents were purchased from Sigma Aldrich and used as received without further purification. 2-(1H-Tetrazol-5-yl)pyridine and 5-phenyl-1H-tetrazole were synthesized according to previously published procedures.<sup>148</sup> 2-(2-tert-Butyltetrazol-5-yl)pyridine and 5-phenyl-2-tert-butyltetrazole were also synthesized according to published procedures.<sup>190,225</sup>

6-cyanopyridine-3-carboxaldehyde was synthesised and characterised consistent with published data.<sup>266</sup> Acidic alumina for column chromatography was of Brockmann I activity. Nuclear magnetic resonance spectra, consisting of <sup>1</sup>H and <sup>13</sup>C, were recorded using a Bruker Avance 400 spectrometer (400.1 MHz for <sup>1</sup>H, 100 MHz for <sup>13</sup>C) at 300 K. <sup>1</sup>H and <sup>13</sup>C chemical shifts were referenced to residual solvent signals. Infrared spectra were recorded in the solid state, using an attenuated total reflectance Perkin-Elmer Spectrum 100 FT-IR, equipped with a diamond stage. Compounds were scanned from 4000 to 650 cm<sup>-1</sup>. The intensities of the IR bands are reported as strong (s), medium (m), or weak (w). Melting points were determined Using a BI Barnstead Electrothermal 9100 apparatus. Elemental analyses were obtained at the Central Science Laboratory, University of Tasmania, using a Thermo Finnigan EA 1112 Series Flash, or by Robert Herman at the Department of Chemistry, Curtin University.

### Photophysical results

Absorption spectra were recorded at room temperature using a Perkin Elmer Lambda 35 UV/Vis spectrometer. Uncorrected steady state emission and excitation spectra were recorded on an Edinburgh FLSP980 spectrometer equipped with a 450 W Xenon arc lamp, double excitation and double emission monochromators and a Peltier cooled Hamamatsu R928P photomultiplier tube (185-850 nm). Emission and excitation spectra were corrected for source intensity (lamp

and grating) and emission spectral response (detector and grating) by a calibration curve supplied with the instrument. According to the approach described by Demas and Crosby,<sup>295</sup> luminescence quantum yields ( $\phi_{em}$ ) were measured in optically dilute solutions (O.D. < 0.1 at excitation wavelength) obtained from absorption spectra on a wavelength scale [nm] and compared to the reference emitter by the following equation:

$$\phi_x = \phi_r \left[ \frac{A_r(\lambda_r) I_r(\lambda_r) n_x^2 D_x}{A_x(\lambda_x) I_x(\lambda_x) n_r^2 D_r} \right] \quad (7.1)$$

where A is the absorbance at the excitation wavelength ( $\lambda$ ), I is the intensity of the excitation light at the excitation wavelength ( $\lambda$ ), n is the refractive index of the solvent, D is the integrated intensity of the luminescence and  $\phi$  is the quantum yield. The subscripts r and x refer to the reference and the sample, respectively. The quantum yield determinations were performed at identical excitation wavelength for the sample and the reference, therefore cancelling the  $I_r/I_x$  term in the equation. All Re(I) complexes were measured against an air-equilibrated water solution of [Ru(bpy)<sub>3</sub>]Cl<sub>2</sub> used as reference ( $\phi_r = 0.028$ ), and organic ligands measured against an air-equilibrated water solution of quinine sulphate in 0.1 M H<sub>2</sub>SO<sub>4</sub> ( $\phi_r = 0.546$ ).<sup>296</sup> Emission lifetimes ( $\tau$ ) were determined with the single photon counting technique (TCSPC) with the same Edinburgh FLSP920 spectrometer using pulsed picosecond LEDs (EPLIED 295 or EPLIED 360, FWHM < 800 ps) as the excitation source, with repetition rates between 10 kHz and 1 MHz, and the above-mentioned R928P PMT as detector. Emission lifetimes ( $\tau$ ) of Ln<sup>3+</sup> cations were determined with a microsecond flash-lamp. The goodness of fit was assessed by minimising the reduced  $\chi^2$  function and by visual inspection of the weighted residuals. To record the 77 K luminescence spectra, the samples were put in glass tubes (2 mm diameter) and inserted in a special quartz dewar filled up with liquid nitrogen. The solvents used for the preparation of the solutions for photophysical investigations was of spectrometric grade. The prepared solution was filtered through a 0.2 mm syringe filter before measurement. Deaerated samples were prepared by the freeze-pump-thaw technique. Experimental uncertainties are estimated to be  $\pm 8\%$  for lifetime determinations,  $\pm 20\%$  for quantum yields,  $\pm 2$  nm and  $\pm 5$  nm for absorption and emission peaks, respectively.

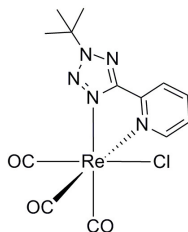
### Electrochemical measurements

A gold microelectrode (made in house and kindly donated by the group of Professor Richard Compton at Oxford University, UK) was polished and modified with a section of disposable micropipette tip into which microlitre quantities of the ionic liquid solvent can be placed. The electrode was then inserted into a

T-cell apparatus as described elsewhere.<sup>2,297</sup> A silver wire (0.5 mm diameter) was inserted from the top and acted as a combined counter and reference electrode. The T-cell was placed inside an aluminium Faraday cage and connected to a vacuum pump (Edwards ES50). The samples for electrochemistry were prepared by dissolving the required amount of rhenium complex in a minimal amount of dichloromethane and then adding this solution to the ionic liquid, 1-hexyl-3-methylimidazolium tris(pentafluoroethyl)trifluorophosphate (C6mim)[FAP], in order to obtain a final concentration of the order of 1 - 10 mM. The solution was left in an open container to allow the dichloromethane to evaporate. 40 L of this sample was transferred into the T-cell with the use of a micropipette. Experiments requiring the use of ferrocene followed the above procedure, however 10 L of a 10 mM solution of ferrocene in acetonitrile was added into the T-cell apparatus along with the ionic liquid containing the rhenium complex. Cyclic voltammetry experiments were performed using a PGSTAT302N potentiostat (Eco-Chemie, Netherlands) interfaced to a PC with GPES (General Purpose Electrochemical System) software. The step potential was fixed at 0.01 V. The potentials are referenced to an internal reference Ferrocene/Ferrocenium redox couple according to IUPAC recommendations and established in ionic liquids.<sup>298-300</sup> Scans were performed using a potential window within the range of -1.7 to 2.5 V reliant on the compound investigated. Reported potentials were obtained from a scan rate of 100 mVs<sup>-1</sup>.

### Computational method

Time-dependent density functional theory calculations were performed with Gaussian 09<sup>301</sup> in order to calculate the absorption spectra of all compounds. Prior to these calculations the structures were relaxed at the CAM-B3LYP level of theory. Re atoms were treated with the StuttgartDresden (SDD) effective core potential,<sup>302</sup> and the 6-311G\*\* basis set for other atoms. The effect of the solvent was mimicked with the PCM solvation model.<sup>303</sup> The low-lying singletsinglet excitation energies were calculated at the same level of theory, and the spectra were reproduced as the superposition of Gaussian functions with heights proportional to the calculated intensities and a variance of 11 nm.

**Synthesis of [Re(<sup>t</sup>BuTzPy)Cl]**


[Re(CO)<sub>5</sub>Cl] (100 mg, 0.27 mmol) and 2-(2-tertbutyl-tetrazol-5-yl)pyridine (100 mg, 0.54 mmol) were combined in toluene (15 mL) and stirred at reflux for 6 hours. The mixture was cooled and the solvent removed under reduced pressure giving a suspension of yellow solid in an oil. The compound was recovered by crystallisation from DCM by the addition of pet spirits, the mixture was filtered and washed with pet spirits giving a bright yellow solid. Single crystals suitable for X-ray diffraction were grown by layering hexanes on a dilute dichloromethane solution of the compound. Yield: 0.145 g (99 %) m.p. 210 - 215 °C.

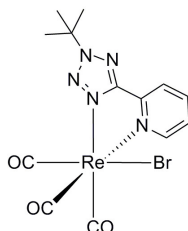
IR  $\nu_{max}/\text{cm}^{-1}$ : 2990 w, 2021 s (CO), 1884 s (CO). 1618 w, 1453 w, 1176 w.

UV-Vis (CH<sub>2</sub>Cl<sub>2</sub>)  $\lambda_{max}/\text{nm}$  ( $10^4\epsilon/\text{M}^{-1}\text{cm}^{-1}$ ): 271(2.90), 353(0.45).

<sup>1</sup>H NMR ( $\delta$ , ppm, CDCl<sub>3</sub>): 9.08 (1H, d, J = 5.4 Hz, **H**<sub>6(py)</sub>), 8.28 (1H, d, J = 8.1 Hz, **H**<sub>(py)</sub>), 8.16-8.11 (1H, m, **H**<sub>(py)</sub>), 7.65-7.60 (1H, m, **H**<sub>(py)</sub>), 1.88 (9H, s, (CH<sub>3</sub>)<sub>3</sub>).

<sup>13</sup>C NMR ( $\delta$ , ppm, CDCl<sub>3</sub>): 196.5 (CO), 194.7 (CO), 188.5 (CO), 166.1 (CN<sub>4</sub>), 153.9, 145.2, 139.8, 128.3, 124.0, 68.4, 29.2.

Anal. Calcd (%) for [Re(<sup>t</sup>BuTzPy)Cl]·(CH<sub>2</sub>Cl<sub>2</sub>) : C 28.31, H 2.55, N 11.79. Found: C 28.53, H 2.53, N 12.05.

**Synthesis of [Re(<sup>t</sup>BuTzPy)Br]**


[Re(CO)<sub>5</sub>Br] (100 mg, 0.27 mmol) and 2-(2-tertbutyl-tetrazol-5-yl)pyridine (100 mg, 0.54 mmol) were combined in toluene (15 mL) and stirred at reflux for 6 hours. The mixture was cooled and the solvent removed under reduced pressure giving a yellow oil. The compound was recovered by crystallisation from DCM by the addition of pet spirits, the mixture was filtered and washed with pet spirits giving a bright yellow solid. Single crystals suitable for X-ray diffraction were grown by layering hexanes on a dichloromethane solution of the compound.

Yield: 0.098 g (65 %) m.p. 207 - 209 °C.

IR  $\nu_{max}/\text{cm}^{-1}$ : 2990 w, 2020 s (CO), 1881 s (CO), 1620 w, 1452 w, 1176 w.

UV-Vis ( $\text{CH}_2\text{Cl}_2$ )  $\lambda_{max}/\text{nm}$  ( $10^4\epsilon/\text{M}^{-1}\text{cm}^{-1}$ ): 268(2.48), 358(0.31).

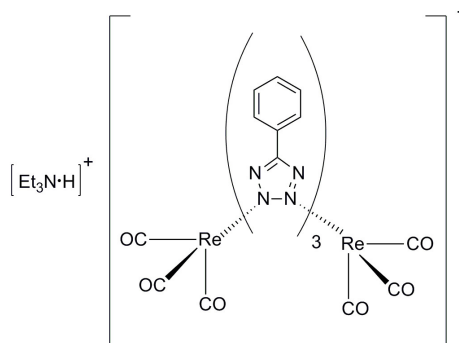
$^1\text{H}$  NMR ( $\delta$ , ppm,  $\text{CDCl}_3$ ): 9.09 (1H, d,  $J = 4.8$  Hz,  $\mathbf{H}_{6(py)}$ ), 8.29 (1 H, d,  $J = 7.8$  Hz,  $\mathbf{H}_{3(py)}$ ), 8.15-8.10 (1H, m,  $\mathbf{H}_{(py)}$ ), 7.64-7.59 (1H, m,  $\mathbf{H}_{(py)}$ ), 1.88 (9H, s,  $(\text{CH}_3)_3$ ).

$^{13}\text{C}$  NMR ( $\delta$ , ppm,  $\text{CDCl}_3$ ): 196.1 (CO), 194.3 (CO), 188.0 (CO), 166.2 ( $\text{CN}_4$ ), 154.8, 145.4, 139.7, 128.2, 124.0, 68.5, 29.5.

Anal. Calcd (%) for  $[\text{Re}(\text{tBuTzPy})\text{Br}] \cdot 1.2(\text{CH}_2\text{Cl}_2)$  : C 26.08, H 2.37, N 10.73.

Found: C 25.82, H 2.22, N 11.12.

### Synthesis of $[\text{HNEt}_3][\text{Re}_2(\text{TzPh})_3]$



$[\text{Re}(\text{CO})_5\text{Br}]$  (100 mg, 0.25 mmol), 5-phenyl-1H-tetrazole (53 mg, 0.36 mmol) and triethylamine (50  $\mu\text{L}$ , 0.36 mmol) were combined in toluene and stirred at reflux for 12 h. The mixture was cooled and the solvent removed under reduced pressure. The residue was added to dichloromethane, and the white solid formed was filtered, washed with dichloromethane, and recrystallized from water, yielding the title compound. Yield: 60 mg (45%). m.p. 258 °C dec.

IR  $\nu_{max}/\text{cm}^{-1}$ : 3650 w, 2024 s (CO), 1901 s (CO), 1610 w, 1449 w, 1140 w, 1062 w.

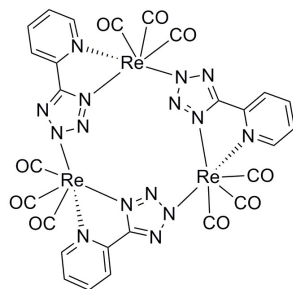
UV-Vis ( $\text{CH}_2\text{Cl}_2$ )  $\lambda_{max}/\text{nm}$  ( $10^4\epsilon/\text{M}^{-1}\text{cm}^{-1}$ ): 253(6.85), 312(0.60).

$^1\text{H}$  NMR ( $\delta$ , ppm, acetone- $d_6$ ): 8.15-8.10 (6H, m  $\mathbf{H}_{(ph)}$ ), 7.53-7.43 (9H, m,  $\mathbf{H}_{(ph)}$ ), 3.42 (6H, q,  $J = 7.2$  Hz,  $\text{NCH}_2\text{CH}_3$ ), 1.39 (9H, t,  $J = 7.2$  Hz,  $\text{NCH}_2\text{CH}_3$ ); solvent peak at 2.80 (s,  $\text{H}_2\text{O}$ ).

$^{13}\text{C}$  NMR ( $\delta$ , ppm, acetone): 196.6 (CO), 167.0 ( $\text{CN}_4$ ), 130.6, 129.7, 129.0, 127.5, 46.90, 9.0.

Anal. Calcd (%) for  $[\text{HNEt}_3][\text{Re}_2(\text{TzPh})_3] \cdot 2(\text{H}_2\text{O})$  : C 35.58, H 3.17, N 16.34.

Found: C 35.82, H 2.89, N 16.32.

Synthesis of [ReTzPy]<sub>3</sub>

[Re(CO)<sub>5</sub>Cl] (300 mg, 0.83 mmol) and 2-(1H-tetrazol-5-yl)pyridine (120 mg, 0.83 mmol) were combined in toluene (25 mL). Triethylamine (114  $\mu$ L, 0.83 mmol) was added and the mixture was stirred at reflux for 12 hours. The mixture was then cooled to room temperature and the solvent was removed under reduced pressure. The resulting solid was dissolved in dichloromethane (50 mL) and sequentially washed with 25 mL of saturated sodium carbonate solution, water, and eventually brine. The organic phase was collected, dried over MgSO<sub>4</sub> and the solvent was reduced to a minimal amount (ca. 2-3 mL). The solution was then charged on an alumina-packed column and dichloromethane was used as the eluent. The first fraction was collected and the solvent was removed to yield a white powder. Single crystals suitable for X-ray diffraction were grown by layering hexanes on a dichloromethane solution of the complex. Similar results were obtained starting from [Re(CO)<sub>5</sub>Br]. Yield: 123 mg (36 %). m.p. > 350 °C.

IR  $\nu_{max}/\text{cm}^{-1}$ : 2027 s (CO), 1917 s (CO), 1898 s (CO), 1621 m, 1568 w, 1449 m, 1288 w, 1254 w, 1158 w, 1105 w, 1047 w, 792 w, 754 w, 724 w.

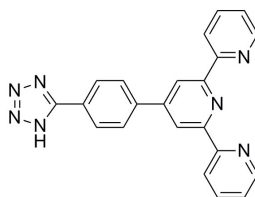
UV-Vis (CH<sub>2</sub>Cl<sub>2</sub>)  $\lambda_{max}/\text{nm}$  ( $10^4\epsilon/\text{M}^{-1}\text{cm}^{-1}$ ): 252(5.26), 283(3.88), 310(2.01).

<sup>1</sup>H NMR ( $\delta$ , ppm, acetone-*d*<sub>6</sub>): 9.28 (1H, d, *J* = 5.8 Hz, **H**<sub>2(py)</sub>), 9.23 (1H, d, *J* = 5.6 Hz, **H**<sub>2(py)</sub>), 9.13 (1H, d, *J* = 5.2 Hz, **H**<sub>2(py)</sub>), 8.53-8.43 (4H, m, **H**<sub>(py)</sub>), 8.32-8.25 (1H, m, **H**<sub>(py)</sub>), 7.89-7.76 (3H, m, **H**<sub>(py)</sub>), 7.63 (1H, d, *J* = 8.1 Hz, **H**<sub>(py)</sub>).

<sup>13</sup>C NMR ( $\delta$ , ppm, acetone-*d*<sub>6</sub>): nine CO peaks expected but due to low intensity and overlapping nature only six could be clearly distinguished; some signals belonging to the tertiary C atoms in the pyridine ring are also overlapping: 198.0 (CO), 197.7 (CO), 195.1 (CO), 194.8 (CO), 194.2 (CO), 193.6 (CO), 168.1 (CN<sub>4</sub>), 167.8 (CN<sub>4</sub>), 166.3 (CN<sub>4</sub>), 155.5, 155.4, 155.3, 149.3, 149.0, 148.2, 142.3, 141.9, 128.6, 128.5, 128.4, 124.0, 123.9, 123.4.

Anal. Calcd (%) for [ReTzPy]<sub>3</sub>: C 25.96, H 0.97, N 16.82. Found: C 26.12, H 0.96, N 16.74.

### Synthesis of HTzPhTpy



To toluene (50 mL) in an ice bath, triethylamine (0.8 mL, 5.8 mmol) and  $\text{HCl}_{(aq)}$  (0.70 mL, 5.8 mmol) were combined and stirred until fuming subsided. **NCPhtpy** (1.93 g, 5.8 mmol) and  $\text{NaN}_3$  (0.4 g, 5.8 mmol) were added and the mixture was stirred at reflux overnight. The solvent was evaporated under reduced pressure and the solid recrystallised from water (50 mL) and then washed with ( $3 \times 20\text{mL}$ ) DCM. Yield: 0.750 g (35 %) m.p. 280 °C dec.

IR  $\nu_{max}/\text{cm}^{-1}$ : 3046 m, 2444 m, 1683 w, 1605 w, 1593 s, 1581 s, 1542 s, 1470 m, 1393 s, 1295 w, 1113 w, 1076 w, 1008 s, 890 w, 842 w, 793 s.

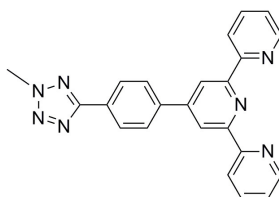
UV-Vis ( $\text{CH}_3\text{CN}$ )  $\lambda_{max}/\text{nm}$  ( $10^4\epsilon/\text{M}^{-1}\text{cm}^{-1}$ ): 295(2.06), 253(1.15), 231(1.51).

$^1\text{H}$  NMR ( $\delta$ , ppm,  $\text{DMSO}-d_6$ ): 8.78-8.75 (4H, m,  $\mathbf{H}_{3',5'}$  &  $\mathbf{H}_{6,6''}$ ), 8.66 (2H, d,  $J = 8$  Hz,  $\mathbf{H}_{3,3''}$ ), 8.26 (2H, d,  $J = 8.8$  Hz,  $\mathbf{H}_o$ ), 8.82 (2H, m,  $J = 2.4$  Hz,  $\mathbf{H}_{4,4''}$ ), 7.97 (2H, d,  $J = 8.4\text{Hz}$ ,  $\mathbf{H}_m$ ), 7.54-7.49 (2H, m,  $\mathbf{H}_{5,5''}$ ).

$^{13}\text{C}$  NMR ( $\delta$ , ppm,  $\text{DMSO}-d_6$ ): 160.3 ( $\text{N}_4\text{C}$ ), 155.7, 155.0, 149.4, 149.2, 137.4, 135.8, 133.6, 127.0, 126.7, 124.5, 120.9, 117.6.

Anal. Calcd (%) for **HTzPhTpy** $\cdot 0.2(\text{H}_2\text{O})$  : C 69.35, H 4.02, N 25.73. Found: C 69.54, H 3.85, N 25.60.

### Synthesis of MeTzPhTpy



**HTzPhTpy** (0.25 g, 0.66 mmol) was combined with  $\text{K}_2\text{CO}_3$  in acetonitrile (15 mL) and stirred for 1 minute.  $\text{CH}_3\text{I}$  (44  $\mu\text{L}$ , 0.66 mmol) was added and the mixture was stirred at reflux. The mixture was filtered and the solvent removed under reduced pressure. The solid was loaded onto Brockmann II basic alumina and eluted with DCM. The first fraction was recovered and identified as the product. Yield: 0.075 g (30 %) m.p. 227 °C dec.

IR  $\nu_{max}/\text{cm}^{-1}$ : 3062 w, 1601 w, 1582 w, 1565 m, 1543 m, 1479 m, 1465 m, 1423 m, 1388 w, 1263 w, 1139 w, 918 w, 845.

UV-Vis ( $\text{CH}_3\text{CN}$ )  $\lambda_{max}/\text{nm}$  ( $10^4\epsilon/\text{M}^{-1}\text{cm}^{-1}$ ): 283(3.93), 255(2.51), 232(1.66).

$^1\text{H}$  NMR ( $\delta$ , ppm,  $\text{CDCl}_3$ ): 8.79 (2H, s,  $\mathbf{H}_{3',5'}$ ), 8.74 (2H, d,  $\mathbf{H}_{6,6''}$ ), 8.68 (2H, d,

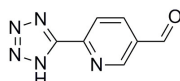
$J = 8$  Hz,  $\mathbf{H}_{3,3''}$ ), 8.28 (2H, d,  $J = 8.4$  Hz,  $\mathbf{H}_o$ ), 8.04 (2H, d,  $J = 8.4$  Hz,  $\mathbf{H}_m$ ), 7.89 (2H, m,  $J = 2.4$  Hz,  $\mathbf{H}_{4,4''}$ ), 7.39 - 7.35 (2H, m,  $\mathbf{H}_{5,5''}$ ), 5.29 (3H, s,  $\mathbf{CH}_3$ ).

$^{13}\text{C}$  NMR ( $\delta$ , ppm,  $\text{CDCl}_3$ ): 165.0 ( $\text{N}_4\text{C}$ ) 156.2, 156.1, 149.5, 149.2, 140.4, 137.1, 128.0, 128.0, 127.5, 124.1, 121.6, 119.0, 39.7 ( $\text{CH}_3$ )

Anal. Calcd (%) for  $\text{MeTzPhTpy}\cdot 0.2(\text{CH}_2\text{Cl}_2)$ : C 68.23, H 4.29, N 24.01.

Found: C 68.27, H 3.98, N 24.14.

### Synthesis of HTzPyCHO



To toluene (40 mL) in an ice bath, triethylamine (0.52 mL, 3.7 mmol) and  $\text{HCl}_{(aq)}$  (0.41 mL, 3.7 mmol) were combined and stirred until fuming subsided.  $\text{NCPy-CHO}$  (0.5 g, 3.7 mmol) and  $\text{NaN}_3$  (0.24 g, 3.7 mmol) were added and the mixture was stirred at reflux overnight. The mixture was extracted with water and the aqueous phase was acidified and filtered. The solid was discarded and the solution was acidified further and extracted with ethyl acetate. The organic phase was collected and dried over magnesium sulphate and the solvent was removed under reduced pressure giving an off-white solid. Yield: 0.32 g (40 %) m.p. 220 °C dec.

IR  $\nu_{max}/\text{cm}^{-1}$ : 2592 m br., 1705 s, 1605 s, 1575 m, 1370 m, 1263 m, 1205 w, 1178 w, 1116 w, 1039 w, 1016 w, 845 w.

$^1\text{H}$  NMR ( $\delta$ , ppm,  $\text{DMSO-}d_6$ ): 10.20 (1H, s,  $\text{CHO}$ ), 9.27 (1H, s,  $\mathbf{H}_{(py)2}$ ), 8.50 (1H, d,  $J = 6.4$  Hz,  $\mathbf{H}_{(py)5}$ ), 8.42 (1H, d,  $J = 8$  Hz,  $\mathbf{H}_{(py)4}$ ), 1.90 ( $\text{CH}_3\text{COOH}$ ).

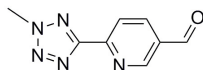
$^{13}\text{C}$  NMR ( $\delta$ , ppm,  $\text{DMSO-}d_6$ ): 191.8 ( $\text{CHO}$ ), 154.6 ( $\text{N}_4\text{C}$ ), 151.7, 147.6, 138.3, 132.3, 123.0.

Anal. Calcd (%) for  $\text{HTzPyCHO}\cdot 0.1\text{CH}_3\text{COOH}$ : C 47.74, H 3.00, N 38.66.

Found: C 47.49, H 2.76, N 38.76. A signal corresponding to acetic acid is observed in the  $^1\text{H}$  NMR spectrum, and is expected to come from extraction of acidic aqueous phase with ethyl acetate.



### Synthesis of MeTzPyCHO



HTzPyCHO (0.45 g, 2.5 mmol) was combined with  $K_2CO_3$  in acetonitrile (25 mL) and stirred for 1 minute.  $CH_3I$  (0.20 mL, 3 mmol) was added and the mixture was stirred at reflux. The mixture was filtered and the solvent removed under reduced pressure. The solid was loaded onto silica and eluted with a mixture of hexanes:ethyl-acetate 1:1. The first fraction was recovered and identified as the N1 isomer and the second fraction was identified as the N2 product. Yield: 0.157 g (33 %) m.p. 178-179 °C

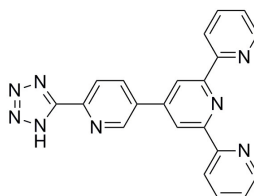
IR  $\nu_{max}/cm^{-1}$ : 2865, 1692 s, 1677 s, 1592 s, 1525 w, 1443 w, 1391 m, 1206 m, 1051 m, 840 m.

$^1H$  NMR ( $\delta$ , ppm,  $CDCl_3$ ): 10.18 (1H, s, CHO), 9.20 (1H, s,  $H_{(py)2}$ ), 8.41 (1H, d,  $J = 6.4$  Hz,  $H_{(py)5}$ ), 8.33 (1H, d,  $J = 6$  Hz,  $H_{(py)4}$ ), 4.48 (3H, s,  $CH_3$ ).

$^{13}C$  NMR ( $\delta$ , ppm,  $CDCl_3$ ): 190.1 (CHO), 164.2 ( $N_4C$ ), 152.5, 151.2, 137.3, 131.9, 122.7, 40.0 ( $CH_3$ ).

Anal. Calcd (%) for MeTzPyCHO $\cdot$ 0.1( $CH_3COOCH_2CH_3$ ) : C 50.90, H 3.89, N 35.91. Found: C 51.27, H 2.96, N 35.65.

### Synthesis of HTzPyTpy



2-acetylpyridine (0.37 mL, 3.32 mmol) was added to a solution of HTzPyCHO (0.2 g, 1.1 mmol) in EtOH (20 mL). KOH pellets (0.2 g, 3.3 mmol) and  $NH_4OH_{(aq)}$  (0.5 mL, 3.3 mmol) were then added to the solution which was stirred overnight at room temperature. The mixture was filtered and the solid left to dry under vacuum for 5 minutes. The solid was then dissolved in minimal water. The water was acidified to yield an off-white solid which was filtered and collected. Yield: 0.13 g (40 %) m.p. 282 °C dec.

IR  $\nu_{max}/cm^{-1}$ : 3370 m, 2701 m, 1618 w, 1597 s, 1563 w, 1530 s, 1497 w, 1435 w, 1338 w, 1300 w, 1278 w, 1239 w, 1172 w, 1007 w, 993 w, 791 w.

UV-Vis ( $CH_3CN$ )  $\lambda_{max}/nm$  ( $10^4\epsilon/M^{-1}cm^{-1}$ ): 295(3.32), 253(2.31), 230(2.16).

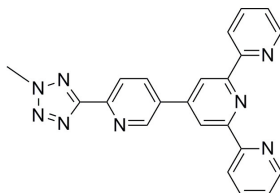
$^1H$  NMR ( $\delta$ , ppm,  $DMSO-d_6$ ): 9.18 (1H, s,  $H_{(py)2}$ ), 8.79-8.78 (4H, m,  $H_{3',5'}$  &  $H_{6,6''}$ ), 8.68 (2H, d,  $J = 8$  Hz,  $H_{3,3''}$ ), 8.39 (1H, d,  $J = 8$  Hz,  $H_{(py)5}$ ), 8.24 (1H, d,  $J = 8.4$  Hz,  $H_{(py)4}$ ), 8.05 (2H, m,  $H_{4,4''}$ ), 7.57-7.53 (2H, m,  $H_{5,5''}$ ).

$^{13}C$  NMR ( $\delta$ , ppm,  $DMSO-d_6$ ): 161.1 ( $N_4C$ ), 156.0, 155.0, 151.8, 149.5, 147.6,

146.9, 137.8, 135.3, 131.6, 124.8, 121.9, 121.2, 118.0.

Reproducible elemental analysis could not be obtained due to hygroscopic nature of this molecule.

### Synthesis of MeTzPyTpy



2-Acetylpyridine (0.2 mL, 1.6 mmol) was added to a solution of **MeTzPy-CHO** (0.15 g, 0.8 mmol) in EtOH (10 mL). KOH pellets (0.1 g, 1.8 mmol) and  $\text{NH}_4\text{OH}_{(aq)}$  (0.24 mL, 2.2 mmol) were then added to the solution which was stirred overnight at room temperature. The mixture was filtered and the solid washed with EtOH (4 mL) and the solid was then collected. Yield: 0.1 g (31 %) M.p. 273 °C

IR  $\nu_{max}/\text{cm}^{-1}$ : 3054 w, 1603 m, 1585 s, 1566 s, 1467 s, 1440 w, 1404 s, 1120 w, 1041 w, 1015 w, 836 m.

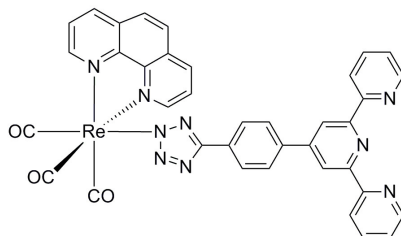
UV-Vis ( $\text{CH}_3\text{CN}$ )  $\lambda_{max}/\text{nm}$  ( $10^4\epsilon/\text{M}^{-1}\text{cm}^{-1}$ ): 282(2.76), 253(2.44).

$^1\text{H}$  NMR ( $\delta$ , ppm,  $\text{CDCl}_3$ ): 9.26 (1H, s,  $\text{H}_{(py)2}$ ), 8.79 (2H, s,  $\text{H}_{3',5'}$ ), 8.74 (2H, d,  $J = 4.4$  Hz,  $\text{H}_{6,6''}$ ), 8.68 (2H, d,  $J = 8$  Hz,  $\text{H}_{3,3''}$ ), 8.41-8.34 (2H, m,  $\text{H}_{(py)4,(py)5}$ ), 7.92-7.88 (2H, m,  $\text{H}_{4,4''}$ ), 7.40-7.37 (2H, m,  $\text{H}_{5,5''}$ ), 4.49 (3H, s,  $\text{CH}_3$ ).

$^{13}\text{C}$  NMR ( $\delta$ , ppm,  $\text{CDCl}_3$ ): 164.8 ( $\text{N}_4\text{C}$ ) 156.5, 155.9, 149.3, 149.0, 147.1, 146.7, 137.2, 136.0, 135.6, 124.3, 122.5, 121.6, 119.0, 39.9 ( $\text{CH}_3$ )

Anal. Calcd (%) for (3-comp : 1-DCM): C 63.76, H 3.99, N 26.63. Found: C 63.15, H 3.47, N 26.59.

### Synthesis of [Re-TzPhTpy]



$[\text{Re}(\text{CO})_3(\text{phen})\text{Cl}]$  (0.1 g, 0.22 mmol) was combined with  $\text{AgCF}_3\text{SO}_3$  (0.06 g, 0.22 mmol) in acetonitrile (20 mL). The mixture was shielded from light and stirred at reflux overnight. The mixture was cooled and filtered through celite and the solution was collected. A separate solution was made of **HTzPhTpy** (0.073 g, 0.22 mmol) and  $\text{Et}_3\text{N}$  (1.0 mL) in acetonitrile (10 mL) and the two solutions were

combined and stirred at reflux overnight. The solvent was then removed under reduced pressure and the resulting solid was loaded onto Brockmann II basic alumina and eluted with DCM. The first fraction was collected and identified as the product. Yield: 0.102 g (60 %) m.p. 180 °C dec.

IR  $\nu_{max}/\text{cm}^{-1}$ : 3400 w, 3060 w, 2021 s (CO), 1893 s (CO), 1632 w, 1603 w, 1583 m, 1567 w, 1543 w, 1467 m, 1428 m, 1390 m, 1035 m, 841 m.

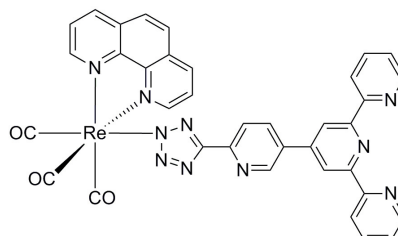
UV-Vis ( $\text{CH}_2\text{Cl}_2$ )  $\lambda_{max}/\text{nm}$  ( $10^4\epsilon/\text{M}^{-1}\text{cm}^{-1}$ ): 278(4.81), 360(0.49).

$^1\text{H}$  NMR ( $\delta$ , ppm,  $\text{CDCl}_3$ ): 9.47 (2H, d, 5.2 Hz,  $\mathbf{H}_{a,h}$ ), 8.70 (2H, d,  $J = 8$  Hz,  $\mathbf{H}_{6,6''}$ ), 8.64 (2H, s,  $\mathbf{H}_{3',5'}$ ), 8.60 (2H, d,  $J = 8$  Hz,  $\mathbf{H}_{3,3''}$ ), 8.45 (2H, d,  $J = 8.2$  Hz,  $\mathbf{H}_{c,f}$ ), 7.88 (2H, s,  $\mathbf{H}_{d,e}$ ), 7.87-7.75 (8H, m,  $\mathbf{H}_{b,g}$  &  $\mathbf{H}_o$  &  $\mathbf{H}_m$  &  $\mathbf{H}_{4,4''}$ ), 7.33-7.30 (2H, m,  $\mathbf{H}_{5,5''}$ )

$^{13}\text{C}$  NMR ( $\delta$ , ppm,  $\text{CDCl}_3$ ): 196.7 (CO), 193.7 (CO), 162.9 ( $\text{N}_4\text{C}$ ), 156.0, 155.8, 153.7, 149.8, 149.0, 147.6, 138.6, 137.9, 137.2, 130.7, 130.5, 127.6, 127.3, 126.9, 126.0, 124.0, 121.5, 118.7.

Anal. Calcd (%) for  $[\text{Re-TzPhTpy}] \cdot 0.5(\text{CH}_2\text{Cl}_2)$ : C 51.81, H 2.67, N 14.50. Found: C 51.96, H 2.31, N 14.58.

### Synthesis of $[\text{Re-TzPyTpy}]$



$[\text{Re}(\text{CO})_3(\text{phen})\text{Cl}]$  (0.1 g, 0.22 mmol) was combined with  $\text{AgCF}_3\text{SO}_3$  (0.07 g, 0.22 mmol) in acetonitrile (20 mL). The mixture was shielded from light and stirred at reflux overnight. The mixture was cooled and filtered through celite and the solution was collected. A separate solution was made of  $\text{HTzPyTpy}$  (0.074 g, 0.22 mmol) and  $\text{Et}_3\text{N}$  (1.0 mL) in acetonitrile (10 mL) and the two solutions were combined and stirred at reflux overnight. The solvent was then removed under reduced pressure and the resulting solid was loaded onto Brockmann II basic alumina and eluted with a mixture of DCM and ethyl acetate in a 1:1 ratio. The first fraction was collected and identified as the product. Yield: 0.102 g (53 %) m.p. 190 °C dec.

IR  $\nu_{max}/\text{cm}^{-1}$ : 3385 w, 3059 w, 2024 s (CO), 1898 s (CO), 1599 m, 1521 w, 1469 m, 1428 m, 1258 m, 1145 m, 1031 w, 847 m.

UV-Vis ( $\text{CH}_2\text{Cl}_2$ )  $\lambda_{max}/\text{nm}$  ( $10^4\epsilon/\text{M}^{-1}\text{cm}^{-1}$ ): 276(4.23), 360(0.39).

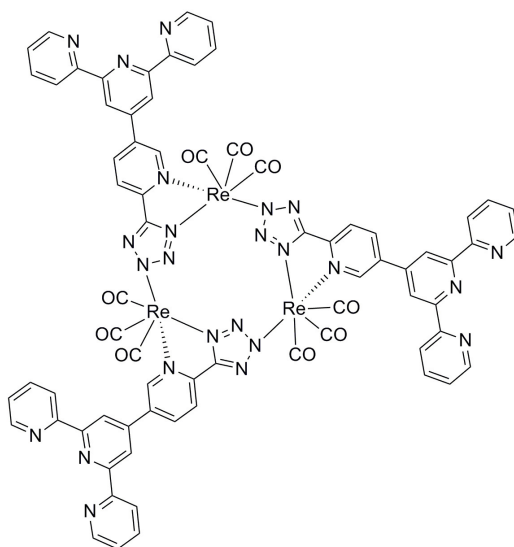
$^1\text{H}$  NMR ( $\delta$ , ppm,  $\text{CDCl}_3$ ): 9.50 (2H, d, 5.2 Hz,  $\mathbf{H}_{a,h}$ ), 8.99 (1H, s,  $\mathbf{H}_{(py)2}$ ), 8.67-8.60 (6H, m,  $\mathbf{H}_{6,6''}$  &  $\mathbf{H}_{3',5'}$  &  $\mathbf{H}_{3,3''}$ ), 8.54 (2H, d,  $J = 8.2$  Hz,  $\mathbf{H}_{c,f}$ ), 8.08 (1H, d,

$J = 8.2$  Hz,  $\mathbf{H}_{(py)5}$ ), 7.95 (2H, s,  $\mathbf{H}_{d,e}$ ), 7.89-7.80 (5H, m,  $\mathbf{H}_{b,g}$  &  $\mathbf{H}_{(py)4}$  &  $\mathbf{H}_{4,4''}$ ), 7.33-7.30 (2H, m,  $\mathbf{H}_{5,5''}$ )

$^{13}\text{C}$  NMR ( $\delta$ , ppm,  $\text{CDCl}_3$ ): 163.6 ( $\text{N}_4\text{C}$ ), 156.3, 156.1, 154.1, 149.8, 149.3, 148.3, 147.7, 147.3, 138.5, 137.0, 135.2, 133.3, 130.6, 127.7, 126.1, 124.1, 122.0, 121.5, 118.8.

Anal. Calcd (%) for  $[\text{Re-TzPyTpy}] \cdot 0.5(\text{CH}_2\text{Cl}_2)$  : C 50.37, H 2.55, N 16.09. Found: C 50.19, H 2.37, N 16.39.

### Synthesis of $[\text{ReTzPyTpy}]_3$



$[\text{Re}(\text{CO})_5\text{Br}]$  (0.1 g, 0.25 mmol) was combined with  $\text{HTzPyTpy}$  (0.1 g, 0.26 mmol) and  $\text{Et}_3\text{N}$  (1 mL) in toluene (15 mL) and stirred at reflux overnight. The solvent was removed under vacuum and the solid dissolved in minimal DCM and loaded onto Brockmann II basic alumina and eluted with DCM. The first fraction was collected and identified as the product. Yield: 0.062 g (39 %) m.p. 230 °C dec.

IR  $\nu_{\text{max}}/\text{cm}^{-1}$ : 3383 w, 3060 w, 2029 s, 1901 s, 1605 m, 1585 m, 1566 m, 1466 m, 1439 m, 1394 m, 1353 w, 1257 m, 1125 w, 845 w.

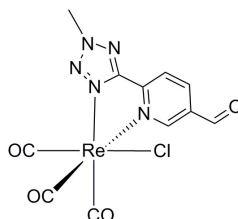
UV-Vis ( $\text{CH}_2\text{Cl}_2$ )  $\lambda_{\text{max}}/\text{nm}$  ( $10^4\epsilon/\text{M}^{-1}\text{cm}^{-1}$ ): 280(8.80), 325(3.77).

$^1\text{H}$  NMR ( $\delta$ , ppm,  $\text{CDCl}_3$ ): 9.54 (1H, s,  $\mathbf{H}_{a(py)2}$ ), 9.44 (1H, s,  $\mathbf{H}_{b(py)2}$ ), 9.33 (1H, s,  $\mathbf{H}_{c(py)2}$ ), 8.90-8.57 (23H, m,  $\mathbf{H}_{abc(3',5')}$  &  $\mathbf{H}_{abc(6,6'')}$  &  $\mathbf{H}_{abc(3,3'')}$  &  $\mathbf{H}_{abc(py)5}$  &  $\mathbf{H}_{bc(py)4}$ ), 8.05 (6H, m,  $\mathbf{H}_{abc(4,4'')}$ ), 7.89-7.80 (1H, d,  $J = 8.4$  Hz,  $\mathbf{H}_{a(py)4}$ ), 7.33-7.30 (6H, m,  $\mathbf{H}_{abc(5,5'')}$ ).

$^{13}\text{C}$  NMR ( $\delta$ , ppm,  $\text{CDCl}_3$ ):  $^{13}\text{C}$ -NMR could not be obtained for this complex due to poor solubility in common solvents.

Anal. Calcd (%) for  $[\text{ReTzPyTpy}]_3 \cdot 0.5(\text{CH}_2\text{Cl}_2)$  : C 43.86, H 2.03, N 16.96. Found: C 43.71, H 1.75, N 16.89.

Synthesis of [Re(MeTzPyCHO)Cl]



[Re(CO)<sub>5</sub>Cl] (0.1 g, 0.25 mmol) was combined with **MeTzPyTpy** (0.07 g, 0.37 mmol) in toluene (10 mL) and stirred at reflux overnight. The solvent was removed under vacuum and the solid dissolved in minimal DCM and loaded onto silica and eluted with a 1:1 mixture of DCM and ethyl acetate. The first fraction was collected and identified as the product. Yield: 0.109 g (88 %) m.p. 240 °C dec.

IR  $\nu_{max}/\text{cm}^{-1}$ : 3042 w, 2024 s, 1882 s, 1698 m, 1618 m, 1566 m, 1574 m, 1454 m, 1433 w, 1395 w, 727 m.

UV-Vis (CH<sub>2</sub>Cl<sub>2</sub>)  $\lambda_{max}/\text{nm}$  ( $10^4\epsilon/\text{M}^{-1}\text{cm}^{-1}$ ): 288(2.62), 403(0.37).

<sup>1</sup>H NMR ( $\delta$ , ppm, CDCl<sub>3</sub>): 10.23 (1H, s, CHO), 9.46 (1H, s, H<sub>2</sub>), 8.61 (1H, d, J = 8 Hz, H<sub>5</sub>), 8.33 (1H, d, J = 8 Hz, H<sub>4</sub>), 4.62 (3H, s, CH<sub>3</sub>).

<sup>13</sup>C NMR ( $\delta$ , ppm, CDCl<sub>3</sub>): 187.0 (CHO), 166.2 (N<sub>4</sub>C), 155.9, 148.7, 139.4, 134.5, 124.4, 42.0 CH<sub>3</sub>.

Reproducible elemental analysis could not be obtained for this complex.



# References

- [1] Werrett, M. V.; Chartrand, D.; Gale, J. D.; Hanan, G. S.; MacLellan, J. G.; Massi, M.; Muzzioli, S.; Raiteri, P.; Skelton, B. W.; Silberstein, M.; Stagni, S. *Inorganic Chemistry* **2011**, *50*, 1229–1241.
- [2] Wright, P. J.; Muzzioli, S.; Werrett, M. V.; Raiteri, P.; Skelton, B. W.; Silvester, D. S.; Stagni, S.; Massi, M. *Organometallics* **2012**, *31*, 7566–7578.
- [3] Lo, K. K.-w. *Topics in Organometallic Chemistry*; Springer Berlin Heidelberg: Heidelberg, 2010; pp 73–114.
- [4] Amoroso, A. J.; Coogan, M. P.; Dunne, J. E.; Fernández-Moreira, V.; Hess, J. B.; Hayes, A. J.; Lloyd, D.; Millet, C.; Pope, S. J. a.; Williams, C. *Chemical Communications* **2007**, 3066–3068.
- [5] Lo, K. K.-W.; Louie, M.-w.; Sze, K.-S.; Lau, J. S.-y. *Inorganic Chemistry* **2008**, *47*, 602–611.
- [6] Kalinowski, J.; Fattori, V.; Cocchi, M.; Williams, J. G. A. G. *Coordination Chemistry Reviews* **2011**, *255*, 2401–2425.
- [7] Evans, R. C.; Douglas, P.; Winscom, C. J. *Coordination Chemistry Reviews* **2006**, *250*, 2093–2126.
- [8] Noh, Y.-Y.; Lee, C.-L.; Kim, J.-J.; Yase, K. *The Journal of Chemical Physics* **2003**, *118*, 2853–2864.
- [9] Lu, Y.; Zhang, M.; Shang, Y.; Xu, H.; Wei, B.; Wang, Z. *Journal of Shanghai University* **2011**, *15*, 256–261.
- [10] Lee, P.; Hsu, S.; Chung, C. *Synthetic Metals* **2006**, *156*, 907–910.
- [11] Lee, C.; Lee, K.; Kim, J. *Applied Physics Letters* **2000**, *77*, 2280–2282.
- [12] Stagni, S.; Palazzi, A.; Zacchini, S.; Ballarin, B.; Bruno, C.; Marcaccio, M.; Paolucci, F.; Monari, M.; Carano, M.; Bard, A. J. *Inorganic Chemistry* **2006**, *45*, 695–709.

- [13] Yu, M.; Zhao, Q.; Shi, L.; Li, F.; Zhou, Z.; Yang, H.; Yi, T.; Huang, C. *Chemical Communications* **2008**, 2115–2117.
- [14] Lo, K. K.-W.; Louie, M.-W.; Zhang, K. Y. *Coordination Chemistry Reviews* **2010**, *254*, 2603–2622.
- [15] Guerchais, V.; Fillaut, J.-L. *Coordination Chemistry Reviews* **2011**, *255*, 2448–2457.
- [16] de Silva, A. P.; Gunaratne, H. Q. N.; Gunnlaugsson, T.; Huxley, A. J. M.; McCoy, C. P.; Rademacher, J. T.; Rice, T. E. *Chemical Reviews* **1997**, *97*, 1515–1566.
- [17] Keefe, M. *Coordination Chemistry Reviews* **2000**, *205*, 201–228.
- [18] Sun, S.; Lees, A. J. *Coordination Chemistry Reviews* **2002**, *230*, 171–192.
- [19] Man, K. Y. K.; Tse, C. W.; Cheng, K. W.; Djurišić, A. B.; Chan, W. K. *Journal of Inorganic and Organometallic Polymers and Materials* **2007**, *17*, 223–233.
- [20] Sahara, G.; Abe, R.; Higashi, M.; Morikawa, T.; Maeda, K.; Ueda, Y.; Ishitani, O. *Chemical Communications* **2015**, *51*, 10722–10725.
- [21] Hwang, J. S.; Chang, J. S.; Park, S. E.; Ikeue, K.; Anpo, M. *Topics in Catalysis* **2005**, *35*, 311–319.
- [22] Koike, K.; Hori, H.; Ishizuka, M.; Westwell, J. R.; Takeuchi, K.; Ibusuki, T.; Enjouji, K.; Konno, H.; Sakamoto, K.; Ishitani, O. *Organometallics* **1997**, *16*, 5724–5729.
- [23] Tsubaki, H.; Sekine, A.; Ohashi, Y.; Koike, K.; Takeda, H.; Ishitani, O. *Journal of the American Chemical Society* **2005**, *127*, 15544–15555.
- [24] Takeda, H.; Koike, K.; Inoue, H.; Ishitani, O. *Journal of the American Chemical Society* **2008**, *130*, 2023–2031.
- [25] Hankache, J.; Wenger, O. S. *Physical Chemistry Chemical Physics* **2012**, *14*, 2685–2692.
- [26] Heinz, L. G.; Yushchenko, O.; Neuburger, M.; Vauthey, E.; Wenger, O. S. *The Journal of Physical Chemistry A* **2015**, *119*, 5676–5684.
- [27] Walther, M. E.; Wenger, O. S. *Dalton Transactions* **2008**, 6311–6318.



- [28] Wenger, O. S.; Leigh, B. S.; Villahermosa, R. M.; Gray, H. B.; Winkler, J. R. *Science* **2005**, *307*, 99–102.
- [29] Hanss, D.; Wenger, O. S. *Inorganica Chimica Acta* **2009**, *362*, 3415–3420.
- [30] Wenger, O. S.; Henling, L. M.; Day, M. W.; Winkler, J. R.; Gray, H. B. *Inorganic Chemistry* **2004**, *43*, 2043–2048.
- [31] Bronner, C.; Wenger, O. S. *Inorganic Chemistry* **2012**, *51*, 8275–8283.
- [32] Wenger, O. S. *Coordination Chemistry Reviews* **2009**, *253*, 1439–1457.
- [33] Wenger, O. S. *Inorganica Chimica Acta* **2011**, *374*, 3–9.
- [34] Freys, J. C.; Wenger, O. S. *European Journal of Inorganic Chemistry* **2010**, *2010*, 5509–5516.
- [35] Hanss, D.; Walther, M. E.; Wenger, O. S. *Coordination Chemistry Reviews* **2010**, *254*, 2584–2592.
- [36] Caspar, J. V.; Meyer, T. J. *The Journal of Physical Chemistry* **1983**, *87*, 952–957.
- [37] Kumar, A.; Sun, S.-s.; Lees, A. J. *Topics in Organometallic Chemistry* **2009**, 1–35.
- [38] Li, X.; Chi, H.-J.; Lu, G.-H.; Xiao, G.-Y.; Dong, Y.; Zhang, D.-Y.; Zhang, Z.-Q.; Hu, Z.-Z. *Organic Electronics* **2012**, *13*, 3138–3144.
- [39] de Bettencourt-Dias, A.; Barber, P. S.; Viswanathan, S. *Coordination Chemistry Reviews* **2014**, *273-274*, 165–200.
- [40] Angelici, R. J.; Kruse, A. E. *Journal of Organometallic Chemistry* **1970**, *22*, 461–471.
- [41] Rouschias, G. *Chemical Reviews* **1974**, *74*, 531–566.
- [42] Lewis, H.; Storhoff, B. *Journal of Organometallic Chemistry* **1972**, *43*, C16.
- [43] Wrighton, M.; Morse, D. L. *Journal of the American Chemical Society* **1974**, *96*, 998–1003.
- [44] Frenzel, B. A.; Schumaker, J. E.; Black, D. R.; Hightower, S. E. *Dalton Transactions* **2013**, *42*, 12440–12451.
- [45] Black, D. R.; Hightower, S. E. *Inorganic Chemistry Communications* **2012**, *24*, 16–19.

- [46] Fiorini, V.; Ranieri, A. M.; Muzzioli, S.; Magee, K. D. M.; Zacchini, S.; Akabar, N.; Stefan, A.; Ogden, M. I.; Massi, M.; Stagni, S. *Dalton Transactions* **2015**, *44*, 20597–20608.
- [47] Amendola, V.; Bacchilega, D.; Costa, I.; Gianelli, L.; Montalti, M.; Pallavicini, P.; Perotti, A.; Prodi, L.; Zaccheroni, N. *Journal of Photochemistry and Photobiology A: Chemistry* **2003**, *159*, 249–252.
- [48] Beer, P. D.; Timoshenko, V.; Maestri, M.; Passaniti, P.; Balzani, V. *Chemical Communications* **1999**, 1755–1756.
- [49] Costa, I.; Montalti, M.; Pallavicini, P.; Perotti, A.; Prodi, L.; Zaccheroni, N. *Journal of Organometallic Chemistry* **2000**, *593-594*, 267–273.
- [50] Kin Chan, W.; King Ng, P.; Gong, X.; Hou, S. *Journal of Materials Chemistry* **1999**, *9*, 2103.
- [51] Xue, W. M.; Kühn, F. E.; Herdtweck, E. *Polyhedron* **2001**, *20*, 791–798.
- [52] Yamamoto, Y.; Sawa, S.; Funada, Y.; Morimoto, T.; Falkenström, M.; Miyasaka, H.; Shishido, S.; Ozeki, T.; Koike, K.; Ishitani, O. *Journal of the American Chemical Society* **2008**, *130*, 14659–14674.
- [53] Ng, P. K.; Gong, X.; Chan, S. H.; Lam, L. S. M.; Chan, W. K. *Chemistry - A European Journal* **2001**, *7*, 4358–4367.
- [54] Panigati, M.; Mauro, M.; Donghi, D.; Mercandelli, P.; Mussini, P.; De Cola, L.; D'Alfonso, G. *Coordination Chemistry Reviews* **2012**, *256*, 1621–1643.
- [55] Mauro, M.; Yang, C.-H.; Shin, C.-Y.; Panigati, M.; Chang, C.-H.; D'Alfonso, G.; De Cola, L. *Advanced Materials* **2012**, *24*, 2054–2058.
- [56] Wang, K.; Huang, L.; Gao, L.; Jin, L.; Huang, C. *Inorganic Chemistry* **2002**, *41*, 3353–3358.
- [57] Chu, W.-K.; Ko, C.-C.; Chan, K.-C.; Yiu, S.-M.; Wong, F.-L.; Lee, C.-S.; Roy, V. a. L. *Chemistry of Materials* **2014**, *26*, 2544–2550.
- [58] Dunn, A. R.; Belliston-Bittner, W.; Winkler, J. R.; Getzoff, E. D.; Stuehr, D. J.; Gray, H. B. *Journal of the American Chemical Society* **2005**, *127*, 5169–5173.
- [59] Del Negro, A. S.; Wang, Z.; Seliskar, C. J.; Heineman, W. R.; Sullivan, B. P.; Hightower, S. E.; Hubler, T. L.; Bryan, S. a. *Journal of the American Chemical Society* **2005**, *127*, 14978–14979.

- [60] Kirgan, R. A.; Sullivan, B. P.; Rillema, D. P. *Photochemistry and Photo-physics of Coordination Compounds II*; Springer Berlin Heidelberg: Berlin, Heidelberg, 2007; Vol. 281; pp 45–100.
- [61] Zhang, J.; Vittal, J. J.; Henderson, W.; Wheaton, J. R.; Hall, I. H.; Hor, T. S. A.; Yan, Y. K. *Journal of Organometallic Chemistry* **2002**, *650*, 123–132.
- [62] Fernández-Moreira, V.; Thorp-Greenwood, F. L.; Coogan, M. P. *Chemical Communications* **2010**, *46*, 186–202.
- [63] Wang, B.; Liang, Y.; Dong, H.; Tan, T.; Zhan, B.; Cheng, J.; Lo, K. K.-W.; Lam, Y. W.; Cheng, S. H. *ChemBioChem* **2012**, *13*, 2729–2737.
- [64] Pierard, F.; Kirsch-De Mesmaeker, A. *Inorganic Chemistry Communications* **2006**, *9*, 111–126.
- [65] Zhao, Q.; Huang, C.; Li, F. *Chemical Society Reviews* **2011**, *40*, 2508–2524.
- [66] Tan, W.; Zhou, J.; Li, F.; Yi, T.; Tian, H. *Chemistry - An Asian Journal* **2011**, *6*, 1263–1268.
- [67] Murphy, L.; Congreve, A.; Pålsson, L.-O.; Williams, J. A. G. *Chemical Communications* **2010**, *46*, 8743–8745.
- [68] Liu, J.; Liu, Y.; Liu, Q.; Li, C.; Sun, L.; Li, F. *Journal of the American Chemical Society* **2011**, *133*, 15276–15279.
- [69] Wu, F.; Tong, B.; Zhang, Q. *Analytical Sciences* **2011**, *27*, 529–533.
- [70] Balzani, V.; Bergamini, G.; Campagna, S. *Topics in Current Chemistry* **2007**, *280*, 1–36.
- [71] Lakowicz, J. R. *Principles of Fluorescence Spectroscopy*; Springer Science+Business Media: New York, 2006.
- [72] Watkis, A.; Hueting, R.; Sørensen, T. J.; Tropiano, M.; Faulkner, S. *Chemical Communications* **2015**, *51*, 15633–15636.
- [73] Záliš, S.; Consani, C.; Nahhas, A. E.; Cannizzo, A.; Chergui, M.; Hartl, F.; Vlček, A. *Inorganica Chimica Acta* **2011**, *374*, 578–585.
- [74] Rossenaar, B. D.; Stufkens, D. J.; Vlcek, A. *Inorganic Chemistry* **1996**, *35*, 2902–2909.
- [75] Stufkens, D.; Vlcek, A. *Coordination Chemistry Reviews* **1998**, *177*, 127–179.

- [76] Liard, D. J.; Busby, M.; Matousek, P.; Towrie, M.; Vlcek, A. *The Journal of Physical Chemistry A* **2004**, *108*, 2363–2369.
- [77] Blanco-Rodríguez, A. M.; Towrie, M.; Collin, J.-P.; Zálíš, S.; Jr., A. V. *Dalton Transactions* **2009**, 3941–3949.
- [78] Blanco Rodríguez, A. M.; Gabrielsson, A.; Motevalli, M.; Matousek, P.; Towrie, M.; Šebera, J.; Zálíš, S.; Vlcek, A. *The Journal of Physical Chemistry A* **2005**, *109*, 5016–5025.
- [79] Gabrielsson, A.; Busby, M.; Matousek, P.; Towrie, M.; Hevia, E.; Cuesta, L.; Perez, J.; Zálíš, S.; Vlcek, A. *Inorganic Chemistry* **2006**, *45*, 9789–9797.
- [80] Atkins, P.; Overton, T.; Rourke, J.; Weller, M.; Armstrong, F. *Shriver & Atkins Inorganic Chemistry*, 4th ed.; Oxford University Press: New York, 2006.
- [81] Villegas, J. M.; Stoyanov, S. R.; Huang, W.; Rillema, D. P. *Inorganic Chemistry* **2005**, *44*, 2297–2309.
- [82] Shankar, B.; Elumalai, P.; Sathiyendiran, M. *Inorganic Chemistry Communications* **2013**, *36*, 109–112.
- [83] He, X.; Zhu, N.; Yam, V. W.-W. *Dalton Transactions* **2011**, *40*, 9703–9710.
- [84] Kumar, R.; Prasad, R. *Journal of Molecular Structure* **2009**, *921*, 199–207.
- [85] Gan, X.; Fu, W.-F.; Lin, Y.-Y.; Yuan, M.; Che, C.-M.; Chi, S.-M.; Li, H.-F. J.; Chen, J.-H.; Chen, Y.; Zhou, Z.-Y. *Polyhedron* **2008**, *27*, 2202–2208.
- [86] Harriman, A.; Khatyr, A.; Ziessel, R. *Research on Chemical Intermediates* **2007**, *33*, 49–62.
- [87] Jia, W. L.; McCormick, T.; Tao, Y.; Lu, J.-P.; Wang, S. *Inorganic Chemistry* **2005**, *44*, 5706–5712.
- [88] Zheng, S.-L.; Chen, X.-M. *Australian Journal of Chemistry* **2004**, *57*, 703–712.
- [89] Leite Ferreira, B.; Brandão, P.; Dos Santos, A.; Gai, Z.; Cruz, C.; Reis, M.; Santos, T.; Félix, V. *Journal of Coordination Chemistry* **2015**, *68*, 2770–2787.
- [90] Nakajima, T.; Seto, K.; Scheurer, A.; Kure, B.; Kajiwara, T.; Tanase, T.; Mikuriya, M.; Sakiyama, H. *European Journal of Inorganic Chemistry* **2014**, *2014*, 5021–5033.

- [91] Amo-Ochoa, P.; Castillo, O.; Gómez-García, C. J.; Hassanein, K.; Verma, S.; Kumar, J.; Zamora, F. *Inorganic Chemistry* **2013**, *52*, 11428–11437.
- [92] García-Giménez, J. L.; Alzuet, G.; González-Álvarez, M.; Castiñeiras, A.; Liu-González, M.; Borrás, J. *Inorganic Chemistry* **2007**, *46*, 7178–7188.
- [93] Gorle, A. K.; Feterl, M.; Warner, J. M.; Wallace, L.; Keene, F. R.; Collins, J. G. *Dalton Transactions* **2014**, *43*, 16713–16725.
- [94] Li, F.; Mulyana, Y.; Feterl, M.; Warner, J. M.; Collins, J. G.; Keene, F. R. *Dalton Transactions* **2011**, *40*, 5032–5038.
- [95] Li, F.; Feterl, M.; Warner, J. M.; Keene, F. R.; Collins, J. G. *Journal of Antimicrobial Chemotherapy* **2013**, *68*, 2825–2833.
- [96] Renfrew, A. K. *Metallomics* **2014**, *6*, 1324–1335.
- [97] Therrien, B.; Süß-Fink, G.; Govindaswamy, P.; Renfrew, A. K.; Dyson, P. J. *Angewandte Chemie International Edition* **2008**, *47*, 3773–3776.
- [98] Süß-Fink, G. *Dalton Transactions* **2010**, *39*, 1673–1688.
- [99] Tao, C.-H.; Yang, H.; Zhu, N.; Yam, V. W.-W.; Xu, S.-J. *Organometallics* **2008**, *27*, 5453–5458.
- [100] Rogers, J. E.; Slagle, J. E.; Krein, D. M.; Burke, A. R.; Hall, B. C.; Fratini, A.; McLean, D. G.; Fleitz, P. A.; Cooper, T. M.; Drobizhev, M.; Makarov, N. S.; Rebane, A.; Kim, K.-Y.; Farley, R.; Schanze, K. S. *Inorganic Chemistry* **2007**, *46*, 6483–6494.
- [101] Yang, C.; Elbjeirami, O.; Gamage, C. S. P.; Dias, H. V. R.; Omary, M. A. *Chemical Communications* **2011**, *47*, 7434–7436.
- [102] Karmakar, S.; Maity, D.; Mardanya, S.; Baitalik, S. *Inorganic Chemistry* **2014**, *53*, 12036–12049.
- [103] Forrest, S. R.; Baldo, M. A.; O'Brien, D. F.; You, Y.; Shoustikov, A.; Sibley, S.; Thompson, M. E. *Nature* **1998**, *395*, 151–154.
- [104] Wenger, O. S. *Accounts of Chemical Research* **2011**, *44*, 25–35.
- [105] Herbst, A.; Bronner, C.; Dechambenoit, P.; Wenger, O. S. *Organometallics* **2013**, *32*, 1807–1814.

- [106] Kalyanasundaram, K.; Graetzel, M.; Nazeeruddin, M. K. *Inorganic Chemistry* **1992**, *31*, 5243–5253.
- [107] Saita, T.; Nitadori, H.; Inagaki, A.; Akita, M. *Journal of Organometallic Chemistry* **2009**, *694*, 3125–3133.
- [108] Adamovich, V.; Brooks, J.; Tamayo, A.; Alexander, A. M.; Djurovich, P. I.; D’Andrade, B. W.; Adachi, C.; Forrest, S. R.; Thompson, M. E. *New Journal of Chemistry* **2002**, *26*, 1171–1178.
- [109] Muñoz-Rodríguez, R.; Buñuel, E.; Fuentes, N.; Williams, J. A. G.; Cárdenas, D. J. *Dalton Transactions* **2015**, *44*, 8394–8405.
- [110] D’Andrade, B.; Brooks, J.; Adamovich, V.; Thompson, M.; Forrest, S. *Advanced Materials* **2002**, *14*, 1032–1036.
- [111] Tapolsky, G.; Duesing, R.; Meyer, T. J. *Inorganic Chemistry* **1990**, *29*, 2285–2297.
- [112] Tapolsky, G.; Duesing, R.; Meyer, T. J. *Journal of Physical Chemistry* **1989**, *93*, 3885–3887.
- [113] Quartapelle Procopio, E.; Mauro, M.; Panigati, M.; Donghi, D.; Mercandelli, P.; Sironi, A.; D’Alfonso, G.; De Cola, L. *Journal of the American Chemical Society* **2010**, *132*, 14397–14399.
- [114] Sathish, V.; Ramdass, A.; Thanasekaran, P.; Lu, K.-L.; Rajagopal, S. *Journal of Photochemistry and Photobiology C: Photochemistry Reviews* **2015**, *23*, 25–44.
- [115] Chen, F. F.; Chen, Z. Q.; Bian, Z. Q.; Huang, C. H. *Coordination Chemistry Reviews* **2010**, *254*, 991–1010.
- [116] Brayshaw, P. A.; Buenzli, J.-C. G.; Froidevaux, P.; Harrowfield, J. M.; Kim, Y.; Sobolev, A. N. *Inorganic Chemistry* **1995**, *34*, 2068–2076.
- [117] Ronson, T. K.; Lazarides, T.; Adams, H.; Pope, S. J. A.; Sykes, D.; Faulkner, S.; Coles, S. J.; Hursthouse, M. B.; Clegg, W.; Harrington, R. W.; Ward, M. D. *Chemistry - A European Journal* **2006**, *12*, 9299–9313.
- [118] Klink, S. I.; Keizer, H.; van Veggel, F. C. J. M. *Angewandte Chemie* **2000**, *39*, 4319–4321.
- [119] Shavaleev, N. M.; Pope, S. J. A.; Bell, Z. R.; Faulkner, S.; Ward, M. D. *Dalton Transactions* **2003**, 808–814.

- [120] Coppo, P.; Duati, M.; Kozhevnikov, V. N.; Hofstraat, J. W.; De Cola, L. *Angewandte Chemie International Edition* **2005**, *44*, 1806–1810.
- [121] Imbert, D.; Cantuel, M.; Bünzli, J.-C. G.; Bernardinelli, G.; Piguet, C. *Journal of the American Chemical Society* **2003**, *125*, 15698–15699.
- [122] Chen, F.-F.; Wei, H.-b.; Bian, Z.-q.; Liu, Z.-w.; Ma, E.; Chen, Z.-n.; Huang, C.-h. *Organometallics* **2014**, *33*, 3275–3282.
- [123] Chen, F.-F.; Bian, Z.-q.; Liu, Z.-w.; Nie, D.-b.; Chen, Z.-q.; Huang, C.-h. *Inorganic Chemistry* **2008**, *47*, 2507–2513.
- [124] Perry, W. S.; Pope, S. J. A.; Allain, C.; Coe, B. J.; Kenwright, A. M.; Faulkner, S. *Dalton Transactions* **2010**, *39*, 10974–10983.
- [125] Lehr, J.; Tropiano, M.; Beer, P. D.; Faulkner, S.; Davis, J. J. *Chemical Communications* **2015**, *51*, 15944–15947.
- [126] Faulkner, S.; Natrajan, L. S.; Perry, W. S.; Sykes, D. *Dalton Transactions* **2009**, 3890–3899.
- [127] Shavaleev, N. M.; Moorcraft, L. P.; Pope, S. J. A.; Bell, Z. R.; Faulkner, S.; Ward, M. D. *Chemistry - A European Journal* **2003**, *9*, 5283–5291.
- [128] Pope, S. J. A.; Coe, B. J.; Faulkner, S.; Laye, R. H. *Dalton Transactions* **2005**, 1482–1490.
- [129] Kennedy, F.; Shavaleev, N. M.; Koullourou, T.; Bell, Z. R.; Jeffery, J. C.; Faulkner, S.; Ward, M. D. *Dalton Transactions* **2007**, 1492–1499.
- [130] Sykes, D.; Parker, S. C.; Sazanovich, I. V.; Stephenson, A.; Weinstein, J. a.; Ward, M. D. *Inorganic Chemistry* **2013**, *52*, 10500–10511.
- [131] Lazarides, T.; Sykes, D.; Faulkner, S.; Barbieri, A.; Ward, M. D. *Chemistry - A European Journal* **2008**, *14*, 9389–9399.
- [132] Iki, N.; Hiro-oka, S.; Tanaka, T.; Kabuto, C.; Hoshino, H. *Inorganic Chemistry* **2012**, *51*, 1648–1656.
- [133] Latva, M.; Takalo, H.; Mikkala, V.-M.; Matachescu, C.; Rodríguez-Ubis, J. C.; Kankare, J. *Journal of Luminescence* **1997**, *75*, 149–169.
- [134] Li, X.-L.; Dai, F.-R.; Zhang, L.-Y.; Zhu, Y.-M.; Peng, Q.; Chen, Z.-N. *Organometallics* **2007**, *26*, 4483–4490.

- [135] Li, X.-L.; Shi, L.-X.; Zhang, L.-Y.; Wen, H.-M.; Chen, Z.-N. *Inorganic Chemistry* **2007**, *46*, 10892–10900.
- [136] Xu, H.-B.; Zhang, L.-Y.; Chen, Z.-H.; Shi, L.-X.; Chen, Z.-N. *Dalton Transactions* **2008**, 4664–4670.
- [137] Xu, H.-B.; Zhang, L.-Y.; Chen, X.-M.; Li, X.-L.; Chen, Z.-N. *Crystal Growth & Design* **2009**, *9*, 569–576.
- [138] Xu, H.-B.; Zhang, L.-Y.; Ni, J.; Chao, H.-Y.; Chen, Z.-N. *Inorganic Chemistry* **2008**, *47*, 10744–10752.
- [139] Ziessel, R.; Diring, S.; Kadjane, P.; Charbonnière, L.; Retaillieu, P.; Philouze, C. *Chemistry: An Asian Journal* **2007**, *2*, 975–982.
- [140] Steemers, F. J.; Verboom, W.; Reinhoudt, D. N.; van der Tol, E. B.; Verhoeven, J. W. *Journal of the American Chemical Society* **1995**, *117*, 9408–9414.
- [141] Charbonnière, L. J.; Faulkner, S.; Platas-Iglesias, C.; Regueiro-Figueroa, M.; Nonat, A.; Rodríguez-Blas, T.; de Blas, A.; Perry, W. S.; Tropicano, M. *Dalton Transactions* **2013**, *42*, 3667–3681.
- [142] Pope, S. J. a.; Coe, B. J.; Faulkner, S. *Chemical Communications* **2004**, *44*, 1550–1551.
- [143] Lazarides, T.; Tart, N. M.; Sykes, D.; Faulkner, S.; Barbieri, A.; Ward, M. D. *Dalton Transactions* **2009**, 3971–3979.
- [144] Tropicano, M.; Record, C. J.; Morris, E.; Rai, H. S.; Allain, C.; Faulkner, S. *Organometallics* **2012**, *31*, 5673–5676.
- [145] Shavaleev, N. M.; Bell, Z. R.; Ward, M. D. *Journal of the Chemical Society, Dalton Transactions* **2002**, 3925–3927.
- [146] Sambrook, M. R.; Curiel, D.; Hayes, E. J.; Beer, P. D.; Pope, S. J. A.; Faulkner, S. *New Journal of Chemistry* **2006**, *30*, 1133–1136.
- [147] Singaravadivel, S.; Babu, E.; Velayudham, M.; Lu, K.-L.; Rajagopal, S. *Inorganica Chimica Acta* **2013**, *400*, 215–221.
- [148] Koguro, K.; Oga, T.; Mitsui, S.; Orita, R. *Synthesis* **1998**, 910–914.
- [149] Chermahini, A. N.; Teimouri, A.; Moaddeli, A. *Heteroatom Chemistry* **2011**, *22*, 168–173.



- [150] Myznikov, L. V.; Efimova, Y. a.; Artamonova, T. V.; Koldobskii, G. I. *Russian Journal of Organic Chemistry* **2011**, *47*, 728–730.
- [151] Reddy, M.; Bhoje, M.; Pasha, M. *Journal of Chemical Sciences* **2011**, *123*, 75–79.
- [152] Demko, Z. P.; Sharpless, K. B. *The Journal of Organic Chemistry* **2001**, *66*, 7945–7950.
- [153] Butler, R. *Advances in Heterocyclic Chemistry*; 1977; Vol. 21; pp 323–435.
- [154] Abdel-Rahman, A. A.-H.; Ali, O. M.; Abdel-Megeed, A. A.-S. *Journal of Heterocyclic Chemistry* **2013**, *50*, 484–489.
- [155] Herr, R. J. *Bioorganic & Medicinal Chemistry* **2002**, *10*, 3379–3393.
- [156] Trécant, C.; Dlubala, A.; George, P.; Pichat, P.; Ripoche, I.; Troin, Y. *European Journal of Medicinal Chemistry* **2011**, *46*, 4035–4041.
- [157] Hansch, C.; Leo, A.; Hoekman, D. H. *Exploring QSAR*; Washington, DC : American Chemical Society, 1995; Chapter 13.
- [158] Wexler, R. R.; Greenlee, W. J.; Irvin, J. D.; Goldberg, M. R.; Prendergast, K.; Smith, R. D.; Timmermans, P. B. M. W. M. *Journal of Medicinal Chemistry* **1996**, *39*, 625–656.
- [159] Noda, K.; Saad, Y.; Kinoshita, A.; Boyle, T. P.; Graham, R. M.; Husain, A.; Karnik, S. S. *Journal of Biological Chemistry* **1995**, *270*, 2284–2289.
- [160] Kubo, K.; Kohara, Y.; Imamiya, E.; Sugiura, Y.; Inada, Y.; Furukawa, Y.; Nishikawa, K.; Naka, T. *Journal of Medicinal Chemistry* **1993**, *36*, 2182–2195.
- [161] Goldgur, Y.; Craigie, R.; Cohen, G. H.; Fujiwara, T.; Yoshinaga, T.; Fujishita, T.; Sugimoto, H.; Endo, T.; Murai, H.; Davies, D. R. *Proceedings of the National Academy of Sciences* **1999**, *96*, 13040–13043.
- [162] Kotoris, C. C.; Chen, M. J.; Taylor, S. D. *Bioorganic & Medicinal Chemistry Letters* **1998**, *8*, 3275–3280.
- [163] Wan, Z.-K.; Follows, B.; Kirincich, S.; Wilson, D.; Binnun, E.; Xu, W.; Joseph-McCarthy, D.; Wu, J.; Smith, M.; Zhang, Y.-L.; Tam, M.; Erbe, D.; Tam, S.; Saiah, E.; Lee, J. *Bioorganic & Medicinal Chemistry Letters* **2007**, *17*, 2913–2920.

- [164] Nachman, R. J.; Zabrocki, J.; Olczak, J.; Williams, H. J.; Moyna, G.; Ian Scott, A.; Coast, G. M. *Peptides* **2002**, *23*, 709–716.
- [165] Palazzi, A.; Stagni, S.; Bordoni, S.; Monari, M.; Selva, S. *Organometallics* **2002**, *21*, 3774–3781.
- [166] Palazzi, A.; Stagni, S.; Selva, S.; Monari, M. *Journal of Organometallic Chemistry* **2003**, *669*, 135–140.
- [167] Palazzi, A.; Stagni, S. *Journal of Organometallic Chemistry* **2005**, *690*, 2052–2061.
- [168] Hassan, N.; Stelzl, J.; Weinberger, P.; Molnar, G.; Bousseksou, A.; Kubel, F.; Mereiter, K.; Boca, R.; Linert, W. *Inorganica Chimica Acta* **2013**, *396*, 92–100.
- [169] Lavrenova, L. G.; Strekalova, A. D.; Bogomyakov, A. S.; Korotaev, E. V.; Virovets, A. V.; Piryazev, D. A.; Sheludyakova, L. A.; Vasilevskii, S. F. *Russian Journal of Coordination Chemistry* **2015**, *41*, 189–196.
- [170] Senthil Kumar, K.; Šalitroš, I.; Heinrich, B.; Fuhr, O.; Ruben, M. *Journal of Materials Chemistry C* **2015**, *3*, 11635–11644.
- [171] Tafli-Kryeziu, M.; Caneschi, A.; Fittipaldi, M.; Spina, G.; Lantieri, M.; Weil, M.; Hasegawa, M.; Linert, W. *Journal of Coordination Chemistry* **2015**, *68*, 3457–3471.
- [172] D'Alessio, D.; Muzzioli, S.; Skelton, B. W.; Stagni, S.; Massi, M.; Ogden, M. I. *Dalton Transactions* **2012**, *41*, 4736–4739.
- [173] Andreiadis, E. S.; Demadrille, R.; Imbert, D.; Pécaut, J.; Mazzanti, M. *Chemistry - A European Journal* **2009**, *15*, 9458–9476.
- [174] Giraud, M.; Andreiadis, E. S.; Fisyuk, A. S.; Demadrille, R.; Imbert, D.; Mazzanti, M. *Inorganic Chemistry* **2008**, *47*, 3952–3954.
- [175] Senthil Kumar, K.; Schäfer, B.; Lebedkin, S.; Karmazin, L.; Kappes, M. M.; Ruben, M. *Dalton Transactions* **2015**, *44*, 15611–15619.
- [176] D'Alessio, D.; Karagiannidis, L. E.; Skelton, B. W.; Massi, M.; Ogden, M. I. *Australian Journal of Chemistry* **2012**, *65*, 819–822.
- [177] D'Alessio, D.; Skelton, B. W.; Lengkeek, N. A.; Fraser, B. H.; Krause-Heuer, A. M.; Muzzioli, S.; Stagni, S.; Massi, M.; Ogden, M. I. *Supramolecular Chemistry* **2015**, *27*, 787–791.

- [178] D'Alessio, D.; Sobolev, A. N.; Skelton, B. W.; Fuller, R. O.; Woodward, R. C.; Lengkeek, N. A.; Fraser, B. H.; Massi, M.; Ogden, M. I. *Journal of the American Chemical Society* **2014**, *136*, 15122–15125.
- [179] Maspero, A.; Galli, S.; Colombo, V.; Peli, G.; Masciocchi, N.; Stagni, S.; Barea, E.; Navarro, J. A. *Inorganica Chimica Acta* **2009**, *362*, 4340–4346.
- [180] Shi, L.; Li, B.; Yue, S.; Fan, D. *Sensors and Actuators B: Chemical* **2009**, *137*, 386–392.
- [181] Degtyarik, M. M.; Lyakhov, A. S.; Ivashkevich, L. S.; Matulis, V. E.; Matulis, V. E.; Gruschinski, S.; Voitekhovich, S. V.; Kersting, B.; Ivashkevich, O. A. *Dalton Transactions* **2015**, *44*, 18518–18526.
- [182] Gabrielli, W. F.; Nogai, S. D.; McKenzie, J. M.; Cronje, S.; Raubenhaimer, H. G. *New Journal of Chemistry* **2009**, *33*, 2208–2218.
- [183] Kieft, R. L.; Peterson, W. M.; Blundell, G. L.; Horton, S.; Henry, R. A.; Jonassen, H. B. *Inorganic Chemistry* **1976**, *15*, 1721–1722.
- [184] Ilie, A.; Rat, C. I.; Scheutzow, S.; Kiske, C.; Lux, K.; Klapotke, T. M.; Silvestru, C.; Karaghiosoff, K. *Inorganic Chemistry* **2011**, *50*, 2675–2684.
- [185] Komeda, S.; Lin, Y.-L.; Chikuma, M. *ChemMedChem* **2011**, *6*, 987–990.
- [186] Jeong, S.; Song, X.; Jeong, S.; Oh, M.; Liu, X.; Kim, D.; Moon, D.; Lah, M. S. *Inorganic Chemistry* **2011**, *50*, 12133–12140.
- [187] Voitekhovich, S. V.; Serebryanskaya, T. V.; Lyakhov, A. S.; Gaponik, P. N.; Ivashkevich, O. A. *Polyhedron* **2009**, *28*, 3614–3620.
- [188] Chen, J.-L.; Tan, X.-Z.; Chen, X.-X.; Wang, J.-Y.; Cao, X.-F.; He, L.-H.; Hua, J.-Y.; Wen, H.-R. *Inorganic Chemistry Communications* **2013**, *30*, 120–123.
- [189] MaGee, K. D. M.; Wright, P. J.; Muzzioli, S.; Siedlovska, C. M.; Raiteri, P.; Baker, M. V.; Brown, D. H.; Stagni, S.; Massi, M. *Dalton Transactions* **2013**, *42*, 4233–4236.
- [190] Downard, A.; Steel, P.; Steenwijk, J. *Australian Journal of Chemistry* **1995**, *48*, 1625–1642.
- [191] Bergmann, L.; Friedrichs, J.; Mydlak, M.; Baumann, T.; Nieger, M.; Bräse, S. *Chemical Communications* **2013**, *49*, 6501–6503.

- [192] Femoni, C.; Muzzioli, S.; Palazzi, A.; Stagni, S.; Zacchini, S.; Monti, F.; Accorsi, G.; Bolognesi, M.; Armaroli, N.; Massi, M.; Valenti, G.; Marcaccio, M. *Dalton Transactions* **2013**, *42*, 997–1010.
- [193] Tong, S.; Yuan, D.; Yi, L. *Spectrochimica Acta Part A: Molecular and Biomolecular Spectroscopy* **2014**, *130*, 280–286.
- [194] Monti, F.; Baschieri, A.; Gualandi, I.; Serrano-Pérez, J. J.; Junquera-Hernández, J. M.; Tonelli, D.; Mazzanti, A.; Muzzioli, S.; Stagni, S.; Roldan-Carmona, C.; Pertegás, A.; Bolink, H. J.; Ortí, E.; Sambri, L.; Armaroli, N. *Inorganic Chemistry* **2014**, *53*, 7709–7721.
- [195] Stagni, S.; Colella, S.; Palazzi, A.; Valenti, G.; Zacchini, S.; Paolucci, F.; Marcaccio, M.; Albuquerque, R. Q.; De Cola, L. *Inorganic Chemistry* **2008**, *47*, 10509–10521.
- [196] Werrett, M. V.; Muzzioli, S.; Wright, P. J.; Palazzi, A.; Raiteri, P.; Zacchini, S.; Massi, M.; Stagni, S. *Inorganic Chemistry* **2014**, *53*, 229–243.
- [197] Stagni, S.; Palazzi, A.; Brulatti, P.; Salmi, M.; Muzzioli, S.; Zacchini, S.; Marcaccio, M.; Paolucci, F. *European Journal of Inorganic Chemistry* **2010**, *2010*, 4643–4657.
- [198] Stagni, S.; Orselli, E.; Palazzi, A.; De Cola, L.; Zacchini, S.; Femoni, C.; Marcaccio, M.; Paolucci, F.; Zanarini, S. *Inorganic Chemistry* **2007**, *46*, 9126–9138.
- [199] Duati, M.; Tasca, S.; Lynch, F. C.; Bohlen, H.; Vos, J. G.; Stagni, S.; Ward, M. D. *Inorganic Chemistry* **2003**, *42*, 8377–8384.
- [200] Zanarini, S.; Bard, A. J.; Marcaccio, M.; Palazzi, A.; Paolucci, F.; Stagni, S. *The Journal of Physical Chemistry B* **2006**, *110*, 22551–22556.
- [201] Shahroosvand, H.; Najafi, L.; Mohajerani, E.; Janghour, M.; Nasrollahzadeh, M. *RSC Advances* **2013**, *3*, 6323–6326.
- [202] Bader, C. a. et al. *RSC Advances* **2014**, *4*, 16345–16351.
- [203] Szabo, A.; Ostlund, N. S. *Modern quantum chemistry : introduction to advanced electronic structure theory*; McGraw-Hill: New York, 1989.
- [204] McWeeny, R.; Sutcliffe, B. T. *Methods of molecular quantum mechanics*; Academic Press: London, 1969.
- [205] Parr, R. G. *Annual Review of Physical Chemistry* **1983**, *34*, 631–656.

- [206] Kohn, W. Nobel Lecture: Electronic structure of matterwave functions and density functionals. 1999.
- [207] Hohenberg, P.; Kohn, W. *Physical Review* **1964**, *136*, B864–B871.
- [208] Parr, R. G.; Yang, W. *Density-functional theory of atoms and molecules*; Oxford University Press: Oxford, 1989.
- [209] Kohn, W.; Sham, L. J. *Physical Review* **1965**, *140*, A1133–A1138.
- [210] Becke, A. D. *The Journal of Chemical Physics* **1993**, *98*, 1372–1377.
- [211] Stephens, P.; Devlin, F. *The Journal of Physical Chemistry* **1994**, *98*, 11623–11627.
- [212] Cai, Z.-L.; Sendt, K.; Reimers, J. R. *The Journal of Chemical Physics* **2002**, *117*, 5543–5549.
- [213] Dreuw, A.; Head-Gordon, M. *Journal of the American Chemical Society* **2004**, *126*, 4007–4016.
- [214] Yanai, T.; Tew, D. P.; Handy, N. C. *Chemical Physics Letters* **2004**, *393*, 51–57.
- [215] Leach, A. R. *Molecular Modelling: Principles and Applications*; Pearson Education, 2001.
- [216] Wright, P. J.; Affleck, M. G.; Muzzioli, S.; Skelton, B. W.; Raiteri, P.; Silvester, D. S.; Stagni, S.; Massi, M. *Organometallics* **2013**, *32*, 3728–3737.
- [217] Runge, E.; Gross, E. K. U. *Physical Review Letters* **1984**, *52*, 997–1000.
- [218] Rao, B. U.; Krishna, V.; Rao, G. N. *International Journal of Pharma and Bio Sciences* **2015**, *6*, 1233–1242.
- [219] Lee, J. H.; Lee, H.; Seo, S.; Jaworski, J.; Seo, M. L.; Kang, S.; Lee, J. Y.; Jung, J. H. *New Journal of Chemistry* **2011**, *35*, 1054–1059.
- [220] Bharty, M.; Dani, R.; Kushawaha, S.; Singh, N.; Kharwar, R.; Butcher, R. *Polyhedron* **2015**, *88*, 208–221.
- [221] Zou, J.-H.; Zhu, D.-L.; Tian, H.; Li, F. F.; Zhang, F. F.; Yang, G.-W.; Li, Q.-Y.; Miao, Y. X. *Inorganica Chimica Acta* **2014**, *423*, 87–94.
- [222] Boldog, I.; Domasevitch, K. V.; Sanchiz, J.; Mayer, P.; Janiak, C. *Dalton Transactions* **2014**, *43*, 12590–12605.

- [223] Wang, B. J.; Zou, J. H.; Li, W. X.; Wang, Z.; Xu, B.; Li, S.; Zhai, Y. S.; Zhu, D. L.; Li, Q. Y.; Yang, G. W. *Journal of Organometallic Chemistry* **2014**, *749*, 428–432.
- [224] Butler, R. N.; Garvin, V. C. *Journal of the Chemical Society, Perkin Transactions 1* **1981**, *2*, 390–393.
- [225] Mosalkova, A. P.; Voitekhovich, S. V.; Lyakhov, A. S.; Ivashkevich, L. S.; Lach, J.; Kersting, B.; Gaponik, P. N.; Ivashkevich, O. A. *Dalton Transactions* **2013**, *42*, 2985–2997.
- [226] Finnegan, W. G.; Henry, R. A.; Lofquist, R. *Journal of the American Chemical Society* **1958**, *80*, 3908–3911.
- [227] Butler, R. N.; Garvin, V. C.; Lumbroso, H.; Ligeois, C. *Journal of the Chemical Society, Perkin Transactions 2* **1984**, *4*, 721–725.
- [228] Kanno, H.; Yamaguchi, H.; Ichikawa, Y.; Isoda, S. *Chemical & Pharmaceutical Bulletin* **1991**, *39*, 1099–1105.
- [229] Henry, R. A. *Journal of Heterocyclic Chemistry* **1976**, *13*, 391–392.
- [230] Zhu, K.-q.; Wang, L.; Chen, Q.; He, M.-y. *Tetrahedron Letters* **2015**, *56*, 4943–4946.
- [231] Donghi, D.; D'Alfonso, G.; Mauro, M.; Panigati, M.; Mercandelli, P.; Sironi, A.; Mussini, P.; D'Alfonso, L. *Inorganic Chemistry* **2008**, *47*, 4243–4255.
- [232] Cebrián, C.; Natali, M.; Villa, D.; Panigati, M.; Mauro, M.; D'Alfonso, G.; De Cola, L. *Nanoscale* **2015**, *7*, 12000–12009.
- [233] Nastasi, F.; Puntoriero, F.; Natali, M.; Mba, M.; Maggini, M.; Mussini, P.; Panigati, M.; Campagna, S. *Photochemical and Photobiological Sciences* **2015**, *14*, 909–918.
- [234] Valenti, G.; Panigati, M.; Boni, A.; D'Alfonso, G.; Paolucci, F.; Prodi, L. *Inorganica Chimica Acta* **2014**, *417*, 270–273.
- [235] Panigati, M.; Donghi, D.; D'Alfonso, G.; Mercandelli, P.; Sironi, A.; D'Alfonso, L. *Inorganic Chemistry* **2006**, *45*, 10909–10921.
- [236] Raimondi, A.; Panigati, M.; Maggioni, D.; D'Alfonso, L.; Mercandelli, P.; Mussini, P.; D'Alfonso, G. *Inorganic Chemistry* **2012**, *51*, 2966–2975.

- [237] Mattes, R.; Weber, H. *Journal of Organometallic Chemistry* **1979**, *178*, 191–196.
- [238] Calhorda, M. J.; de C.T. Carrondo, M. A.; Dias, A. R.; Félix, V.; Galvão, A. M.; Garcia, M.; Matias, P. M.; Villa de Brito, M. J. *Journal of Organometallic Chemistry* **1993**, *453*, 231–240.
- [239] Zangrando, E.; Casanova, M.; Alessio, E. *Chemical Reviews* **2008**, *108*, 4979–5013.
- [240] Morimoto, T.; Nishiura, C. *Journal of the American Chemical Society* **2013**, *135*, 13266–13269.
- [241] Slone, R. V.; Benkstein, K. D.; Bélanger, S.; Hupp, J. T.; Guzei, I. a.; Rheingold, A. L. *Coordination Chemistry Reviews* **1998**, *171*, 221–243.
- [242] Ishitani, O.; Kanai, K.; Yamada, Y.; Sakamoto, K. *Chemical Communications* **2001**, 1514–1515.
- [243] Woessner, S. M.; Helms, J. B.; Shen, Y.; Sullivan, B. P. *Inorganic Chemistry* **1998**, *1*, 5406–5407.
- [244] Sun, S.-S.; Lees, A. J. *Journal of the American Chemical Society* **2000**, *122*, 8956–8967.
- [245] Thanasekaran, P.; Lee, C.-C.; Lu, K.-l. *Accounts of Chemical Research* **2012**, *45*, 1403–1418.
- [246] Coogan, M. P.; Fernández-Moreira, V.; Kariuki, B. M.; Pope, S. J. a.; Thorp-Greenwood, F. L. *Angewandte Chemie International Edition* **2009**, *48*, 4965–4968.
- [247] Spellanet, P.; Watts, R. J. *Inorganic Chemistry* **1993**, *32*, 5633–5636.
- [248] Silvester, D. S.; Uprety, S.; Wright, P. J.; Massi, M.; Stagni, S.; Muzzioli, S. *The Journal of Physical Chemistry C* **2012**, *116*, 7327–7333.
- [249] Bullock, J. P.; Carter, E.; Johnson, R.; Kennedy, A. T.; Key, S. E.; Kraft, B. J.; Saxon, D.; Underwood, P. *Inorganic Chemistry* **2008**, *47*, 7880–7887.
- [250] Baldo, M.; Thompson, M.; Forrest, S. *Nature* **2000**, *403*, 750–753.
- [251] Kimura, M.; Takahashi, A.; Sakata, T.; Tsukahara, K. *Bulletin of the Chemical Society of Japan* **1998**, *71*, 1839–1845.

- [252] Demas, J.; DeGraff, B. *Coordination Chemistry Reviews* **2001**, *211*, 317–351.
- [253] Xie, H.; Lu, G. *Journal of Rare Earths* **2013**, *31*, 639–644.
- [254] Hamilton, J. M.; Anhorn, M. J.; Oscarson, K. A.; Reibenspies, J. H.; Hancock, R. D. *Inorganic Chemistry* **2011**, *50*, 2764–2770.
- [255] Xie, J.; Shu, H.-M.; Hu, H.-M.; Han, Z.-X.; Shen, S.-S.; Yuan, F.; Yang, M.-L.; Dong, F.-X.; Xue, G.-L. *ChemPlusChem* **2014**, *79*, 985–994.
- [256] Mukkala, V.-M.; Takalo, H.; Liitti, P.; Hemmilä, I. *Journal of Alloys and Compounds* **1995**, *225*, 507–510.
- [257] Goodall, W.; Williams, J. a. *Chemical Communications* **2001**, 2514–2515.
- [258] Mutai, T.; Cheon, J.-D.; Arita, S.; Araki, K. *Journal of the Chemical Society, Perkin Transactions 2* **2001**, 1045–1050.
- [259] Hong, Y.; Chen, S.; Leung, C. W. T.; Lam, J. W. Y.; Liu, J.; Tseng, N.-W.; Kwok, R. T. K.; Yu, Y.; Wang, Z.; Tang, B. Z. *ACS Applied Materials & Interfaces* **2011**, *3*, 3411–3418.
- [260] Goodall, W.; Williams, J. A. G. *Chemical Communications* **2001**, 2514–2515.
- [261] Wang, J.; Hanan, G. S. *Synlett* **2005**, 1251–1254.
- [262] Cargill Thompson, A. M. W. *Coordination Chemistry Reviews* **1997**, *160*, 1–52.
- [263] Vaduvescu, S.; Potvin, P. G. *European Journal of Inorganic Chemistry* **2004**, *8*, 1763–1769.
- [264] Thomas, E. W.; Cudahy, M. M. *The Journal of Organic Chemistry* **1993**, *58*, 1623–1627.
- [265] Koelsch, C. F.; Whitney, A. G. *The Journal of Organic Chemistry* **1941**, *06*, 795–803.
- [266] Ashimori, A.; Ono, T.; Uchida, T.; Ohtaki, Y.; Fukaya, C.; Watanabe, M.; Yokoyama, K. *Chemical & Pharmaceutical Bulletin* **1990**, *38*, 2446–2458.
- [267] Wang, D.; Xu, Q.-L.; Zhang, S.; Li, H.-Y.; Wang, C.-C.; Li, T.-Y.; Jing, Y.-M.; Huang, W.; Zheng, Y.-X.; Accorsi, G. *Dalton Transactions* **2013**, *42*, 2716–2723.



- [268] Helberg, L. E.; Barrera, J.; Sabat, M.; Harman, W. D. *Inorganic Chemistry* **1995**, *34*, 2033–2041.
- [269] Laramée-Milette, B.; Lachance-Brais, C.; Hanan, G. S. *Dalton Transactions* **2015**, *44*, 41–45.
- [270] Sato, S.; Sekine, A.; Ohashi, Y.; Ishitani, O.; Blanco-Rodríguez, A. M.; Vlcek, A.; Unno, T.; Koike, K. *Inorganic Chemistry* **2007**, *46*, 3531–3540.
- [271] Sato, S.; Ishitani, O. *Coordination Chemistry Reviews* **2015**, *282–283*, 50–59.
- [272] Bünzli, J.-C. G., Eliseeva, S. V. In *Springer Series on Fluorescence, Vol. 7*; Hänninen, P., Härmä, H., Eds.; Springer Series on Fluorescence; Springer Berlin Heidelberg: Berlin, Heidelberg, 2011; Vol. 7; pp 1–45.
- [273] Vleck, J. H. V. *The Journal of Physical Chemistry* **1937**, *41*, 67–80.
- [274] Andreiadis, E. S.; Gauthier, N.; Imbert, D.; Demadrille, R.; Pécaut, J.; Mazzanti, M. *Inorganic Chemistry* **2013**, *52*, 14382–14390.
- [275] Molloy, J. K.; Pillai, Z.; Sakamoto, J.; Ceroni, P.; Bergamini, G. *Asian Journal of Organic Chemistry* **2015**, *4*, 251–255.
- [276] Leonard, J. P.; Nolan, C. B.; Stomeo, F.; Gunnlaugsson, T. *Photochemistry and Photophysics of Coordination Compounds II*; Springer Berlin Heidelberg: Berlin, Heidelberg, 2007; pp 1–43.
- [277] Bunzli, J.-C. G. *Chemical Reviews* **2010**, *110*, 2729–2755.
- [278] Carnall, W. T. *The Journal of Chemical Physics* **1968**, *49*, 4424–4442.
- [279] Carnall, W. T. *The Journal of Chemical Physics* **1968**, *49*, 4443–4446.
- [280] Carnall, W. T. *The Journal of Chemical Physics* **1968**, *49*, 4447–4449.
- [281] Carnall, W. T. *The Journal of Chemical Physics* **1968**, *49*, 4450–4455.
- [282] Sénéchal-David, K.; Pope, S. J. A.; Quinn, S.; Faulkner, S.; Gunnlaugsson, T. *Inorganic Chemistry* **2006**, *45*, 10040–10042.
- [283] Huetting, R.; Tropiano, M.; Faulkner, S. *RSC Advances* **2014**, *4*, 44162–44165.
- [284] Hehlen, M. P.; Brik, M. G.; Krämer, K. W. *Journal of Luminescence* **2013**, *136*, 221–239.

- [285] de Bettencourt-Dias, A.; Barber, P. S.; Bauer, S. *Journal of the American Chemical Society* **2012**, *134*, 6987–6994.
- [286] Zhu, B. H.; Liu, Y. H.; Jin, X. Y.; Xu, H. Y.; Han, Y. Y.; Zhao, Q. *Polyhedron* **2014**, *74*, 67–71.
- [287] Aebischer, A.; Gumy, F.; Bünzli, J.-C. G. *Physical Chemistry Chemical Physics* **2009**, *11*, 1346–1353.
- [288] Supkowski, R. M.; Bolender, J. P.; Smith, W. D.; Reynolds, L. E.; Horrocks Jr, W. D. *Coordination Chemistry Reviews* **1999**, *185-186*, 307–319.
- [289] Faulkner, S.; Burton-Pye, B. P.; Khan, T.; Martin, L. R.; Wray, S. D.; Skabara, P. J. *Chemical Communications* **2002**, 1668–1669.
- [290] Horrocks, W. D.; Bolender, J. P.; Smith, W. D.; Supkowski, R. M. *Journal of the American Chemical Society* **1997**, *119*, 5972–5973.
- [291] He, H.; Sykes, A. G.; May, P. S.; He, G. *Dalton Transactions* **2009**, 7454–7461.
- [292] Werrett, M. V.; Huff, G. S.; Muzzioli, S.; Fiorini, V.; Zacchini, S.; Skelton, B. W.; Maggiore, A.; Malicka, J. M.; Cocchi, M.; Gordon, K. C.; Stagni, S.; Massi, M. *Dalton Transactions* **2015**, *44*, 8379–8393.
- [293] Beeby, A.; Faulkner, S.; Williams, J. A. G. *Dalton Transactions* **2002**, 1918–1922.
- [294] Koullourou, T.; Natrajan, L. S.; Bhavsar, H.; Pope, J.; Feng, J.; Narvainen, J.; Shaw, R.; Scales, E.; Kauppinen, R.; Kenwright, A. M.; Faulkner, S. *Journal of the American Chemical Society* **2008**, *130*, 2178–2179.
- [295] Crosby, G. A.; Demas, J. N. *The Journal of Physical Chemistry* **1971**, *75*, 991–1024.
- [296] Eaton, D. F. *Pure and Applied Chemistry* **1988**, *60*, 1107–1114.
- [297] Silvester, D. S.; Wain, A. J.; Aldous, L.; Hardacre, C.; Compton, R. G. *Journal of Electroanalytical Chemistry* **2006**, *596*, 131–140.
- [298] Gritzner, G.; Kuta, J. *Pure and Applied Chemistry* **1984**, *56*, 461–466.
- [299] Barrosse-Antle, L. E.; Bond, A. M.; Compton, R. G.; O'Mahony, A. M.; Rogers, E. I.; Silvester, D. S. *Chemistry - An Asian Journal* **2010**, *5*, 202–230.

- [300] Rogers, E.; Silvester, D.; Poole, D.; Aldous, L.; Hardacre, C.; Compton, R. *Journal of Physical Chemistry C* **2008**, *112*, 2729–2735.
- [301] Frisch, M. J. et al. Gaussian 09. 2013.
- [302] Andrae, D.; Hauzermann, U.; Dolg, M.; Stoll, H.; Preuz, H. *Theoretica Chimica Acta* **1990**, *77*, 123–141.
- [303] Tomasi, J.; Mennucci, B.; Cammi, R. *Chemical Reviews* **2005**, *105*, 2999–3094.

Every reasonable effort has been made to acknowledge the owners of copyright material. I would be pleased to hear from any copyright owner who has been omitted or incorrectly acknowledged.



# Appendix A

**Table 7.1:** Crystal data and structure refinement for [Re(*t*BuTzPy)Cl].

Identification code	[Re( <i>t</i> BuTzPy)Cl]
Empirical formula	C <sub>14</sub> H <sub>15</sub> Cl <sub>3</sub> N <sub>5</sub> O <sub>3</sub> Re
Formula weight	593.86
Temperature	100(2) K
Wavelength	0.71073 Å
Crystal system	Monoclinic
Space group	P2 <sub>1</sub> /n
Unit cell dimensions	a = 10.8488(5) Å b = 11.4278(4) Å c = 16.6365(4) Å β = 106.769(4)°
Volume	1974.85(12) Å <sup>3</sup>
Z	4
Density (calculated)	1.997 Mg/m <sup>3</sup> 6.583 mm <sup>-3</sup>
Crystal size	0.58 × 0.35 × 0.26 mm <sup>3</sup>
θ range for data collection	3.77 to 37.61°.
Index ranges	-18 ≤ h ≤ 18, -19 ≤ k ≤ 19 -28 ≤ l ≤ 28
Reflections collected	64078
Independent reflections	10156 [R(int) = 0.0324]
Completeness to θ = 37.00°	99.5 %
Absorption correction	Analytical
Max. and min. transmission	0.366 and 0.128
Refinement method	Full-matrix least-squares on F <sup>2</sup>
Data / restraints / parameters	10156 / 0 / 268
Goodness-of-fit on F <sup>2</sup>	1.176
Final R indices [I > 2σ(I)]	R1 = 0.0293, wR2 = 0.0583
R indices (all data)	R1 = 0.0331, wR2 = 0.0596
Largest diff. peak and hole	2.907 and -3.251 e.Å <sup>-3</sup>

**Table 7.2:** Selected bond lengths [ $\text{\AA}$ ] and angles[ $^\circ$ ] for  $[\text{Re}(^t\text{BuTzPy})\text{Cl}]$ .

Re(1)-C(1)	1.911(2)
Re(1)-C(2)	1.920(3)
Re(1)-C(3)	1.938(3)
Re(1)-N(4)	2.1585(19)
Re(1)-N(52)	2.214(2)
Re(1)-Cl(1)	2.4605(6)
C(1)-Re(1)-C(2)	88.42(11)
C(1)-Re(1)-C(3)	90.37(11)
C(2)-Re(1)-C(3)	90.83(11)
C(1)-Re(1)-N(4)	171.28(9)
C(2)-Re(1)-N(4)	99.18(9)
C(3)-Re(1)-N(4)	93.77(10)
C(1)-Re(1)-N(52)	97.61(9)
C(2)-Re(1)-N(52)	173.10(9)
C(3)-Re(1)-N(52)	92.49(10)
N(4)-Re(1)-N(52)	74.57(7)
C(1)-Re(1)-Cl(1)	93.32(8)
C(2)-Re(1)-Cl(1)	92.82(8)
C(3)-Re(1)-Cl(1)	174.88(8)
N(4)-Re(1)-Cl(1)	82.10(6)
N(52)-Re(1)-Cl(1)	83.51(5)

**Table 7.3:** Crystal data and structure refinement for [Re(*t*BuTzPy)Br].

Identification code	[Re( <i>t</i> BuTzPy)Br]
Empirical formula	C <sub>14</sub> H <sub>14</sub> BrCl <sub>3</sub> N <sub>5</sub> O <sub>3</sub> Re
Formula weight	672.76
Temperature	100(2) K
Wavelength	0.71073 Å
Crystal system	Monoclinic
Space group	P2 <sub>1</sub> /c
Unit cell dimensions	a = 8.6560(2) Å b = 18.0418(2) Å c = 13.2050(4) Å β = 92.829(3)°
Volume	2071.13(8) Å <sup>3</sup>
Z	4
Density (calculated)	2.158 Mg/m <sup>3</sup>
μ	8.208 mm <sup>-1</sup>
F(000)	1272
Crystal size	0.53 × 0.43 × 0.09 mm <sup>3</sup>
θ range for data collection	3.65 to 41.07°.
Index ranges	-15 ≤ h ≤ 15, -33 ≤ k ≤ 31 -24 ≤ l ≤ 24
Reflections collected	53110
Independent reflections	13425 [R(int) = 0.0382]
Completeness to θ = 40.00°	99.9 %
Absorption correction	Analytical
Max. and min. transmission	0.451 and 0.065
Refinement method	Full-matrix least-squares on F <sup>2</sup>
Data / restraints / parameters	13425 / 0 / 247
Goodness-of-fit on F <sup>2</sup>	0.921
Final R indices [I > 2σ(I)]	R1 = 0.0229, wR2 = 0.0388
R indices (all data)	R1 = 0.0400, wR2 = 0.0403
Largest diff. peak and hole	1.455 and -1.200 e.Å <sup>-3</sup>

**Table 7.4:** Selected bond lengths [ $\text{\AA}$ ] and angles[ $^\circ$ ] for  $[\text{Re}(^t\text{BuTzPy})\text{Br}]$ .

Re(1)-C(3)	1.8998(17)
Re(1)-C(2)	1.9145(16)
Re(1)-C(1)	1.9240(16)
Re(1)-N(4)	2.1396(13)
Re(1)-N(52)	2.2159(12)
Re(1)-Br(1)	2.62869(18)
C(3)-Re(1)-C(2)	89.38(7)
C(3)-Re(1)-C(1)	86.99(7)
C(2)-Re(1)-C(1)	88.41(6)
C(3)-Re(1)-N(4)	97.86(6)
C(2)-Re(1)-N(4)	96.92(6)
C(1)-Re(1)-N(4)	172.81(6)
C(3)-Re(1)-N(52)	95.00(6)
C(2)-Re(1)-N(52)	170.23(6)
C(1)-Re(1)-N(52)	100.51(5)
N(4)-Re(1)-N(52)	73.86(5)
C(3)-Re(1)-Br(1)	177.90(5)
C(2)-Re(1)-Br(1)	92.41(5)
C(1)-Re(1)-Br(1)	91.97(5)
N(4)-Re(1)-Br(1)	83.01(4)
N(52)-Re(1)-Br(1)	83.40(3)

**Table 7.5:** Hydrogen bonds for  $[\text{Re}(^t\text{BuTzPy})\text{Br}]$  [ $\text{\AA}$  and  $^\circ$ ].

D-H...A	d(D-H)	d(H...A)	d(D...A)	$\angle(\text{DHA})$
C(0)-H(0)...Br(1)	1.00	2.79	3.7385(16)	157.9



**Table 7.6:** Crystal data and structure refinement for  $[\text{Re}_2(\text{}^t\text{BuTzPh})\text{Br}_2]$ .

Identification code	$[\text{Re}_2(\text{}^t\text{BuTzPh})]\text{Br}_2$
Empirical formula	$\text{C}_{18}\text{H}_{16}\text{Br}_2\text{Cl}_2\text{N}_4\text{O}_6\text{Re}_2$
Formula weight	987.47
Temperature	100(2) K
Wavelength	0.71073 Å
Crystal system	Monoclinic
Space group	$\text{P}2_1/\text{n}$
Unit cell dimensions	$a = 10.7387(2)$ Å $b = 16.7806(2)$ Å $c = 14.5656(2)$ Å $\beta = 104.820(2)^\circ$
Volume	$2537.43(7)$ Å <sup>3</sup>
Z	4
Density (calculated)	2.585 Mg/m <sup>3</sup>
$\mu$	12.934 mm <sup>-1</sup>
Crystal size	$0.35 \times 0.23 \times 0.075$ mm <sup>3</sup>
$\theta$ range for data collection	3.65 to 34.00°.
Index ranges	$-16 \leq h \leq 16$ , $-26 \leq k \leq 26$ $-22 \leq l \leq 22$
Reflections collected	63567
Independent reflections	10334 [R(int) = 0.0393]
Completeness to $\theta = 34.00^\circ$	99.9 %
Absorption correction	Analytical
Max. and min. transmission	0.383 and 0.070
Refinement method	Full-matrix least-squares on $F^2$
Data / restraints / parameters	10334 / 0 / 310
Goodness-of-fit on $F^2$	1.079
Final R indices [ $I > 2\sigma(I)$ ]	R1 = 0.0209, wR2 = 0.0404
R indices (all data)	R1 = 0.0267, wR2 = 0.0417
Largest diff. peak and hole	1.037 and -1.154 e.Å <sup>-3</sup>

**Table 7.7:** Selected bond lengths [ $\text{\AA}$ ] and angles[ $^\circ$ ] for  $[\text{Re}_2(^t\text{BuTzPh})]\text{Br}_2$ .

Re(1)-C(12)	1.899(2)
Re(1)-C(11)	1.913(2)
Re(1)-C(13)	1.915(2)
Re(1)-N(1)	2.2067(19)
Re(1)-Br(2)	2.6414(2)
Re(1)-Br(1)	2.6499(2)
Re(2)-C(21)	1.899(2)
Re(2)-C(22)	1.907(2)
Re(2)-C(23)	1.919(3)
Re(2)-N(2)	2.185(2)
Re(2)-Br(2)	2.6390(2)
Re(2)-Br(1)	2.6411(2)
C(12)-Re(1)-C(11)	88.83(10)
C(12)-Re(1)-C(13)	87.73(10)
C(11)-Re(1)-C(13)	87.63(10)
C(12)-Re(1)-N(1)	96.76(9)
C(11)-Re(1)-N(1)	96.07(8)
C(13)-Re(1)-N(1)	174.22(9)
C(12)-Re(1)-Br(2)	92.61(7)
C(11)-Re(1)-Br(2)	178.24(7)
C(13)-Re(1)-Br(2)	93.44(7)
N(1)-Re(1)-Br(2)	82.75(5)
C(12)-Re(1)-Br(1)	174.25(7)
C(11)-Re(1)-Br(1)	96.92(7)
C(13)-Re(1)-Br(1)	92.18(7)
N(1)-Re(1)-Br(1)	82.98(5)
Br(2)-Re(1)-Br(1)	81.656(7)
C(21)-Re(2)-C(22)	89.99(10)
C(21)-Re(2)-C(23)	87.54(10)
C(22)-Re(2)-C(23)	87.61(10)
C(21)-Re(2)-N(2)	94.89(9)
C(22)-Re(2)-N(2)	92.66(9)
C(23)-Re(2)-N(2)	177.55(8)
C(21)-Re(2)-Br(2)	175.08(7)
C(22)-Re(2)-Br(2)	94.51(7)
C(23)-Re(2)-Br(2)	94.63(7)
N(2)-Re(2)-Br(2)	82.93(5)
C(21)-Re(2)-Br(1)	93.47(7)
C(22)-Re(2)-Br(1)	173.82(7)
C(23)-Re(2)-Br(1)	97.65(7)
N(2)-Re(2)-Br(1)	81.94(5)
Br(2)-Re(2)-Br(1)	81.867(7)
Re(2)-Br(1)-Re(1)	88.617(7)
Re(2)-Br(2)-Re(1)	88.841(7)

**Table 7.8:** Crystal data and structure refinement for  $[\text{Re}_2(\text{TzPh})_2]^-$ .

Identification code	$[\text{Re}_2(\text{TzPh})_2]^-$
Empirical formula	$\text{C}_{33}\text{H}_{35}\text{N}_{13}\text{O}_8\text{Re}_2$
Formula weight	1114.14
Temperature	100(2) K
Wavelength	0.71073 Å
Crystal system	Monoclinic
Space group	C2/n
Unit cell dimensions	a = 20.5571(5) Å b = 12.1245(2) Å c = 16.5533(4) Å $\beta = 105.931(3)^\circ$
Volume	3967.36(15) Å <sup>3</sup>
Z	4
Density (calculated)	1.865 Mg/m <sup>3</sup>
$\mu$	6.162 mm <sup>-1</sup>
Crystal size	0.37 × 0.22 × 0.11 mm <sup>3</sup>
$\theta$ range for data collection	3.44 to 30.00°.
Index ranges	-28 ≤ h ≤ 28, -17 ≤ k ≤ 17 -23 ≤ l ≤ 23
Reflections collected	41968
Independent reflections	5755 [R(int) = 0.0366]
Completeness to $\theta = 30.00^\circ$	99.7 %
Absorption correction	Analytical
Max. and min. transmission	0.589 and 0.292
Refinement method	Full-matrix least-squares on F <sup>2</sup>
Data / restraints / parameters	5755 / 0 / 290
Goodness-of-fit on F <sup>2</sup>	0.971
Final R indices [I > 2σ(I)]	R1 = 0.0180, wR2 = 0.0420
R indices (all data)	R1 = 0.0234, wR2 = 0.0428
Largest diff. peak and hole	3.567 and -0.809 e.Å <sup>-3</sup>

**Table 7.9:** Selected bond lengths [ $\text{\AA}$ ] and angles[ $^\circ$ ] for  $[\text{Re}_2(\text{TzPh})_2]^-$ .

Re(1)-C(2)	1.916(2)
Re(1)-C(3)	1.926(3)
Re(1)-C(1)	1.927(2)
Re(1)-N(23)	2.1748(19)
Re(1)-N(22) <sup>1</sup>	2.1792(19)
Re(1)-N(12)	2.209(2)
C(2)-Re(1)-C(3)	88.58(11)
C(2)-Re(1)-C(1)	89.85(10)
C(3)-Re(1)-C(1)	89.87(10)
C(2)-Re(1)-N(23)	177.42(8)
C(3)-Re(1)-N(23)	92.84(9)
C(1)-Re(1)-N(23)	92.31(9)
C(2)-Re(1)-N(22) <sup>1</sup>	93.52(9)
C(3)-Re(1)-N(22) <sup>1</sup>	92.57(9)
C(1)-Re(1)-N(22) <sup>1</sup>	175.89(8)
N(23)-Re(1)-N(22) <sup>1</sup>	84.27(7)
C(2)-Re(1)-N(12)	91.90(9)
C(3)-Re(1)-N(12)	178.90(8)
C(1)-Re(1)-N(12)	91.13(9)
N(23)-Re(1)-N(12)	86.64(7)
N(22) <sup>1</sup> -Re(1)-N(12)	86.42(7)
O(1)-C(1)-Re(1)	178.8(2)
O(2)-C(2)-Re(1)	179.2(2)
O(3)-C(3)-Re(1)	178.9(2)

Symmetry transformations used to generate equivalent atoms:<sup>1</sup> 1-x,y,3/2-z**Table 7.10:** Hydrogen bonds for  $[\text{Re}_2(\text{TzPh})_2]^-$ . [ $\text{\AA}$  and  $^\circ$ ].

D-H...A	d(D-H)	d(H...A)	d(D...A)	<(DHA)
N(1)-H(1)...O(4)	0.93	1.81	2.729(7)	169.4

**Table 7.11:** Crystal data and structure refinement for [ReTzPy]<sub>3</sub>.

Identification code	[ReTzPy] <sub>3</sub>
Empirical formula	C <sub>29</sub> H <sub>16</sub> Cl <sub>4</sub> N <sub>15</sub> O <sub>9</sub> Re <sub>3</sub>
Formula weight	1418.97
Temperature	180(2) K
Wavelength	0.71073 Å
Crystal system	Monoclinic
Space group	P2 <sub>1</sub> /n
Unit cell dimensions	a = 10.2409(2) Å b = 24.9665(5) Å c = 17.3333(3) Å β = 91.082(2)°
Volume	4430.98(15) Å <sup>3</sup>
Z	4
Density (calculated)	2.127 Mg/m <sup>3</sup>
μ	8.480 mm <sup>-1</sup>
Crystal size	0.37 × 0.03 × 0.03 mm <sup>3</sup>
θ range for data collection	2.84 to 28.00°.
Index ranges	-13 ≤ h ≤ 13, -32 ≤ k ≤ 32 -22 ≤ l ≤ 22
Reflections collected	83582
Independent reflections	10698 [R(int) = 0.0733]
Completeness to θ = 28.00°	99.9 %
Absorption correction	Analytical
Max. and min. transmission	0.784 and 0.261
Refinement method	Full-matrix least-squares on F <sup>2</sup>
Data / restraints / parameters	10698 / 0 / 569
Goodness-of-fit on F <sup>2</sup>	1.320
Final R indices [I > 2σ(I)]	R1 = 0.0801, wR2 = 0.1642
R indices (all data)	R1 = 0.0839, wR2 = 0.1659
Largest diff. peak and hole	4.094 and -1.964 e.Å <sup>-3</sup>

**Table 7.12:** Selected bond lengths [ $\text{\AA}$ ] and angles[ $^\circ$ ] for  $[\text{ReTzPy}]_3$ 

Re(1)-C(12)	1.887(13)
Re(1)-C(11)	1.915(13)
Re(1)-C(13)	1.959(13)
Re(1)-N(34)	2.145(10)
Re(1)-N(12)	2.181(10)
Re(1)-N(352)	2.199(11)
Re(2)-C(21)	1.905(13)
Re(2)-C(22)	1.908(16)
Re(2)-C(23)	1.929(15)
Re(2)-N(14)	2.171(10)
Re(2)-N(22)	2.176(11)
Re(2)-N(152)	2.213(12)
Re(3)-C(33)	1.890(18)
Re(3)-C(31)	1.924(15)
Re(3)-C(32)	1.930(14)
Re(3)-N(24)	2.145(12)
Re(3)-N(252)	2.190(12)
Re(3)-N(32)	2.195(10)
C(12)-Re(1)-C(11)	90.0(5)
C(12)-Re(1)-C(13)	90.7(5)
C(11)-Re(1)-C(13)	89.2(6)
C(12)-Re(1)-N(34)	95.6(4)
C(11)-Re(1)-N(34)	96.6(5)
C(13)-Re(1)-N(34)	171.4(5)
C(12)-Re(1)-N(12)	177.3(4)
C(11)-Re(1)-N(12)	89.4(5)
C(13)-Re(1)-N(12)	92.0(5)
N(34)-Re(1)-N(12)	81.8(4)
C(12)-Re(1)-N(352)	92.4(5)
C(11)-Re(1)-N(352)	170.5(5)
C(13)-Re(1)-N(352)	100.0(5)
N(34)-Re(1)-N(352)	74.0(4)
N(12)-Re(1)-N(352)	87.6(4)
C(21)-Re(2)-C(22)	87.3(6)
C(21)-Re(2)-C(23)	89.3(6)
C(22)-Re(2)-C(23)	90.9(5)
C(21)-Re(2)-N(14)	100.5(5)
C(22)-Re(2)-N(14)	95.4(5)
C(23)-Re(2)-N(14)	168.6(5)
C(21)-Re(2)-N(22)	92.0(5)
C(22)-Re(2)-N(22)	173.1(5)
C(23)-Re(2)-N(22)	95.9(5)
N(14)-Re(2)-N(22)	78.0(4)
C(21)-Re(2)-N(152)	174.3(5)
C(22)-Re(2)-N(152)	94.8(5)

Continued from previous page

C(23)-Re(2)-N(152)	95.9(5)
N(14)-Re(2)-N(152)	74.1(4)
N(22)-Re(2)-N(152)	85.3(4)
C(33)-Re(3)-C(31)	89.1(7)
C(33)-Re(3)-C(32)	90.6(7)
C(31)-Re(3)-C(32)	86.9(5)
C(33)-Re(3)-N(24)	169.4(6)
C(31)-Re(3)-N(24)	100.2(5)
C(32)-Re(3)-N(24)	95.0(5)
C(33)-Re(3)-N(252)	96.1(6)
C(31)-Re(3)-N(252)	174.5(5)
C(32)-Re(3)-N(252)	95.0(5)
N(24)-Re(3)-N(252)	74.5(4)
C(33)-Re(3)-N(32)	95.9(6)
C(31)-Re(3)-N(32)	92.4(5)
C(32)-Re(3)-N(32)	173.5(5)
N(24)-Re(3)-N(32)	78.8(4)
N(252)-Re(3)-N(32)	85.1(4)

**Table 7.13:** Crystal data and structure refinement for [Re-TzPhTpy].

Identification code	[Re-TzPhTpy]
Empirical formula	C <sub>40</sub> H <sub>25</sub> Cl <sub>9</sub> N <sub>9</sub> O <sub>3</sub> Re
Formula weight	1184.94
Temperature	100(2) K
Wavelength	0.71073 Å
Crystal system	Triclinic
Space group	P $\bar{1}$
Unit cell dimensions	a = 10.8953(3) Å b = 11.2245(3) Å c = 18.6620(4) Å $\alpha$ = 85.806(2)° $\beta$ = 82.125(2)° $\gamma$ = 82.588(2)°
Volume	2238.27(10) Å <sup>3</sup>
Z	2
Density (calculated)	1.758 Mg/m <sup>3</sup>
$\mu$	3.302 mm <sup>-1</sup>
Crystal size	0.37 × 0.19 × 0.05 mm <sup>3</sup>
$\theta$ range for data collection	2.72 to 37.32°.
Index ranges	-18 ≤ h ≤ 18, -18 ≤ k ≤ 19 -31 ≤ l ≤ 31
Reflections collected	82022
Independent reflections	22495 [R(int) = 0.0407]
Completeness to $\theta = 36.00^\circ$	99.8 %
Absorption correction	Analytical
Max. and min. transmission	0.852 and 0.410
Refinement method	Full-matrix least-squares on F <sup>2</sup>
Data / restraints / parameters	22495 / 0 / 559
Goodness-of-fit on F <sup>2</sup>	1.065
Final R indices [I > 2 $\sigma$ (I)]	R1 = 0.0299, wR2 = 0.0631
R indices (all data)	R1 = 0.0354, wR2 = 0.0653
Largest diff. peak and hole	1.711 and -1.548 e.Å <sup>-3</sup>



**Table 7.14:** Selected bond lengths [ $\text{\AA}$ ] and angles[ $^\circ$ ] for [Re-TzPhTpy].

Re(1)-C(1)	1.9099(17)
Re(1)-C(3)	1.9212(18)
Re(1)-C(2)	1.9359(17)
Re(1)-N(2)	2.1638(13)
Re(1)-N(11)	2.1735(14)
Re(1)-N(21)	2.1742(14)
C(1)-Re(1)-C(3)	88.88(7)
C(1)-Re(1)-C(2)	87.92(7)
C(3)-Re(1)-C(2)	87.48(7)
C(1)-Re(1)-N(2)	94.37(6)
C(3)-Re(1)-N(2)	92.68(6)
C(2)-Re(1)-N(2)	177.71(6)
C(1)-Re(1)-N(11)	172.29(6)
C(3)-Re(1)-N(11)	98.45(6)
C(2)-Re(1)-N(11)	94.74(6)
N(2)-Re(1)-N(11)	82.97(5)
C(1)-Re(1)-N(21)	96.53(6)
C(3)-Re(1)-N(21)	173.93(6)
C(2)-Re(1)-N(21)	95.43(6)
N(2)-Re(1)-N(21)	84.20(5)
N(11)-Re(1)-N(21)	76.04(5)

**Table 7.15:** Crystal data and structure refinement for [Re-TzPyTpy].

Identification code	[Re-TzPyTpy]
Empirical formula	C <sub>36</sub> H <sub>21</sub> N <sub>10</sub> O <sub>3</sub> Re·H <sub>2</sub> O
Formula weight	845.84
Temperature	100(2) K
Wavelength	0.71073 Å
Crystal system	Triclinic
Space group	P $\bar{1}$
Unit cell dimensions	a = 6.6242(3) Å b = 12.7559(4) Å c = 19.4567(6) Å $\alpha$ = 102.608(3)° $\beta$ = 90.982(3)° $\gamma$ = 91.645(3)°
Volume	1603.28(10) Å <sup>3</sup>
Z	2
Density (calculated)	1.752 Mg/m <sup>3</sup>
$\mu$	3.849 mm <sup>-1</sup>
F(000)	832
Crystal size	0.57 × 0.05 × 0.02 mm <sup>3</sup>
Reflections collected	17418
Independent reflections	8709 [R(int) = 0.0555]
Absorption correction	Analytical
Refinement method	Full-matrix least-squares on F <sup>2</sup>
Data / restraints / parameters	8709 / 17 / 454
Goodness-of-fit on F <sup>2</sup>	1.003
Final R indices [I > 2 $\sigma$ (I)]	R1 = 0.00453, wR2 = 0.0932
Largest diff. peak and hole	1.88 and -2.35 e.Å <sup>-3</sup>

**Table 7.16:** Selected bond lengths [ $\text{\AA}$ ] and angles $^{\circ}$ ] for [Re-TzPyTpy].

Re(1)-C(1)	1.924(5)
Re(1)-C(2)	1.917(5)
Re(1)-C(3)	1.928(6)
Re(1)-N(2)	2.183(4)
Re(1)-N(11)	2.172(3)
Re(1)-N(21)	2.179(4)
C(3)-Re(1)-C(1)	88.0(2)
C(1)-Re(1)-C(2)	89.3(2)
C(3)-Re(1)-C(2)	85.7(2)
C(1)-Re(1)-N(2)	92.7(2)
C(3)-Re(1)-N(2)	95.1(2)
C(2)-Re(1)-N(2)	177.9(2)
C(1)-Re(1)-N(11)	17.3(2)
C(3)-Re(1)-N(11)	101.2(2)
C(2)-Re(1)-N(11)	94.3(2)
N(2)-Re(1)-N(11)	83.6(1)
C(1)-Re(1)-N(21)	94.9(2)
C(3)-Re(1)-N(21)	177.1(2)
C(2)-Re(1)-N(21)	94.6(2)
N(2)-Re(1)-N(21)	84.6(1)
N(11)-Re(1)-N(21)	75.9(1)

**Table 7.17:** Hydrogen bonds for [Re-TzPyTpy]. [ $\text{\AA}$  and  $^{\circ}$ ].

D-H...A	d(D-H)	d(H...A)	d(D...A)	$\angle$ (DHA)
O(1)W-H(1)WA...N(82)	0.85(1)	2.01(2)	2.845(10)	169(6)
O(1)W-H(1)WA...N(82')	0.85(1)	2.12(2)	2.963(10)	173(5)
O(1)W-H(1)WB...N(4 <sup>i</sup> )	0.85(1)	2.12(2)	2.965(6)	177(6)

Symmetry code: (i) x+1,y,z.